

**EXPERIMENTAL AND NUMERICAL ANALYSIS  
OF FLOW AND HEAT TRANSFER IN  
DOUBLE SKIN FACADE CAVITIES**

**A Thesis Submitted to  
The Graduate School of Engineering and Sciences of  
Izmir Institute of Technology  
In Partial Fulfillment of the Requirements for the Degree of**

**DOCTOR OF PHILOSOPHY**

**in Architecture**

**by  
Tuğba İNAN**

**July 2016  
İZMİR**

We approve the thesis of **Tuğba İNAN**

**Examining Committee Members :**

---

**Assoc. Prof. Dr. Tahsin BAŞARAN**

Department of Architecture, Izmir Institute of Technology

---

**Prof. Dr. Aytunç EREK**

Department of Mechanical Engineering, Dokuz Eylül University

---

**Assoc. Prof. Dr. Mustafa Emre İLAL**

Department of Architecture, Izmir Institute of Technology

---

**Prof. Dr. Serdar KALE**

Department of Architecture, Izmir Institute of Technology

---

**Assoc. Prof. Dr. Müjde Altın**

Department of Architecture, Dokuz Eylül University

**28 July 2016**

---

**Assoc. Prof. Dr. Tahsin BAŞARAN**

Supervisor, Department of Architecture  
Izmir Institute of Technology

---

**Assoc. Prof. Dr. Şeniz ÇIKIŞ**

Head of the Department of Architecture

---

**Prof. Dr. Bilge KARAÇALI**

Dean of the Graduate School of  
Engineering and Sciences

## **ACKNOWLEDGMENTS**

I would like to gratefully thank to my supervisor Assoc. Prof. Dr. Tahsin BAŞARAN for his supervision, encouragement, instructive comments and for providing a productive atmosphere throughout my thesis study. I also thank to my thesis progress juries Prof. Dr. Aytunç EREK and Assoc. Prof. Dr. Mustafa Emre İLAL for their technical supports and suggestions. I would like to express special thanks to Assist. Prof. Dr. Mehmet Akif EZAN for his supports and assistance.

I sincerely thank to my friends Pınar KUTLUAY and Betül PERÇİN for their all friendly help and supports.

This study was supported by the Scientific and Technological Research Council of Turkey (TÜBİTAK) Foundation under Grant 112M170. I also thank to TÜBİTAK for its financial support.

Finally, I would like to express my gratitude to my parents Mehmet and Sultan İNAN and my brother Zeynel İNAN for their encouragement, help, immense patience and trust throughout my education and in every moment of my life. This thesis would not have accomplished without their endless supports.

# **ABSTRACT**

## **EXPERIMENTAL AND NUMERICAL ANALYSIS OF FLOW AND HEAT TRANSFER IN DOUBLE SKIN FACADE CAVITIES**

In this study, airflow and heat transfer in a double skin facade (DSF) cavity were examined numerically and experimentally under natural and forced flow conditions. An experimental setup was constructed in the laboratory environment. Experiments were performed for two different DSF's airflow modes; buffer zone and external air channel. These experiments were conducted with and without a solar simulator integrated to the system. Furthermore, the effect of pressure drop elements in the cavity of DSF were analyzed experimentally. After the numerical results (CFD and nodal network) were verified with experimental measurements, dimensionless heat transfer correlations were developed for the natural and forced convections. As a result, an extensive experimental data set was obtained for different working conditions of DSF. So, the dimensionless pressure loss coefficients were calculated experimentally based on the geometric configuration of the pressure drop elements in the cavity. In natural convection, with Rayleigh numbers ranging from  $8.59 \times 10^9$  to  $1.41 \times 10^{10}$  and the increasing tendency of the average Nusselt numbers from 142.6 to 168.8 were shown. A correlation for a cavity characteristic length of 0.116 was constructed to evaluate the heat flux. In forced convection, another dimensionless correlations were developed to predict the heat transfer by using Nusselt numbers with the Reynolds numbers ranging from 28000 to 56000 for a DSF with an external airflow mode. These correlations could be used for different characteristic lengths ranged between 0.1 and 0.16. These correlations were used for the energy performance of DSF applications for different directions and climatic zones in Turkey and compared with the single skin facade.



## ÖZET

### ÇİFT CİDARLI CEPHE KAVİTELERİNDEKİ AKIŞ VE ISI TRANSFERİNİN DENEYSEL VE SAYISAL ANALİZİ

Bu çalışmada, çift cidarlı cephe (ÇCC) kavitesindeki akış ve ısı transferi, doğal ve zorlanmış akış durumları için deneysel ve sayısal olarak irdelenmiştir. Deneysel bir düzenek laboratuvar ortamında kurulmuştur. Deneyler, tampon bölge ve dış hava perdesi akış modu olarak, çift cidarlı cephedeki iki farklı hava akış modu için gerçekleştirilmiştir. Bu deneyler, sisteme entegre bir solar simülatörü kullanımı ile ve simülatörsüz olarak gerçekleştirilmiştir. Ayrıca ÇCC kavitesindeki basınç düşürücü elemanların etkisi deneysel olarak analiz edilmiştir. Sayısal sonuçlar (CFD ve nodal ağ modeli) deneysel ölçümlerle doğrulandıktan sonra, doğal ve zorlanmış taşınım koşullarında, boyutsuz ısı transfer korelasyonları geliştirilmiştir. Sonuç olarak ÇCC'deki farklı çalışma koşulları için geniş bir deneysel veri takımı elde edilmiştir. Buna göre, boyutsuz basıç kayıp katsayıları, kavitedeki basıç düşürücü elemanın geometrik konfigürasyonuna bağlı olarak, deneysel olarak hesaplanmıştır. Doğal taşınımında, Rayleigh sayısının  $8.59 \cdot 10^9$  ile  $1.41 \cdot 10^{10}$  aralığındaki değişimi için, ortalama Nusselt sayılarında; 142.6'dan 168.8'e artan bir eğilim görülmüştür. Elde edilen boyutsuz ısı transferi korelasyonu, kavite en-boy oranının 0.116 olduğu kavite için geliştirilmiştir. Zorlanmış taşınımında, dış hava perdesi akış modunun olduğu ÇCC'de ısı transferini belirlemek için, 28000 ile 56000 aralığında değişen Reynolds sayılarına karşılık; Nusselt sayısı için başka boyutsuz korelasyonlar geliştirilmiştir. Bu korelasyonlar, 0.1 ile 0.16 aralığındaki farklı kavite karakteristik uzunluklar için kullanılabilir. Doğal ve zorlanmış akış için elde edilen bu korelasyonlar, Türkiye'deki farklı iklim bölgelerindeki ve farklı yönlerdeki ÇCC uygulamalarının enerji performansı için kullanıldı ve tek cidarlı cephe ile karşılaştırıldı.

# TABLE OF CONTENTS

LIST OF TABLES .....	xi
LIST OF FIGURES .....	xiii
CHAPTER 1. INTRODUCTION .....	21
1.1. Purpose of the Study .....	22
1.2. Significance of the Study .....	23
1.3. Limits of the Study.....	25
1.4. Methodology .....	26
CHAPTER 2. LITERATURE .....	29
2.1. Experimental Studies on Double Skin Facades .....	29
2.1.1. Saelens's Experimental Study .....	29
2.1.2. Stec's Experimental Study .....	31
2.1.3. Corgnati, Porino and Serra's Experimental Study .....	31
2.1.4. Zanghirella's Experimental Study .....	32
2.1.5. Gavan's Experimental Study .....	33
2.2. Other Studies related to DSF .....	33
CHAPTER 3. EFFECTIVE DESIGN DECISIONS ON ENERGY	
PERFORMANCE OF DOUBLE SKIN FACADES .....	40
3.1. General View on Double Skin Facades.....	40
3.2. Definitions of Double-Skin Facade Systems .....	42
3.3. Classification of Double-Skin Facade Systems .....	43
3.3.1. Architectural Configuration Issues of Double Skin Facades.....	44
3.3.1.1. Double Skin Facade Types.....	46
3.3.2. Ventilation Types in the cavity.....	49
3.3.3. Airflow modes in the cavity.....	50
3.4. Samples of Buildings with Double Skin Facade.....	52
3.4.1. DSF Practices in the World.....	52
3.4.1.1. Dusseldorf City Gate .....	53

3.4.1.2. Deichtor Office Building .....	54
3.4.1.3. GSW Building.....	55
3.4.1.4. Sysopen Tower .....	57
3.4.1.5. Moravian Library .....	58
3.4.1.6. Watling House.....	59
3.4.1.7. Greater London Authority (GLA).....	60
3.4.1.8. Beetham Tower .....	61
3.4.1.9. Sanomatalo.....	62
3.4.1.10. Arlanda, Pir F, Sigtuna .....	63
3.4.1.11. DVV Building .....	64
3.4.1.12. Seattle Justice Centre .....	65
3.4.2. DSF Practices in Turkey .....	66
3.4.2.1. İstanbul Sapphire .....	66
3.4.2.2. Küçükçekmece Municipal Services Building.....	68
3.4.2.3. Istanbulbloom .....	70
3.4.2.4. Ankara Telecom Headquarter .....	72
3.5. Advantages-Disadvantages of Double-Skin Facade Systems.....	74
3.6. Design Considerations .....	80
3.6.1. Daylighting .....	80
3.6.2. Glazing.....	81
3.6.3. Building Geometry/Design.....	82
3.6.4. Solar shading devices .....	83
3.6.5. Climatic Conditions .....	84
3.6.6. Width of cavity .....	85
3.6.7. Height of facade and size of openings.....	85
3.6.8. Orientation of DSFs.....	86
 CHAPTER 4. DOUBLE SKIN FACADE: EXPERIMENTAL SETUP .....	 90
4.1. Experimental Setup: Indoor Environment (I) .....	91
4.2. Experimental Room: Outdoor Environment (II).....	95
4.3. Experimental Room: Intermediate Partition (Cavity-III) .....	95
4.4. Solar Simulator Unit (VI) .....	96
4.5. Mechanical Ventilation System (VII) .....	97

4.6. Ventilation of Solar Simulator.....	100
4.7. HIOKI Data Logger (LR 8402-20) .....	101
4.8. Measurement Systems .....	102
4.8.1. EKO MS-410 Pyranometer .....	102
4.8.2. Differential Pressure Measurement (DPT 2500-R8 model) .....	102
4.8.3. Velocity Measurement between Double Skin Facades.....	103
4.8.4. Temperature Measurements .....	104
4.9. Experimental Study.....	108
4.10. Calibration Process .....	111
4.11. Uncertainty Analysis .....	119
 CHAPTER 5. EXPERIMENTAL AND NUMERICAL ANALYSIS .....	 122
5.1. Case 1: Experimental investigation of the pressure loss through the DSF by using perforated plates .....	 122
5.1.1. Experimental setup.....	123
5.1.2. Perforated plates.....	123
5.1.3. Experimental results and discussions.....	125
5.2. Case 2: Experimental and numerical investigation of natural convection in a DSF by using CFD tool .....	 135
5.2.1. Experimental setup.....	135
5.2.2. Experimental results.....	137
5.2.3. Numerical Study.....	141
5.2.3.1. Meshing and solution method.....	141
5.2.3.2. The validation of the solution method .....	143
5.2.3.3. Numerical model.....	145
5.2.3.4. Results and Discussions.....	147
5.3. Case 3: Experimental and numerical investigation of forced convection in a double skin facade by using CFD tool .....	 154
5.3.1. Experimental Study .....	154
5.3.2. Numerical Study.....	164
5.3.3. Numerical Results .....	165
5.3.3.1. Velocity changes on the horizontal lines which are in the middle of the channel: Cavity 25 cm .....	 166

5.3.3.2. Velocity changes on the horizontal lines which are in the middle of the channel: Cavity 32.5 cm.....	168
5.3.3.3. Velocity changes on the horizontal lines which are in the middle of the channel: Cavity 40 cm .....	169
5.3.3.4. Temperature changes on the top horizontal line which is located in the middle of the channel.....	171
5.3.3.5. Distributions of velocity on the vertical section in the middle of the channel: Cavity 25 cm .....	174
5.3.3.6. Distributions of velocity on the vertical section in the middle of the channel: Cavity 32.5 cm .....	175
5.3.3.7. Distributions of velocity on the vertical section in the middle of the channel: Cavity 40 cm .....	175
5.3.3.8. Velocity Streamlines in the vertical section in the middle of the channel: Cavity 25 cm .....	176
5.3.3.9. Velocity Streamlines in the vertical section in the middle of the channel: Cavity 32.5 cm .....	177
5.3.3.10. Velocity Streamlines in the vertical section in the middle of the channel: Cavity 40 cm .....	178
5.3.3.11. The average pressure drop on the vertical section in the middle of the channel: Cavity 25 cm .....	179
5.3.3.12. Temperature distributions on the vertical section in the middle of the cavity: Cavity 25cm .....	181
5.3.3.13. Temperature distributions on the vertical section in the middle of the cavity: Cavity 32.5 cm .....	182
5.3.3.14. Temperature distributions on the vertical section in the middle of the cavity: Cavity 40 cm .....	183
5.4. Case 4: Experimental and numerical investigation of forced convection in a double skin facade by using nodal network approach .....	193
5.4.1. Experimental inputs .....	193
5.4.2. Nodal Network Approach .....	195
5.4.3. Discussion and Results of Steady-State Study .....	200
5.4.4. Discussion and Results of Unsteady Study .....	209

5.5. Case 5: Experimental and numerical investigation of natural convection in a double skin facade by using nodal network approach.....	222
5.5.1. Experimental results.....	222
5.5.2. Thermal Balance of the Experimental System.....	227
5.5.3. Nodal Network Approach and the numerical results .....	230
5.5.4. Discussion and Results of Unsteady Study .....	238
CHAPTER 6. CONCLUSIONS .....	242
REFERENCES .....	246
APPENDIX A. MEASUREMENT DEVICES .....	259

# LIST OF TABLES

<b><u>Table</u></b>	<b><u>Page</u></b>
Table 2.1. Pressure drop ( $\Delta P$ ) elements in the DSF cavity on the literature.....	40
Table 3.1. Investigated DSFs in the world .....	52
Table 3.2. Advantages of Double Skin Facades (2001-2015).....	75
Table 3.3. Disadvantages of Double Skin Facades (2001-2015) .....	77
Table 4.1. Experimental study list.....	108
Table 4.2. PT-100 reference and measurement values in 3-9 channel (in °C) .....	112
Table 4.3. Thermocouple reference and measurement values in 2-9 channel (in °C).....	112
Table 4.4. Calibration of flow meter .....	114
Table 4.5. Measurement results of heat flux .....	116
Table 4.6. Calibration due to the position of the pyranometer.....	119
Table 4.7. The uncertainty value of each independent property used in experimental studies.....	120
Table 5.1. General parameters used in the case studies .....	122
Table 5.2. Characteristics of the perforated plates .....	124
Table 5.3. Experimental results.....	128
Table 5.4. Air flow measurements in the duct and the variation of pressure drop induced by using distinct perforated plates in the cavity.....	131
Table 5.5. Effect of the hole geometric parameters upon the dimensionless pressure loss coefficient, $E_u$ (Malavasi et al, 2012).....	134
Table 5.6. Experimental measurement values and calculated Rayleigh numbers .....	147
Table 5.7. Average Nusselt numbers at the hot surface of the cavity for each experimental case.....	152
Table 5.8. Experimental results (CFD inputs) .....	157
Table 5.9. CFD outputs of heat and mass transfer rates for Experiment 1 .....	188
Table 5.10. CFD outputs and energy/mass balance .....	186
Table 5.11. Average Nusselt and Reynold numbers at the PF surface of the cavity for each experimental case.....	189
Table 5.12. Experimental inputs .....	194

Table 5.13. Convection and radiation coefficients and related Nusselt and Reynolds numbers.....	201
Table 5.14. Experimental measurements .....	223
Table 5.15. Heat transfer rate values using constant temperature water bath.....	227
Table 5.16. Heat loss/gain values from/to the indoor environment. ....	228
Table 5.17. Heat transfer convective coefficients, $h_{ca}$ in the cavity's surfaces namely SF and PF.....	233
Table 5.18 Heat transfer convective coefficients, $h_{in}$ in the inside's surface .....	235



# LIST OF FIGURES

<b><u>Figure</u></b>	<b><u>Page</u></b>
Figure 3.1. Effective parameters on Double Skin Facades .....	44
Figure 3.2. Effective parameters on Double Skin Facades .....	45
Figure 3.3. Box window facade .....	46
Figure 3.4. Shaft-box façade .....	47
Figure 3.5. Multi-storey facade.....	48
Figure 3.6. Main airflow modes in the cavity .....	51
Figure 3.7. Düsseldorf Stadttor Building .....	53
Figure 3.8. Deichtor Office Building .....	54
Figure 3.9. GSW building .....	55
Figure 3.10. SysOpen Tower .....	57
Figure 3.11. Moravian Library .....	58
Figure 3.12. Watling House .....	59
Figure 3.13. Greater London Authority .....	60
Figure 3.14. Beetham Tower .....	61
Figure 3.15. Sanomatalo .....	62
Figure 3.16. Arlanda, Pir F, Sigtuna .....	63
Figure 3.17. DVV Building .....	64
Figure 3.18. Seattle Justice Centre .....	65
Figure 3.19. İstanbul Sapphire .....	66
Figure 3.20. Küçükçekmece Municipal Services Building .....	68
Figure 3.21. Istanbulbloom building .....	70
Figure 3.22. Ankara Telecom Headquarter .....	72
Figure 3.23. The percentages of the advantages of DSFs mentioned by some researchers on literature .....	79
Figure 3.24. The percentages of the disadvantages of DSFs mentioned by some researchers on literature .....	79
Figure 4.1. Experimental Setup .....	90
Figure 4.2. Layout of the experimental setup .....	91
Figure 4.3. Experimental setup plan .....	93

Figure 4.4. Indoor environment of the experimental room and the cooling-heating water bath.....	94
Figure 4.5. Outdoor environment of the experimental setup and the cooling unit .....	95
Figure 4.6. Cavity of experimental room and moving mechanism .....	96
Figure 4.7. Solar simulator unit .....	97
Figure 4.8. Fan system and its connections .....	98
Figure 4.9. General view of the channel system.....	99
Figure 4.10. Entry organization to the double skin facade at the outdoor environment simulating portion of the experimental setup .....	99
Figure 4.11. Determination of channel air flow rate.....	100
Figure 4.12. Ventilation of solar simulator .....	101
Figure 4.13. HIOKI Data Logger.....	101
Figure 4.14. MS-410 Pyranometer and its position on the experimental room.....	102
Figure 4.15. Differential pressure measurement system.....	103
Figure 4.16. Velocity measurement system .....	104
Figure 4.17. Surfaces on the Double Skin Facade .....	105
Figure 4.18. Layout of thermocouples inside the cavity (in cm) .....	105
Figure 4.19. Temperature measurement points at indoor and outdoor simulation rooms of experimental set up (in cm) .....	106
Figure 4.20. Temperature measurement points at indoor simulation room .....	106
Figure 4.21. Temperature measurement points on cavity surfaces .....	107
Figure 4.22. Calibration device.....	111
Figure 4.23. Calibration curve of temperature values in 3-9 PT-100 channel.....	113
Figure 4.24. Calibration curve of temperature values in 2-9 termocouple channel.....	113
Figure 4.25. Radiation measuring points on the outer glass surface .....	115
Figure 4.26. Heat flux distribution curves for the first and second measurement.....	117
Figure 4.27. Heat flux for 25 cm cavity.....	118
Figure 4.28. Heat flux for 35 cm cavity.....	118
Figure 5.1. Two different perforated plates.....	123
Figure 5.2. Plans and dimensions of perforated plates (in mm) .....	124
Figure 5.3. Layout of perforated plates in the cavity of DSF .....	125

Figure 5.4. Temperature distributions in the cavity at the bottom (b) and top (t) levels for three experiments (1, 4 and 7) on big (B) hole perforated plate.....	126
Figure 5.5. Temperature distributions in the cavity at the bottom (b) and top (t) levels for three experiments (3, 6 and 9) on big (S) hole perforated plate.....	127
Figure 5.6. Pressure drop on small hole perforated plate for three distinct flow rates for the experiments numbered S1, S2 and S3.....	129
Figure 5.7. Pressure drop on big hole perforated plate for three distinct flow rates for the experiments numbered B1, B2 and B3. ....	130
Figure 5.8. Variation of pressure drop induced by using distinct perforated plates and flow rate .....	133
Figure 5.9. Dimensionless pressure loss coefficients versus Reynolds numbers. ....	133
Figure 5.10. General view of the experimental setup .....	136
Figure 5.11. Plan view of the experimental setup .....	136
Figure 5.12. Layout of the thermocouples in the cavity .....	137
Figure 5.13. Variation of temperature in the cavity surfaces for the first experiment ..	138
Figure 5.14. Variation of temperature in both interior surfaces along the cavity height for the first experiment.....	138
Figure 5.15. Variation of temperatures in both inner surfaces along the cavity height for the first experiment .....	139
Figure 5.16. Variation of air temperature in the cavity for the first experiment .....	140
Figure 5.17. Variation of temperature in the cavity for the first experiment .....	140
Figure 5.18. Grid configurations.....	141
Figure 5.19. The velocity profile and variation of the Nusselt number on the hot surface .....	144
Figure 5.20. Velocity and temperature fields on the $z = L/2$ plane.....	144
Figure 5.21. Test room geometry and boundary conditions .....	145
Figure 5.22. Velocity variations inside the cavity for different numerical experiments at $y=1.73$ m .....	147
Figure 5.23. Temperature variations on the $z = L/2$ plane for different Ra numbers ...	148
Figure 5.24. The temperature distributions along the cavity width for different numerical experiments at $y=1.73$ m.....	149

Figure 5.25. Variations of the heat fluxes along the cavity height at the cold and hot surfaces for different numerical experiments .....	150
Figure 5.26. Variations of the Nusselt numbers at the hot surface along the cavity height for different numerical experiments.....	151
Figure 5.27. Nusselt numbers as a function of Rayleigh numbers for the experimental case.....	152
Figure 5.28. The mechanism which is used to adjust the depth of the cavity and the cavity air inlet vent.....	154
Figure 5.29. Model geometry.....	155
Figure 5.30. Variation of temperature from indoor environment to the outdoor environment for the 25 cm cavity width condition (Exp1, Exp2 and Exp3).....	158
Figure 5.31. Variation of temperature from indoor environment to the outdoor environment for the 32.5 cm cavity width condition (Exp4, Exp5 and Exp6).....	160
Figure 5.32. Variation of temperature from indoor environment to the outdoor environment for the 32.5 cm cavity width condition (Exp7, Exp7 and Exp9).....	162
Figure 5.33. Grid configurations.....	164
Figure 5.34. Velocity profiles and experimental measurement results at different cavity heights (Cavity: 25 cm, low flow).....	166
Figure 5.35. Velocity profiles and experimental measurement results at different cavity heights (Cavity: 25 cm, medium flow) .....	166
Figure 5.36. Velocity profiles and experimental measurement results at different cavity heights (Cavity: 25 cm, high flow) .....	166
Figure 5.37. Velocity profiles and experimental measurement results at different cavity heights (Cavity: 32.5 cm, low flow).....	167
Figure 5.38. Velocity profiles and experimental measurement results at different cavity heights (Cavity: 32.5 cm, medium flow) .....	168
Figure 5.39. Velocity profiles and experimental measurement results at different cavity heights (Cavity: 32.5 cm, high flow) .....	168
Figure 5.40. Velocity profiles and experimental measurement results at different cavity heights (Cavity: 40 cm, low flow).....	169

Figure 5.41. Velocity profiles and experimental measurement results at different cavity heights (Cavity: 40 cm, medium flow) .....	170
Figure 5.42. Velocity profiles and experimental measurement results at different cavity heights (Cavity: 40 cm, high flow) .....	170
Figure 5.43. Numerical temperature profiles and their comparison with the experimental results (Cavity: 25 cm, three different flow rates) .....	171
Figure 5.44. Numerical temperature profiles and their comparison with the experimental results (Cavity: 32.5 cm, three different flow rates) .....	172
Figure 5.45. Numerical temperature profiles and their comparison with the experimental results (Cavity: 40 cm, three different flow rates) .....	172
Figure 5.46. Distributions of velocity on the vertical section (Cavity: 25 cm.....	173
Figure 5.47. Velocity distributions in the vertical section: Cavity: 32.5 cm.....	174
Figure 5.48. Velocity distributions on the vertical section: Cavity 40 cm.....	175
Figure 5.49. Streamlines in the velocity field through the DSF's cavity for different mass flow rates (Cavity: 25 cm).....	176
Figure 5.50. Streamlines in the velocity field through the DSF's cavity for different mass flow rates (Cavity: 32.5 cm).....	177
Figure 5.51. Streamlines in the velocity field through the DSF's cavity for different mass flow rates (Cavity:40 cm).....	178
Figure 5.52. Pressure drops: cavity: 25 cm.....	179
Figure 5.53. Pressure drop: Cavity :32.5 .....	179
Figure 5.54. Pressure drop: Cavity :40 cm .....	179
Figure 5.55. Temperature distributions through the DSF's cavity for different mass flow rates (Cavity: 25 cm) .....	181
Figure 5.56. Temperature distributions through the DSF's cavity for different mass flow rates (Cavity: 32.5 cm) .....	182
Figure 5.57. Temperature distributions through the DSF's cavity for different mass flow rates (Cavity: 40 cm.....	183
Figure 5.58. Variations of the Nusselt numbers at the hot surface along the cavity height for different flow rates (cavity width: 25 cm).....	187
Figure 5.59. Variations of the Nusselt numbers at the hot surface along the cavity height for different flow rates (cavity width 32.5 cm).....	187

Figure 5.60. Variations of the Nusselt numbers at the hot surface along the cavity height for different flow rates (cavity width 40 cm).....	187
Figure 5.61. Nusselt numbers as a function of Reynolds numbers for the experimental cases 1, 2 and 3.....	189
Figure 5.62. Nusselt numbers as a function of Reynolds numbers for the experimental cases 4, 5 and 6.....	190
Figure 5.63. Nusselt numbers as a function of Reynolds numbers for the experimental cases 7, 8 and 9.....	190
Figure 5.64. Nusselt numbers as a function of Reynold numbers for the averages of Reynolds and Nusselt numbers.....	191
Figure 5.65. Schematic view of DSF.....	194
Figure 5.66. Nodal model of DSF.....	196
Figure 5.67. Temperatures by measurements and nodal model.....	201
Figure 5.68. Temperatures by measurements and nodal model.....	203
Figure 5.69. Temperatures by measurements and nodal model.....	204
Figure 5.70. Temperatures by measurements and nodal model.....	205
Figure 5.71. Temperatures by measurements and nodal model.....	206
Figure 5.72. Temperatures by measurements and nodal model.....	207
Figure 5.73. Temperature distribution for north and south facade on January at 12 am.....	209
Figure 5.74. Heat transfer rate per unit area due to temperature difference for DSF using monthly average daily climatic data in January for İstanbul. ....	210
Figure 5.75. Heat transfer rate per unit area due to temperature difference for DSF using monthly average daily climatic data in July for İstanbul. ....	210
Figure 5.76. Schematic view and nodal model of Single Skin Facade (SSF) .....	211
Figure 5.77. Heat transfer rate per unit area due to temperature difference for SSF using monthly average daily climatic data in January for İstanbul .....	212
Figure 5.78. Heat transfer rate per unit area due to temperature difference for SSF using monthly average daily climatic data in July for İstanbul .....	213
Figure 5.79. Heat gain from the solar radiation transmitted from SF and PF of DSF by using monthly average daily data of January in İstanbul for different directions .....	213

Figure 5.80. Heat gain from the solar radiation transmitted from SSF by using monthly average daily data of January in İstanbul for different directions .....	214
Figure 5.81. Heat gain from the solar radiation transmitted from SF and PF of DSF by using monthly average daily data of July in İstanbul for different directions .....	214
Figure 5.82. Heat gain from the solar radiation transmitted from SSF by using monthly average daily data of July in İstanbul for different directions ....	215
Figure 5.83. Air energy rate gain per unit area of DSF through the cavity by using monthly average daily data of January in İstanbul for different directions .....	216
Figure 5.84. Air energy rate gain per unit area of DSF through the cavity by using monthly average daily data of July in İstanbul for different directions.....	217
Figure 5.85. Heat transfer comparision of DSF and SSF for different orientation and season in İstanbul .....	218
Figure 5.86. Heat transfer comparision of DSF and SSF for different orientation and season in İstanbul .....	218
Figure 5.87. Heat transfer comparision of DSF and SSF for different orientation and season in İzmir .....	220
Figure 5.88. Variation of temperature in the cavity surfaces for the first experiment.....	222
Figure 5.89. Variation of temperature in both interior surfaces along the cavity height for the first experiment.....	223
Figure 5.90. Variation of temperatures in both inner surfaces along the cavity height for the first experiment (Exp.1).....	224
Figure 5.91. Variation of air temperature in the cavity for the first experiment.....	224
Figure 5.92. Variation of the temperature from the indoor to the outdoor environment for the Experiments numbered 1, 3 and 5.....	225
Figure 5.93. Variation of the temperature from the indoor to the outdoor environment for the Experiments numbered 2, 4 and 6.....	226
Figure 5.94. Schematic view of DSF .....	229
Figure 5.95. Nodal model of DSF.....	229

Figure 5.96. Temperatures measurements (denoted by M) versus nodal network model results (denoted by N) for the experiment numbered 46 .....	235
Figure 5.97. Temperatures measurements (denoted by M) versus nodal network model results (denoted by N) for the experiment numbered 47 .....	235
Figure 5.98. Temperatures measurements (denoted by M) versus nodal network model results (denoted by N) for the experiment numbered 48 .....	236
Figure 5.99. Temperatures measurements (denoted by M) versus nodal network model results (denoted by N) for the experiment numbered 49 .....	236
Figure 5.100. Temperatures measurements (denoted by M) versus nodal network model results (denoted by N) for the experiment numbered 50 .....	237
Figure 5.101. Temperatures measurements (denoted by M) versus nodal network model results (denoted by N) for the experiment numbered 51 .....	237
Figure 5.102. Heat transfer rate per unit area due to temperature difference for DSF and SSF using monthly average of January daily climatic data in Ankara for south direction .....	238
Figure 5.103. Heat gain from the solar radiation transmitted from DSF and SSF by using monthly average daily data of January in Ankara for south direction.....	238
Figure 5.104. Heat transfer rate per unit area due to temperature difference for DSF and SSF using monthly average of July daily climatic data in Ankara for south direction .....	239
Figure 5.105. Heat gain from the solar radiation transmitted from DSF and SSF by using monthly average daily data of July in Ankara for south different directions .....	239
Figure 5.106. Heat transfer comparison of DSF and SSF for different orientation in Ankara for January .....	240
Figure 5.107. Heat transfer comparison of DSF and SSF for different orientation in Ankara for July.....	240



# CHAPTER 1

## INTRODUCTION

The search for sustainable buildings increasingly occupy a significant role in architecture. In national as well as international scale, this concern leads authorities to redefine building performance standards and demands for a revision of architectural thinking. In this respect, in architectural discourse, it is possible to notice a rising interest in building skin configurations which promise to help minimizing the loss of energy while maximizing its gain.

Innovative facade concepts are today more relevant than ever. The demand for natural ventilation in commercial buildings is increasing due to growing environmental consciousness while at the same time energy consumption for buildings has to be reduced. An advanced facade should allow for a comfortable indoor climate, sound protection and good lighting, while minimizing the demand for auxiliary energy input.

Double skin facade (DSF) is an envelope construction consisting of two transparent facades separated by a cavity. Each of these two facades is commonly called a skin. A cavity -having a width which can range from several centimeters to several meters – can be located between these two skins. (Saelens, 2002). An adjustable sun-shading device is usually installed in this cavity for solar energy.

The DSF is rapidly becoming a common design feature in European architecture, driven by the following main factors (Poirazis, 2006):

- the aesthetic desire for an all glass-facade that leads to increased transparency, creation of a closer link to the outside,
- the practical need for a more natural indoor environment,
- the need for supporting the acoustic comfort in buildings against the noise polluted areas,
- the reduction of energy uses during the occupation stage of a building.

Moreover, they can provide a thermal zone, solar preheating of HVAC system, wind and pollutant protection with open windows, night cooling, protection of shading devices.

It is possible to see that the use of double skin glass facades globally pervades. These systems are nowadays accepted by many architects and developers in the world. The basic presumption behind this global proliferation is that, considering the climatic conditions, the double-skin glass facades can provide the advantages of energy gaining and controlled ventilation. However, this technology still has several unknowns that need to be questioned. Because, not all the DSF buildings show great performance in the last years. This mostly depends on the architectural design decisions in the initial part of the architectural design stage. If a DSF system has not properly designed, it causes many problems. For instance, if the temperature in the cavity increases, overheating problem can occur in the cavity and interior space. This condition adversely affects on thermal comfort. The usages of air conditioning systems are required in order to overcome the overheating problem. But this time, the energy consumption in the building will increase. This study examines the architectural feasibility of DSF systems with highlighting local climatic conditions. Effective design factors on energy performance of DSF systems are examined in detail with experimental measurements and numerical analysis rather than a simple design assumptions accepted by an architect.

An extensive data set detailing air and surface temperatures on the DSF, together with airflow rates will be measured and provided for different climatic conditions in Turkey with the comprehensive analysis. On the other hand, fluid flow and heat transfer are investigated numerically and experimentally. Thus, nondimensional heat transfer correlations are developed for natural and forced flow conditions inside the cavity of DSF. Another significant study in this thesis is to analyze the effect of pressure drop elements in the cavity.

## **1.1. Purpose of the Study**

All over the world DSF applications multiply day by day. This technology is still quite new in our country and it is not possible to find many applications or researches done on this subject. This interdisciplinary study aims to be a technical questioning which excludes the presumptions hidden in the architectural discourse and handles the subject in a scientific, unbiased way. DSF systems have a high initial investment costs and a minor design fault can led to serious economic losses. Moreover,

increases in the extra heating/cooling loads can cause increases in the operating costs. The aim of the study includes not only an understanding related to the behavior of DSF, but also it includes developing different design strategies based on the climatic zones of Turkey. Simply, the main objective of the study is to examine the energy performance of DSF systems and bring investigate the use of double-skin glass facades in Turkey. This study may open the door for the local production of alternative energy efficient DSF systems in Turkey. Moreover, dimensionless correlations are developed for heat transfer calculations. The effect of pressure drop elements inside the DSF cavity are also investigated in this thesis.

Secondary objectives of the study are as follows:

- To adapt DSFs to the local climatic and production conditions with increasing the energy efficiency.
- To develop recommendations on the implementations of DSFs which are not defined in the Energy Performance of Building Regulation.
- To differentiate the configurations of DSF according to the local conditions and thus, provide flexibility for different architectural designs
- To develop appropriate strategies for DSFs with analyzing the energy performance of these systems on different climatic and flow (natural and forced) conditions.
- To analyze the DSFs considering the effects of elements in the cavity that create pressure drop by performing energy performance and fluid flow.
- To suggest appropriate energy efficient solutions with the evaluation of the parameters affecting air flow and energy performance on different configurations of DSFs.

## **1.2. Significance of the Study**

The build environment in Turkey has a great potential for improving its sustainable development. Office and commercial buildings are using a great percentage of the total energy. Thus it is important to develop buildings that consume less operational energy during its life cycle. Especially in moderate to cold climates like Northern Europe new concepts were tested. They took into account the outdoor

conditions and tried to create a climatic responsive building (Givoni, 1992; Szokolay 1980; Wigginton, 1996). Especially for the top-end market sector advanced facade technologies were developed (Wigginton, 2002). They tried to integrate more and more building services into the facade system. This has the advantage of reducing the space needed inside the building and reducing initial overall costs.

One promising development of advanced facade systems is the double skin facade (DSF). It is possible to see that the use of double-skin glass facades globally pervades. These systems use the least energy against changing climatic conditions and capable of establishing a balance between internal and external climate. Therefore, an efficient facade system which provides energy conservation in buildings is becoming a necessity to increase the energy performance of buildings. However, little work has been done on the behaviour of DSFs for different climatic conditions. This is particularly interesting since the building types and the climates are different in Turkey. This study takes the climatic factors into account to find out how the energy performance of a DSF can be developed in Turkey.

DSF systems have a common area of usage in Northern Europe and North America. However, the suitability of these systems on southern area and alternative design suggestions than can be applicable awaits to be investigated. Moreover, there are studies related to the energy and flow analysis in the cavity of DSF. However, a comprehensive study is not found relevant with the effect of pressure reducing element used in the cavity. Furthermore, the majority of analyzes focused on the energy performance-oriented examinations and detailed numerical flow analysis supported by experimental studies under controlled climatic environment in the laboratory condition have been limited. Most of the studies were realized for boundary conditions of cold climatic regions.

DSF technology is still quite new in our country and it is not possible to find many applications or researches done on this subject. There are no experimental studies on DSF specific to Turkey. Thus, the aim of filling this gap strengthens the significance of this study. The data obtained from this study will constitute an extensive data set for DSFs that can be applied in our country and obtained correlations can be useable for any applications limited in the conditions explained in the thesis. Thus, it will fill the gap in the literature. The obtained results from the study will have application potential. Because, the DSF technology is a new production area in building sector in Turkey.

This questioning may open the door for the local production of alternative energy-efficient facade systems in Turkey.

The significant contribution of this research would be that:

- a) Nondimensional heat transfer correlations were obtained for natural and forced flow in through the cavity of DSF
- b) Nondimensional pressure drop correlations were developed inside the DSF.
- c) Tests the applicability of the concept in different climatic zones in Turkey
- d) Puts forth a simplistic method for energy analysis of DSF.
- e) Identifies issues that affect or influence the functioning of these DSFs.

### **1.3. Limits of the Study**

Due to the complexity of the research topic, certain careful control and defining the scope of the research is needed. Firstly, the research is only deal with the issue at hand in the climatic conditions on southern areas like Turkey. This is seen as a positive approach because there isn't much research being done in that particular region which relates to the topic. Furthermore, it is hoped that the finding of the research will contribute to the knowledge in that particular area. This research mainly explores the viability of DSFs utilizing natural and forced flow for energy efficiency of buildings. It will be realized with experimental measurements and parametric analysis with computational fluid dynamic (CFD) software simulations.

Secondly a more specific 'domain' is needed to test the theory of the research and to apply any useful finding onto it in order to realize the impact of the research work. Turkey is chosen as the 'domain' and it is seen as an appropriate choice because there is not a comprehensive study pertaining to DSF in Turkey. This technology is quite new in our country although its applications multiply day by day.

Thirdly the construction costs or cost effectiveness of DSF systems are not covered in this research. Others had covered these topics quite comprehensively in different published books and journals.

Fourthly, there are numerous methods and techniques that could be employed to examine the energy performance of DSFs. However, the research area is new therefore there isn't much existing information in terms of measured data, etc. and not many constructed similar buildings directly related to the field, especially in Turkey. In fact,

there isn't any naturally ventilated cavity DSF building in our country during this research is being carried out. Therefore, a test cell having DSF will be constructed in a laboratory field to provide a controlled environment condition. Alternative design solutions and flow analysis are performed by using CFD simulations. The measured data taken from test cell provide the validation of the simulation models.

Notwithstanding constraints of the research mentioned above, it is a constructive challenge throughout and the research will provide a specific answer to a specific issue and filling up a gap within the knowledge in the mentioned field.

#### **1.4. Methodology**

This section sets out the method part of the study. This research is carried out using the combined research strategies by integrating experimental research strategy with simulation research strategy. By combining experimental and simulation results conclusions are established for different DSF configuration.

Experimental and numerical studies have been conducted. Experimental setup consists of two rooms which can be simulated based on conditioning indoor and outdoor environments. These rooms are separated by a DSF application. Accordingly, two areas are created with well insulated sandwich panels. The indoor temperature is regulated by water conditioned cooling/heating bath through copper pipes installed on the walls. The energy transferred in and out of the area is determined by flowmeter and PT 100 probes located on suitable spots close to entry and exit zones. Outdoor temperature is regulated with an air-based heat pump in order to meet the high energy need and provide summer-winter conditions. Heat exchanger of the heat pump utilized as evaporator to reach different temperature is placed on the interior part of the opaque walls of experimental set up simulating outdoor area. A solar simulator placed out of this room creates solar radiation effect and is separated with a conventional single-glass to keep ambient conditions and decrease heat transfer through convection and transmission as much as possible. Solar simulator is designed by using lamps suitable with solar radiation spectrum according to the size of single-glazed side of experimental setup as portable and in an adjustable position.

Exterior side of DSF, temperature of which can be regulated, consists of a portable conventional single-glass. The interior side of DSF is designed as air-proof,

well insulated double glass, which enables the area behind single and double glasses to be available for parametrical study to be conducted on different depths. In addition, a space is preserved for two canals in the upper and lower area of the single-glazed facade in order to ensure air inlet/outlet. The air inlet at the bottom is used to create effect of embedded HVAC system or outdoor wind effect by linking to a duct with centrifugal fan. A perforated plate is placed into a diffuser part in the canal to obtain uniform airflow in the DSF into the whole canal.

Experiments to be made after the construction of experimental set-up are carried out by evaluation of different parameters to determine the performance of flow and energy in DSF. Temperature of the area simulating indoor environment is kept at a stable level for summer and winter conditioning while the area corresponding to the outdoor environment is prepared for experiments under different temperature levels. Thus, the experiments listed below will be conducted:

- Air inlets in the upper and lower area of the exterior single glass facade are closed. For different interior and exterior temperature levels and different solar radiation rates measured with pyrometer and temperature distributions occurring with natural convection in the closed cavity are measured. Experiments are repeated for different working conditions with and without solar simulator usage.
- Air inlets in the upper and lower area of the exterior single glass facade is linked to the fan and the fan can be operated in different velocity to create forced fluid flow that can be experienced in real conditions, for different interior and exterior temperature levels and different solar radiation rates measured with pyrometer, airflow and temperature distributions occurring with forced convection in the cavity of DSF are measured. Experiments are repeated for dimensionless characteristic length of DSF cavity.
- Air inlets in the upper and lower area of the exterior single glass facade which is also linked to the fan are opened and two distinguished perforated plates are installed inside of the DSF's cavity for creating pressure drop. Fluid velocity, temperature and solar radiation are measured with pressure loss measurement in the cavity for simulating different kind of elements which cause the pressure drop.

Possible results and examinations gained from evaluation of the data out of these experiments maybe listed as follows:

- Effects of forced convection are evaluated experimentally and numerically for different values of the dimensionless characteristic length (depth/height rate) of the DSF cavity.
- Effects of natural convection are investigated for different boundary conditions of the DSF experimentally and numerically.
- With evaluation of different positions of pressure drop elements in the cavity under the effects of forced convection, the effects of these elements on the sizing of DSF is examined.
- Temperature and velocity profiles are detected, pressure drops are measured for DSF cavity under different conditions and the acquired data is examined.
- The effect of DSF application on required energy input and output for interior area conditioning under different conditions are evaluated.

The cavity part of experimental set up is modelled by CFD software and experimental results are compared with numerical results and validity check is made for numerical results. After validation of numerical results, parametrical studies conducted by CFD software are evaluated by nondimensional heat transfer characteristics for natural convection inside of an enclosure DSF's cavity and forced convection through the different site of DSF's cavity. These nondimensional correlations are also used for heat transfer calculations by using energy balance nodal approach for different working conditions and different climatic conditions of Turkey. Moreover, the effect of pressure drop elements usages in the DSF's cavity is investigated experimentally. Therefore, two different perforated plates are used in the cavity for different working conditions.



## **CHAPTER 2**

### **LITERATURE**

This section presents a comprehensive literature review on flow analysis of double skin facades and their energy performance. There are numerous papers on DSF written both by architects and engineers. It makes a review of main papers about DSF and summarizes the findings of this literature review, especially in last ten years.

#### **2.1. Experimental Studies on Double Skin Facades**

Experimental approaches provide reliable information regarding airflow, heat flux, solar radiation and temperature distribution in DSF. However, it is not an easy task and the results are highly dependent on procedure and accuracy of measurement. Although there are many studies on double skin facades in the international scale, the number of the experimental studies is limited. Also, most of these experimental studies are based on the observation of the data gathered from the existing double skin facade buildings. As it is almost impossible to control the environmental factors which affect the building outside, depending on the fact that the behaviours of the building users cannot be foreseen, the comparison of the measurement data taken from a real building and the results of the simulations does not give reliable results. In the laboratory environment where the environmental factors can be controlled, the data taken from the experimental setup allows to obtain more flexible and reliable data.

##### **2.1.1. Saelens's Experimental Study**

Saelens (2002) analyzed the natural and mechanical ventilation effects in Belgium, in the experimental setup of double skin facade with a sun shading device which is located in the middle of the cavity for his doctoral dissertation. The experimental setup is open to the exterior environmental conditions. Therefore, the solar radiation and air temperature cannot be controlled; but they can be observed. The inside of the double skin duct (0.5 m x 1.2 m x 2.7 m) consists of double glass whereas the its

outside consists of a single glass. There is also a sun shading device with reels in the middle of the duct between the two glass building skins. This sun shading device has an automatic control system. When the sun radiation exceeds  $150 \text{ W/m}^2$ , the device blinds shut down completely and automatically. While the internal air curtain flow mode is used for the mechanical ventilation in the experimental setup, external air curtain flow mode is used for the natural ventilation.

On the experimental setup, temperature and air flow measurements have been taken during summer and winter period. The air flow rate in the cavity has been observed with watcher gas method. For all of the configurations, the air flow rate varies between  $20 \text{ m}^3/(\text{h.m})$  and  $80 \text{ m}^3/(\text{h.m})$ . While surface temperatures have been measured on only the surface of the single glass facing the cavity, they have been measured on both surfaces of the double glass. By positioning sensors at 3 different heights vertically on both surfaces of the sun shading device which is located in the middle of the cavity, vertical temperature profiles have been measured. The air temperatures in the duct located on the portion of the sun shading device which faces both the interior and exterior glass have been examined. Air inlet temperature, air outlet temperature and interior room temperature have been measured.

During the measurements in winter, it has been observed that the glass inside was hotter than the glass outside in the exterior air curtain. Saelens stated that the air in the cavity can be used as pre-heated air in the interior environment. It has been seen that with the solar radiation, the difference between the temperature of air inlet and air outlet mostly does not exceed  $10^\circ\text{C}$ , but it even reaches  $20^\circ\text{C}$ . While the air inlet temperature difference is defined as the temperature difference between the outside air and the air inlet, the air outlet temperature difference is defined as the temperature difference between the outside air and upper air outlet temperature. While there was ventilation in external air curtain mode in the cavity during winter, it was observed that the temperature in the cavity was  $2.8^\circ\text{C}$  higher than the air in the external environment. It was also observed that by closing all of the air entrance and exit spans in the cavity, in the buffer zone mode, the air temperature in the cavity is  $6.4^\circ\text{C}$  higher than the exterior environment. During the measurements taken in summer, it was observed that there were higher increases in the temperatures in the cavity comparing to the interior environment and those increases could even reach  $28^\circ\text{C}$  in daytime.

### **2.1.2. Stec's Experimental Study**

Stec (2006) conducted his study in the double skin experiment room which was installed in the outside environment, in Tu Delft, Holland. While in the double skin duct (0.15 m x 1 m x 2.2 m), the outer skin consists of a single glass, the inner glass consists of an opaque wall which has openable and motorized glass windows. There is a venetian blind in the middle of the cavity. Air supply and air exhaust flow modes were used. Solar radiation, surface temperatures and wind velocity were measured and the air flow in the cavity was analyzed with gas watching method. For the calibration of the air flow, by using measurements developed by the author and producing various scenarios, the effects of the glass types at different dimensions, the spans of the air inlet/outlet and the sun shading systems were examined. Due to the fact that the experimental setup was installed under the outside environment conditions, the number of the parameters that could be tested is limited. Simulations were summed up by being compared to the measurements and results on any limit conditions such as outside air temperature, solar radiation, wall surface temperatures were not presented.

### **2.1.3. Corgnati, Porino and Serra's Experimental Study**

An existing office building whose facade faces south in Italy has a double skin facade with mechanical ventilation. The outer skin (0.14 m x 1.2 m x 2.7 m) of the double skin facade consists of double glass whereas the inner skin consists of a single glass. There is a venetian blind in the middle of the cavity. In the facade, internal air curtain flow mode was used. Temperature, air flow, heat flow and solar radiation were measured. On both surfaces of the glasses, temperatures were measured via the thermocouples. The air temperature was measured on both sides of the sun shading device in the cavity. By measuring the air temperatures via the sensors located at three different heights in the duct, temperature values throughout the duct were measured. Air inlet, air outlet and interior environment temperatures were measured. Also, for the control of the balance of the energy in the cavity, heat flow meters were placed on the glass surface. For solar radiation, two pyronometers were used. One of them was placed on the outer surface of the double skin facade, whereas the other one was placed to the glass surface in the office part of the inner facade. The air rate in the duct was measured

with anemometer. It was observed that when the solar radiation was low, the air temperature in and out of the double skin were close to each other. During noon, it was observed that the air temperature in the double skin facade was higher than the interior environment and sun shading device had a 52°C. temperature exceeding all of the temperature values. In winter and summer periods, it was observed that the air flow rates were  $50 \text{ m}^3/(\text{h.m}) - 75 \text{ m}^3/(\text{h.m})$ . While these values do not cause any problems regarding the energy performance of the double skin facade, due to the excessive heating of the cavity in summer, it requires extra cooling of the building (Corgnati, Porino ve Serra, 2007).

#### **2.1.4. Zanghirella's Experimental Study**

This experimental setup which was installed in Italy, consists of two similar setups juxtaposed with the name TWINS. While one of the setups consists of only 8/12/6 mm traditional double glass, the other one has a double skin facade. The traditional setup which only includes double glass without a cavity was prepared to test the setup with the double skin facade so that they had the exact same features. For the ventilation of the double skin facade (0.28 m x 1.6 m x 2.6 m), external air curtain and air supply flow modes were used. There is a sun shading device in the cavity of the double skin facade. The planned values were 20°C for winter, 26°C for summer and 23°C for the transition period. Temperature, heat flow, solar radiation and air flow in the cavity measurements were conducted. Sensors were placed at three different points along the height of the cavity. To measure the natural ventilation air flow rate, a pressure difference manometer was placed but according to Zanghirella, expected results could not be provided. During two time intervals, measurements were taken. The first lasted from March 2005 to January 2006 and the second lasted from May 2006 to February 2007. While during the first experimental measurement air flow rates ranged in the interval of  $17.5 \text{ m}^3/(\text{m.h}) - 63 \text{ m}^3/(\text{m.h})$ , in the period of the second experimental study, it was observed that air flow rates were in the interval of  $146 \text{ m}^3/(\text{h.m}) - 316 \text{ m}^3/(\text{h.m})$ . Regarding the glass type and sun shading device, the effect of these parameters to the energy performance was examined. It was also observed that double skin facade provides that solar radiation decreases at the rates of %38- %46 comparing to the traditional facade without a cavity and there were higher temperatures than the all

temperatures measured in the sun shading device (43°C- 50°C.) It was stated that the best performance belonged to the double skin facade configuration with the high air flow rate (Zanghirella, 2008).

### **2.1.5. Gavan's Experimental Study**

The study was conducted on an experimental setup called Minibat and installed in the laboratory environment. It consists of two identical experimental rooms juxtaposed. It was designed that the width of the experimental room is 3.1 m and height of the experimental room is 2.5 m. It has a climatization generator which provides the exterior environment conditions in the laboratory environment and a solar simulator. It was emphasized in the study that the air flow rate in the duct, surface temperatures and the angles of the sun shading devices have determining effects on the performance.

## **2.2. Other Studies related to DSF**

Experimental approaches are very lengthy processes and they take a long time to record the performance of DSF under real conditions. In this regard, various mathematical models have been developed to study the behavior of DSF or to optimize its performance. The modeling varies from very complex numerical modeling like CFD to simplified and analytical models. Although numerical modeling might apply to many cases envisaged, it needs to be validated with experimental data or analytical models before making any judgment based on the result of numerical modeling.

The flow and energy analysis of DSF have been evaluated on various studies in the literature. In some studies, different behaviors of the flow regarding the fact that they are natural and/or forced have been experimentally and/or numerically examined in the computer environment. DSF systems are divided into three groups based on ventilation types in the cavity. These are natural ventilation, mechanical ventilation and hybrid ventilation (both natural and mechanical). Basically there are three types of commonly encountered DSF application with mechanical ventilation. These are internal air curtain, air supply and air exhaust. Each one has a different thermal behavior and each DSF may be arranged to have one of them (Loncour etc., 2004). One of the studies done related to the double skin facades with mechanical ventilation, Marques da Silva

etc. (2009)'s study is based on observing the thermal behavior of a building, overheating due to the conflict of high air temperature and high solar radiation and getting rid of that heat to emphasize the requirement of increasing the velocity of the ventilation in the air shaft as the effective solution proposal. Also, the contribution of using a white blinds set in reducing energy consumption via reducing the temperature in the air shaft and on the interior window glass has been examined. Haddad and Elmahdy (1998, 1999) have focused on the studies on the effects of air supply and air exhaust windows on the thermal performance and compared them with the traditional windows. With this comparison, they have concluded that windows with air exhaust causes high heat gain especially in cold seasons. Also, due to the requirement of the thermal comfort, they have also concluded that air exhaust window is more primary than air supply window. Park etc., (2004) has developed a rotating motorized blind lath placed in the void in order to optimize the performance of the double skin facade system and a ventilated design on the glass inside and outside and below. An important feature of the system is that it shows a dynamic reaction in terms of energy, visuality and thermal comfort via real time optimizations for the environmental input data. Chen (2009) analyzed the tools used to predict ventilation performance in buildings. The CFD models were most popular and contributed to 70 % of the literature found in the study. The applications of the CFD models were mainly for studying indoor air quality, natural ventilation, and stratified ventilation as they were difficult to be predicted by other models.

Most of the model applications of computational fluid dynamics are for analyzing parameters such as indoor air quality and natural ventilation. Conducting these and flow evaluation is not possible only by using commercial codes which analyzes energy. Accordingly, advantages offered by the computational fluid dynamics will be benefitted in this study.

Unlike the facades with mechanical ventilation, facades with natural ventilation are characterized depending on the meteorological conditions (wind, temperature differences etc.) These parameters significantly complicate both the facade design and prediction of the thermal and ventilation performance. While indication of the performances of the systems with mechanical ventilation is predicted, the same situation is not valid for the systems with natural ventilation. Because, the performance of the natural ventilation depends on the meteorological conditions (Loncour, et al. 2004).

Double skin facades with natural ventilation do not need fan power; however, double skin facades with mechanical ventilation shows a better performance in summer time depending on their places of use. The fact that mechanically ventilated double skin facades have %25 more heat load than naturally ventilated double skin facades has been emphasized in (Li, 2001)'s study. In this study, the performance of a double skin facade has been determined experimentally. It has been conducted by applying an experimental model of one storey double skin facade to the south facade. In the setups of double skin facade models supported by natural or mechanical ventilation, by observing the performances of these two systems, the ratio mentioned above has been reached. Furthermore, in the passive systems, it has been observed that there is a higher difference of temperature between the inside and outside glass surfaces comparing to the active systems. Zerefos (2007) has compared the heating and cooling loads in different climates for single skin facade and double skin facade. The study has been combined with WINDOW by applying in ECOTECT simulation software. It was presumed that the double skin facade was naturally ventilated and the blind is in between the two glasses in the air duct. It is considered that double skin facades are better in cooling seasons in the Mediterranean climate zone (annually %29-%35 gain). Unlike these conditions, in places like Moscow with cold continental climate and London with warm climate, the difference between the performances of double skin and single skin facades decrease especially in heating seasons. As this study emphasizes, the thermal behaviors of double skin facades in different regions differ from each other.

In some studies, the effects of DSF on energy performance are analyzed by energy simulation programs. Gratia and Herde (2007) concentrated on the possibility of natural ventilation during the daytime in relation to the orientation of the double skin and the speed and the orientation of the wind. The purpose of the study was to examine how natural ventilation can be provided during a sunny summer day in an office building with a double skin facade. To realize the study, an office building with a high level of thermal insulation was chosen. With the thermal simulation software, TAS, various features of the double skin simulated in order to understand how the double skin operates. The study demonstrated that efficient natural cross ventilation is possible on condition that various orientations of the openings at the top of the double skin must be planned. In this study, it was determined in which the double skin windows should be opened, and the necessary size of openings. However, it was emphasized that this

cannot be generalized for other configurations. Grabe et al. (2001) carried out a detailed study of the effects of ventilation with double-skin facades which provides important guidelines in using CFD simulation for double-skin facade investigation. They determined that the simulation of a double-skin facade must yield the following information:

- a) The air mass flow through the facade gap to control the possibility of natural ventilation of the room behind.
- b) The temperature of the facade air related to the height of the facade, which determines the temperature of the supply air in the case of natural ventilation. It also helps in estimating the cooling load required in the case of conditioning.
- c) The temperature of the facade perimeter to predict possible deformations of the materials due to thermal elongation.

Sun etc. (2008) have researched whether double skin can be solution for the energy efficiency of buildings with excessive ratios of glass. In this study, the heating and cooling load of a double skin office room have been compared with an office room with a single skin and traditional window walled facade and analyses have been conducted. From the simulation results, it has been noted that heating and cooling energy gains can be attained when a reflective double skin facade and suitable ventilation method. Haase et al. (2010) compared thermal building simulations and measured data of an existing building. They showed good agreement with each other. It was stated that the results could be used to reduce the high peak cooling loads during the summer period. Moreover, the results of the study could be used to reduce surface temperatures by using different materials for the roller blind that is positioned in the cavity of the double-skin facade. Saelens et al. (2008) described how to optimize the energy performance of single-story multiple-skin facades by changing the settings of the facades and HVAC-system according to the net energy demand of the building. A mechanically ventilated airflow window, a naturally ventilated double-skin facade and a mechanically ventilated supply window were analyzed by simulation tool. It was found that both the heating and cooling demand might significantly be improved by implementing control strategies such as controlling the airflow rate and the recovery of air returning from the multiple-skin facades. Furlotto et al. (2010) carried out a decoupling method capable to evaluate thermal performances and analyze fluid



phenomena in a DSF. The solar radiation effects were evaluated with an analytical model and computational fluid dynamics (CFD) simulations were used to evaluate complex flow and thermal effect on a commercial DSF. CFD approach agrees well with the experimental data. The method could be used to establish a database to develop a tool for DSF design.

The depth of the void, sun blinds, glass type and natural/mechanical ventilation etc. are parameters which are effective on the energy performance of the building. These parameters lead to different performances in double skin facades. In this respect, regarding the energy efficiency of the double skin facades, a comprehensive study will be conducted for various double skin facade configurations especially for cities of Turkey.

In some studies, the effects of solar shading devices and plants especially on energy performance were investigated. There are various studies related to this condition. They are summarized in Table 2.1.

Gratia and Herde (2007) examined the influence of the position and the colour of the blinds on the cooling consumption of an office building with a double-skin facade with the use of thermal simulation software, TAS. It was found that a cooling consumption decreasing until 23.2% could be reached by paying attention to

- the location of the blinds,
- the colour of the blinds,
- the opening of the double skin,

Suitable location of the blinds provides saving up to 14.1% of the cooling consumption of all the building during sunny summer day. The correct color choice provides saving up to 3.5%. The impact of the opening ratio of dampers was from 7.4 to 12.6 reduction of the cooling energy consumption. The effects of different plant applications placed between the double skin facade to the energy performance are analyzed in Stec et al. (2005) study by use of experimental and an energy analysis code. The effects of perforated elements such as solar shading devices and plants on energy performance were investigated in various studies. They are summarized in Table 2.1.

Table 2.1. Pressure drop ( $\Delta P$ ) elements in the DSF cavity on the literature

#	$\Delta P$ element	Tools & models	Parameters	Findings
Safer et al. (2005)	Venetian blind	CFD forced porous steady	slat tilt angle blind position air outlet position 2D/3D comparison	The distance between the blind and outdoor glass had a significant effect on the velocity profiles inside the cavity. Porous media approximation for blind simplified the model and provided results which agreed with real venetian model.
Jiru and Haghighat, (2008)	Venetian blind	experimental zonal model forced/ natural unsteady	cavity height mass flow rate venetian blind position inlet-outlet temp. difference @Torino, Italy	Inlet-outlet temperature difference increased with DSF height and installing venetian blinds in the cavity. The influence of each parameter was more apparent in daytime.
Gavan et al. (2010)	Venetian blind	experimental forced/ natural steady	variation of airflow different angle of shading device @laboratory	Experimental data set was obtained. Air and surface temperatures in DSF were affected by the venetian blind angle and airflow rate.
Stec and van Paassen (2005)	Shading device	experimental simulation program forced/ natural unsteady	comparison of DSF with single skin facade external/internal shading different ventilation strategy @Delft, Netherlands & laboratory	Energy performance comparison of different facade applications. Annual cost was analyzed and compared each other considering facade, HVAC and energy. DSF with HVAC installation was found to be more economical solution.
Zeng et al. (2012)	Venetian blind	CFD experimental natural porous steady	outdoor wind speed different solar radiation two different CFD models @Tsinghua University, China	The porous media model showed good computational accuracy. It also significantly reduced the mesh number and computing time. Effective natural vent. occurred in each case. Pressure drop versus air velocity through blind was obtained.
Kuznik et al. (2011)	Shading device	experimental zonal model forced steady	different airflow rates different angles of the solar shading devices @laboratory	Temperature of the exterior glazing increased relatively small and interior temperature decreased when the tilt angles increased. Temperature values in the cavity decreased when the flowrate increased.
Iyi et al. (2014)	Venetian blind	CFD natural steady	blind tilt angles and positions different model strategy considering with internal and external environment conditions	When blinds positioned about one third from the external facade, optimum energy saving was provided. Blind tilt angle, 30°, decreased incoming solar energy to indoor space by about 85%.

(cont.on next page)

Table 2.1 (cont.)

$\neq$	$\Delta P$ element	Tools & models	Parameters	Findings
Silva et al. (2015)	Venetian blind	experimental natural steady	tree different slat angles different solar radiation different wind velocity @Laboratory	Temperature profiles were quite different between the cases with the slats in the closed and maximum open positions. Wind pressure coefficient for different direction considering upper and lower parts. Buoyancy and wind driven pressure effect were compared each other for different situations.
Pappas and Zhai, (2008)	Roller blind	CFD simulation program natural steady	cavity geometries shading device type different solar radiation	Correlations were performed for DSFs with buoyancy-driven airflow. Correlations were developed for airflow rate in cavity versus average and peak cavity-outdoor air temperature difference. Air temperature difference versus pressure difference between cavity and outside.
Stec et al. (2005)	Plant and blind	experimental simulation program forced unsteady	no shading plants blinds @laboratory	Plants provided comfortable indoor climate and energy savings. The positive influence of plants on the cooling system was obtained. Plants were more effective shading system than blinds. Temperature of each surfaces in a DSF with plant was generally much lower than blind.
Larsen et al. (2014)	Plant	simulation program forced unsteady	two different simulation models @Salta, Argentine weather data	Heat gain and heat loss were reduced to 30% and 63%, respectively by using plants.
Fang et al. (2011)	Plant	experimental forced unsteady	different plant density @Shanghai, China	Solar heat gain coefficients (SHGC) of DSF were obtained for different plant density. SHGC and cavity temperature decreased with the increase of plant density which did not solve overheating in the cavity.

## **CHAPTER 3**

### **EFFECTIVE DESIGN DECISIONS ON ENERGY PERFORMANCE OF DOUBLE SKIN FACADES**

Sustainability, and correspondingly the search for sustainable buildings increasingly occupy a significant role in architecture. In national as well as international scale, this concern leads authorities to redefine building performance standards and demands for a revision of architectural thinking. In this respect, in architectural discourse, it is possible to notice a rising interest in building skin configurations which promise to help minimizing the loss of energy while maximizing its gain. In parallel, it is possible to see that the use of double-skin glass facades globally pervades. These systems use the least energy against changing climatic conditions and capable of establishing a balance between internal and external climate. Therefore, an efficient facade systems which provide energy conservation in buildings is becoming a necessity to increase the energy performance of buildings from the architectural design process. The design of DSF involves numerous architectural decisions such as the geometric configuration and orientation of DSF, the glass types, the size of cavity, positioning of openings, ventilation strategy and application of shading devices. In this Chapter, double skin facade systems, which are accepted as an energy efficient building skin, are investigated and the effective design decisions on energy performance of this systems will be discussed in a comprehensive way in architectural perspective.

#### **3.1. General View on Double Skin Facades**

There is a world-wide tendency for a sustainable development. All over the world as our country, the considerable proportion of the total energy is used for heating, cooling, air conditioning, ventilation and lighting purposes. Approximately 20% of the total energy in Turkey is used by transport, 40% by industry and buildings being responsible for 40% of the total energy. Thus it is significant to design buildings that consume less operational energy during its life cycle (Haase, M., and Amato, A., 2005). 82% of the total energy is used for heating in buildings in Turkey. Energy loss from a

typical building occurs 40 % through external walls, 30% through windows, 17% through doors, 7% through roof, and 6% from floors, approximately. For this reason, architects and engineers should be focused on the designs solutions providing energy savings (Arıcı and Karabey, 2010).

One of the most popular methods of energy saving in a building is by properly designing of its facade (Widdington and Harris 2002). These systems called double skin facade, use the least energy against changing climatic conditions and capable of establishing a balance between the outdoors and the internal spaces. The energy gain depends on the climatic conditions and the proper double skin facade configuration.

The concept of DSF is not new and it is based on dates back to many years ago in central Europe when the box window types were used for thermal insulation purposes (Oesterle, 2001). Although that the concept of Double Skin Facades is not new, there is a growing tendency by architects and engineers to use this system. Architects working in collaboration with engineers have already begun to present an energy-effective approach to the design of building facades, since a building's facade supports both its embodied and operating energy (Karsai, 1997). All over the world double-skin facade applications multiply day by day. DSF buildings are claimed to be energy efficient, “environmentally friendly” and architecturally innovative solutions. Therefore, this condition have led to a rapid adoption of the double-skin facade technology. Predominantly seen in the European countries, the concept is now commonly designing in the USA and also other Australasian countries. This technology is still quite new in our country and it is not possible to find many applications or researches done on this subject.

Although, the DSF concept is not new in the world, this concept is quite complicated and its usage and function affects different parameters of the building. These parameters usually interact with each other such as daylight, natural ventilation, indoor air quality, acoustics, thermal and visual comfort, daylight energy use, etc. There are still relatively few buildings consisting of DSF. Moreover, there is not sufficient information on their design parameters which are effective in the architectural design stage.

The design of DSF depends on various architectural decisions. The effective decision parameters are the geometric configuration and orientation of DSF, the glass types, the size of cavity, positioning of openings, ventilation strategy and application of

shading devices. In this study, effective design decision parameters on energy performance of DSF systems will be discussed in a comprehensive way in architectural perspective by reviewing previous studies. A new classification of DSF system is proposed based on the effective design decision parameters. This classification is adapted from the literature studies. Moreover, advantages and disadvantages of this facade technology are discussed extensively. This study is expected to support further design improvements of the Double Skin Facade systems.

### **3.2. Definitions of Double-Skin Facade Systems**

The Double skin facade systems are called in numerous ways in the literature. The commonly encountered ones are; Double-skin facade, Double Facade, Double glass envelope system, Ventilated facade, Multiple-skin facade, Energy saving facade and active facade. There are various definitions related to double-skin facade systems.

Saelens (2002) defines double skin facade as an envelope construction consisting of two transparent surfaces separated by a cavity, which behave like an air channel. This cavity space creates a useful zone to protect solar shading devices from weather conditions, which are usually positioned in the cavity. This definition emphasizes the construction of the building skins, the transparency of the surfaces and the role of cavity in airflow.

Loncour et al. (2004) state that a ventilated double skin facade can be described as a conventional single facade doubled fundamentally by a second glass facade surface. These surfaces are called as skins. A ventilated cavity is positioned between these two skins, which can range from several centimetres to several metres.

Chan et al. (2009) explain that Double skin facade mention of a building facade consisting one or several stories with multiple glazed skins. There is an air cavity between these two skins and the width of the air cavity can range from 200 mm to more than 2m. These two skins can be air tight or naturally/mechanically ventilated. While the outer skin is usually a single glazing and can be completely glazed, inner skin can consist of insulated double glazing and it is not fully glazed in most applications. These air tight facades increase the thermal resistance of the building in order to reduce the heat losses in winter. Furthermore, moving cavity air can absorb the heat energy and reduce the heat gain and the cooling demand of a building in summer season.

According to Jiru, Tao and Haghighat (2011) Double-skin facades (DSFs) are described as building envelopes consisting of two glasses and a ventilated air cavity between these glasses. Solar shading devices are placed within the cavity. The ventilated cavity works like a thermal buffer zone. It reduces undesired heat gain during cooling period and heat loss during heating period. Moreover, these systems provide glare control and maximization of day lighting.

A DSF has many features similar with a glazed sun space or an atrium. However, the cavity in a DSF is used for ventilation purposes; it does not offer a space for occupants (Wachenfeld and Bell, 2003).

Double skin facade acting as a new second building envelope usually comprises of an external glazed skin and an internal skin which is made of glazed or partially glazed material. These skins separated from each other by an air cavity. The width of this air cavity can vary from 200 mm to more than 2m. This cavity behaves like a thermal buffer zone and it can be ventilated by naturally or by using mechanical system. DSF systems are generally proposed to decrease indoor heating demands in winter through increasing outside temperature of the internal facade using sunshine, and decrease indoor cooling demands in summer by lowering the temperature due to ventilation in the cavity. The air inlet and outlet vents are opened in summer to decrease high temperatures in the cavity via ventilation. The air inlet and outlet vents are closed in winter for storing heat in the cavity coming from sunshine and then transfer it indoor via internal skin.

### **3.3. Classification of Double-Skin Facade Systems**

Double skin facades can be called as a pair of glass skins separated by an air channel and this channel usually contains shading device, acts as insulation against excessive temperatures, wind loads, solar radiation and noise. DSF system is different from the double-glazing system because the thickness of the air channel may vary with a distance from 20 cm up to 2 m.

The classification of the double skin facade systems has significant effects on the design stage. It is necessary to define architectural and technical parameters in the early stage of design to increase the energy performance of the system. This contributes to understanding possible problems and improving problem-oriented solutions for them.

Various classifications on DSF can be found in literature, for instance, in Gertis (1999), Baker et al. (2000), Oesterle (2001), Arons and Glicksman (2001), Compagno (2002), and Parkin (2003). Modifications were performed to this proposed classification by merging some of the main characteristics with other various classification systems, such as the method made in the USA (Perino, M 2005). In this paper, the proposed classification categorizes DSF systems depends on three crucial parameters. This classification is based on primarily architectural configuration of the cavity based on the effective parameters which played determinative role on energy performance of a DSF, and secondarily its interaction with the type of ventilation and airflow modes in the cavity. This proposed classification based on these effective parameters can be presented as follows in Figure 3.1:

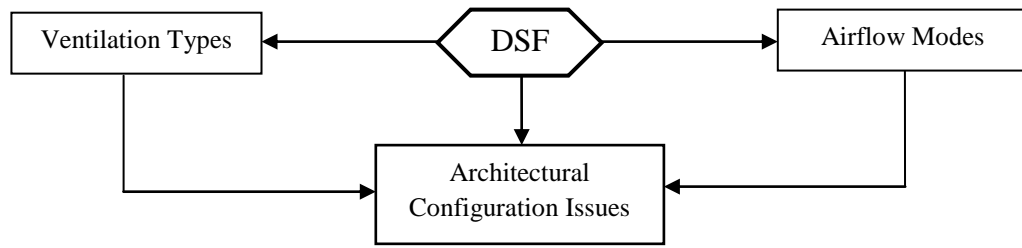


Figure 3.1. Effective parameters on Double Skin Facades

### 3.3.1. Architectural Configuration Issues of Double Skin Facades

When looking at the architectural configuration concepts it is significant to notice that all types of double-skin facades can be combined with both types of ventilation and all types of airflow concepts. This condition creates a great variety of double-skin facade configurations. It draws attention to the proper combination of the all parameters proposed in the classification. Effective parameters in architectural configuration issues are illustrated in Figure 3.2.



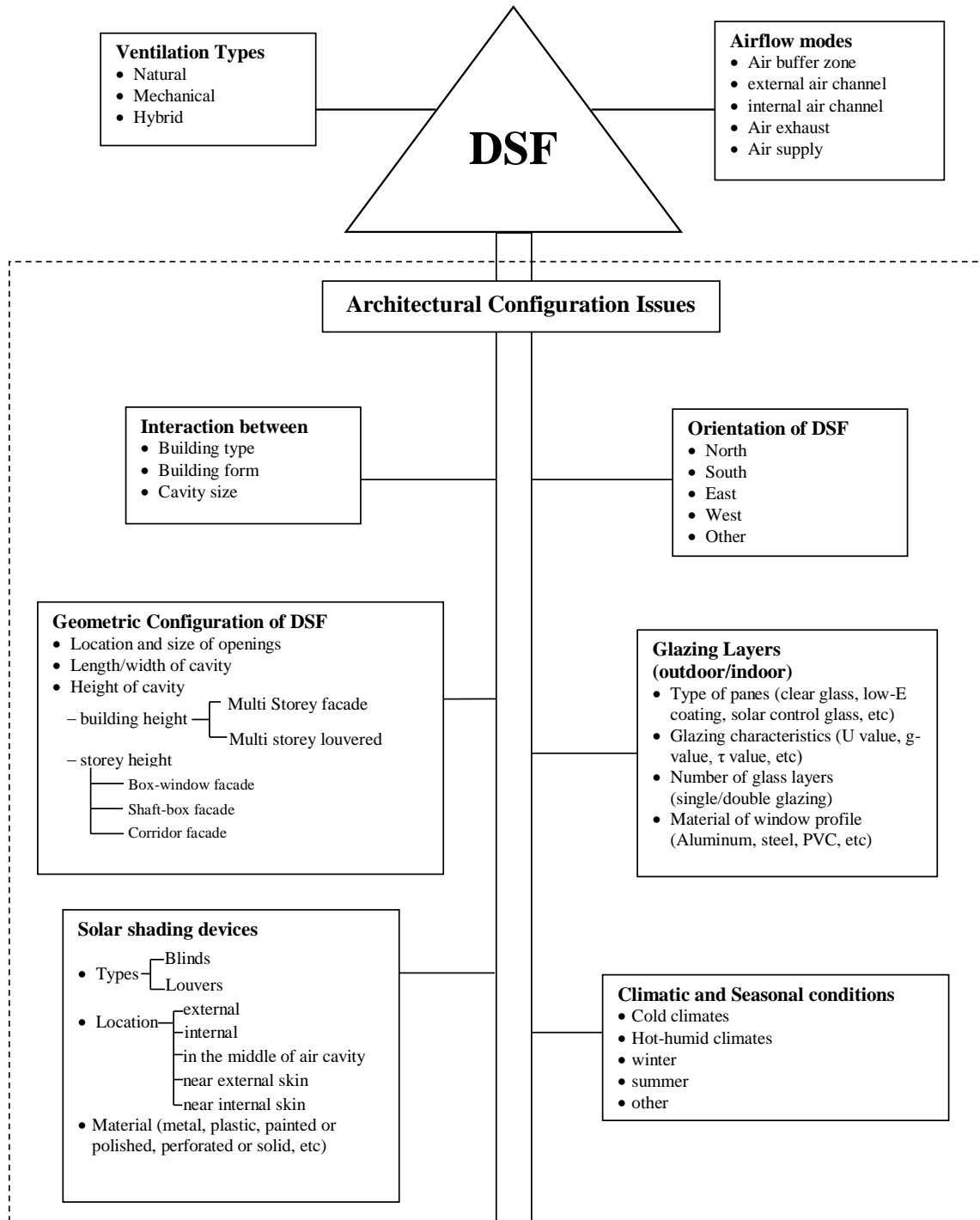


Figure 3.2. Effective parameters on Double Skin Facades

### 3.3.1.1. Double Skin Facade Types

Since the beginning of the first usage of the DSF systems, there have been some incoherencies and uncertainties in their classifications. Oesterle et al. (2001) classified double-skin facades into four different types based on geometric configuration. These are box window facades, shaft-box facades, corridor facades and multi-story facades. The Belgian Building Research Institute (BBRI, 2004) adds a new category for this classification called as Louvered facades.

- **Box window facade:** The box window is the first type of DSF introduced to the building industry. (Jon, 2008) The DSF is divided into smaller and independent boxes by horizontal and vertical partitioning. The cavity has horizontal partitions at each floor and vertical partitions on each window. Each box-window is provided with an air entrance and outlet at the bottom and at the top of the floor (Figure 3.3). It is generally used to prevent high external noise levels or provide special sound insulation between adjoining rooms (Oesterle et al. 2001, Wong 2008). Box type windows are also commonly used for retrofitting the buildings in order to improve their energy performance (Jon, 2008). This type is applicable for solid facades with punched openings and it is commonly used for buildings where privacy is important (Tascón, 2008).

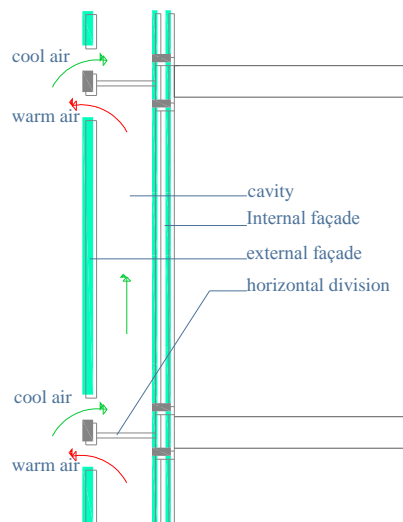


Figure 3.3. Box window facade

Most of the mechanically ventilated facades in Belgium are this kind of facade. The size of the cavity is generally 15 cm. Internal glazing facade can be opened for cleaning and maintenance demands (Loncour et al 2003).

- **Shaft box facade:** In this type, a set of box window modules are placed in the facade. These modules are connected via vertical shafts positioned in the facade (Figure 3.4). These vertical shafts encourage the stack effect. The stack effect draws the air from the box windows into the vertical shafts and from there up to the top, where it is exhausted (Oesterle 2001). This type of facade and partitioning is applied only naturally ventilated facades (Loncour 2003). At both sides of the central shaft, the box window areas exhaust air into the central zone. The air is warmed and goes towards to the shaft at the top level. It is exhausted from this shaft. These facade types have many external openings and this condition creates stronger thermal uplift within the stack. However, there are some problems related to how high a building with a double skin facade can be due to the limitation of stack effect (Wong, 2008). This type of DSF provides a high sound insulation against external noise. This system is best used in low-rise buildings and it is suitable in high noise areas (Oesterle 2001).

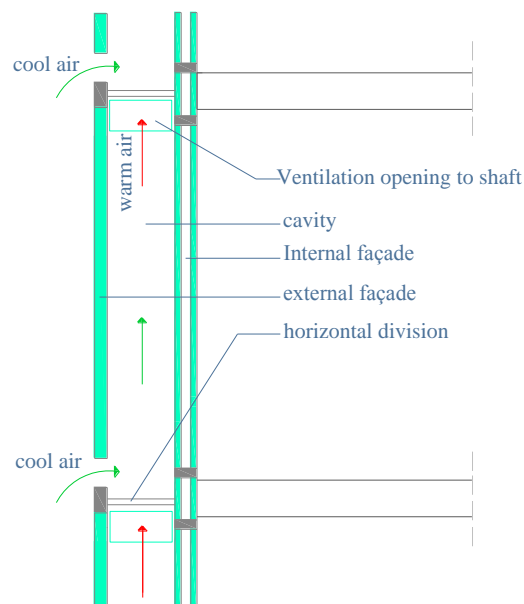


Figure 3.4. Shaft-box facade

- **Corridor facade:** In the corridor facade type, the air cavity is separated into horizontal compartments, generally at the level of each storey. Besides, vertical partitioning elements are used in some applications to control fire and sound. There are openings in the cavity at each storey level. The air supply and air exhaust openings in the external facade are located near ground level and the floor ceiling respectively for each storey of the building. These openings are laid in staggered form from on every level in order to prevent mixture supply and exhaust air (Oesterle 2001). Corridor facades do not create a limitation in the height of buildings. However, they do not utilize the stack effects as much as a shaft-box type of facade (Jon, 2008). Each floor has independent air circulation cells that are terminated on each floor.

- **Multi-storey Facades:** In this facade type, there is no horizontal or vertical partitioning between two glass skins. The air cavity extends along the height of the building that behaves like an air channel (Figure 3.5). It has only one inlet and one outlet opening along the building height. Air enters through the opening located on ground floor of the cavity and exhaust through opening on the upper floor of the cavity. This facade type is used differently in summer and winter season. It is used as an air supply facade in winter and air exhaust facade in summer. It is applicable for the usage of buildings having high external noise levels (Wong 2008).

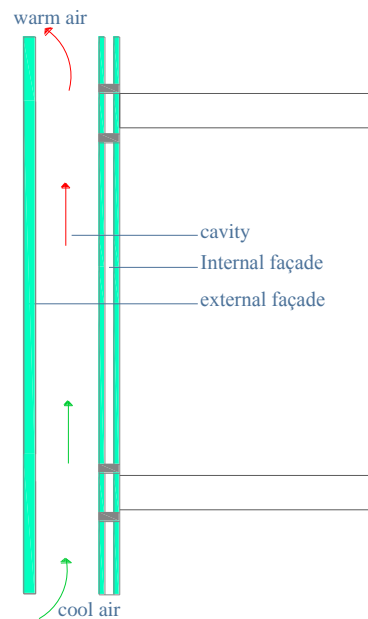


Figure 3.5. Multi-storey facade

- **Multi-Storey Louvered Facades:** This facade type is similar to a multi storey facade. The difference between this type of facade and multi storey facade is that the outdoor facade is composed of pivoting louvers rather than a traditional monolithic facade.

Buildings with double skin facade are commonly located in Continental/Northern European countries - Germany, Switzerland, Finland, France and Belgium. Japan also contributes a large percentage. According to Perino and Serra's research (2006), Natural ventilation (58.1 %), MultiStorey (47 %) configuration and external air channel are the most common solutions.

### 3.3.2. Ventilation Types in the cavity

The type of ventilation is related to the driving force used to ventilate the air channel (cavity) located between two glass envelopes. Three types of ventilation can be observed in the cavity (Renckens 2000, Oesterle 2001, Parkin 2003). These are:

- **Natural ventilation:** The goal of modern natural ventilation is to benefit from the natural driving forces as effectively as possible to minimize the use of energy for fans and mechanical cooling (Kleiven, 2003). The driving forces can be wind, buoyancy or a combination of both (Li, 2001). The performance of natural ventilation can change based on wind and temperature difference. The temperature difference is created by the stack effect that is an event related to the rising of hot air and dropping of cold air. (BBRI Report, 2004) Tanaka et al. (2009) have found that the maximum air change rate of natural ventilation by the exhaust opening varied between 20 and 25 [1/h]. Moreover, the reduction rate of the solar heat gain is about 25 % as compared with non-natural ventilated. Most researchers state that natural ventilation is possible in summer season even in multi-storey DSF configuration type (Wong, 2008).

- **Mechanical Ventilation:** In this type of ventilation, powered equipment is used to provide air movement (Loncour, 2004). Internal air curtain, air exhaust and air supply are commonly observed airflow modes in a mechanically ventilated DSF.

- **Hybrid ventilation:** Hybrid ventilation is a controlled comprise of natural and mechanical ventilation. In this type, natural ventilation is used as much as possible. The

mechanical ventilation is only used when the driving forces of natural ventilation are becoming inadequate to realize the desired performances. Only a few examples of facades using this type of ventilation exist in the world. According to Perino and Serra's research (2006), while natural ventilation is commonly observed solution as a percentage of 58.1 % among the investigated 215 buildings, the percentage of the buildings with hybrid ventilation approximately only 9 %.

### 3.3.3. Airflow modes in the cavity

The airflow mode is the condition related to the beginning of the airflow and destination of the air circulation in the cavity. It is significant to perceive that all types of double skin facades can be combined with each ventilation types and airflow modes in the cavity (Haase 2005). In this way, numerous DSFs can be generated. In order to take the fresh air to the DSF building, different types of ventilation can be applied in different climates, orientations, locations, etc to improve energy performance and make comfortable living spaces for the occupants (Pasquay 2004, Lancour 2004, Gosselin J.R, 2005). Figure 3.6 shows the main airflow modes in the cavity.

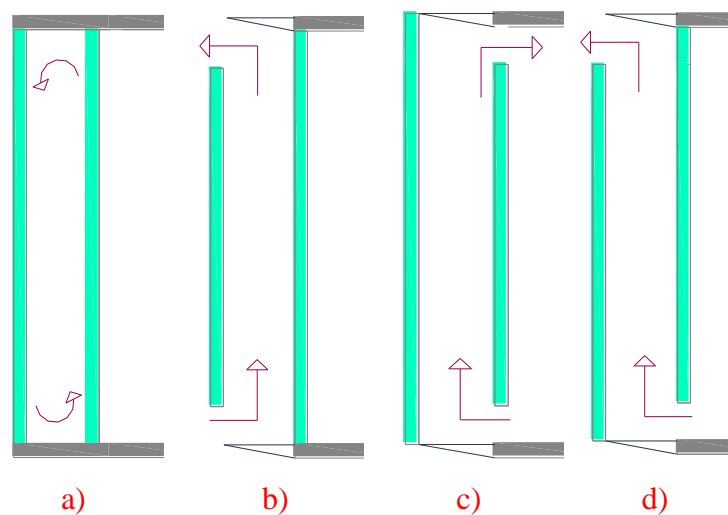
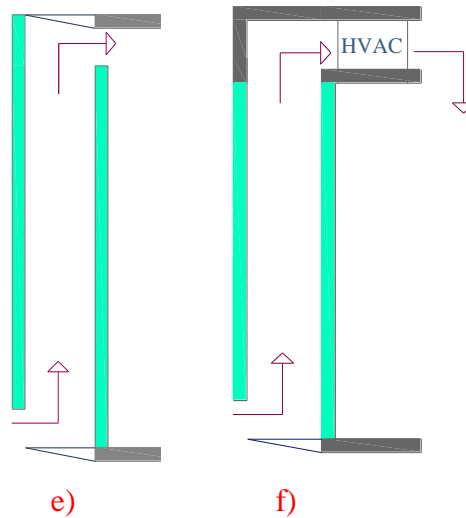


Figure 3.6. Main airflow modes in the cavity

(cont.con next page)



a) Air buffer zone b) External air channel c) Internal air channel d) Air exhaust e) Air supply f) Air preheating for HVAC

Figure 3.6. (cont.)

**a) Air buffer zone:** In this ventilation mode, both internal and external glass skins of double facade are designed as airtight. The cavity behaves like a tampon zone between the indoor and outdoor. Thus, there is no ventilation in the cavity.

**b) External air curtain:** The air is taken to the cavity from the external facade opening in the lower part of the cavity and is released from the external facade opening in the upper part of the cavity.

**c) Internal air curtain:** The air is taken to the cavity from the internal facade opening in the lower part of the cavity and is sent to the internal facade opening in the upper part of the cavity. The mechanically ventilated facades, usually called as active facades, are generally arranged by a single airflow mode of the internal air channel (BBRI, 2004).

**d) Air exhaust:** The air comes to the cavity from the internal facade opening in the lower part and is evacuated towards outside from the external opening located upper part of the cavity.

**e) Air supply:** The outdoor air is taken into the cavity from the opening located in the lower part of the external facade. The air is heated and is brought to the inside from the upper opening located internal facade.

**f) Air preheating for HVAC:** The ventilation air is taken into the cavity from the air vent at the bottom and preheated along the cavity. Then, it is taken to the HVAC system and transfer to the building.

### 3.4. Samples of Buildings with Double Skin Facade

It is possible to observe different type of DSF applications according to the variations in climatic conditions. Various DSF design combinations can be derived based on different architectural design decisions such as geometric configuration of DSF cavity, ventilation type in cavity, size and position of air vents, types of glasses, types of shading devices and their position on DSF, etc. Diversity of applications can be observed in the constructed DSF buildings. In this section, double skin facade practices applied on the worldwide have been investigated.

#### 3.4.1. DSF Practices in the World

In this part, examples of double skin facade buildings built in the world are investigated in detail. The influences of climatic conditions on design decision of DSFs are examined. Investigated buildings in the world are illustrated in Table 3.1.

Table 3.1. Investigated DSFs in the world

<b>Buildings</b>	<b>Location</b>
Dusseldorf City Gate	Germany
Deichtor Office Building	Germany
GSW Building	Germany
Sysopen Tower	Finland
Moravian Library	Czech Republic
Watling House	United Kingdom
Greater London Authority (GLA)	United Kingdom
Beetham Tower	United Kingdom
Sanomatalo	Finland
Arlanda, Pir F, Sigtuna	Sweden
DVV Building	Belgium
Seattle Justice Centre	United States of America



### 3.4.1.1. Dusseldorf City Gate

Architect:	Petzinka, Pink & Partners, 1998
Location:	Düsseldorf, Germany
Utilization:	Office building
Building information:	The height of building is 56 m and it has 16 stories with a central atrium (Figure 3.7).



a)



b)



c)

Figure 3.7. Düsseldorf Stadttor Building

(Source: a- <http://panoramio.com/photo/9668628>, b- <http://inhabitat.com/dusseldorfs-hi-tech-energy-efficient-gate/>, c-BBRI Report, 2004)

Facade Type:	The facade is designed as corridor facade. The building has two different cavity depth (90 cm and 140 cm) and 20 m length. DSF continue along the storey height.
Ventilation of the cavity:	Natural ventilation is used approximately 70-75% of the year. However, mechanical ventilation is used at peak hot temperatures in summer and peak cold temperatures in winter. Moreover, office building is equipped with chilled ceiling.
Glass Type:	While inner facade consists of a low-e glass with a wooden frame, the outer facade compose of a 12 mm safety glass
Shading device:	Featured highly reflective solar blinds are located near the outer glass in the cavity.

#### 3.4.1.2. Deichtor Office Building

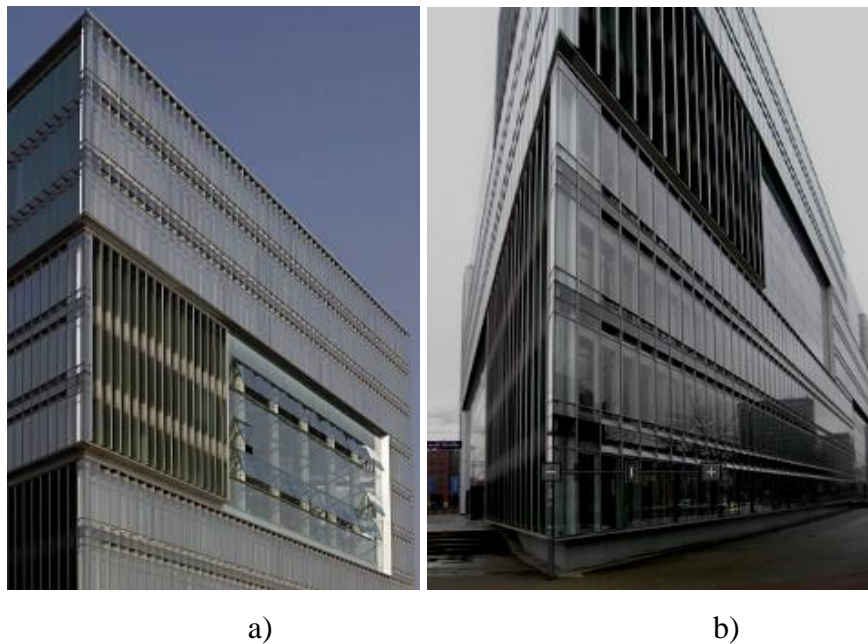


Figure 3.8. Deichtor Office Building

(Source: <http://www.panoramio.com/photo/22361320>)

Architect:	BRT Architecture, 2002
Location:	Hamburg, Germany

Utilization:	Office building
Building information:	It is a 12-story building with a triangular form. Each storey is 3.60 m. The building has 4 winter garden (Figure 3.8).
Facade Type:	Building has two DSF type. One is corridor, the other is multi storey facade. The building is located in an area subjected to heavy traffic noise. The chosen DSF facade types provide noise control.
Ventilation of the cavity:	The building is naturally ventilated. Office rooms are located facing winter gardens or in the direction of the DSF.
Glass Type:	No information
Shading device:	Blinds are used in the interior facade.

### 3.4.1.3. GSW Building

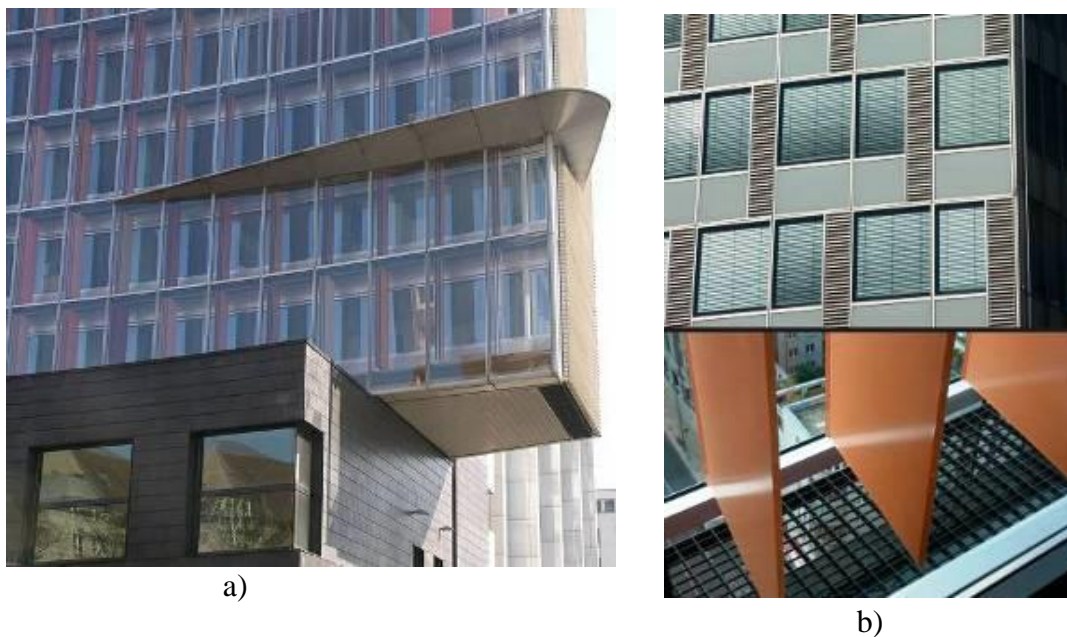


Figure 3.9. GSW building

(Source:<http://architecturerevived.blogspot.com/2010/04/gsw-headquarters-berlin-germany.html> )

Architect:	Sauerbruch Hutton, 1999
Location:	Berlin, Germany
Utilization:	Office building
Building information:	The building has 22-storey and the width of the building is 11 m. It is directed toward East and West.
Facade Type:	The facade is in the form of multi-storey DSF. It continues throughout the height of the building and has walking paths. The DSF is designed on West facade. the width of the cavity is 0.9 m (Figure 3.9).
Ventilation of the cavity:	The building is naturally ventilated primarily. However, the building is benefited from mechanical system at peak temperatures in summer and winter seasons. It is possible to take advantage of natural ventilation approximately 70% in the period of the year. The air is taken into the space from the eastern facade and is excreted from the DSF via cross ventilation. The west facade behave like a 20-storey solar shaft. Vertical airflow occurs in this shaft through stack effect and thermal buoyancy. Openable vents in the DSF cavity are closed during the heating season. Thus, the cavity acts as a thermal buffer zone. Hot air is returned to the central facility via risers for heat recovery. Radiant heating and cooling are provided. Thermal storages have been created in the floor and ceiling.
Glass Type:	East facade comprises of triple-glazed windows. West facade consists of a DSF. While inner glass of western facade consists of double-glazed windows, a sealed 10 mm glazing is used on outer facade of DSF.
Shading device:	Automatically deployable and manually adjustable aluminum louvers are used on Eastern facade. Colored vertical perforated aluminum shutters were used to organize solar gain and natural lighting. All the shutters

can be extended along the front to shade the facade completely.

#### 3.4.1.4. Sysopen Tower



a)



b)

Figure 3.10. SysOpen Tower

(Source: <http://taloforum.fi/viewtopic.php?t=457>)

Architect:	Arkkitehdit Tommila Oy, 2001
Location:	Helsinki, Pitäjänmäki, Finland
Utilization:	Office building
Building information:	The building has 19-storey, one of them is under the ground level. The total height of the building is 70 m (Figure 3.10).
Facade Type:	The DSF type of box-window is used in this building. The cavity depth is 55 cm.
Ventilation of the cavity:	No information
Glass Type:	Tempered glass with a 8 mm thickness is used in exterior facade.
Shading device:	Automatically controllable solar blinds are positioned in the cavity.



### 3.4.1.5. Moravian Library



a)



b)



c)

Figure 3.11. Moravian Library  
(Poirazis, 2004)

Architect:	No information for architect, 2011
Location:	Brno, Brno, Czech Republic
Utilization:	Library building
Building information:	It has two double skin facade placed on south direction. The total area of the DSF is 1135 m <sup>2</sup> . The building has eight storey and DSF go along the total height of the building. The facade is 50 m long. Galvanized steel elements were used in the building (Figure 3.11).

Facade Type:	It is designed as box window facade. Walkways are constructed on the level of each floor. The cavity width is 55 cm.
Ventilation of the cavity:	The building has openable windows. These provides natural ventilation of building during cooling period. Air inlets are positioned on the ground level of the DSF.
Glass Type:	The external skin of the facade consists of single hardened glass of 10 mm thickness. Internal skin comprises of double glazed windows.
Shading device:	Two types of shading devices are used in the building. These are fixed horizontal load bearing shading devices and motorized vertical shading devices used on internal facade.

#### **3.4.1.6. Watling House**

Architect:	GMW, Arup associates, 1992
Location:	London, United Kingdom
Utilization:	Residential building
Building information:	The total built area is 7900 m <sup>2</sup> . It has 7 storeys. Solid components are used on facade (Figure 3.12).



Figure 3.12. Watling House  
(Source: Tascon, 2008)

Facade Type:	It is designed as shaft box window facade.
Ventilation of the cavity:	Fully HVAC
Glass Type:	Triple glasses are used.
Shading device:	Shading devices are used inside and outside of the building facade.

### 3.4.1.7. Greater London Authority (GLA)



Figure 3.13. Greater London Authority  
(Source: Tascon, 2008)

Architect:	Norman Foster, Arup associates, 2002
Location:	London, United Kingdom
Utilization:	City Hall
Building information:	It is a high rise building. The total height of the building is 45 m. It has 11 storeys. It has 15000 m <sup>2</sup> floor area. The building has steel frame with circular columns (Figure 3.13).
Facade Type:	Highly insulated panels are used with double skin facade modules.
Ventilation of the cavity:	The facade has locally controlled natural ventilation. When the air vents are opened, heating and air conditioning systems deactivate themselves.
Glass Type:	Low-e glasses are used.



Shading device: Photovoltaic panels and shading devices are used in the building.

#### 3.4.1.8. Beetham Tower



Figure 3.14. Beetham Tower  
(Source: Tascon, 2008)

Architect: Ian Simpsons Architects, 2006.

Location: London, United Kingdom

Utilization: Hotel and residential building

Building information: It is a high rise building. The total height of the building is 180 m. It has 51 storeys.

Facade Type: The building is constructed as multi storey double skin facade type (Figure 3.14).

Ventilation of the cavity: No information

Glass Type: Clear glass is used on facade.

Shading device: No information

### 3.4.1.9. Sanomatalo



Figure 3.15. Sanomatalo (BBRI report, 2004)

Architect:	Arkkitehtitoimisto Jan Söderlund & Co.Oy, 2000
Location:	Helsinki, Finland
Utilization:	Commercial and office building
Building information:	It is a high tech building. It has 12 storeys and 3 of them is underground. The total area is 43000 m <sup>2</sup> . Double skin facade has a 5000 m <sup>2</sup> area. The building has a modern sprinkler system. It has a good fire protection. Concrete slabs and columns are used.
Facade Type:	The building has double facade on east west and south direction. Facade is designed as box window. Inner facade was made of prefabricated elements. Galvanized steel and glass elements are used (Figure 3.15).
Ventilation of the cavity:	The cavity is 70 cm. This is closed or can be vented by motor-operated vents controlled by thermostats.

Glass Type:	While toughened and laminated glass (6 mm + 4 mm) are used inner facade, toughened and coated selective sun protection glass (6mm) are used middle facade. Argon and krypton gas are used between the glass space. Toughened and laminated glass (6 mm + 6 mm) glass are used outer facade.
Shading device:	Blinds are positioned inside the inner facade.

#### 3.4.1.10. Arlanda, Pir F, Sigtuna



Figure 3.16. Arlanda, Pir F, Sigtuna (BBRI report 2004)

Architect:	KHR AS Architects, 2001
Location:	Sweden
Utilization:	Terminal building
Building information:	It has a 67500 m <sup>2</sup> floor area and 13000 m <sup>2</sup> double skin facade area.
Facade Type:	Building facade is multi storey type. Cavity width is 60 cm (Figure 3.16).
Ventilation of the cavity:	No information

Glass Type:	Outer skin is 6 mm float glass and inner skin is Planitherm futur, 20 mm argon, 6 mm clear float.
Shading device:	Venetian blinds are used in the cavity.

#### 3.4.1.11. DVV Building



Figure 3.17. DVV Building (BBRI report 2004)

Architect:	No information.
Location:	Belgium
Utilization:	Office building
Building information:	It has 4 storeys. Box window is used between 1st to 3rd floor (Figure 3.17).
Facade Type:	Facade is designed as box window type. The cavity is 15 cm.
Ventilation of the cavity:	The building has a central mechanical system. The heat is removed with exhaust air. After, the exhaust air is brought to the climate facade. The air is centrally conditioned.
Glass Type:	It has a double glass positioned on outer facade ( $U= 1.8 \text{ W/ m}^2\text{K}$ ) and single glass positioned on inner facade.



Shading device:	Solar shading device is located in the cavity near to the inner glass. It is controlled centrally based on orientation and storey.
-----------------	--

### 3.4.1.12. Seattle Justice Centre



Figure 3.18. Seattle Justice Centre

(Source: [http://www.pambeyette.com/artplans.php?item\\_id=35&page=1](http://www.pambeyette.com/artplans.php?item_id=35&page=1))

Architect:	Hegedus
Location:	Seattle, United States of America
Utilization:	Office building
Building information:	It has 9 storey.
Facade Type:	Multi storey facade type is used in the building (Figure 3.18).
Ventilation of the cavity:	No information.
Glass Type:	Monolithic glazing on the outside and insulated glass on the inside.
Shading device:	No information

### 3.4.2. DSF Practices in Turkey

As the buildings consume almost 50% of the energy in the world, in terms of the renewed EU directive, The Energy Performance in Buildings Directive, designs which include the optimum energy efficiency and cost should be produced in Turkey similar to the buildings in the all over the world. In this respect, facade systems which are building skins playing an active role in the energy efficiency of the buildings have began to gain importance in Turkey as well and double skin facade systems which are widely used in the world have become popular in Turkey gradually. In this section, double skin facade buildings in Turkey will be examined.

#### 3.4.2.1. İstanbul Sapphire



a)



b)



c)



d)

Figure 3.19. İstanbul Sapphire  
(Source: <http://www.arkiv.com.tr/p9568>)

Architect:	Tabanlıoğlu Architecture, 2010
Location:	İstanbul, Turkey
Utilization:	Residential, shopping and entertainment centers
Building information:	<p>The first example for double skin facade building is Sapphire skyscraper in Turkey. It is a high-tech structure that consists of 64 stories (54 on surface and 10 underground), communal living stories, extensive parking spaces, a large shopping mall, and 47 stories for residences. It is the first ecological building of Turkey with a height of 261 meters with antenna, having two special glass shells called as double skin facade. The building is oriented to east and west. The north and east facade is designed as cold front. This architectural decision is important in terms of heat gains rather than view. Thanks to this facade system, the inhabitants of the building will be protected by the negative weather conditions and external urban noise, in addition to providing a buffer zone between the exterior and interior atmosphere. Absorption of the sunlight and ultraviolet beams will be ensured by a special curtain system that's automatically controlled through a computer, depending on the season, day and hour.</p>
Facade Type:	<p>It is designed as multi storey facade. Vertical gardens are designed at every 3 stories and every 9 floors are separated from each other by a communal living area or mechanical floors. Sliding joints are used in the interior facade that provide going out garden or balcony owing to double skin facade (Figure 3.19).</p>
Ventilation of the cavity:	<p>In Sapphire building, the natural air demands for gardens are provided from movable vents located outside facade. The building can take the outside fresh air naturally by vents located at base of every 3 stories and release dirty air by vents located at upper of every 3 stories. Thus, natural</p>

ventilation is used in the cavity of the building and this approximately provides 30 % energy saving.

Glass Type: No information

Shading device: Aluminum shading devices are positioned to be closer to the inside of the exterior facade.

### 3.4.2.2. Küçükçekmece Municipal Services Building



a)



b)



c)

Figure 3.20. Küçükçekmece Municipal Services Building

(Source: <http://www.ilkdogadostukamubinası.com/images/etc/Kucukcekmece-Yeni-Binası-Tanitim.pdf>)

Architect: Mutlu Çilingiroğlu, MİAR Architecture, 2014

Location: İstanbul, Turkey



Utilization:	Office building
Building information:	It is the first public building that takes BREEAM green building certificate. It gets this certificate owing to passive climatization, green roofs, natural lighting with double skin facades, galleries, selection of recyclable materials and suitable plants. The structure has a circular plan formed by bringing together three circle form. The building was constructed on a sloping terrain and it has three entries in three different grades. Whole facade is made of curved glass. The building has 9 storeys, two of them are underground. In addition , the public building has an inner court. Thus, daylight can be taken into the space. Moreover, ice is produced and stored during the night with ice storage system in the building.
Facade Type:	It is designed as multi-storey facade. Storeys are separated by a horizontal dividing element from the ground floor in every 2 floors (Figure 3.20).
Ventilation of the cavity:	The ventilation between two glass layers can be ensured with natural air circulation vents in every two floors. Ice stored in tanks is used for cooling of the building for peak demands when the temperature is high during the daytime. Hence, this system can be reduced the consumption of electricity during daylight hours. A large part of the hot water requirements is planned to be provided with solar water panels. The efficient management of energy is taken under the control with the building automation system.
Glass Type:	While the outer surface consists of high solar control glasses, low solar control glasses is preferred on inner surface.
Shading device:	Venetian blinds with aluminum lamella were used in the cavity.

### 3.4.2.3. Istanbulbloom

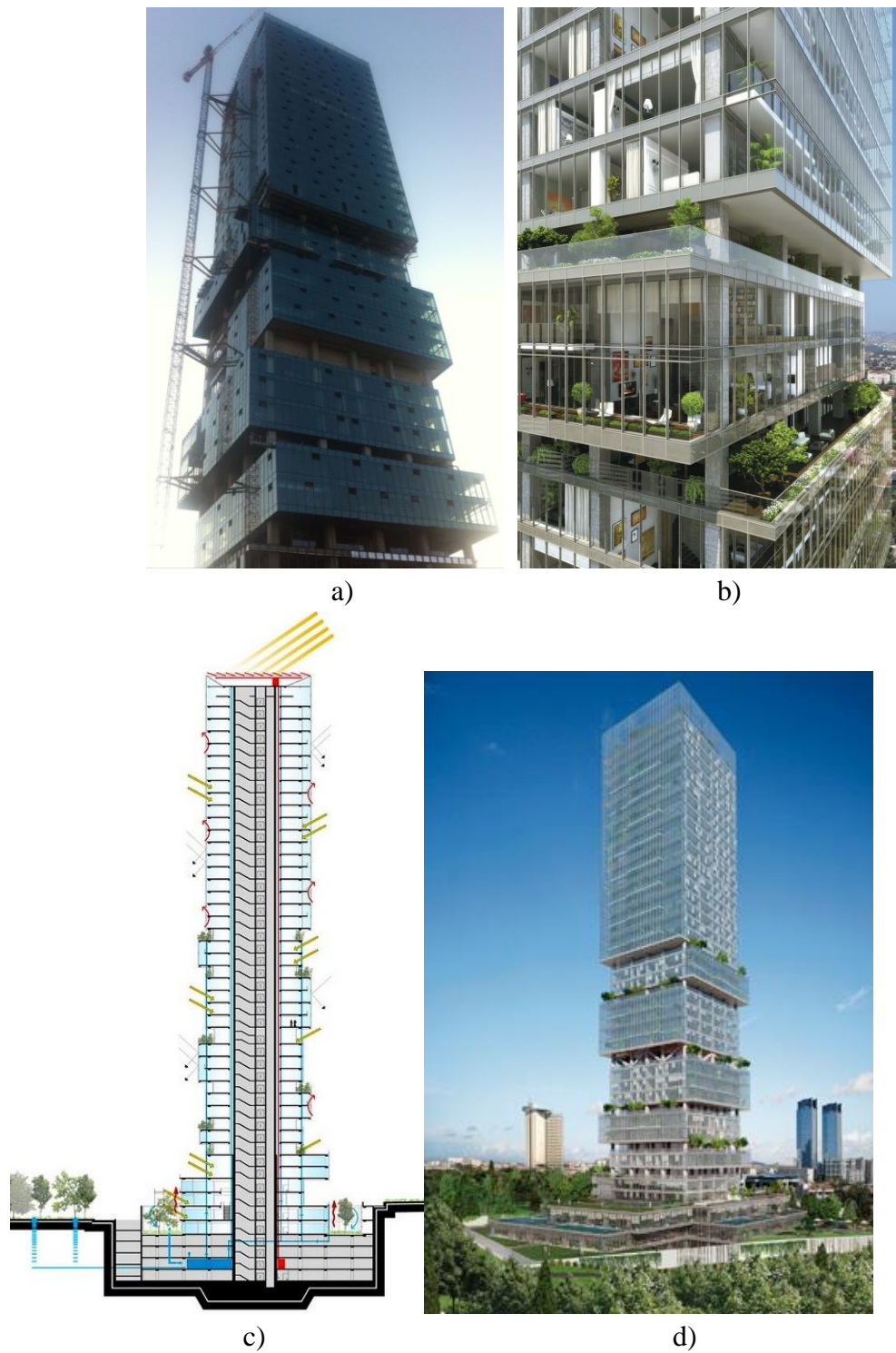


Figure 3.21. Istanbulbloom building  
(Source: <http://www.arkiv.com.tr/proje/istanbloom/2704>)

Architect:	DB Architects, 2014
Location:	İstanbul, Turkey
Utilization:	Residential and office building
Building information:	The building has a 79.571 m <sup>2</sup> constructed area. The 46-storey building consists of housing units, offices and social areas. The total height of the building is 160 m. Building has LEED Gold Certification. There are solar panels on the roof. Moreover, the building has skylight. Electric obtained from the solar collector is used for lighting of the spaces. It provides approximately 15 % of electricity saving. Double skin facade system provides maximum isolation. Heat recovery system ensures approximately 20 % of energy saving. Rain water is collected and re-evaluated. Thus, 30 % of water saving is supplied.
Facade Type:	The building has multi storey facade and aluminum profiles are used. Building with natural climate control has 6 court gardens and floor gardens (Figure 3.21).
Ventilation of the cavity:	Air ventilation in spaces is provided by air conditioned fresh air.
Glass Type:	No information
Shading device:	The building is protected from the sun emission thanks to the materials used in the roof and exterior facade of the building.

### 3.4.2.4. Ankara Telecom Headquarter

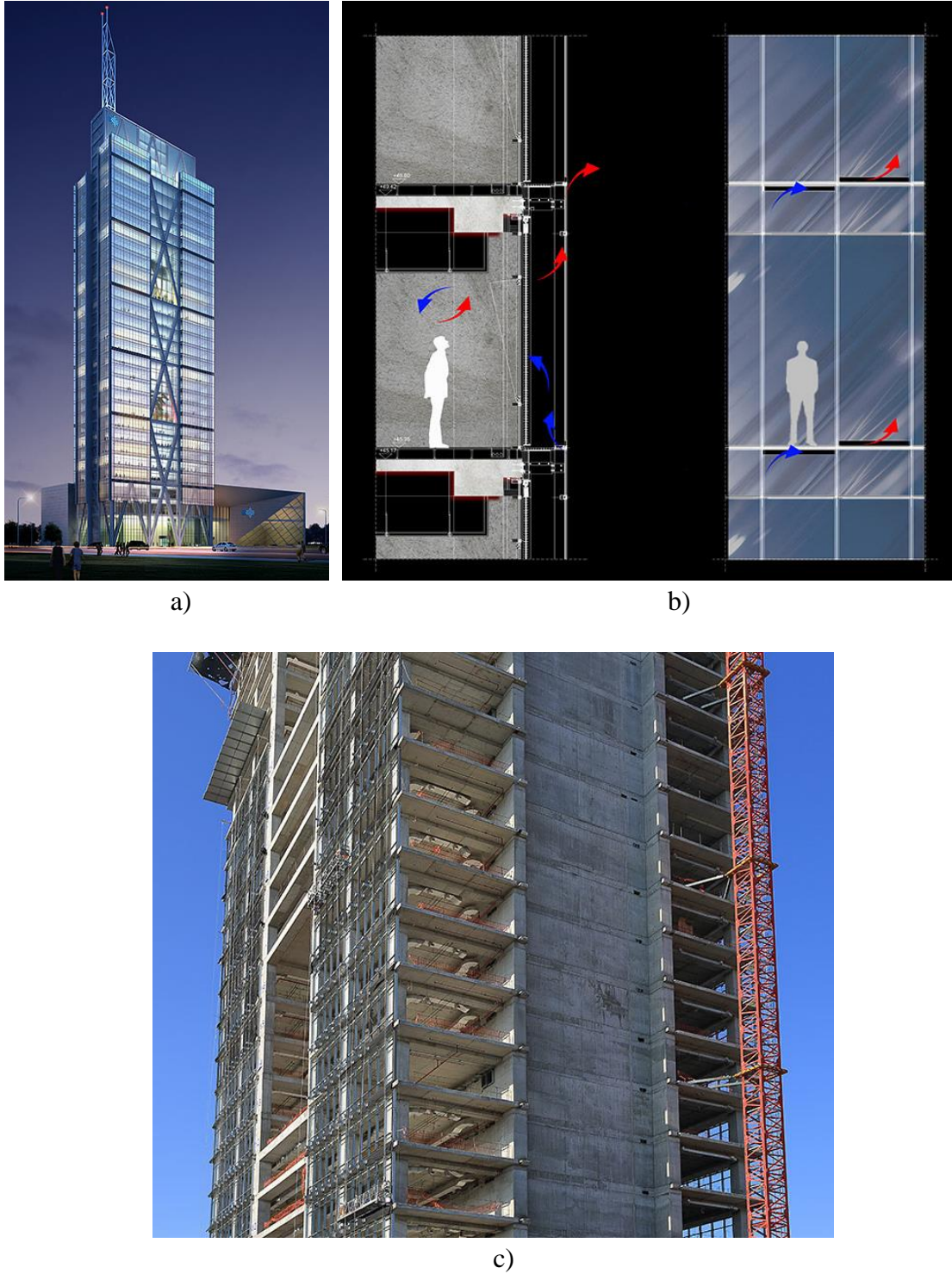


Figure 3.22. Ankara Telecom Headquarter  
(Source: <http://www.atarim.com.tr/tr/proje/turk-telekom>)

Architect:	A Design Architecture
Location:	Ankara, Turkey
Utilization:	Office building
Building information:	The building has a 54000 m <sup>2</sup> constructed area. It consists of 36 storey, three of them are under the ground level. The total height of the building is 150 m. It has both single and double facades. It has diagonal members on exterior facade. It is an environment and energy-sensitive building. It is designed in accordance with green building concept. The building has smart building technology and optimum energy usage is targeted in the building. There are solar panels on the roof. In the building, maximum usage of daylight is taken into consideration. The building has benefited from the solar energy for hot water supply and lighting automation. Natural and recycled materials are used in the exterior and interior facade of the building.
Facade Type:	The building is designed as having a multi storey facade and aluminum profiles are used. An interior garden is designed every 5th floor of the building (Figure 3.22).
Ventilation of the cavity:	Automatic vent elements inside the DSF controlled building automation are closed in very cold and windy weather. On the other hand, these elements are opened in the transition of seasons and especially spring season. Thus, natural ventilation of building is ensured. Commonly used airflow modes of external air curtain and air supply flow modes are used in the building.
Glass Type:	No information
Shading device:	No information

### **3.5. Advantages-Disadvantages of Double-Skin Facade Systems**

The main function of a DSF is to behave like a double building envelope with an air cavity, providing thermal and acoustic insulation and taking into fresh air by operable windows. Solar shading devices are positioned between these two envelopes, which protects them from the high wind loads, weather conditions and air pollution. The tendency on advantages and disadvantages of the DSF systems mentioned in the different literature sources are investigated in detail to determine the most effective factors on energy performance of DSF used in the architectural design stage. The advantages and disadvantages of DSF systems mentioned in the literature are summarized in Tables 3.2 and Table 3.3 and the percentages of these issues are illustrated in Figures 3.23 and 3.24. The percentages of the advantages or disadvantages of DSFs are constructed based on the assets and drawbacks of the authors about DSF in the evaluated studies.



Table 3.2. (cont.)

[illegible]



Table 3.3. Disadvantages of Double Skin Facades (2001-2015)

Disadvantages emphasized by the Researchers	Oester et al., (2001)	Li, (2001)	Hendriksen et al., (2002)	Zöllner et al., (2002)	Saelens et al., (2003)	Jager (2003)	Loncour et al., (2005)	Yilmaz and Çetintaş., (2005)	Safer, et al., (2005)	Ding et al. (2005)	Faggenbau (2006)	Poizaris (2006)	Bestfacade (WP5), 2007	Gratia and Herde, (2007)	Haase et al. (2007)	Asdrubal and Baldinelli., (2007)	Gavan et al. (2007)	Høseggen et al. (2008)	Haase et al., (2009)	Tanaka et al., (2009)	Chou et al., (2009)	Chan et al., (2009)	Guardo et al., (2009)	Haase and Amato, (2009)
Overheating problems in cavity /high temperatures	✓	-	-	✓	✓	✓	✓	-	✓	✓	✓	✓	✓	✓	-	✓	✓	✓	✓	✓	-	✓	✓	-
Daylight	✓	-	✓	-	-	-	✓	-	-	-	-	✓	✓	-	✓	-	✓	✓	✓	-	-	-	-	✓
Acoustic insulation problems	✓	✓	✓	-	-	✓	-	-	-	-	-	✓	✓	✓	-	-	-	-	-	-	-	-	-	-
High construction costs	✓	-	-	-	-	✓	-	-	-	-	✓	✓	✓	✓	-	✓	-	✓	-	-	-	✓	✓	-
Extra maintenance and operational costs	✓	-	-	-	-	✓	-	-	-	-	✓	✓	✓	-	-	✓	-	✓	-	-	✓	✓	-	-
Fire protection problem	✓	-	✓	-	-	✓	✓	-	-	-	-	✓	✓	-	-	✓	-	-	-	-	-	-	-	-
Reduction of inhabited spaces	✓	-	-	-	-	✓	-	-	-	-	✓	✓	✓	-	✓	✓	-	✓	-	-	-	-	-	-
Increased air flow velocity	-	-	✓	-	-	-	✓	-	-	-	-	✓	✓	-	-	-	-	-	-	-	-	-	-	-
Increased weight of the structure	-	-	-	-	-	✓	-	-	-	-	-	✓	✓	-	-	-	-	-	-	-	-	-	-	-
Visual discomfort related condensation	-	-	-	-	-	-	✓	-	-	-	-	-	✓	-	-	-	-	-	-	-	✓	-	-	-

Table 3.3. (cont.)

Disadvantages emphasized by the Researchers	Gavan et al., (2010)	Serra et al., (2010)	Zhou and Chen, (2010)	Azarbayjani and Anderson, (2010)	Jiru et al., (2011)	Annex 44, (2011)	Mingotti et al., (2011)	Zang and Altan, (2011)	Shameri et al., (2011)	He et al.,(2012)	Chow., (2012)	Zhoue and Xue, (2012)	Radhi vd., (2013)	Shameri vd., (2013)	Moon vd., (2014)	Joe vd., (2014)	Andeković vd., (2015)	Lopez vd., (2015)
Overheating problems in cavity /high temperatures	✓	✓	✓	-	✓	✓	✓	-	✓	-	✓	-	✓	✓	✓	✓	✓	✓
Daylight	-	✓	-	-	-	✓	-	✓	✓	✓	-	-	✓	✓	-	-	-	-
Acoustic insulation problems	-	-	-	-	-	✓	-	✓	-	-	-	-	-	✓	-	-	-	-
High construction costs	-	-	-	-	-	✓	-	-	✓	-	-	-	-	-	-	-	-	-
Extra maintainence and operatical costs	-	-	-	-	-	✓	-	-	-	-	-	-	-	-	-	-	-	-
Fire protection problem	-	-	-	-	-	✓	-	-	✓	-	✓	-	-	✓	-	-	-	-
Reduction of inhabited spaces	-	-	-	-	-	-	✓	-	-	-	-	-	-	✓	-	-	-	-
Increased air flow velocity	-	-	✓	✓	-	✓	✓	-	-	-	-	-	-	✓	-	-	-	-
Increased weight of the structure	-	-	-	-	-	-	-	-	-	-	-	-	-	✓	-	-	-	-
Visual discomfort related condensation	✓	✓	-	-	-	✓	-	-	-	✓	-	-	-	-	-	-	-	-

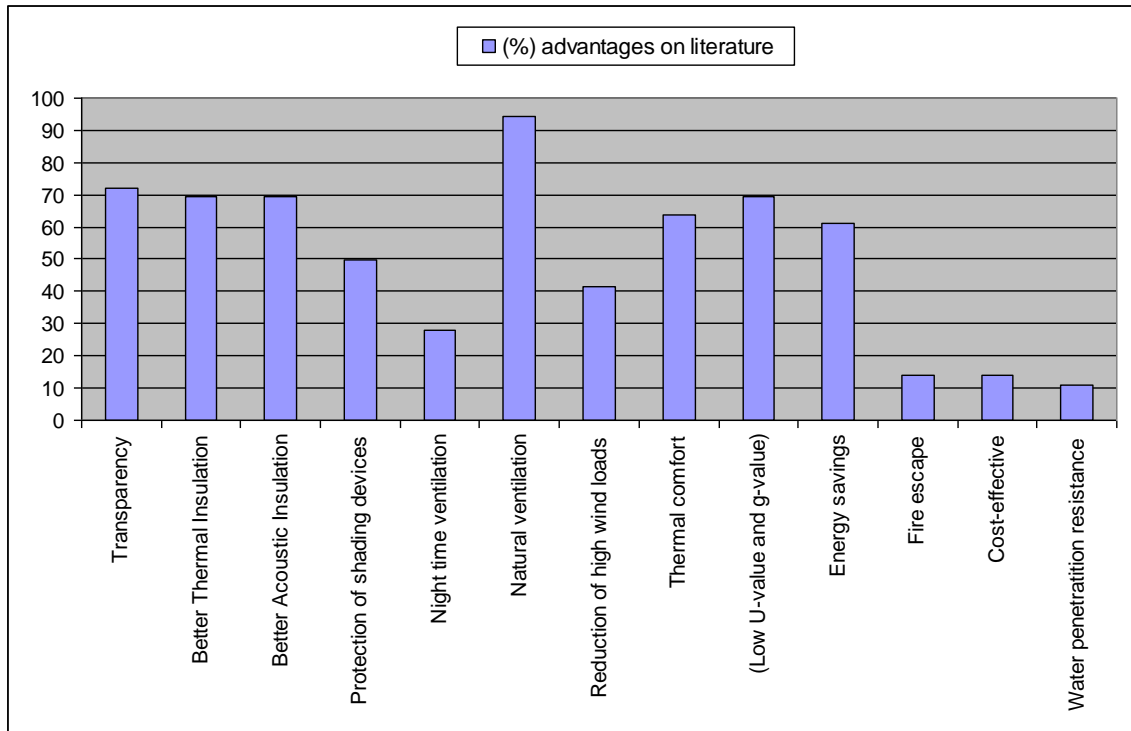


Figure 3.23. The percentages of the advantages of DSFs mentioned by some researchers on literature

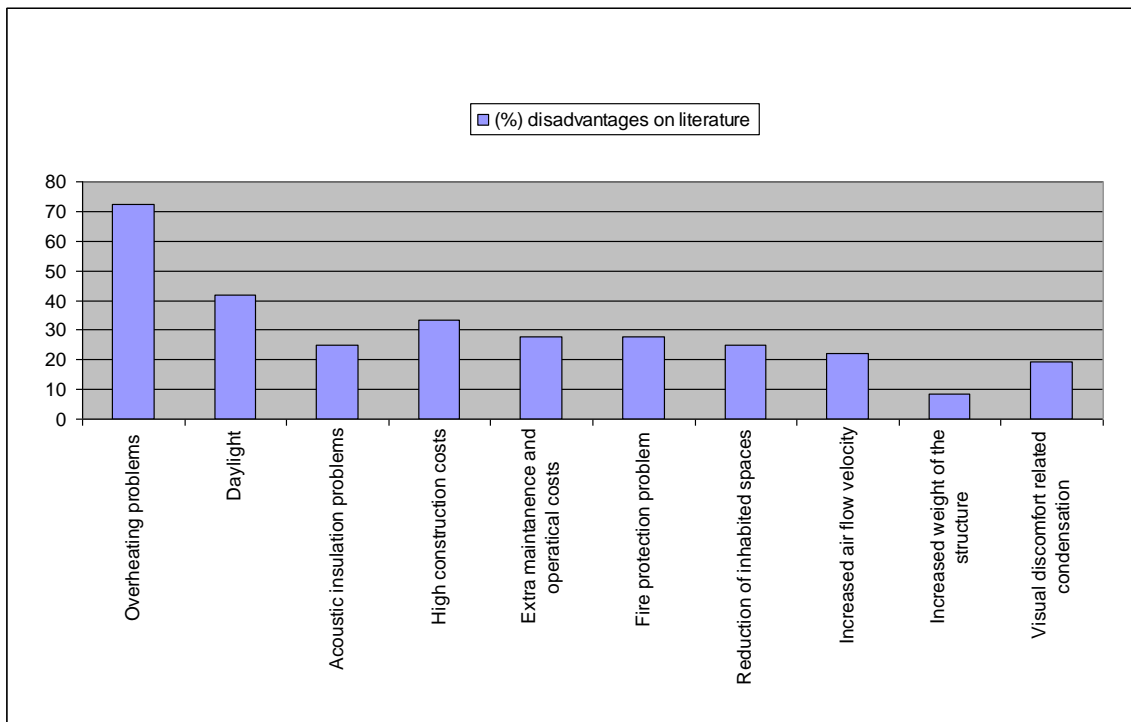


Figure 3.24. The percentages of the disadvantages of DSFs mentioned by some researchers on literature

The main advantages of the DSF accepted by most of the researchers are natural ventilation, transparency, better thermal and acoustic insulation and reduction in the thermal transmission and solar heat gain values (Figure 3.23). There is discrepancy about the cost effectiveness of the system and fire escape. In the literature, the main agreement of the most researchers is the overheating problem in the cavity. Daylight and high construction costs are also the significant disadvantages of the DSFs (Figure 3.24).

### **3.6. Design Considerations**

Performance of a DSF system is considerably related with the geometric configuration of the cavity, air flow modes, and the control system used to activate different modes. This presents a complex engineering challenge (Ralph et al, 2011). Design process should be integrated carefully in order to support desired goals from the DSF systems, especially in terms of energy performance. The designer needs to have a good understanding about the principles of double skin facade systems in order to realize problems in advance that may occur. This is significant in terms of developing problem-oriented design solutions. The proper behavior of a DSF is the key to support energy performance. However, the proper behavior depends on the effective design parameters of a DSF (Pasut and De Carli, 2011). In this study, architectural configuration issues in designing a DSF will be evaluated to give a comprehensive overview of DSFs in line with the purposes of the study.

#### **3.6.1. Daylighting**

Except from the advantages of energy savings of DSF, the other considerable benefit lies on natural lighting sense. These systems improve the internal visual comfort (Asdrubalı and Baldinelli, 2007). However, the main requirement of daylighting is not only maximization of the amount of natural light, but also the better performance in the light quality. DSFs provide good daylighting in overcast sky conditions. On the other hand, large glazed skins may create glare problems.

The performance of the double-skin facade in terms of daylight availability inside the building is lower in comparison with the single-skin models, mainly because

of the extra layer of glass. Moreover, shading devices located in the cavity can decrease the lighting levels inside the room. If the louvers are fitted in the cavity, artificial lighting can be demanded for adequate lighting in the building. While reduction of solar radiation can be provided by using controlled solar shading devices, they create constraints from maximizing the use of daylight (Haase et al. 2009).

### **3.6.2 Glazing**

Double skin facades can decrease the solar heat gains and can provide environmental benefits (Lstiburek, 2008 and Chow 2012). One of the significant thermal loads in the heat gain of building envelope is the heat transfer through window glazing of the external wall of the building (Chan et al., 2009). With the proper selection of the glazing types in building facade, the cooling load can be significantly decreased (Singh et al., 2008).

The glazing on external facade generally consist of a thermally-insulated double glazing. This glazing provides good thermal performance with preventing condensation inside the facade. The external glass of DSF generally accepts as colorless transparent glass, minimizing the unfavorable effects of light occurred due to the glass reflection (Zhou and Xue, 2012). On the other hand, the inside facade generally consists of a reinforced single glazing (BBRI, Gratia et al. 2004, Wong et al. 2008, Eicker et al. 2008). However, these two types of glazing are located on opposite order in some studies (Jiru et al. 2004 and Park, 2004). In a study, single inner and double outer glazed panes provides better decrease in cooling energy loads (Chan et al., 2009).

Haase et al. (2009) presents the influence of window-wall ratio (WWR) on annual cooling load for a south facing facade. While the cooling loads for clear glazing varies between 142 and 171 kWh/m<sup>2</sup>, it is between 135 and 155 kWh/m<sup>2</sup> for reflective glazing. For solar control glazing 136 and 157 kWh/m<sup>2</sup>. The reflective glazing show similar performance with solar control glazing. Clear glazing is the worst solution. Moreover, the WWR has a significant influence on annual cooling load. DSF systems provide different window size for the internal layer. The amount of heat gain via the envelope of the building can be reduced considerably by designing a ventilated DSF consisting of two clear glazing in both internal and external layer. In Chou et al. (2009) are observed that the solar heat gain coefficients (SHGC) are considerably higher in the

East, West facing facade than the North, South facing facade for summer condition. Depending on their results, a double skin facade building having window to wall ratio (WWR) of 0.3 has showed acceptable envelope thermal transfer coefficient (ETTV) reduction of up to 45 %. When WWR gets close to 0.9, the potential of using DSF to reduce SHG has been observed to diminish. Chan et al. (2009) obtain that the double skin facades having single clear glazing as the inner pane and double reflective glazing as the outer pane can provide an annual saving of about 26 % in the cooling energy demand of building, as compared with a single skin facade having single absorptive glazing.

On the other hand, small tempered glass panels perform better than larger sheets in terms of thermal resistance against higher thermal stress (Chow and Hung 2006). Moreover, optical properties of glazing depend on the incident angle between the surface and the ray direction of sun: as this angle deviates from the normal direction ( $0^\circ$ ), transmittance decreases, and increases in reflectance and absorbance (Asdrubali and Baldinelli, 2007).

### **3.6.3. Building Geometry/Design**

Double skin facade systems are sophisticated. Because, various parameters affect the design process such as geometric, thermophysical, optical, and aerodynamic properties of the various components of the double skin facade and the geometry of the building itself (Hensen et al., 2002). The architectural configuration issues have a significant role on better performance of buildings.

The building height can have a significant effect on the ventilation strategy and the cavity of the facade (BBRI, 2004). The environment of the building can define the design decisions. For instance, while the building located in the city centre needs acoustical precautions, in the country side, it is not a significant problem.

Hamdan (1994) states that the appropriate configuration of a facade, a maximum reduction value in thermal gain of 40% in the summer and 80% in the winter can be provided. Energy performance of a DSF in winter is two times greater than in summer. Gavan et. al. (2007) presents that while the annual energy consumptions for heating and cooling as low as 44 kWh/m<sup>2</sup>· year in a traditional facade, it is recorded as 38.7

kWh/m<sup>2</sup>·year in a DSF. Saelens et al. (2008) found quite similar results although the geometry and the climate are different.

#### **3.6.4. Solar shading devices**

The shading devices in a DSF can be located in the external facade, internal facade and in the cavity. Some architects consider that external solar shading devices can not be a better solution if maintenance and aesthetic reasons are taken into account. Moreover, internal shading devices are not effective to control the solar gains. However, the shading devices in the middle of the cavity provide an effective control of solar gains and also provide a protected area for shading devices. Moreover, it can be used under all meteorological conditions (Loncour et al, 2003). On the other hand, when it is positioned in the cavity, it causes difficulties in removing the absorbed solar heat (Saelens et al. 2003).

The distance between the blind and the external glazing is a significant parameter in terms of air velocity profiles inside the double-skin facade channel (Safer et al 2005). Oesterle et al. (2001) emphasize that the position of the shading devices affects the thermal performance of DSFs. When the shading devices located towards to the external skin, this improves ventilation and decrease overheating in the cavity. They offer to locate the shading devices to the first third of the cavity and at least 150 mm from the external skin to prevent overheating.

Colour the angle of shading devices are another effective factor on DSF performance. Haase et al (2009) present that the color of roller blind is significant. Black roller blind is largely responsible for high gap temperatures. For instance, a white colored roller blind reduces gap temperatures by 11 K. In Gavan et al. (2010) the authors analyze of the temperature profiles inside the DSF through a test cell. It shows that the surface and air temperatures are mainly determined by the sun-shading device angle. If the shading device is left on closed positioned, the outdoor air cavity of the facade and the shading device itself take higher temperatures than the opened position. Yuan et al. (2007) concludes from their case study for ventilated DSF that it is possible to reduce 40% of the heat gain in summer by place the cavity shading close to the inner glazing. This emphasizes the positive effects of natural ventilation on overheating in a DSF system.

The material of shading device is another important issue. The surfaces of shading devices expose to high temperatures due to the sun and excessive temperatures accumulate on the shading device. To decrease this condition, the aluminum profiles can be substituted with photovoltaic modules. This contributes the energy performance of the facade (Infeld, Mei and Eicker 2004). On the other hand, Stec et al. (2005) use plants as shading device in their study and they suggest that plants create a more effective shading device element than blinds. They provide reduction of temperature and cooling energy.

### **3.6.5. Climatic Conditions**

The complexity and adaptability to different climatic conditions of double skin facade systems indicate the importance of designing carefully. If the concept of double skin facade and the desired performance requirements are understood clearly, DSFs can be adapted on all climatic conditions. Pasquay (2004) states that the double skin facades are not the best selection for every building in every location. Moreover, each building must be considered independently. Nowadays studies related on double skin facade are undertaken not only cold climates, but also in different climatic conditions such as hot and humid and moderate climates.

The architectural design decisions is quite important in order to support energy performance of double skin facade. It is quite significant to reduce the high peak cooling loads during summer period especially in hot and humid climates. This is provided by a carefully designed double facade that supports energy efficiency (Haase, Marques da Silva, and Amoto, 2009). DSFs help to insulate the building and reduce energy consumption for heating. This is important for cool climates with strong winter seasons (Park, C.S., 2003). Saelens et al. (2003) say that multiple-skin facades can improve the energy performance. It is concluded from the analysis that multiple-skin facades show better energy performance in winter owing to that variants performing well in winter. However, they are not useful in summer. On the contrary, Asdrubali and Baldinelli (2007) presents that the DSF system can provide energy saving both in winter and summer season, where savings up to 28% could be reached in winter and allowing a cooling reduction of up to 14 % in summer. Saelens et al.(2012) state that energy performance of multiple-skin facade cannot be evaluated by merely considering the



losses and gains. They emphasize that the enthalpy change of the cavity air and a whole energy analysis of buildings is conceived.

DSF systems can be applicable and they can support energy performance of buildings for every climatic condition if the architectural configuration issues are understood sufficiently to generate energy efficient solutions for them.

### **3.6.6. Width of cavity**

The ventilation and temperature in the DSF depend on the width of the cavity. When the cavity is narrower, the higher overheating risk occurs in the facade (Balocco, 2002). Oesterle et al. (2001) emphasize that the reduction in the cavity width causes considerable pressure losses in the cavity. This point out that airflow in the cavity is related with the form and size of the facade. Zöllner et. al. (2009) defines in their study that the distance of cavity between the internal and external facade varies from 0.3-1.5 m and the aspect ratios depended on a typical storey height is about 4 m of  $3 < H/S < 15$ . Moreover, based on the compartmentalization of the spacing the aspect ratio,  $B/S$  varies in a range of 0.5-500. ( $H$  is the total height of the cavity,  $S$  is the distance between external and internal facade and  $B$  is the width of the building).

Yuan et al. (2007) states that energy performance can be achieved by increase the cavity depth if the depth is less than 1 m. Based on fire protection issues (Chow and Hung 2006), some experimental investigations indicated that the cavity depth is the significant factor: wider cavity depths are safer, as well as a horizontal partition of the facade.

### **3.6.7. Height of facade and size of openings**

A construction of a second glass facade in front of the building with openings provides to reduce pressure fluctuation and enable one to design openings on external facade for natural ventilation at wind speeds up to 10 m/s (Zöllner et al 2002).

Mingotti et al. (2011) have studied how the height of the facade and the sizes of the openings in the room. They present that the DSF can be optimized for each of flow mode. The laboratory experiments and the quantitative model show that the small openings on the facade favorable in colder seasons to decrease great heat losses.

However, large openings on the facade are suitable in warmer seasons in order to minimize the overheating problems. Moreover, to prevent overheating in the cavity of DSF, one more opening can be added at the base of the facade providing that they operate in warm season mode.

The sizes and positions of both air inlet and outlet have considerable effects on energy saving of DSFs (Oesterle et al. 2001). Different vent configuration is designed and each vent is designed as same cross section. Two air inlet vent with three air outlet vent show better energy performance than three air inlet vent with two air outlet vent. Return flow zone is larger in the model having two air outlet openings. Return flow zone positioned on both sides is useful to reducing indoor thermal radiation. This condition provides energy saving (Zhou and Xue, 2012). Though larger opening areas between indoor and the DSF space provide high ventilation rate, they are unfavorable on upper floors in terms of pressure difference. To provide favorable ventilation performance through the top floor, opening areas should not be less than  $2 \text{ m}^2$  (Ding et al. 2005). Compagno et al. (2002) states that the position of the inlets and outlets depend on the wind pressure conditions in the building skin and the stack effect of the openings. The author gives the priority to the pressure difference between the inlet and outlet openings that determines airflow in the cavity.

Adjustable vents are suggested that may be opened or closed depends on the climatic conditions. In summer, the cavity should be ventilated as much as possible. This decreases the transmission gains and thus cooling loads. Cooling loads get higher if there is not airflow in the cavity (Saelens et al. 2003).

### **3.6.8. Orientation of DSFs**

The orientation of the facade has been defined as having significant effects on annual heating and cooling loads. DSF systems positioned on South, South east and South west orientation are the most efficient (Haase et al. 2009, Chan et al. 2009). A study shows, in contrast to other studies related to this issue that a DSF applied on east facade in Norway, the heating energy demand is greatly decreased (by 16 %) as compared to a conventional single glass solution. Besides, cooling energy demand does not increase (H  seggen et al 2008). Wong et al (2008) pointed out that double skin facade facing on eastern and western walls of building can considerably conserve

cooling energy by protecting buildings from solar radiation and reducing the heat by way of natural ventilation.

The climate facades or DSFs show better performance in each season and for each configuration, in terms of both energy efficiency and thermal comfort issues than the other type of facades. However, it is still not competitive with opaque facades. This facade technology needs further precautions in order to prevent overheating in cooling periods. Besides, it behaves like a solar collector in the heating season. Therefore, this condition should be improved effectively (Serra et al 2006).

To sum up:

- The double skin facade systems have been discussed and continue to do so in so many studies by the different disciplines with an increasing momentum from 1990's to date. In this sense, the efficiency of the energy should be examined in consideration of the climate conditions of our country for the double skin facade systems suggested as the energy active structure coat in the Europe and North America.
- Architecture design decisions that required to be considered in the starting phase of the design and playing an determinant role over the energy performance of the double skin facade systems carry great importance (geometric configuration of the double skin facade, the direction of the facade, glass types used in the facade, the size of the air channel used between the two facades, flow mode types within the air channel, the location and size of the culverts etc) (Figure 3.2).
- The design of the building geometry and double skin facade systems shaped accordingly are the important architecture design decision that triggers the energy performance. The architecture design factors (Figure 3.2) specified with building geometry and double skin facade interaction should be analyzed with developing the variations.
- When all of the studies made with the double skin facade systems in the last decade is examined, the common advantage that agreed by the researchers is that it has natural ventilation. The disadvantages mostly accepted by the researchers overheating problem formed between the double skin facades negatively affects the heat comfort of the place.

- The suitable glass selection on the double skin facade surfaces and location of the sunshade elements in the air channel between the two facades provide protection in the negative climate conditions of the outside except for the determinant role over the energy efficiency of these elements. Furthermore, it has been observed that overheating problem can be prevented that has been seen as the biggest disadvantages by most of the researchers in the event suitable locating the sunshades in the air channel found in the double skin facade.
- Air channel found between the double skin facades is in the role of buffer zone. It prevents the unwanted heat loss in the period of heating. In the cooling period, it can evacuate unwanted heat gains by enabling natural ventilation with air vent located at the facade. Enabling natural ventilation by absorbing the wind velocities at height structures is the important advantage of the double skin facade systems.
- Even though double skin facade systems enables natural ventilations and evacuate the unwanted heat gains at the cooling term, it is required to pay attention to the selection of the parameters (Figure 3.2) that are effective in the architecture design according to the climate conditions of the country of the double skin facade systems in particular to the hot-humid countries. As a result of the literature review that has been examined, overheating problem between the two facades can be observed due to the insufficient natural ventilation in the air channel in the hot-humid countries. The most cited problem in the double skin facades is the overheating problem. The overheating problem negatively affects the heat comfort of the user and the energy cost, as well. It is required to prevent the overheating problem with natural ventilation. The size of the air vents in the double skin facade and location of the facade are the important architecture decision for this to be effective.
- It is required to prevent the increase in the energy consumption due to the overheating in the cooling period with the architectural design decisions from the double skin facade systems suggested as the energy effective structure coat by providing gains in the energy consumption during the heating period. That is, gains in the cooling energy consumptions in the hot-humid regions are the important design decisions to be considered rather than the gains in the heating system.
- There should not be a single design model for double skin facade systems that purpose to decrease the heat loss in the heating term and decrease in the heat gains in the cooling term. That means that several variations can be derived with the

combinations of the architectural design parameters (Figure 3.2) and one of them may be more suitable than the others in the different climate region. For that reason, design decisions (Figure 3.2) that are effective in the design of the double skin facade systems should be examined comprehensively with experimental measurements and simulations.

## CHAPTER 4

### DOUBLE SKIN FACADE: EXPERIMENTAL SETUP

Experimental aspect of the study shown in Figure 4.1 includes double facade (III) application between the two environments where indoor (I) and outdoor (II) environmental conditions are created. Indoor environment and outdoor environment are conditioned with a heating/cooling water bath (IV) and a cooling group (V) are placed outside the building, respectively (Figure 4.1a and 4.1b). Also, a solar simulator (VI) and air flow fan and integrated duct system (VII) are used to provide the required conditions in the experimental study. A data logger system (VIII) records temperature, differential pressure, velocity and heat flux measurements at different points. Effects of dimensionless characteristic length (depth / height ratio) of the double facade intermediate region (III) designed as moving and use of components present at the intermediate region which induce a pressure drop on flow are studied by creating natural and forced convection conditions. In this way, effect of dimensionless characteristic length important in architectural design and use of components such as damper, sunshade, loophole which induce a pressure drop are observed experimentally by performing a detailed flow analysis. Also, their potential impact on energy consumption is determined.



a) Experimental setup layout in the laboratory



b) Outside section of cooling group

Figure 4.1. Experimental Setup

Experimental setup has been built at the Building Physics Laboratory, which is 11.9 m in width, 17.8 m in length and with a height of 4m, on the ground floor of Block B of Faculty of Architecture, İzmir Institute of Technology. Layout of the experimental setup in the laboratory can be seen in Figure 4.2.

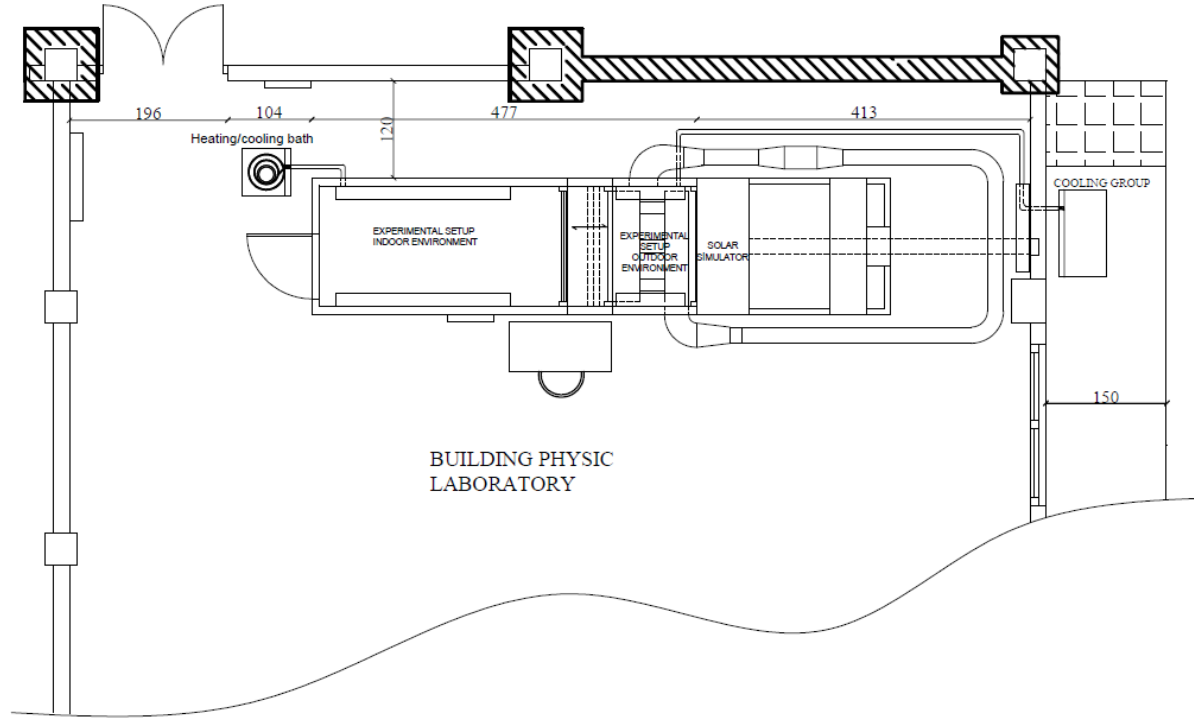


Figure 4.2. Layout of the experimental setup

General plan of the experimental setup is seen in Figure 4.2. Accordingly, system consists of 7 major parts which are coded from I to VII in the Figure 4.2 and 4.3: I: indoor environment, II: outdoor environment III: cavity, IV: heating and cooling water bath, V: cooling group, VI: solar simulator, VII: air flow fan and duct system, VIII: Data logger.

#### 4.1 Experimental Setup: Indoor Environment (I)

Indoor Environment Simulation Setup shown as I on Figures 4.1 and 4.3, which is 1.5 m in width, 3m in length and 3m in height, was manufactured using 10-cm-thick polyurethane thermal insulation panels. One of the short walls was double-glazed with dimensions of 4–12–4 mm. Heating/cooling serpantines, which is 2.5m in length and

made up of thin aluminum sheets around copper pipes and where water coming from the constant temperature bath can circulate (Fig. 4.1a), are placed on long walls of the setup in such a way that they face each other (Figure 4.4a). A thermally insulated door which can be opened both from inside and outside is placed at the other short wall of the indoor environment setup. Via this door, indoor environment can be accessed to place measuring probes and other possible interventions. This thermally insulated door is manufactured in such a way that it can be opened from inside in case it gets closed while working inside or it is locked from outside in a way ensuring security.



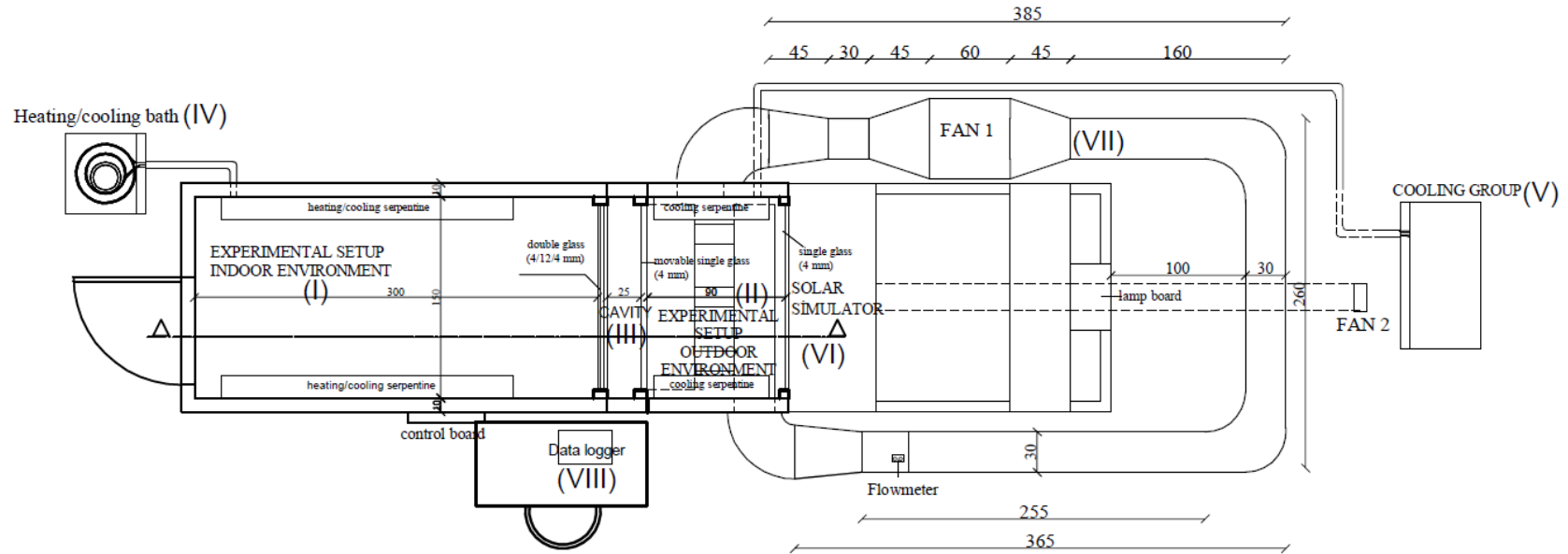


Figure 4.3. Experimental setup plan

where I: indoor environment, II: outdoor environment III: DSF cavity, IV: heating and cooling water bath, V: cooling group, VI: solar simulator, VII: air flow fan and duct system (in cm), VIII: data logger.

Cooling and heating of indoor environment simulation room is performed by circulating cold-hot water in radiator panels by using a pump shown in (IV in Figure 4.4b). The water temperature can be maintained at a desired level by a thermostat located within the room. Water inlet / outlet temperature and flow rate are stored in a data logger by measuring with a setup (consisting of temperature probes and flow meters) which is positioned just outside the room. Thus, amount of heat extracted from the indoor environment unit or transferred to the unit can be determined. A cooling-heating water bath outside the room is used in order to cool or heat the water (Figure 4.4b and 4.4c). The cooling-heating water bath has a size of 50x50x50 cm water tank and it can continuously circulate the water. Water circulation is kept continuous in order to prevent icing in the boiler at low temperatures. Volumetric flow rate of the fluid in the cooling-heating bath are measured by using a rotameter, in the order of 350-380 liters per hour during the experiments.

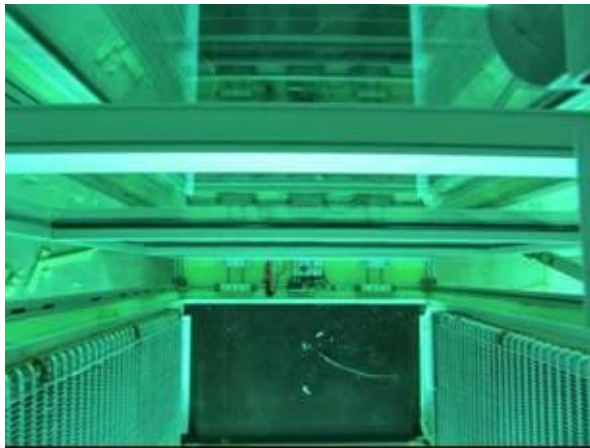


a) Indoor environment (I)      b) heating/cooling water bath and pump system (IV)      c) heating/cooling water bath (IV)

Figure 4.4. Indoor environment of the experimental room and the cooling-heating water bath

## 4.2. Experimental Room: Outdoor Environment (II)

Outdoor Environment Simulation Setup shown as II in Figures 4.1 and 4.3, which is 1.5 m in width, 0.9 m in length and 3 m in height, is manufactured by using polyurethane thermal insulation panels which are 10 cm in thickness same as indoor environment. Its surface on solar simulator side is single-glazed 4mm in thickness. Other surface is in contact with the cavity double facade which separates indoor and outdoor environments of the experiment room from each other. Cooling of the environment is performed with air to refrigerant compact heat exchanger wall grids to be hung on the two opposite wall surfaces (Figure 4.5a). The outer unit of the cooling system is located outside the building (Figure 4.1b and Figure 4.3) and it maintains the environment at the required temperature by directly circulating the coolant through the heat exchangers (as V in Figure 4.5b). In here, the extracted amount of heat is not measured and required temperature is provided to be kept constant with automation.



a) outdoor environment



b) cooling unit

Figure 4.5. Outdoor environment of the experimental setup and the cooling unit

## 4.3. Experimental Room: Intermediate Partition (Cavity-III)

Experimental room intermediate partition designed to simulate the double facade shown as III in Figures 4.1 and 4.3 is seen in Figure 4.6. Single-glass component 4 mm in thickness on the outer surface of the double facade is mounted on the moving mechanism of this system positioned between the outdoor and indoor environments of the experiment room (Figure 6a). Other surface of the intermediate region is empty and

overlaps with the double facade of the indoor environment. Intermediate region is also insulated against heat transfer in the same way as indoor and outdoor environments. Collapsible clearances which are 20cm in height and compose of the same type of glass are available at the lower and upper parts of the single-glass component (Figure 4.6a and 4.6b). Thus, it is provided to work on air flow modes within the double facade.



a) bottom view of cavity

b) top view of cavity

Figure 4.6. Cavity of experimental room and moving mechanism

#### 4.4. Solar Simulator Unit (VI)

Solar simulator unit shown as VI in Figures 4.1 and 4.3 is automatic air-cooled closed matrix type (Figure 4.7). Whole support structure is made of aluminum. Weight is evenly distributed in the system and the tilting angle is set to approximately 45 degrees. A completely modular system is chosen in relation to design. This modular system allows one change sizes of all required parts and, in case of transportation, each part of it can be disassembled in the form of legos and pieced together. System can be moved up/down for 40 cm in the vertical direction with a motor controlled from the control panel. It is electrically protected and, in case of any fault, it can turn off itself automatically by cutting off the system's energy ensuring safety. System's lightness and easy movement as well as its stability are provided with fixable casters. System consists of 12 lamps, 3 fans, one scissor jack type, moving partition and control board. Lamps are located so as to constitute a 3x4 matrix (Figure 4.7a). Total electrical power is on the order of 13kW approximately. Lamps consume 12kW of this while the remaining is consumed by the fans and the control board (Figure 4.7b). Since a high electrical charge

exists in the laboratory where the experimental setup is to be installed, additional improvements close to the maximum load which electrical installation of the building can withstand have been made at the electrical installation of the building within the bounds of possibility in cooperation with the Directorate of Construction and Technical Works of İzmir Institute of Technology in order to avoid any adverse situation. Following the system start-up, fans are automatically initiated or put into use manually. Sockets used in the lamps are of E40 type. General characteristics of the system are given in Table A1 (Appendix A).



a) Solar simulator unit  
(lamps are closed)



a) Solar simulator unit  
(lamps are opened)

Figure 4.7. Solar simulator unit

#### 4.5. Mechanical Ventilation System (VII)

Fan and channel system shown as VII in Figure 4.1 and 4.3 is integrated into the system in order to ventilate the double facade. For this purpose, a Venco branded, 500W, radial fan type is used. Fan characteristic is given in Appendix A Figure A1. This capacity meets effect of pressure drops and the required flow rate values within the double facade.

Fan sucks air from the outdoor environment simulating portion of the experimental setup (Figure 4.8) and air returns again the same portion via a 315mm spiral channel system. Components are used at entry and exit points of the section which simulate the outdoor environment and also at entry and exit points of the fan

system for transition from a rectangular cross section (400\*250mm and 600\*300mm, respectively for the aforementioned entry and exit points) to a circular cross section (Figure 4.9). In Figure 4.10 where an image of the section simulating the outdoor environment is found, it can be seen that sucking is performed from the bottom-left section and entry to the double facade is carried out with distribution hoods. Flexible channels with a diameter of 150mm are used due to moving hood mounted on the double facade. Moreover, the flow is made as homogeneous as possible by adding a perforated sheet at the outlet of the hood (entry to the double skin facade).



Figure 4.8. Fan system and its connections



Figure 4.9. General view of the channel system



Figure 4.10. Entry organization to the double skin facade at the outdoor environment simulating portion of the experimental setup

Approximately eight times of the diameter seen at the front side in Figure 4.9 is left in order to determine clearly the straight channel fluid flow. Velocity pressure is obtained with the apparatus which makes measurements according to working principle of Pitot tube located as shown in Figure 4.11a. For this aim, HK Instruments DPT



(Differential Pressure Transmitter) 2500 – R8 model is used (it is mounted at outdoor unit wall as shown in Figure 4.11b). This differential pressure measurement system operates in the range of 0 – 100 Pa. This velocity pressure is measured with the differential pressure meter and this is recorded as voltage in the data recording system; then, these values are converted to differential pressures which are finally converted to velocity by using Bernoulli Equation.

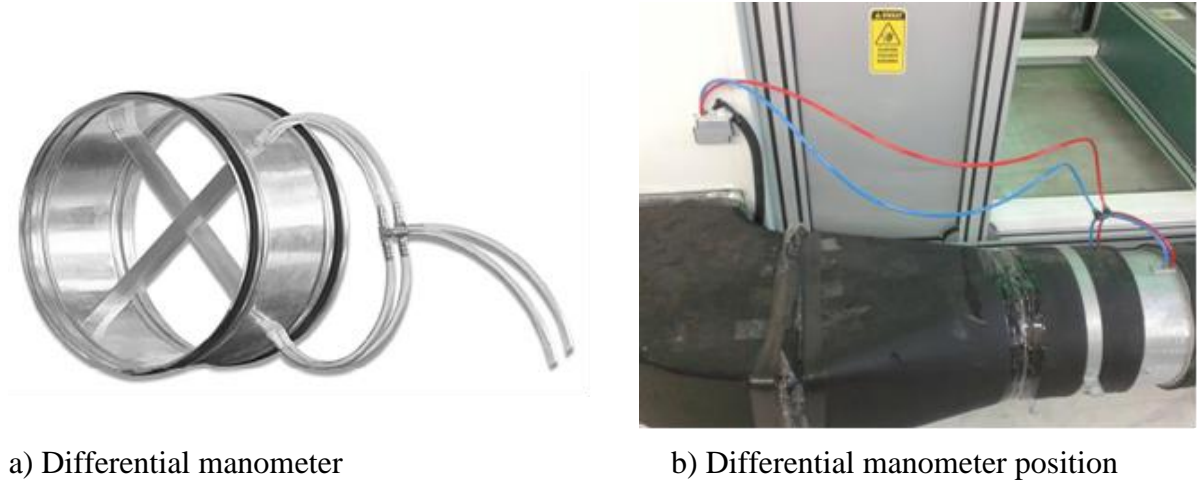


Figure 4.11. Determination of channel air flow rate

## 4.6 Ventilation of Solar Simulator

A significant portion of the energy released from the solar simulator moves past to the laboratory environment where the experimental study is conducted and a considerable increase in the laboratory ambient temperature is seen in short period of time. This situation, beyond worsening operating conditions, causes adverse effects within the context of taking the experimental measurements in a reliable manner due to problems such as potential heat gains in the system and overheating of the electrical systems. A wall fan system is used for the removal of released energy and the fan rejects air at high temperature through a channel system with a diameter of 315mm (Figure 12). Here, a Fanline branded, 284W, round radial wall fan is used (KV 315 C). Also, two fans available in the solar simulator unit contribute to this system. Moving vent opening placed in the outdoor environment is opened when the system is initiated and rejects hot air outside while it is kept closed when the simulator is off (fan is linked to the solar simulator also electrically and initiates simultaneously) (moving lid present on the cooling group represented as V in Figure 4.12).





Figure 4.12. Ventilation of solar simulator

#### 4.7 HIOKI Data Logger, LR 8402-20 (VIII)

Temperature measurements taken at different points of the experimental setup with T-type thermocouples and PT-100 probes are recorded with the data logger shown as VIII in Figures 4.1a and 4.3). Moreover, velocity measurements from different points of the cavity, measurements of pressure difference in the cavity and measurement of pressure difference (velocity pressure) for determination of air velocity and flow rate in the air channel shown in Figure 4.13 and heat flux values measured by pyranometer are also recorded. Data logger properties can be seen in Appendix A, Figure A2.

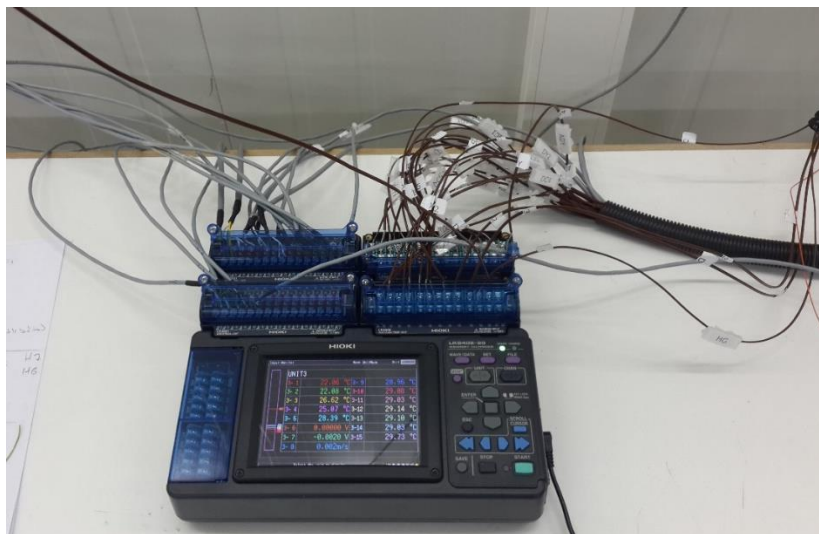


Figure 4.13. HIOKI Data Logger

## 4.8. Measurement Systems

### 4.8.1 EKO MS-410 Pyranometer

Heat flux of the energy obtained from the solar simulator on the outer surface of double facade (outdoor environment part of the experiment room) as shown in Figure 4.14a will be measured with the MS-410 pyranometer presented in Figure 4.14b. Device is compatible with the measurement sampling of solar radiation with a 10-minute average value. Analog output of the device in mV will be converted to  $W/m^2$  and recorded by the data logger. General information about the device is given in Appendix A, Table A2.



a) Position of pyranometer



b) MS-410 pyranometer

Figure 4.14. MS-410 Pyranometer and its position on the experimental room

### 4.8.2 Differential Pressure Measurement (DPT 2500-R8 model)

Differential pressure measurement is performed via two points placed within double facade at 120 cm intervals (marked with flags in Figure 4.15a – aims to avoid accidental contacts). For this purpose, HK Instruments DPT (Differential Pressure Transmitter) 2500 – R8 model is used (the above one from those two small sized apparatuses mounted on the wall in Figure 4.15a and its enlarged view is also given Figure 4.15b). This differential pressure measurement system operates in the range of 0

-25 Pa as minimum and 0 – 250 Pa as maximum. This differential pressure meter is put into use in the experimental study with respect to usage of components which are placed in double facade and will induce a pressure drop and operated in the range of 0 – 25 Pa. Also, by using the other differential pressure meter shown in Figure 15b (HK Instruments DPT-Differential Pressure Transmitter 2500 – R8 model), differential pressure measurements in air channel are performed in the range of 0 – 100 Pa and flow rates are obtained (Figure 4.11b). Measurements are recorded as volt in data logger and converted to differential pressure values in Pascal. The properties of the DPT can be seen in Appendix A, Table A3.



a) Differential pressure measurement      b) HK Instruments DPT

Figure 4.15. Differential pressure measurement system

### 4.8.3 Velocity Measurement between Double Skin Facades

Delta Ohm HD 4V3T S1 device placed between the double facades for velocity measurement (Figure 4.16a) is used in order to perform velocity measurements following the flow are fully developed. Prob of the measurement system shown in Figure 4.16b is linked to the data logger with the bottom one from those two small sized apparatuses mounted on the wall and velocity measurements are performed by positioning its probe in the other photograph within the cavity and by manually

positioning from the outside of the experimental setup. The properties of the Delta Ohm HD 4V3T S1 device is shown in Appendix A, Table A4.



a) Probe of the velocity measurement   b) Velocity measurement device connection

Figure 4.16. Velocity measurement system

#### 4.8.4 Temperature Measurements

T-type thermocouples and PT100 probes are used for temperature measurements at different surface and environments of the experimental setup. One T-type thermocouple and one PT100 probe measures the temperature of the laboratory air where the experimental setup is in. In the experimental setup, PT 100 probes are used for temperature measurements of the indoor environment as well as inlet-outlet temperatures of heating-cooling water bath. T-type thermocouples are used in other parts. Accordingly, when the cavity cross section in Figure 4.17 is considered, different view directions are given.

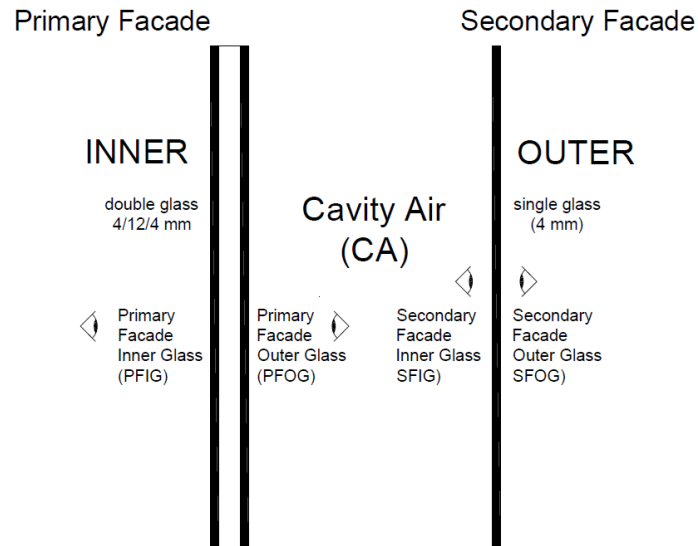


Figure 4.17. Surfaces on the Double Skin Facade

Eight thermocouples are placed inside the cavity in order to determine variation of the air temperature. Thermocouple layout is shown in Figure 4.18 and numbered from CA1 to CA8.

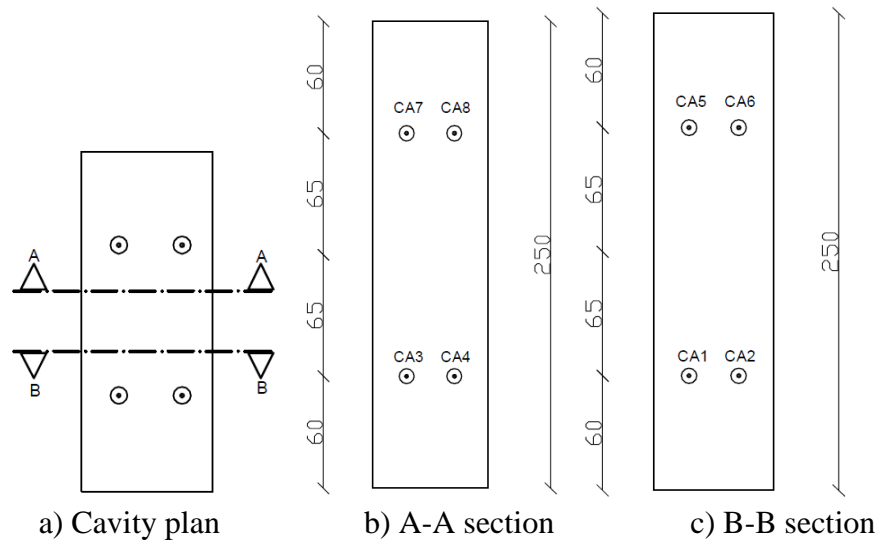


Figure 4.18. Layout of thermocouples inside the cavity (in cm)

Air temperature inside the environment simulating the outdoor environment is measured with two thermocouples which are numbered as D1 and D3 in Figure 4.19 at 2 different points. Air temperature in the section simulating the indoor environment is measured at 3 different points (AI1, AI2 and AI3 in Figure 4.19) and also inner surface temperatures of this environment is measured and recorded. Here, representation coded

with AT is related with the top surface. In Figure 4.20, temperature measurement points placed on the other two sides of the room can be seen (coded as IW and IL).

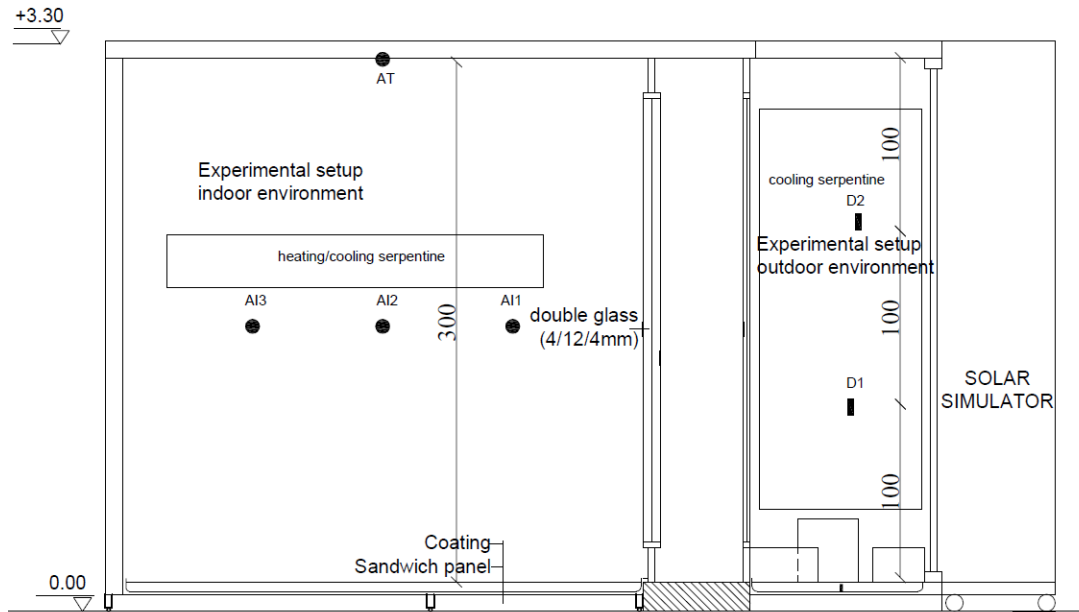


Figure 4.19. Temperature measurement points at indoor and outdoor simulation rooms of experimental set up (in cm)

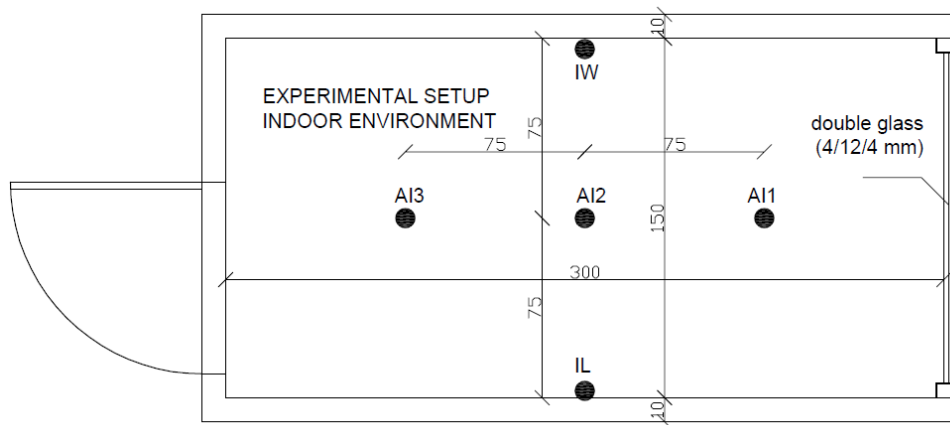


Figure 4.20. Temperature measurement points at indoor simulation room

Six T-type thermocouples are placed at each two different surfaces in order to measure inner surface temperatures of the double facade. These thermocouples are coded in Figure 4.21 from PFOG1 to 6 for the portion of the cavity facing the inner room and from SFIG1 to 6 for the portion of the cavity facing the outer room. Measurements are also taken with two probes at each surface of these two glass surfaces of the double facade facing the portions simulating the indoor environment and

simulating the outdoor environment (PFIG1 and 2 and SFOG1 and 2). Also, heat transferred from aluminum frames on which glasses are fitted is determined by performing temperature measurements at inner and outer surfaces of these components (AIY, AAIY, AADY and ADY). Probes are either covered with aluminum foils (in air temperature measurements) or coated with a special paste with a high thermal conductivity (at the surfaces) against thermal radiation. Cavity inlet (AI) and outlet (AO) fluid temperatures are also measured with different probes. All T-type thermocouples and PT100 probes are linked to the data logger. These connections and data logger is shown in Figure 4.13.

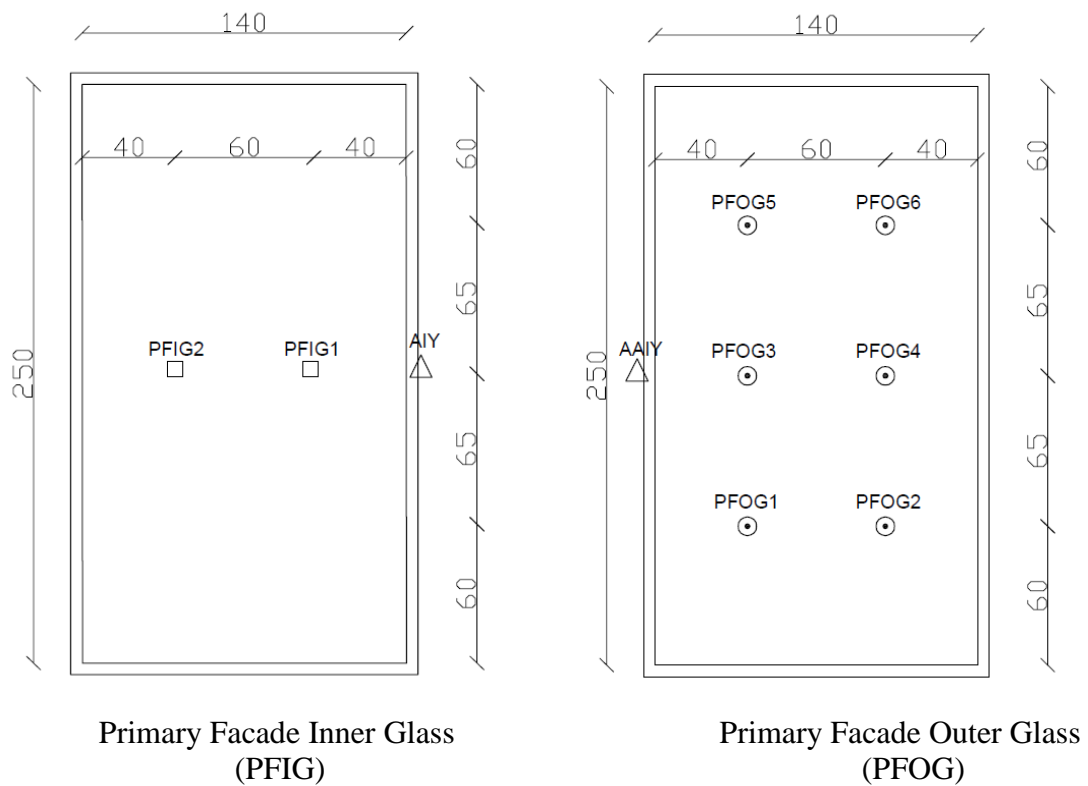


Figure 4.21. Temperature measurement points on cavity surfaces

(cont. on next page)

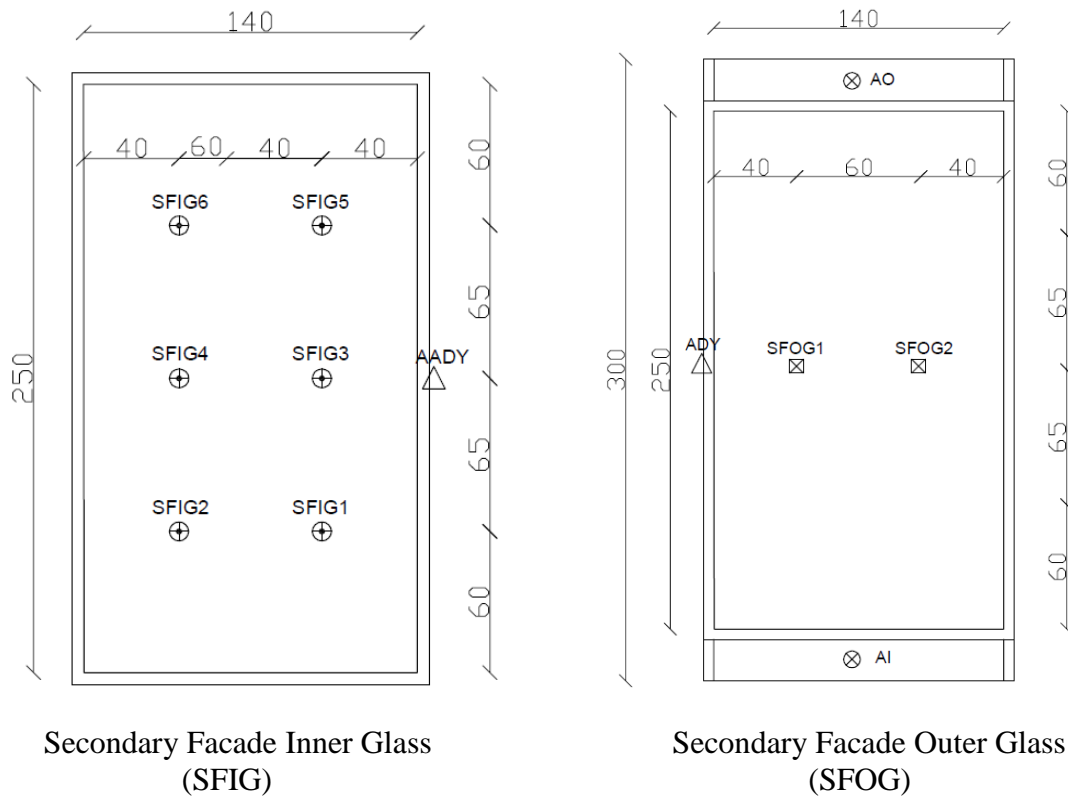


Figure 4.21. (cont.)

## 4.9. Experimental Study

Experimental studies were conducted on the experimental setup at different times and under different conditions. Table 4.1 defines general specifications related with all experimental studies

Table 4.1. Experimental study list

1	2	3	4	5	6	7	8	9	10	11
#	Code	Time	NC	FC	S	TS	Flow	SS	ΔP	cavity
1	Case3-1	11/09/2014	-	√	√	-	low	-	-	25cm
2	Case3-2	11/09/2014	-	√	√	-	medium	-	-	25cm
3	Case3-3	11/09/2014	-	√	√	-	high	-	-	25cm
4	Case3-4	11-12/09/2014	-	√	√	-	low	-	-	32.5cm
5	Case3-5	11-12/09/2014	-	√	√	-	medium	-	-	32.5cm
6	Case3-6	11-12/09/2014	-	√	√	-	high	-	-	32.5cm
7	Case3-7	12/09/2014	-	√	√	-	low	-	-	40 cm
8	Case3-8	12/09/2014	-	√	√	-	medium	-	-	40 cm
9	Case3-9	12/09/2014	-	√	√	-	high	-	-	40 cm
10	Case4-10	17/09/2014	-	√	√	-	low	4 lamp	-	35 cm
11	Case4-11	17/09/2014	-	√	√	-	medium	4 lamp	-	35 cm

(cont. on next page)



Table 4.1. (cont.)

#	Code	Time	NC	FC	S	TS	Flow	SS	ΔP	cavity
12	Case4-12	17/09/2014	-	√	√	-	high	4 lamp	-	35 cm
13	Case4-13	18/09/2014	-	√	√	-	low	8 lamp	-	35 cm
14	Case4-14	18/09/2014	-	√	√	-	medium	8 lamp	-	35 cm
15	Case4-15	18/09/2014	-	√	√	-	high	8 lamp	-	35 cm
16	Case4-16	23/09/2014	-	√	√	-	low	4 lamp	-	25 cm
17	Case4-17	23/09/2014	-	√	√	-	medium	4 lamp	-	25 cm
18	Case4-18	23/09/2014	-	√	√	-	high	4 lamp	-	25 cm
19	Case4-19	23/09/2014	-	√	√	-	low	8 lamp	-	25 cm
20	Case4-20	23/09/2014	-	√	√	-	medium	8 lamp	-	25 cm
21	Case4-21	23/09/2014	-	√	√	-	high	8 lamp	-	25 cm
22	Case4-22	25/09/2014	-	√	√	-	low	4 lamp	-	25 cm
23	Case4-23	25/09/2014	-	√	√	-	medium	4 lamp	-	25 cm
24	Case4-24	25/09/2014	-	√	√	-	high	4 lamp	-	25 cm
25	Case4-25	26/09/2014	-	√	√	-	low	4 lamp	-	35 cm
26	Case4-26	26/09/2014	-	√	√	-	medium	4 lamp	-	35 cm
27	Case4-27	26/09/2014	-	√	√	-	high	4 lamp	-	35 cm
28	Case1-S1	19/11/2014	-	√	√	-	low	-	small	25 cm
29	Case1-S2	19/11/2014	-	√	√	-	medium	-	small	25 cm
30	Case1-S3	19/11/2014	-	√	√	-	high	-	small	25 cm
31	Case1-S4	20/11/2014	-	√	√	-	low	4 lamp	small	25 cm
32	Case1-S5	20/11/2014	-	√	√	-	medium	4 lamp	small	25 cm
33	Case1-S6	20/11/2014	-	√	√	-	high	4 lamp	small	25 cm
34	Case1-S7	21/11/2014	-	√	√	-	low	8 lamp	small	25 cm
35	Case1-S8	21/11/2014	-	√	√	-	medium	8 lamp	small	25 cm
36	Case1-S9	21/11/2014	-	√	√	-	high	8 lamp	small	25 cm
37	Case1-B1	23-24/11/2014	-	√	√	-	low	-	big	25 cm
38	Case1-B2	23-24/11/2014	-	√	√	-	medium	-	big	25 cm
39	Case1-B3	23-24/11/2014	-	√	√	-	high	-	big	25 cm
40	Case1-B4	24/11/2014	-	√	√	-	low	4 lamp	big	25 cm
41	Case1-B5	24/11/2014	-	√	√	-	medium	4 lamp	big	25 cm
42	Case1-B6	24/11/2014	-	√	√	-	high	4 lamp	big	25 cm
43	Case1-B7	25/11/2014	-	√	√	-	low	8 lamp	big	25 cm
44	Case1-B8	25/11/2014	-	√	√	-	medium	8 lamp	big	25 cm
45	Case1-B9	25/11/2014	-	√	√	-	high	8 lamp	big	25 cm
46	Case5-46	03/12/2014	√	-	√	-	-	2 lamp	-	25 cm
47	Case5-47	03-04/12/2014	√	-	√	-	-	4 lamp	-	25 cm
48	Case5-48	10/12/2014	√	-	√	-	-	6 lamp	-	25 cm
49	Case5-49	04/12/2014	√	-	√	-	-	8 lamp	-	25 cm
50	Case5-50	11/12/2014	√	-	√	-	-	10 lamp	-	25 cm
51	Case5-51	04/12/2014	√	-	√	-	-	12 lamp	-	25 cm
52	Case2-1	09/12/2014	√	-	√	-	-	-	-	25 cm
53	Case2-2	01/12/2014	√	-	√	-	-	-	-	25 cm
54	Case2-3	09/12/2014	√	-	√	-	-	-	-	25 cm
55	Case2-4	12/12/2014	√	-	√	-	-	-	-	25 cm
56	Case2-5	15/12/2014	√	-	√	-	-	-	-	25 cm
57	Case2-6	16/12/2014	√	-	√	-	-	-	-	25 cm
58	Case2-7	17/12/2014	√	-	√	-	-	-	-	25 cm

Accordingly, the first column and the second column are the coding used in relation to numbering and experiments, respectively. Dates of experiments are shown in the third column. It is specified if the study is natural (NC) or forced convection (FC) in the fourth and fifth columns. It is specified whether the experiment is steady state (SS) or transient (TS) in the sixth and seventh columns. 3 distinct air mass flows created by the fan for the air flows through the cavity are named in the eighth column. It is given in the ninth column how many lamps from a total of 12 are used in the experiments where the solar simulator (SS) is used in order to achieve different heat flux values. In the tenth column, information is given about two different perforated sheets with various hole diameters used to create a pressure drop in the cavity. Values regarding cavity depth are given in the eleventh and the last column.

Experiments given in Table 4.1 can be grouped under 4 main titles. According to this, by considering the chronology, following operations are carried out respectively:

1. In the first part from one to nine (Case 3), by actuating the air channel without using the solar simulator, experimental studies are carried out at different air flow rates for various cavity depth values.

2. The second part includes the one with the solar simulator, which is numbered from 10 to 27 (Case 4), and experimental studies are carried out at various cavity depth values for different air flow rates depending on the lamp configurations.

3. In the experimental studies from 28 to 45 (Case 1), in order to create a pressure drop in the cavity, two distinct perforated metal sheets are used and experiments are performed with and without the solar simulator.

4. Following these three parts where the air channel is active and which are forced convection, the cavity is blocked for entry of air flow and, first of all, experiments from 46 to 58 are performed for the natural convection under the steady state condition by using solar simulator numbered from 46 to 51 (Case 5), and without solar simulator numbered from 52 to 58 (Case 2).

In each experimental study, the whole system is activated in order to equilibrate at the desired conditions and following the thermal equilibrium is reached, measurements are performed at the steady state.

#### 4.10. Calibration Process

Calibrations of each one of all PT-100 probes and thermocouples used in the experimental setup are performed in calibration laboratories of İzmir Chamber of Mechanical Engineers (KALMEM).

PT-100 and thermocouple samples placed in the calibration bath are given in Figure 4.22. These placements are made depending on the certain rules. All PT-100 probes and thermocouples to be calibrated are placed in such a way that they are at least 1 cm above the ground of the liquid bath tank and it is performed carefully that at least 1 cm is left between the cable connected with the calibrated multimeter displaying temperature values and calibrated PT-100 probes and thermocouples.



a) Calibration system



b) PT-100 and thermocouples in calibration bath

Figure 4.22. Calibration device

Calibration process consists of PT-100 and thermocouples placed in the calibration bath and required to be calibrated and a multimeter which enables reading these values (Figure 4.22). Alcohol at a temperature up to 24°C is put in the calibration bath and, then for higher set temperature values, alcohol is emptied as it is volatile and it is replaced with water. After all calibration process is completed.

Based on the results of experimental measurements, when the temperatures obtained from the experiments are taken into account, reference temperature intervals are specified and deviation of values of these specified set temperature values read on PT-100 and thermocouple with respect to reference set temperature values are

determined and calibrated (Tables 4.2 and 4.3). In Table 4.2, PT-100 reference and measurement values in 3-9 channel in the data logger and in Table 4.3, thermocouple reference and measurement values in 2-9 channel in the data logger are given. It can be seen that a higher deviation is present in PT-100 probe compared to the thermocouples. A deviation curve of  $y=1.004x-2.1431$  is seen in PT-100 probe while a deviation curve of  $y=0.9954x-0.0219$  is calculated for the selected thermocouple. It means that a reference temperature value such as 4.06 °C can be read as 4.13 °C, which is approximately the same value, with the thermocouple while a higher deviation is seen in PT-100 probe since a value of 6.18 °C is read, which is a quite different value. Figures 4.23 and 4.24 contain graphs relating to them.

Table 4.2. PT-100 reference and measurement values in 3-9 channel (in °C) in the data logger

Channel	reference	measurement
<b>3-9</b>	4.06	6.18
	7.96	10.06
	11.95	14.04
	15.97	18.04
	20.00	22.08
	24.00	26.03
	28.01	30.03
	31.92	33.92

Table 4.3. Thermocouple reference and measurement values in 2-9 channel (in °C) in the data logger

Channel	reference	measurement
<b>2-9</b>	4.06	4.13
	7.96	7.99
	11.95	12.07
	15.97	16.07
	20.00	20.00
	24.00	24.15
	28.01	28.23
	31.92	32.07

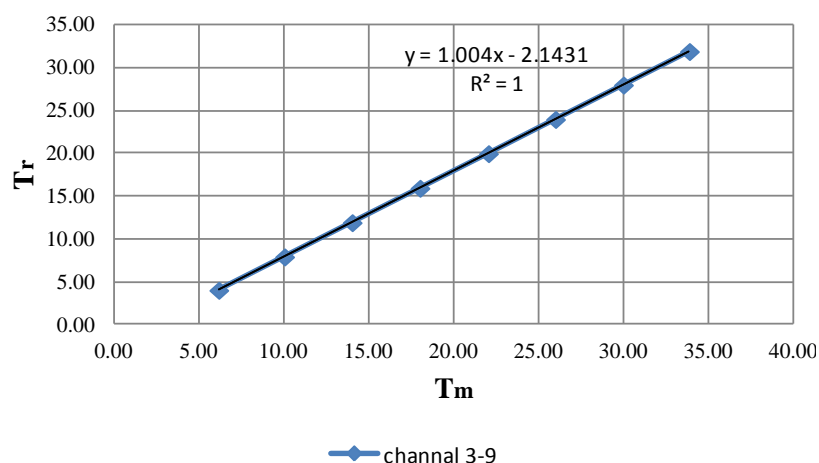


Figure 4.23. Calibration curve of temperature values in 3-9 (PT-100) channel in the data logger

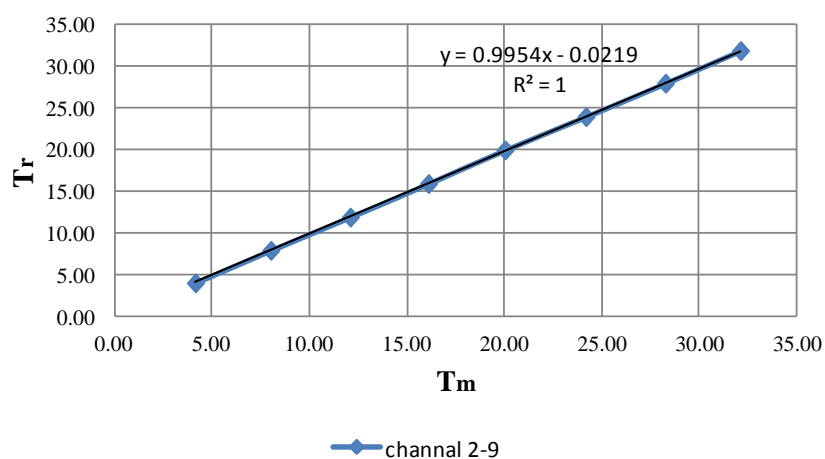


Figure 4.24. Calibration curve of temperature values in 2-9 (thermocouple) channel in the data logger

Flow rate measurements of heating-cooling bath are performed with a variable cross-section flow meter. Calibration of this measurement system is also performed classically by specifying the flow mass for a specified time period. Process performed in accordance with this is shown in Table 4.4.

Table 4.4. Calibration of the flowmeter

<i>Water temperature 19°C density 998.2 kg/m<sup>3</sup> flow meter: 350 litre/saat</i>					
<b>Measurement number:</b>	<b>time[s]</b>	<b>volume[cc]</b>	<b>liter</b>	<b>Flow rate[l/h]</b>	
<b>1</b>	42.11	4200	4.2	359.1	
<b>2</b>	42.39	4290	4.29	364.3	
<b>3</b>	42.34	4295	4.295	365.2	
<b>4</b>	46.25	4695	4.695	365.4	
<b>5</b>	43.44	4420	4.42	366.3	
<b>6</b>	36.3	3680	3.68	365.0	
<b>7</b>	36.3	3680	3.68	365.0	
<b>8</b>	32.07	3290	3.29	369.3	
<b>9</b>	31.15	3195	3.195	369.2	
<b>10</b>	38.94	3990	3,99	368.9	<b>Mass flow [kg/s]</b>
			<b>Avg.</b>	365.8	0.101

Differential pressure measurement systems are self-calibrated and, in case pressure values are same at the two openings where the pressure difference is measured and no pressure generating effect is available, measurement system is set to zero.

Air velocity measurement system for the present study performed according to the calibration certificate are calibrated. Similarly, pyranometer system is also used as calibrated. Firstly, the position of the pyranometer is determined. For that, two different measurements have been conducted in the points set forth in the Figure 4.25 over the glass surface by changing the distance between the outer glass surface and two glass surfaces to the solar simulator. The results have been set forth in the Table 4.5.

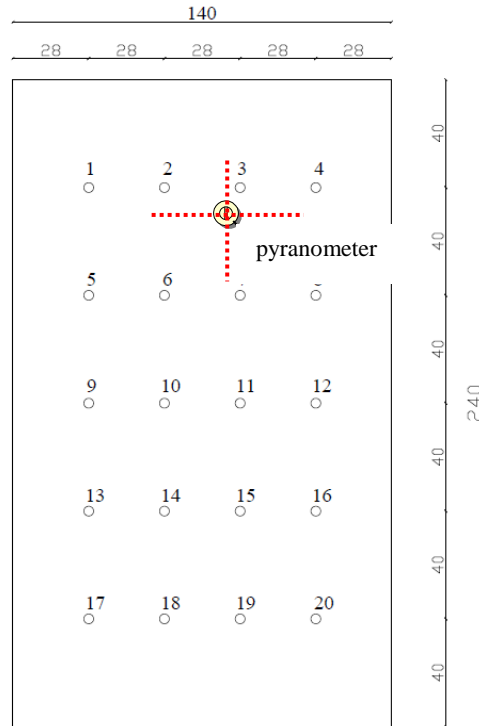


Figure 4.25. Radiation measuring points on the outer glass surface

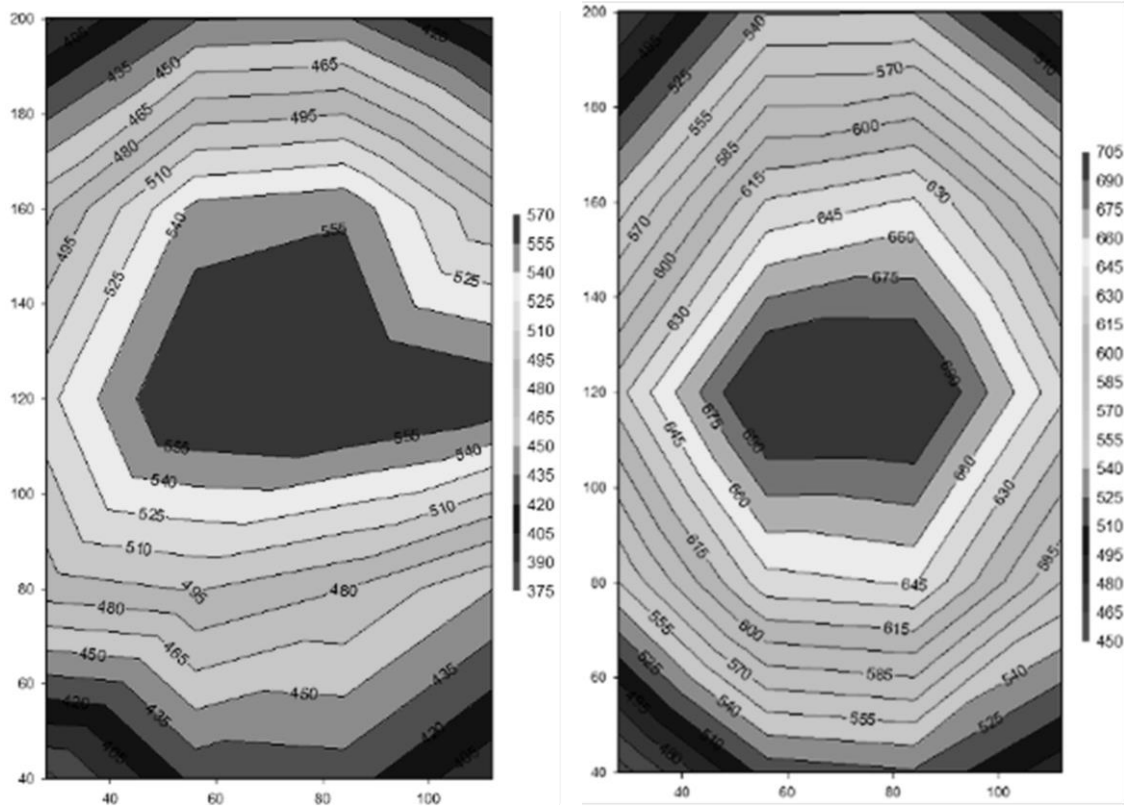
The distance between the outer glass and inner glass that is mobile in the first measurement is minimum 15 cm. In the second measurement, outer glass has been approached more to the solar simulator and the distance between the two glasses increased to 40 cm (Table 4.5). For the measurement end of the pyranometer during the measuring is in the front by 13 cm, the measurements get ahead by 13 cm from the specified distance. The change of heat flow over the glass surface has been specified by measuring from two different distances and the position over the outer glass surface of the pyranometer by calculating the average heat flux for both situations (Figure 4.25).

Table 4.5. Measurement results of heat flux

Measurement points	Measurement 1	Measurement 2
1	387.4	464.8
2	433.6	538.6
3	437.1	539.1
4	393.9	474.3
5	475.8	546.7
6	544.2	631.6
7	551.7	647.2
8	495.9	577.8
9	520.1	624.6
10	577.2	717.0
11	581.1	716.5
12	567.9	633.6
13	487.9	554.7
14	496.3	639.6
15	480.7	646.7
16	450.3	569.8
17	370.8	442.2
18	423.6	515.5
19	426.6	523.1
20	392.9	484.9

When we consider the outer glass surface for the first measurement, the average radiation value coming to pyranometer is  $474.8 \text{ W/m}^2$ . The standard deviation value is  $66.8 \text{ W/m}^2$ . While average radiation value that comes to pyranometer for the second measurement is  $574.5 \text{ W/m}^2$ , the standard deviation value is found  $80.1 \text{ W/m}^2$ . Even though standard deviations and average heat flux values over the glass surface are different for two measurements, it has been found that pyranometer should be located under the 55 cm of the upper glass surface and right at the middle axis (Figure 4.25). This point reflects the average heat flux values for the both measurement. The heat flux distribution curves on the surface of the both measurement have been shown in Figure 4.26.





a) First measurement

b) Second measurement

Figure 4.26. Heat flux distribution curves for the first and second measurement

The measurements have been carried out with pyranometer in all experiments that solar simulator has been used except for this preliminary study. It is required to calibrate the values read since measurement point of pyranometer is in front of the glass surface. For that purpose, an experiment has been carried out for the two different cavity gap composed of 25cm and 35cm each and measurement has been conducted for the two different lamp configurations used in the experiments. According to that, first experiment has been shown in the Figure 4.27 for the 25cm cavity. According to the time, stable heat flux is for the operation of the 4 lamps after approximately 2000 seconds and after approximately 6500 seconds, 8 lamps have been operated. Similar measurement has been shown for the 35cm in the Figure 4.28. The reason why these values are relatively high is for pyranometer is closer to the solar simulator.

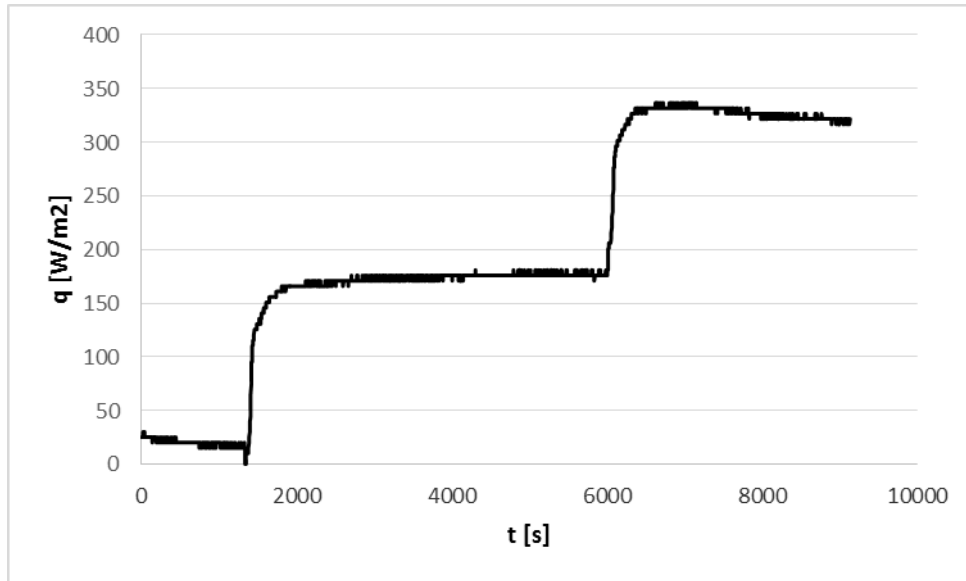


Figure 4.27. Heat flux for 25 cm cavity

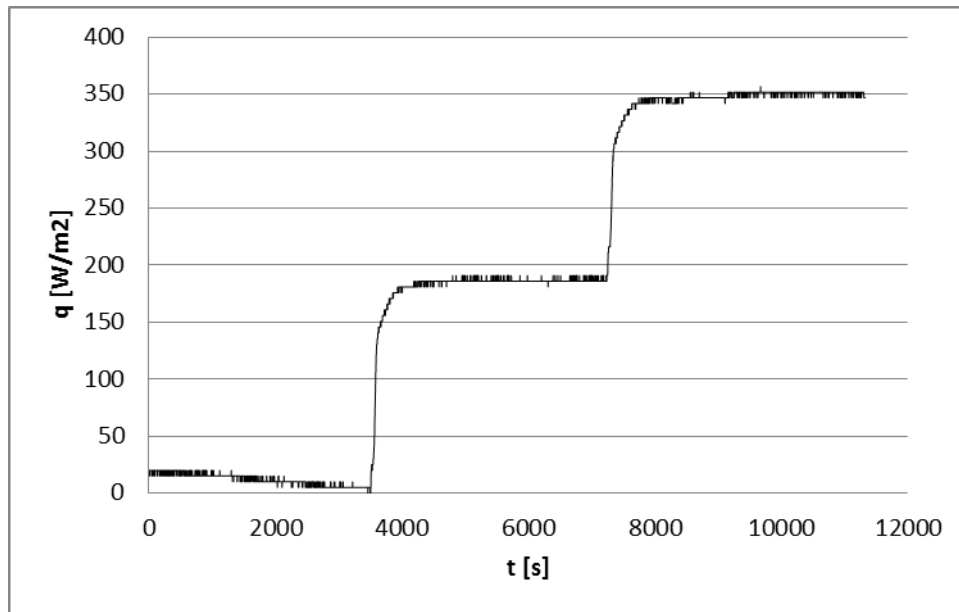


Figure 4. 28. Heat flux for 35 cm cavity

The average values obtained according to the results of the Figure 4.27 and 28 have been compared with the values measured in the other experiments. According to that, the calibration of the measurement carried out in the experiments has been realized (Table 4.6).

Table 4.6. Calibration due to the position of the pyranometer

	4 lamp		8 lamp	
Cavity depth	25 cm	35 cm	25 cm	35 cm
Real condition	175.0	186.5	322.7	350.7
Experiment	184.8	200.9	337.7	365.6

#### 4.11. Uncertainty Analysis

The experimental uncertainty calculations have been carried out in the scope of the method followed by the Holman (2011) and Tokuç et al (2015). According to that, the uncertainty of each device measured according to that will affect the total uncertainty of the value ( $R$ ) obtained with the use of these devices. If  $R$  value is expressed depending on the independent variables of  $x_1, x_2, x_3 \dots x_n$  given in Equation 4.1:

$$R=R(x_1, x_2, x_3 \dots x_n) \quad (4.1)$$

If we define the  $\omega_R$  as the uncertainty of the value calculated, we obtained Equation 4.2 formulas in consideration of the uncertainty of the all independent variables.

$$\omega_R = \left[ \left( \frac{\partial R}{\partial x_1} \omega_1 \right)^2 + \left( \frac{\partial R}{\partial x_2} \omega_2 \right)^2 + \dots + \left( \frac{\partial R}{\partial x_n} \omega_n \right)^2 \right]^{1/2} \quad (4.2)$$

The uncertainty analysis of the amount of the energy transferred to or taken from the system from the double skin facade for the experimental works in the steady-state condition and the amount of the energy transferred to or taken from the inner environment through water used in the heating and cooling bath have been conducted. According to that, the amount of energy transferred to or taken to the system by the air or water has been defined in Equation 4.3:

$$\dot{Q} = \dot{m} c_p \Delta T \quad (4.3)$$

The uncertainty in relation to the Equation 4.3 has been due to the thermophysical properties of the air and water ( $\rho$  and  $c_p$ ), velocity of the air ( $V_a$ ), cross

section that the air passes ( $A_c$ ), volumetric flow rate of the water ( $\dot{V}_w$ ) and the difference of in and out of the fluids ( $\Delta T_w$ ). According to that, parameters that affect the heat transfer have been defined separately for air and water in the Equations 4.4 and 4.5:

$$\dot{Q}_a = f(\rho_a, c_{pa}, V_a, A_c, \Delta T_a) \quad (4.4)$$

$$\dot{Q}_w = f(\rho_w, c_{pw}, \dot{V}_w, \Delta T_w) \quad (4.5)$$

The uncertainty value of each independent property has been given in the Table 4.7. According to that the uncertainty of the energy transfer rate values to be calculated depending on the parameters defined in the Equations 4.4 and 4.5 for air and water has been specified with the solution of the partial differential equation in the Equation 4.2. According to that total uncertainty in the energy transfer velocity of the air and water has been calculated in consideration of the values in the Table 4.7 as 5.4 % and 2.5 % respectively. Furthermore, the uncertainty in relation to the differential pressure meter has been defined as  $\pm\%1.5+1\text{Pa}$ . The uncertainty of the pyranometer has been given as  $7.00\mu\text{V}/\text{Wm}^{-2}$ .

Table 4.7. The uncertainty value of each independent property used in the experimental studies (Holman, 2011)

Variables	Value	Uncertainty	Comment
Air density, $\rho_a$	1.184kg/m <sup>3</sup> @25°C	$\pm\%0.02$	uncertainties in the thermophysical properties of the selected heat transfer fluid
Specific heat of air, $c_{pa}$	1007J/kg K @25°C	$\pm\%0.3$	
Air velocity, $V_a$	0.1-10 m/s	$\pm\%5$	uncertainty from the volumetric flow measurements
Sectional area which the air passes, $A_c$	0.37-0.66m <sup>2</sup>	$\pm\%2$	uncertainty from the measurement of sectional area which the air passes
Air temperature difference, $\Delta T_a$	0-100°C	$\pm 0.034^\circ\text{C}$	uncertainty from the measurements with thermocouples
Water density, $\rho_w$	997 kg/m <sup>3</sup> @25°C	$\pm\%0.02$	uncertainties in the thermophysical properties of the selected heat transfer fluid
Specific heat of water, $c_{pw}$	4180 J/kg K @25°C	$\pm\%0.3$	

(cont.on next page)

Table 4.7. (cont.)

Variables	Value	Uncertainty	Comment
volumetric flow rate of water, $\dot{V}_w$	10-1000 l/h	$\pm\%2.5$	uncertainty from the volumetric flow measurements
Water temperature difference, $\Delta T_w$	0-100°C	$\pm 0.018^\circ\text{C}$	uncertainty from the measurements with Pt-100 probes

In calculation of the uncertainty values for the thermocouples and Pt-100 probes in Table 4.7, the total uncertainty has been evaluated together with the uncertainty of the devices used in consideration of the calibration proceeding. According to that, the uncertainty values for Pt-100 probes can be calculated by using Equation 4.6.

$$\sqrt{\left(\frac{refPt100}{2}\right)^2 + \left(\frac{T_{cc}/2}{\sqrt{3}}\right)^2 + \left(\frac{refmm}{2}\right)^2 + St^2 + B_{sta}^2} = \pm 0.018^\circ\text{C} \quad (4.6)$$

The maximum resolution for *refPt100* value for Pt-100 probe used as a reference in the calibration in Equation has been taken as  $0.02^\circ\text{C}$  ( $0.01^\circ\text{C}$  for  $0^\circ\text{C}$  and  $0.02^\circ\text{C}$  for  $100^\circ\text{C}$ ). Test device, the resolution of Hioki LR 8401-20,  $T_{cc}$  is maximum  $0.01^\circ\text{C}$  for Pt-100 probes (this value is  $0.1^\circ\text{C}$  for thermocouples). The resolution value of the reference multimeter used in the calibration, *refmm*, is  $0.0024^\circ\text{C}$ . Standard deviation, *St*, is maximum  $0.01^\circ\text{C}$  and bath stability,  $B_{sta}$  is taken as  $0.01^\circ\text{C}$ . According to Equation 4.6, uncertainty value for thermocouples has been also calculated as  $\pm 0.034^\circ\text{C}$ .

## CHAPTER 5

### EXPERIMENTAL AND NUMERICAL ANALYSIS

In this thesis five main case studies were constituted based on different parameters which play a decisive role on the energy performance of DSF systems. These parameters were summarized in Table 5.1.

Table 5.1. General parameters used in the case studies

#	NC	FC	Flow			Solar Simulator							$\Delta P$		Cavity width			
			low	medium	high	-	2	4	6	8	10	12	3mm	5mm	25	32.5	35	40
Case 1	-	√	√	√	√	√	-	√	-	√	-	-	√	√	√	-	-	-
Case 2	√	-	-	-	-	-	-	-	-	-	-	-	-	-	√	-	-	-
Case 3	-	√	√	√	√	-	-	-	-	-	-	-	-	-	√	√	-	√
Case 4	-	√	√	√	√	-	-	√	-	√	-	-	-	-	√	-	√	-
Case 5	√	-	-	-	-	-	√	√	√	√	√	√	-	-	√	-	-	-

#### 5.1. Case 1: Experimental investigation of the pressure loss through the DSF by using perforated plates

The aim of this study is to analyze the effect of perforated elements on pressure drop in a double skin facade cavity. This cavity separates the exterior and interior space as thermally controllable. The temperatures of the surfaces facing cavity and exterior and interior spaces have been determined experimentally. The behavior of the double skin facade system with perforated elements is examined under different airflow conditions. Two distinct perforated plates having different circular hole dimensions are positioned in the double skin facade cavity in order to create a pressure drop in the cavity. The effect of these elements on pressure drop and air flow were experimentally analyzed. Moreover, temperature changes in the cavity for different working conditions were examined according to the experimental results from the measurements. The results show the surface and air temperature distributions in the cavity and pressure drops under three different air flow rates and two different perforated plates. The dependence of the dimensionless pressure drop coefficient,  $Eu$ , versus Reynolds number

is investigated experimentally for different geometric characteristic of the perforated plates.

### **5.1.1. Experimental setup**

General view of the experimental setup in the laboratory can be seen in Figures 4.1. and 4.2 in Chapter 4. Moreover, general plan of experimental setup can be also seen in Figure 4.3. All information related to technical information related to experimental set up is described in Chapter 4.

### **5.1.2. Perforated plates**

Two different kind of perforated plates shown in Figure 5.1 are placed individually in the cavity. Plates' thickness is 2mm each, holes are arranged staggered form through the perforated plates, and diameter of them are 5mm and 3mm called big and small holes in Figure 5.2, respectively. The plates configuration is also characterized by different pitches between hole centers and the dimensions are given in mm in Figure 5.2. The other characteristic dimensions are also given in Table 5.2.



Figure 5.1. Two different perforated plates.

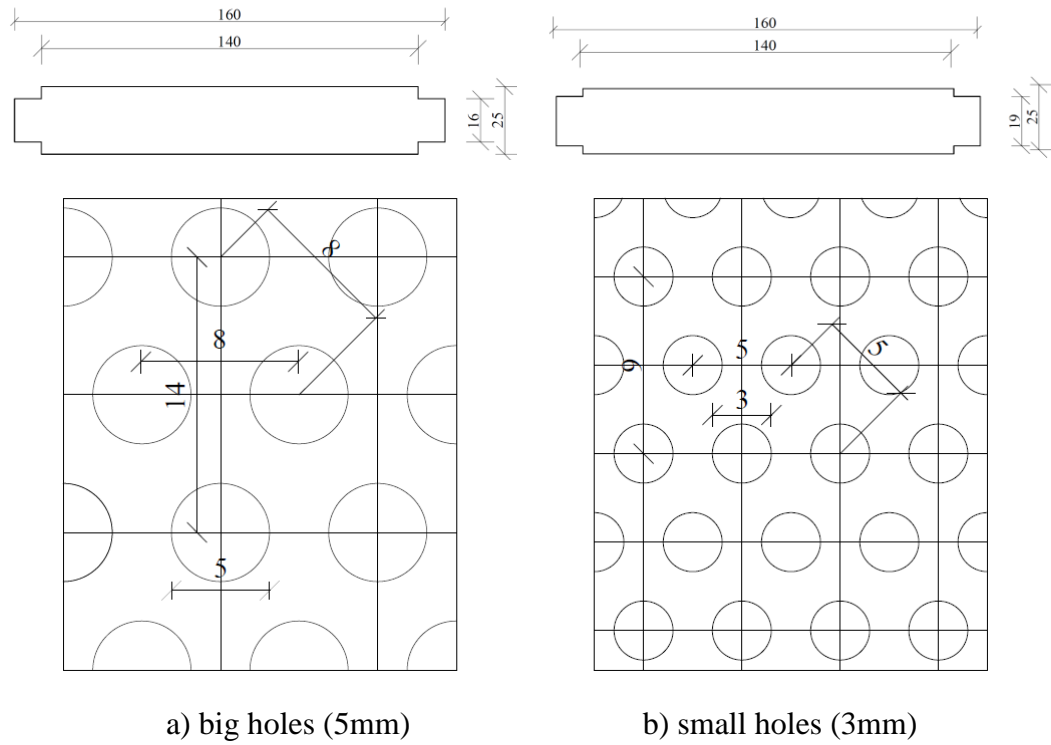


Figure 5.2. Plans and dimensions of perforated plates (in mm)

Table 5.2. Characteristics of the perforated plates

Geometric definition	Perforated plates	Perforated plates
	with big holes	with small holes
hole diameter	5 mm	3 mm
maximum distance between two adjacent holes	14 mm	9 mm
minimum distance between two adjacent holes	8 mm	5 mm
thickness of plate/hole diameter	0.40	0.67
number of holes	5140	16235
area of total holes	1008.98 cm <sup>2</sup>	1146.19 cm <sup>2</sup>
area of plate	3820 cm <sup>2</sup>	3880 cm <sup>2</sup>
porosity	0.264	0.295
plate net area/area of total holes	2.79	2.38
equivalent porosity ratio	0.51	0.54



### 5.1.3. Experimental results and discussions

Perforated plates shown in Figure 5.3 were placed in the cavity of the DSF in the experimental setup. In here, dimensions of circular holes on the plate, 5mm were greater than the other plate used and as shown by the experimental results (Figures 5.4, 5.5), pressure drop generated by it was lower. After finishing nine experimental studies with big hole plate, small hole (3mm) plate was used another nine experiments under steady state conditions. General view of the perforated plates and their dimensions were seen in Figures 5.1 and 5.2. Detailed geometric configurations of the plates were also given in Table 5.2.

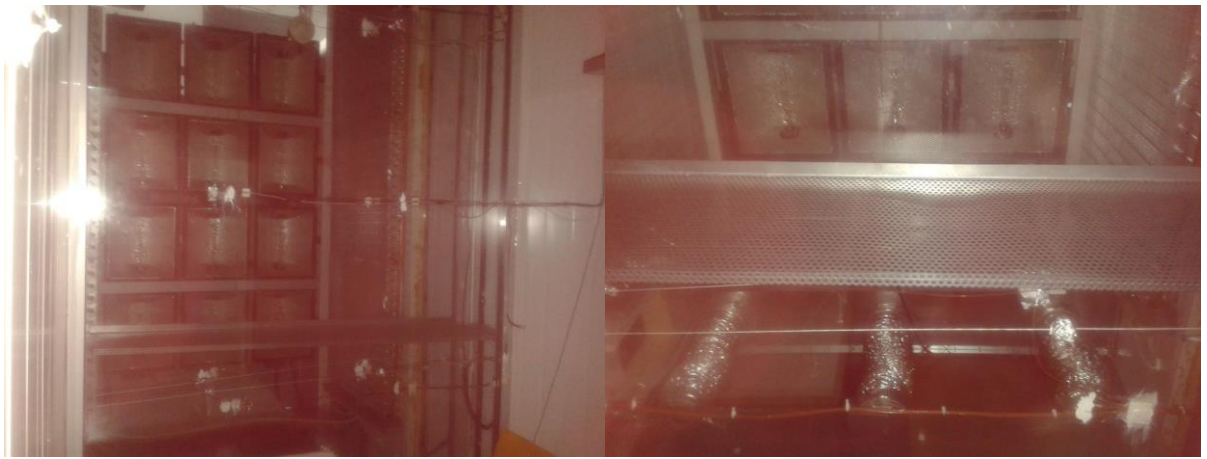


Figure 5.3. Layout of perforated plates in the cavity of DSF

Totally 18 experimental measurements were conducted by using two different size perforated plates in this study. The experimental setup was run for each test and steady-state conditions were waited before measurements were taken. Temperature values at each point in the experimental setup mentioned in Figures 4.18 and 4.19 were recorded at 2 seconds intervals. All system was thermal equilibrium in the beginning, and after that different temperatures were created inside of the indoor and outdoor environments by using a constant temperature water bath and a refrigeration-based cooling system, respectively, as shown in Figures 4.1 and 4.3. Solar simulator system was also run in the some of the experiments. These different temperatures for two environments become stable after a while. The temperature values which were in the indoor environment reflected the average value of 3 thermocouples (AI1-3 in Figure

4.19). Thermocouples AO1 and 2 (Figure 4.19) gave the average temperature values of the exterior environment.

The average temperature distribution on the two different height (mentioned b, bottom and t, top) section of the cavity after steady state condition were given in Figures 5.4 and 5.5 for the six experiments on the big (mentioned B1, 4 and 7 in Figure 5.4) and small (mentioned S3, 6 and 9 in Figure 5.5) hole perforated plates individually. Average temperature values of the cavity air at two levels for each measurement were given in the middle and the temperatures on the two sides referred to the average surface temperatures. All measurements were obtained by using two thermocouples at different depth at the same level. Heat transfer occurred due to these temperature differences from two surfaces to the air because of heated surfaces by solar radiation at the experiments numbered B4, 7 and S6, 9. High solar radiation created bigger temperature changes relatively at the B7 and S9. On the other hand, heat transferred from relatively hot air (cavity air inlet temperature is a small quantity bigger than the outside temperature:  $24.98^{\circ}\text{C} > 24.32^{\circ}\text{C}$  for B1;  $27.31^{\circ}\text{C} > 26.69^{\circ}\text{C}$  for S3 given in Table 5.3) to the surfaces at no solar radiation situations at the experiments B1 and S3.

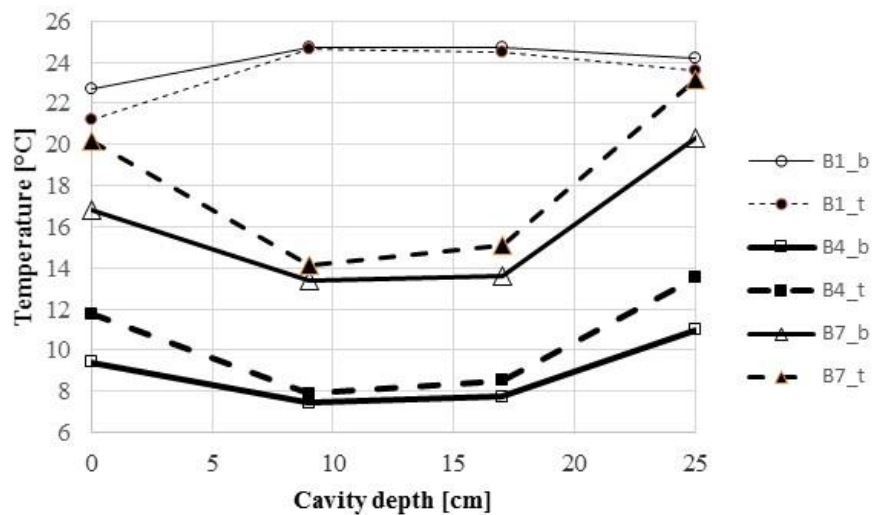


Figure 5.4. Temperature distributions in the cavity at the bottom (b) and top (t) levels for three experiments (1, 4 and 7) on big (B) hole perforated plate.

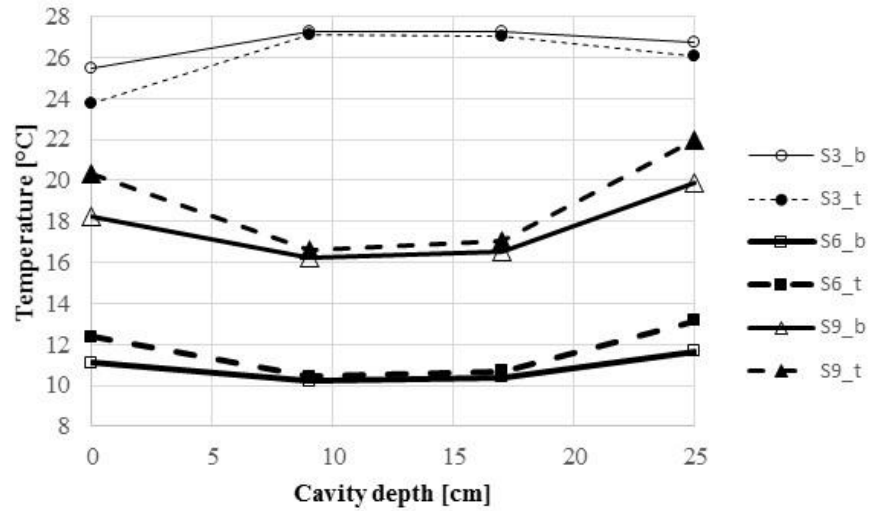


Figure 5.5. Temperature distributions in the cavity at the bottom (b) and top (t) levels for three experiments (3, 6 and 9) on big (S) hole perforated plate.

All the temperature measurements with the heat radiation values at the steady state condition were given in Table 5.3. Air flow rate at three different levels mentioned low, medium and high; and the relative size of perforated plate's hole could be seen in the first two columns of the table. Third column was about the number of experiment. Solar radiation values at fourth column were created by solar simulator (numbered VI in Figures 4.1 and 4.3) and measured by the pyranometer shown in Figure 4.14 separately. The other columns were about the average temperature values measured by thermocouples and probes mentioned in Figure 4.19.

Table 5.3. Experimental results

#			[W/m <sup>2</sup> ]	In [°C]	Out [°C]	PFOG [°C]			SFIG [°C]			Cav. [°C]	Cavity (CA) [°C]			
			Rad.	avg (AI1-3)	avg (AO1-2)	avg (1-2)	avg (3-4)	avg (5-6)	avg (1-2)	avg (3-4)	avg (5-6)	Inlet	avg (1-3)	avg (2-4)	avg (5-7)	avg (6-8)
Low flow	Big hole (5mm)	B1	0	12.86	24.32	22.71	21.43	21.23	24.22	23.65	23.58	24.98	24.75	24.74	24.61	24.50
		B4	195.55	11.32	14.24	9.41	11.80	11.79	10.98	13.13	13.53	7.31	7.45	7.75	7.91	8.53
		B7	322.29	18.92	23.08	16.85	20.65	20.20	20.34	23.12	23.13	12.39	13.41	13.65	14.10	15.07
	Small hole (3mm)	S1	0	13.39	24.55	23.03	21.85	21.43	24.53	24.01	23.84	25.22	25.07	25.07	24.91	24.82
		S4	200.71	12.40	15.87	10.77	12.95	13.20	12.27	14.08	14.81	8.90	9.01	9.30	9.46	9.98
		S7	328.17	19.52	24.46	18.01	21.56	21.64	21.58	24.00	24.44	13.43	14.51	15.07	15.28	16.13
Medium flow	Big hole (5mm)	B2	0	12.90	25.21	23.80	22.48	22.24	25.19	24.60	24.48	25.88	25.77	25.75	25.61	25.25
		B5	191.10	10.93	12.66	9.30	11.13	11.03	10.13	11.77	12.25	8.03	7.94	8.16	8.26	8.68
		B8	328.77	18.94	21.49	17.03	20.07	19.52	19.29	21.74	21.99	13.96	14.52	14.69	15.03	15.77
	Small hole (3mm)	S2	0	13.56	25.62	24.28	23.08	22.58	25.60	25.09	24.90	26.30	26.15	26.14	26.03	25.93
		S5	195.60	11.97	14.63	11.03	12.67	12.75	11.91	13.27	13.95	9.90	9.82	10.03	10.12	10.49
		S8	330.25	19.48	23.02	18.18	20.91	20.75	20.50	22.46	23.09	15.25	15.82	16.22	16.31	16.97
High flow	Big hole (5mm)	B3	0	13.20	26.22	24.91	23.65	23.35	26.22	25.68	25.56	26.84	26.74	26.72	26.61	26.50
		B6	198.28	10.42	10.30	8.83	10.36	10.19	9.27	10.38	10.93	7.79	7.68	7.86	7.93	8.24
		B9	337.80	19.15	19.33	17.19	19.78	19.20	18.86	20.78	21.14	14.64	15.10	15.23	15.48	16.08
	Small hole (3mm)	S3	0	14.11	26.69	25.44	24.29	23.79	26.77	26.30	26.10	27.31	27.24	27.23	27.10	27.03
		S6	197.84	11.39	12.77	11.11	12.40	12.36	11.65	12.47	13.15	10.32	10.21	10.38	10.43	10.69
		S9	326.45	19.17	20.44	18.25	20.57	20.32	19.85	21.33	22.00	15.80	16.20	16.51	16.57	17.09

For the small hole perforated plate, time dependent behavior of pressure drops obtained with respect to different flow rates applied in the experimental studies numbered S1 to S3 were shown in Figure 5.6 for the case following the experiment come at steady state. System firstly reached the steady-state condition thermally after 8000 s for the first experiment called S1. The empty areas shown in Figures 5.6 and 5.7 were about unsteady condition between recorded measurement data.

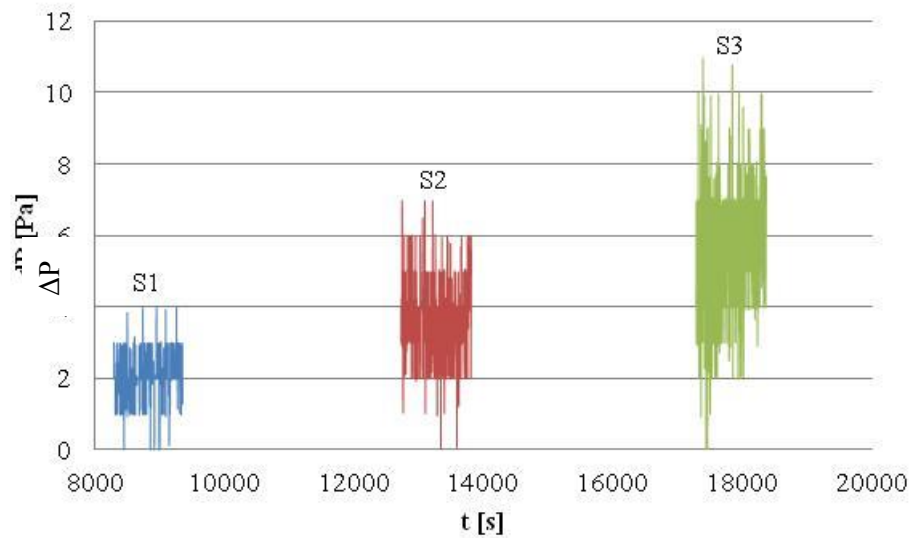


Figure 5.6. Pressure drop on small hole perforated plate for three distinct flow rates for the experiments numbered S1, S2 and S3.

Pressure drop in large hole perforated plate was given Figure 5.7. Pressure drop with respect to Figure 5.6 somewhat decreased in Figure 5.7 due to large holes. Mean values showed this decrease more clearly. Pressure drop also increased instinctively by an increase in the flow rate values for each cases that can be seen in Figures 5.6 and 5.7.

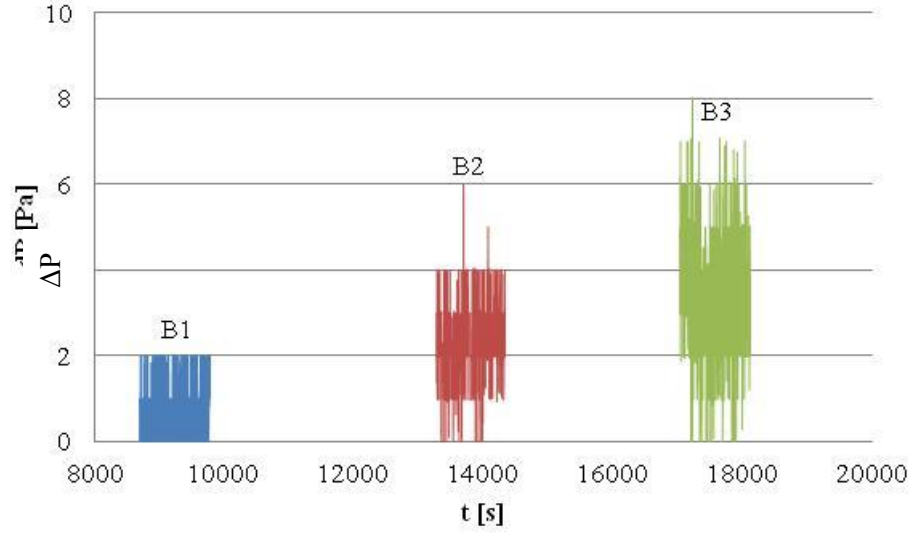


Figure 5.7. Pressure drop on big hole perforated plate for three distinct flow rates for the experiments numbered B1, B2 and B3.

Experimental results, variation of pressure drop induced by using distinct perforated plates with the mass flow rate were given in Table 5.4. In here, mass flow rate was calculated by averaging steady-state pressure drop values measured and recorded in circular duct for each case and then using mean value of velocity obtained from Bernoulli equation. Density of air was used separately for the value corresponding to the relevant temperature. Duct system and the pressure drop measurement used for the calculation of the mass flow rate in the duct were shown in Figure 4.9 and Figure 4.11b, respectively. Calculated mass flow rate values with average velocity induced by measured pressure drop values were given in the columns together at the duct section. Cavity's columns were about the calculations of the cavity air in DSF. Average velocity values at the cavity were determined using mass flow rates in the duct and obtained lower values because of increasing cross section area of the cavity. Reynolds numbers,  $Re$ , were calculated by using these velocity values with hydraulic diameter and kinematic viscosity of air:

$$Re = \frac{VD_h}{\nu} \quad (5.1)$$

where  $V$ ,  $D_h$  and  $\nu$  were defined as velocity, hydraulic diameter and kinematic viscosity of air. Euler numbers,  $Eu$ , dimensionless pressure drop coefficients, were used in the definition of the flow in the perforated plate applications and defined as;

$$Eu = \frac{\Delta P}{\frac{1}{2}\rho V^2} \quad (5.2)$$

where  $\Delta P$  was defined as pressure drop between downstream and upstream. In here,  $\Delta P$  was measured by the differential pressure measurement system shown in Figure 4.11b. So,  $Eu$  numbers were calculated using measured pressure drop ( $\Delta P$ ) and average velocity ( $V$ ) values with air density ( $\rho$ ) in Equation 5.2.

Table 5.4. Air flow measurements in the duct and the variation of pressure drop induced by using distinct perforated plates in the cavity

#			Duct			Cavity			
			$\Delta P$ [Pa]	$V$ [m/s]	$\dot{m}$ [kg/s]	$V$ [m/s]	$Re$ [-]	$\Delta P$ [Pa]	$Eu$ [-]
Low flow	Big hole (5mm)	B1	8.590	3.81	0.352	0.78	20510	0.784	2.188
		B4	7.382	3.43	0.336	0.70	20529	0.831	2.705
		B7	6.879	3.35	0.322	0.68	19388	0.122	0.425
	Small hole (3mm)	S1	10.371	4.19	0.386	0.84	22509	2.061	4.932
		S4	9.414	3.88	0.378	0.78	23008	2.219	5.855
		S7	6.877	3.35	0.321	0.67	19280	1.488	5.362
Medium flow	Big hole (5mm)	B2	22.098	6.12	0.563	1.25	32747	2.251	2.448
		B5	20.239	5.68	0.556	1.16	33884	1.880	2.229
		B8	21.156	5.88	0.562	1.20	33679	1.584	1.802
	Small hole (3mm)	S2	24.364	6.43	0.591	1.29	34390	3.705	3.766
		S5	21.755	5.91	0.574	1.19	34830	3.778	4.309
		S8	21.232	5.90	0.562	1.18	33611	3.215	3.754

Table 5.4. (cont.)

#			Duct			Cavity			
			$\Delta P$ [Pa]	$V$ [m/s]	$\dot{m}$ [kg/s]	$V$ [m/s]	$Re$ [-]	$\Delta P$ [Pa]	$Eu$ [-]
High flow	Big hole (5mm)	B3	37.756	8.01	0.735	1.63	42653	3.415	2.172
		B6	37.656	7.75	0.758	1.58	46222	3.465	2.213
		B9	37.965	7.88	0.753	1.61	41778	3.415	2.159
	Small hole (3mm)	S3	39.392	8.19	0.750	1.65	43541	5.599	3.522
		S6	37.802	7.79	0.756	1.57	45850	6.301	4.136
		S9	35.659	7.65	0.728	1.53	43461	5.129	3.564

Graphical representation for the values given in Table 5.4 was cited in Figure 5.8. Pressure drops induced by using distinct perforated plates versus different mass flow rates could be seen for the experimental results mentioned different markers in the Figure 5.8. Pressure drop generated by small hole plate was significantly higher than the big one and it could be clearly seen that the difference become to be bigger with the increase in mass flow rate. The pressure drop values depended to a power function of the mass flow rate values. The lines were drawn using average (mentioned A in Figure 5.8) values and defined as;

$$\Delta P_S = 0.694e^{2.831\dot{m}} \quad (5.3)$$

$$\Delta P_B = 0.144e^{4.353\dot{m}} \quad (5.4)$$

where the equations numbered 5.3 and 5.4 were derived for the small (S) and big (B) hole perforated plates, respectively.  $R^2$  values were calculated as 0.9998 and 0.9797, respectively.



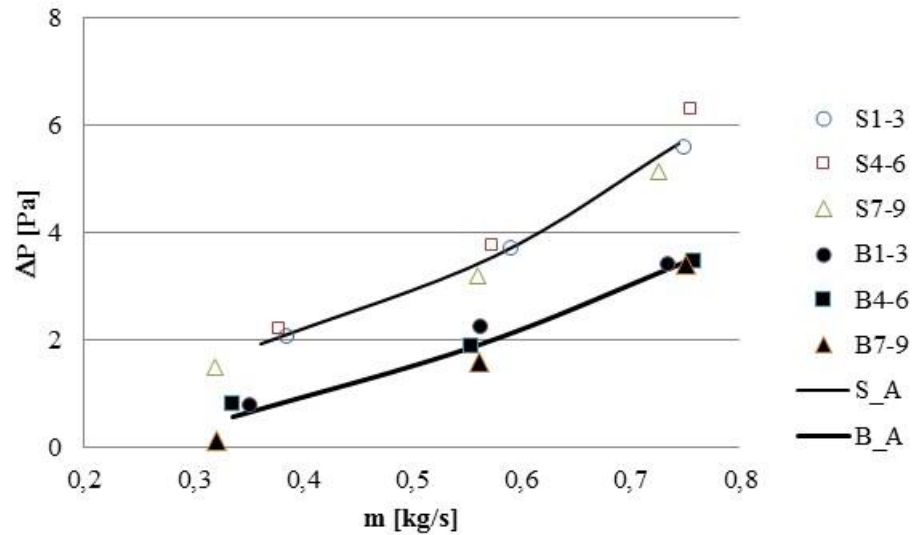


Figure 5.8. Variation of pressure drop induced by using distinct perforated plates and flow rate

The changes of  $Eu$  as a function of  $Re$  given in Table 5.4 was given in Figure 5.9 for two perforated plates. Pressure drop dimensionless coefficient,  $Eu$ , was stabilized after first three experiments for each hole case. Average  $Eu$  numbers were calculated considered this second part of the straight lines on the Figure 5.9. This values were given in Table 5.5 with the other values in the literature (Weber et al. 2000).

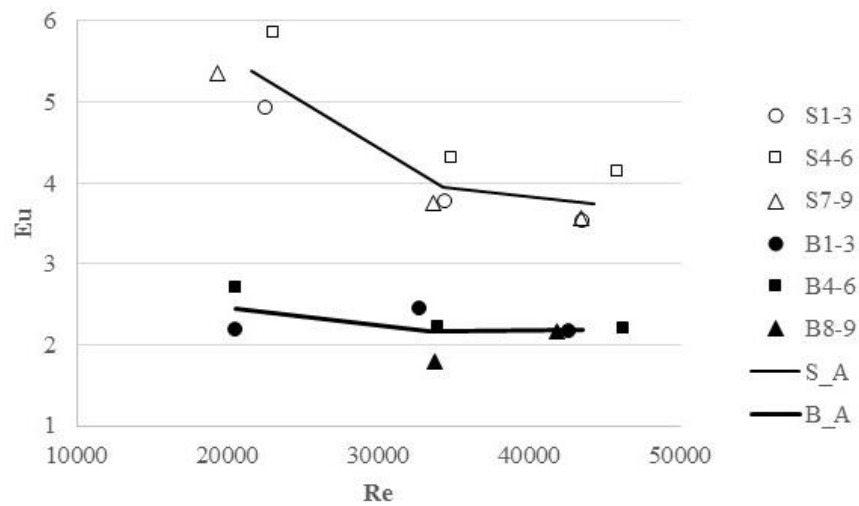


Figure 5.9. Dimensionless pressure loss coefficients versus Reynolds numbers.

In this study, the dimensionless parameters found that thickness of the plate divided by hole diameter were measured as 0.40 and 0.67, respectively. But, equivalent

porosity ratios were calculated as 0.51 and 0.54 close each other. These values were very effective of the dimensionless pressure loss coefficient,  $Eu$  numbers of the big and small hole perforated plates were calculated as 2.2 and 3.8, respectively. These values could be acceptable considering Weber et al. (2000)'s study.

Table 5.5. Effect of the hole geometric parameters upon the dimensionless pressure loss coefficient,  $Eu$  (Malavasi et al, 2012).

	thickness of the plate/hole diameter [-]	number of holes [number]	equivalent porosity ratio [-]	$Eu$ [-]
Current study	0.40	5140	0.51	2.2
Current study	0.67	16235	0.54	3.8
Weber et al. (2000)	0.48	3052	0.48	21.0
		7103		18.8
Weber et al. (2000)	0.32	1948	0.57	10.8
		4534		9.9
Weber et al. (2000)	0.32	3048	0.71	2.4
		7093		3.2

Two distinct perforated plates were installed inside the DSF's cavity for investigating of the pressure drop effect experimentally under different working conditions. Different kind of solar shading devices, plants and the perforated elements installed in the corridor type DSF were the different type of pressure loss elements in the cavity. Here, that pressure loss effect was created by using two different perforated elements and findings and major conclusions can be described as:

- Pressure drops created by perforated plates and temperature distributions created by water and refrigeration based systems with a solar simulator in the cavity of DSF were examined based on experimental measurements. All experimental results with the surface and air temperature distributions in the cavity and pressure drops under three different air flow rates and two distinct perforated plates having different geometric configurations were fully described in the study.
- There is no significant relation between the solar radiation effect along the dimensionless pressure drop coefficient. Solar radiation affected the surface temperature values of the cavity.

- Two correlations included the pressure drop and the mass flow rate values were constructed to evaluate the pressure loss in the DSF's cavity under mentioned working conditions of the study.
- Big diameter perforated plate created lower pressure drop relatively comparing with the small one.
- The dimensionless pressure drop coefficient,  $Eu$ , versus Reynolds number were determined experimentally for different geometric characteristic of the perforated plates.  $Eu$  numbers is insensitivity of the  $Re$  numbers after 30000 approximately as mentioned.
- Results from the 18 experimental studies under steady-state conditions were collected to create an extended data set for the validation of numerical studies. A porous media approximation can be useful to predict the air flow characteristics in the cavity for future studies.

## **5.2. Case 2: Experimental and numerical investigation of natural convection in a double skin facade by using CFD tool**

In this study, airflow and heat transfer in a rectangular cavity that simulates a double skin facade and includes natural convection were examined numerically and experimentally. A full-scale experimental setup was built, and the aspect ratio of the cavity was 8.64. The numerical model was validated based on existing experimental studies in the literature, and the results were examined in relation to the flow and heat transfer in the cavity. a correlation based on both Rayleigh and Nusselt numbers was determined for an airtight double skin facade

### **5.2.1. Experimental setup**

A general view of the experimental setup part used in this case study is shown in Figure 5.10. The experimental study included flow and heat transfer analysis for the buffer zone condition of the double skin facade (B) between the indoor (A) and outdoor (C) environmental conditions.

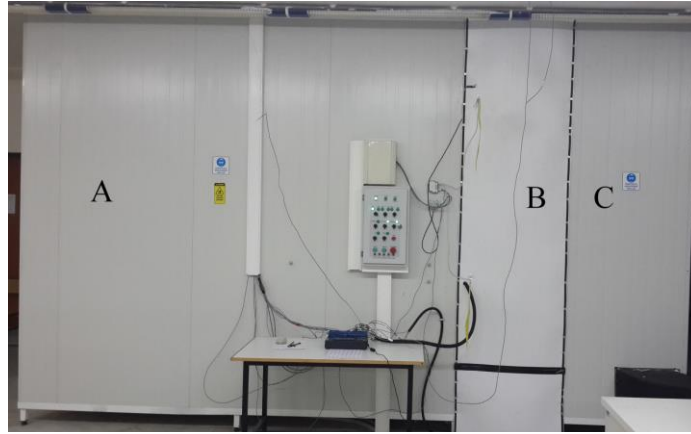


Figure 5.10. General view of the experimental setup

The Experimental Setup shown as A in Figures 5.10 and 5.11, which is 1.5 m in width, 3 m in length and 3 m in height, was manufactured using 10-cm-thick polyurethane thermal insulation panels.

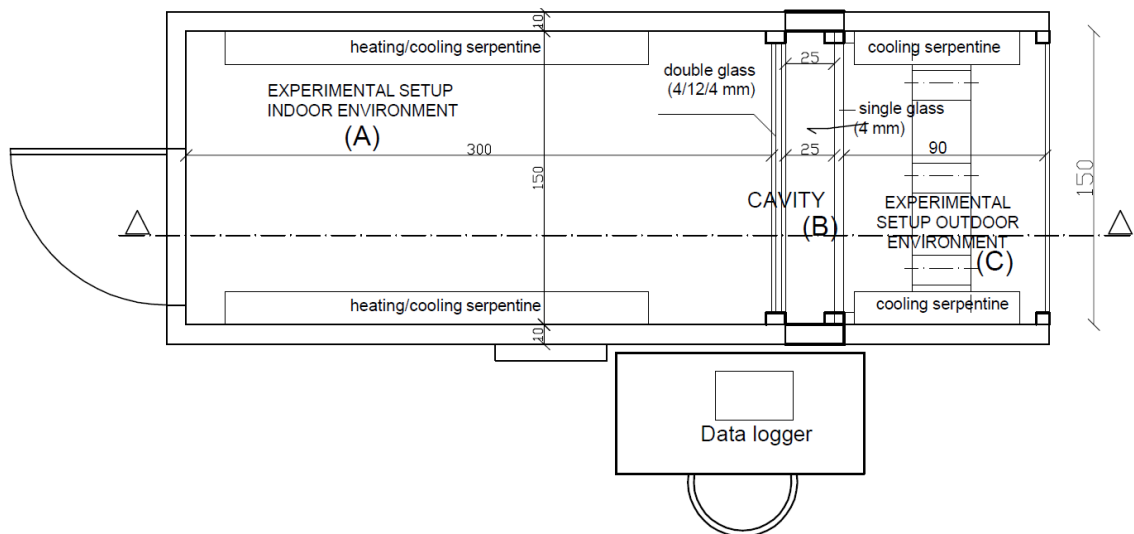


Figure 5.11. Plan view of the experimental setup

The Indoor and Outdoor Environment Simulation Setup were shown in Figures 5.10 and 5.11. The cavity as shown B was highly insulated against heat transfer. Thus, the outdoor and indoor environment simulation setup dimensions decreased from 3 m in height and 1.5 m in width to 2.16 m in height and 1.5 m in width. The cavity was closed, and only natural convection was considered. The difference in the dimensions is

related to the additional insulation. The insulation provided one-dimensional heat transfer through only the glass.

Cavity height and the positions of the thermocouples were changed due to the insulation in the cavity. The cavity was enclosed for evaluating natural flow conditions. Temperature measurements at different points of the experimental setup were taken with the T-type thermocouples mentioned Figure 5.12

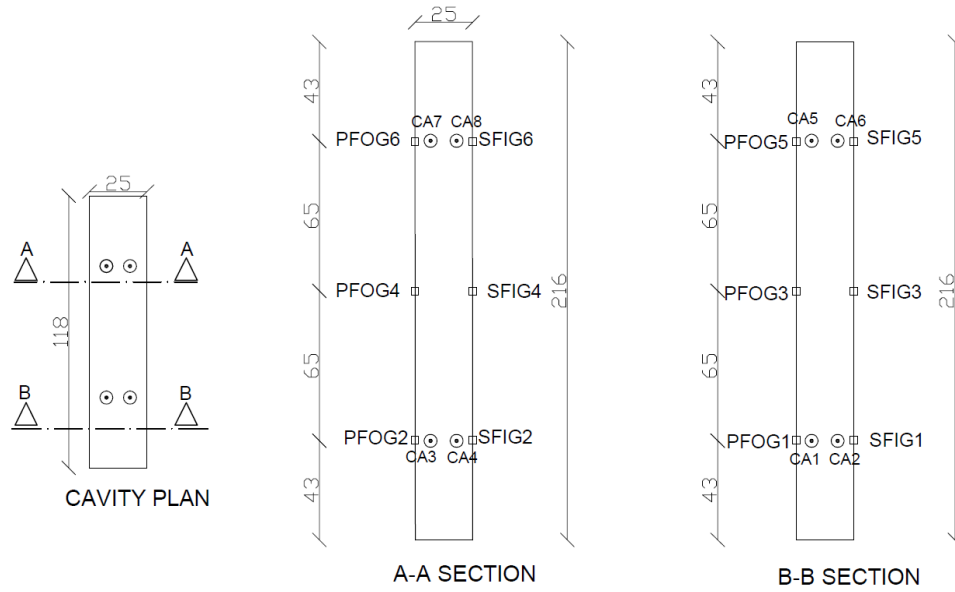


Figure 5.12. Layout of the thermocouples in the cavity

### 5.2.2. Experimental results

In this study, seven experimental measurements were taken. At the start of each test, the experimental setup was run for a different time period at steady state conditions before the measurements were taken. For the first experimental result, the changes in the average temperatures on the interior surfaces of the cavity are shown in Figure 5.13. Accordingly, the system that was thermally stable in the beginning, based on the different temperatures on the interior and exterior, became stable after some time. Because the part that simulates the exterior environment was relatively colder, a temperature difference existed between the two interior surfaces of the cavity. The temperature values on the interior of the surface facing the exterior space of the cavity reflect the average value of the six thermocouples (SFIG1-6) after the temperature

stabilized. Thermocouples PFOG1–6 give the average temperature values of the interior of the surface facing the interior cavity space.

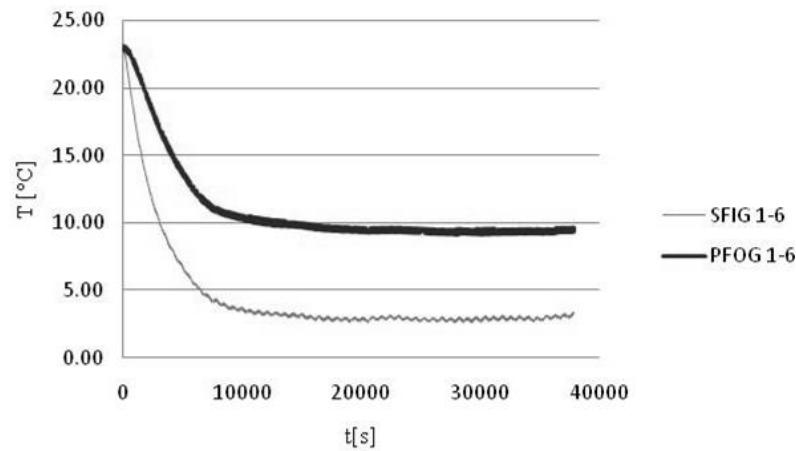


Figure 5.13. Variation of temperature in the cavity surfaces for the first experiment

The surface temperature averages given in Figure 5.13 come from six thermocouples and are used in the calculation of the Rayleigh numbers ( $Ra$ ). Along the interior glass surfaces of the cavity, temperature changes occur. This change is shown in Figure 5.14. Each point refers to the average of two thermocouples placed at the same height of the cavity. As shown in Figure 5.14, the temperature values increase depending on the height. The figure also shows the linear equality that clearly reflects this change. In the numerical study, as a boundary condition, these changes in the temperature were considered, and these linear equations were used.

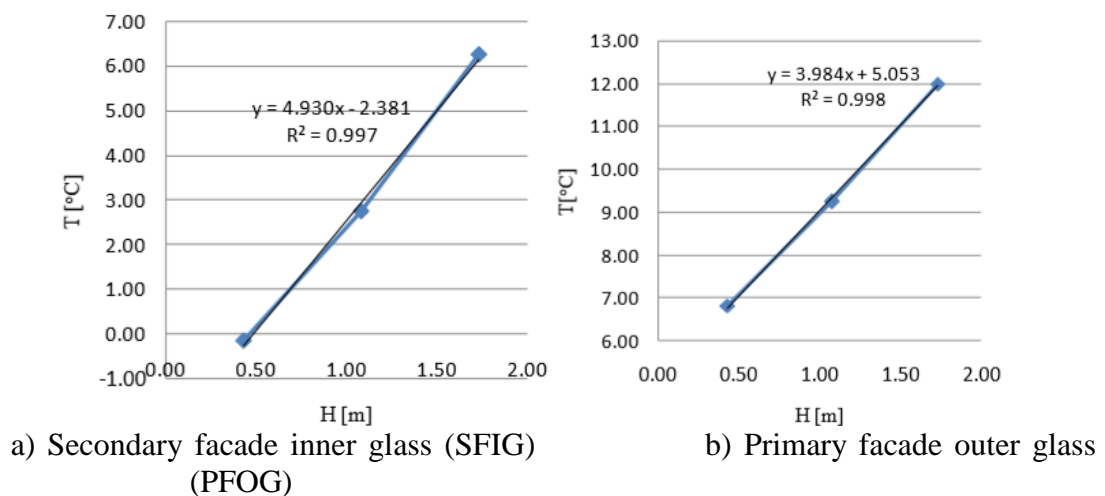


Figure 5.14. Variation of temperature in both interior surfaces along the cavity height for the first experiment

For the first experimental results, to show the oscillation of the temperature values due to the activation of the cooling and heating system after the steady state condition, the average temperature changes on the interior surfaces of the cavity are shown in Figure 5.15. As shown in Figure 5.15, the temperatures were calculated in a very stable way, and the standard deviation for both of the temperature averages is only  $0.1^{\circ}\text{C}$ .

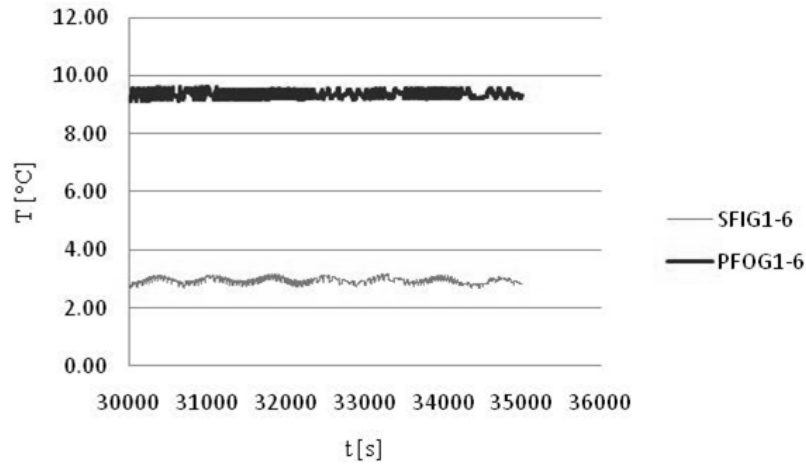


Figure 5.15. Variation of temperatures in both inner surfaces along the cavity height for the first experiment

For the first experimental study, another time-dependent temperature change after the steady state condition is shown in Figure 5.16. With the effect of natural convection, the high temperature air is located at the top. “CA1-4” shows the average temperature of the four thermocouples at the bottom, whereas “CA5-8” is the average temperature of the top four thermocouples.

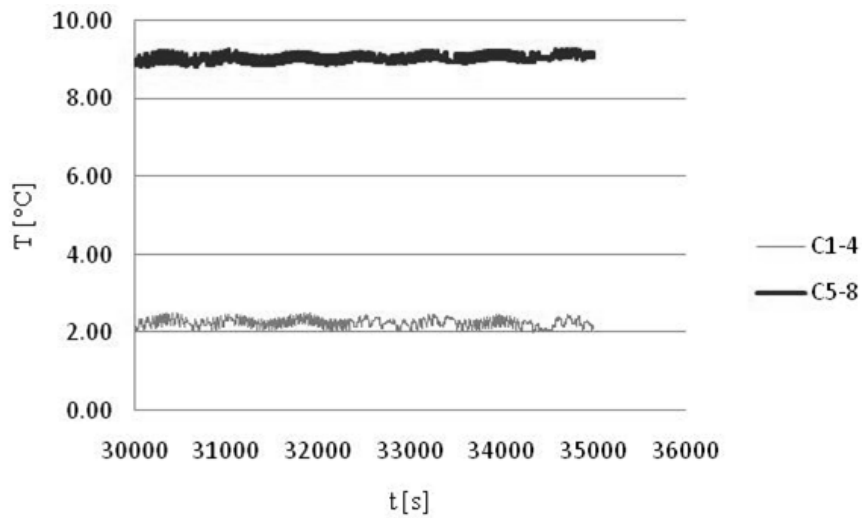


Figure 5.16. Variation of air temperature in the cavity for the first experiment

In the first experimental study, the average temperature ranges of the two different height sections of the cavity after the steady state condition are shown in Figure 5.17. The two points in the middle give the air temperature, and the temperatures on the sides refer to the average surface temperatures measured by two thermocouples each. Heat transfer occurs due to these temperature differences between the air and the surface. Additionally, the change in the air temperature depending on the height can be observed.

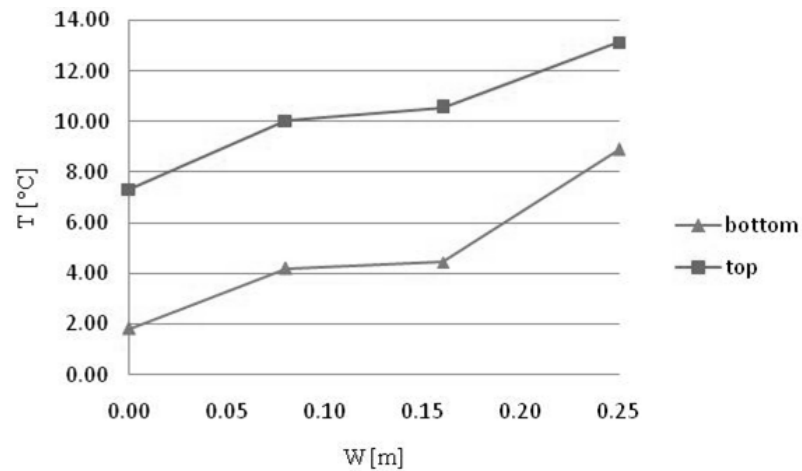


Figure 5.17. Variation of temperature in the cavity for the first experiment



### 5.2.3. Numerical Study

#### 5.2.3.1. Meshing and solution method

A finite volume–based solver (ANSYS-FLUENT v14.5) was used to predict the velocity and temperature distributions inside the three-dimensional cavity. A preliminary mesh independency survey revealed that a total of  $1.3 \times 10^6$  control volumes is optimum considering both the computational time and accuracy. To capture the high gradients near the solid surfaces, the mesh intensity increased close to the walls. Figure 5.18 shows the mesh structure of the cavity on the x-y and y-z planes.

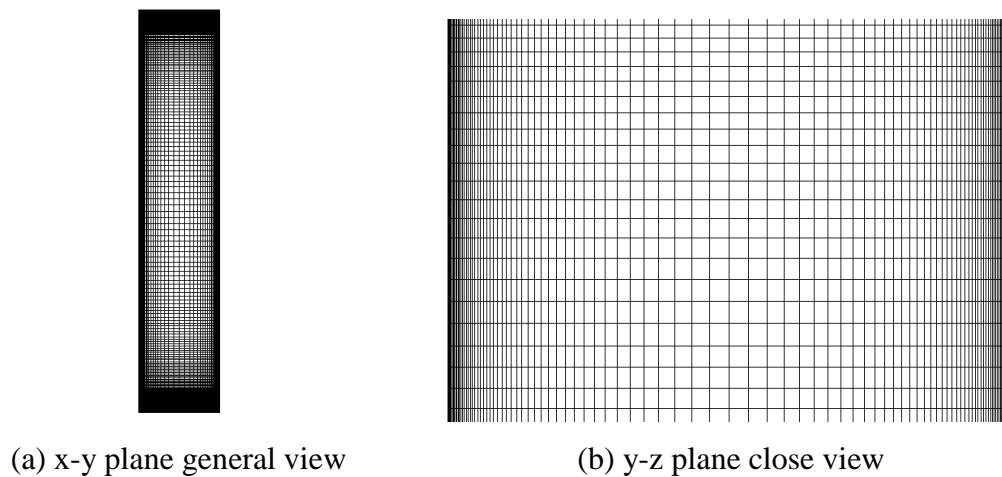


Figure 5.18. Grid configurations

The following assumptions were considered in the current study:

- The fluid is Newtonian and incompressible.
- The flow is steady, fully turbulent and three dimensional.
- The thermo-physical properties of the air were assumed to be constant except for the density. The Boussinesq approximation was used to account for the buoyancy term in the momentum equation.
- Viscous dissipation and radiation effects were neglected.

These simplifications reduce the governing equations into following forms:

Mass

$$\frac{\partial}{\partial x}(\rho u) + \frac{\partial}{\partial y}(\rho v) + \frac{\partial}{\partial z}(\rho w) = 0 \quad (5.5)$$

x-momentum

$$\frac{\partial}{\partial x}(\rho uu) + \frac{\partial}{\partial y}(\rho vu) + \frac{\partial}{\partial z}(\rho wu) = -\frac{\partial p}{\partial x} + (\mu + \mu_t) \left[ \frac{\partial^2 u}{\partial x^2} + \frac{\partial^2 u}{\partial z^2} + \frac{\partial^2 u}{\partial y^2} \right] \quad (5.6)$$

y-momentum

$$\frac{\partial}{\partial x}(\rho uv) + \frac{\partial}{\partial y}(\rho vv) + \frac{\partial}{\partial z}(\rho wv) = -\frac{\partial p}{\partial y} + (\mu + \mu_t) \left[ \frac{\partial^2 v}{\partial x^2} + \frac{\partial^2 v}{\partial y^2} + \frac{\partial^2 v}{\partial z^2} \right] - \rho g \beta (T_\infty - T) \quad (5.7)$$

z-momentum

$$\frac{\partial}{\partial x}(\rho uw) + \frac{\partial}{\partial y}(\rho vw) + \frac{\partial}{\partial z}(\rho ww) = -\frac{\partial p}{\partial z} + (\mu + \mu_t) \left[ \frac{\partial^2 w}{\partial x^2} + \frac{\partial^2 w}{\partial y^2} + \frac{\partial^2 w}{\partial z^2} \right] \quad (5.8)$$

Energy

$$\begin{aligned} \frac{\partial}{\partial x}(\rho u c_p T) + \frac{\partial}{\partial y}(\rho v c_p T) + \frac{\partial}{\partial z}(\rho w c_p T) = & \frac{\partial}{\partial x} \left( k \frac{\partial T}{\partial x} \right) + \frac{\partial}{\partial y} \left( k \frac{\partial T}{\partial y} \right) + \frac{\partial}{\partial z} \left( k \frac{\partial T}{\partial z} \right) \\ & - \frac{\partial}{\partial x_i} \left( \frac{\partial T}{\partial x_i} \frac{c_p \mu_t}{\sigma_t} \right) \end{aligned} \quad (5.9)$$

Here velocity, pressure and temperature are defined as time-averaged. Turbulence can be determined for each computational node in the domain in terms of the local turbulence kinetic energy ( $k$ ) and the diffusion rate ( $\varepsilon$ ),

$$\mu_t = \rho C_\mu \frac{k^2}{\varepsilon} \quad (5.10)$$

To resolve the turbulence energy and diffusion rate terms, the Realizable k-epsilon turbulence model was used. In comparison to the classical k-epsilon method, the realizable model is more successful and accurate for the problems with flow separation, re-attachment and complicated secondary flows (ANSYS Theory Guide, 2009). In the realizable k-epsilon method, the following additional equations are resolved to evaluate the kinetic energy and the dissipation rate,

$$\frac{\partial}{\partial x_j}(\rho k u_j) = \frac{\partial}{\partial x_j} \left[ \left( \mu + \frac{\mu_t}{\sigma_k} \right) \frac{\partial k}{\partial x_j} \right] + G_k + G_b - \rho \varepsilon - Y_M + S_K \quad (5.11)$$

$$\frac{\partial}{\partial x_j}(\rho \varepsilon u_j) = \frac{\partial}{\partial x_j} \left[ \left( \mu + \frac{\mu_t}{\sigma_\varepsilon} \right) \frac{\partial \varepsilon}{\partial x_j} \right] + \rho C_1 S \varepsilon - \rho C_2 \frac{\varepsilon^2}{k + \sqrt{\nu \varepsilon}} + C_{1\varepsilon} \frac{\varepsilon}{k} C_{3\varepsilon} G_b + S_\varepsilon \quad (5.12)$$

The details of the terms and constants that are given in the governing equations can be found in the theory book (ANSYS Theory Guide, 2009). The SIMPLE algorithm of Patankar (1980) was used to solve the pressure-velocity coupling. In the decomposition of the pressure term, the PRESTO method was used, whereas for the other transport equations, the QUICK (Leonard and Mokhtari, 1990) scheme was applied. In the analyses, for the all of the transport parameters, the convergence criterion has been defined as  $10^{-7}$ .

### 5.2.3.2. The validation of the solution method

To validate the current solution methodology, a similar experimental study from the literature was resolved, and the comparative results are presented. King (1989) carried out experimental measurements for natural convection flow inside a tall cavity with dimensions of  $H=2.5$  m,  $W=0.5$  m and  $L=1.0$  m. In the experimental study, the hot and cold surfaces were kept at the temperatures of  $T_H=77.2^\circ\text{C}$  and  $T_C=31.4^\circ\text{C}$ , respectively. According to the geometric and boundary conditions, the corresponding Ra number is calculated as  $4.6 \times 10^{10}$ . In the experimental setup, the temperature values inside the cavity were measured by a thermocouple traversing mechanism. A Laser Doppler Anemometer (LDA) system was used to capture the velocity variations near the cavity walls. The temperature measurement sensors have an accuracy of  $\pm 0.2$  K, and the uncertainty of the velocity measurements is 0.02 m/s. This comprehensive experimental study by King (1989) is preferred by various researchers for validating natural convection simulations inside tall cavities (King, 1989 and Lau et al. 2012).

The velocity profile and variation of the Nusselt number on the hot surface is compared with the reference study in Figure 5.19. Here, both experimental and numerical data were obtained on a mid-surface of  $z=L/2$  and  $y=H/2$ . The comparison shows that the numerical results have a similar tendency as the experimental measurements. To validate the predicted velocity field and temperature distributions

inside the cavity, another set of comparisons was conducted based on the numerical results from Lau et al. (2012). Lau et al. (2012) conducted an analysis based on time-dependent Large-Eddy-Simulation (LES) as the turbulence model. Although steady state RANS (Reynolds-Averaged Navier Stokes) equations were solved in the current model, similar variations can be seen in Figure 5.20.

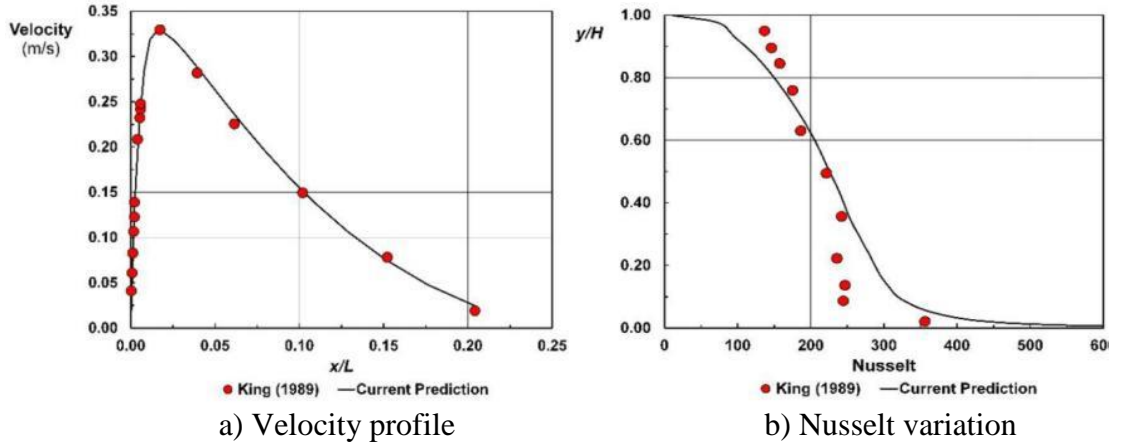


Figure 5.19. The velocity profile and variation of the Nusselt number on the hot surface

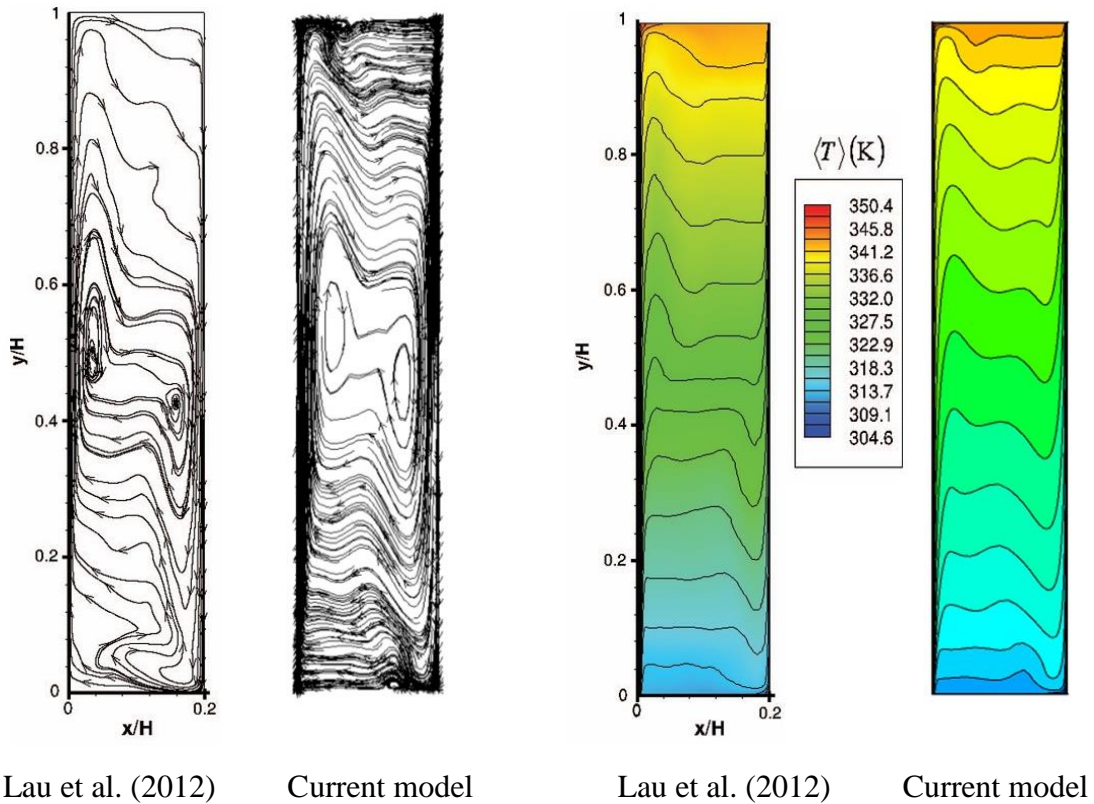


Figure 5.20. Velocity and temperature fields on the  $z = L/2$  plane

### 5.2.3.3. Numerical model

In Figure 5.21, the reduced geometry of the test room is shown with the boundary conditions. The height, width and depth of the test room were  $H=2.16$  m,  $W=0.25$  m and  $L=1.18$  m. The aspect ratio ( $W/H$ ) of the cavity was 0.116. Apart from the side surfaces that had constant temperatures of  $T_H$  and  $T_C$ , all of the surfaces are regarded as adiabatic.

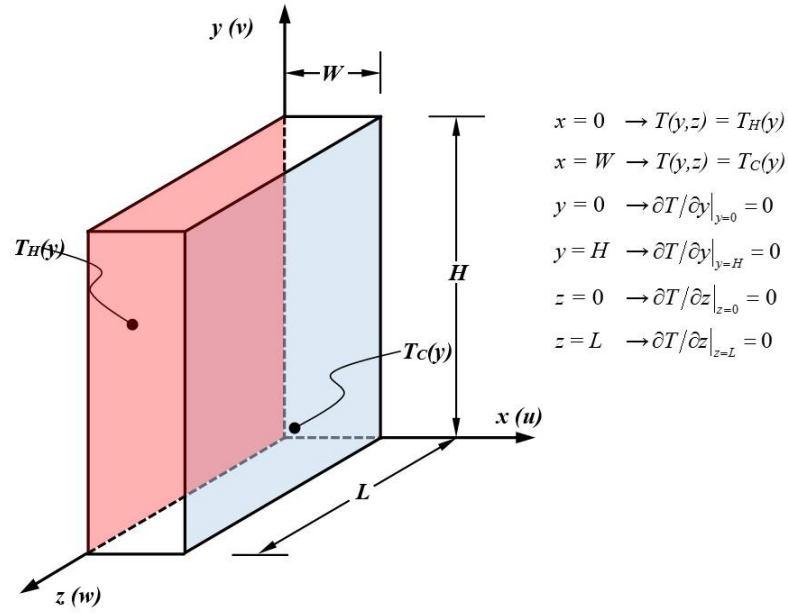


Figure 5.21. Test room geometry and boundary conditions

In the experimental studies, along the three lines indicated on the side surfaces of the cavity ( $y=0.43$  m,  $1.08$  m and  $1.73$  m), the temperature values were measured with thermocouples, and the temperature changes were determined for each experiment. The experimental measurement results and the corresponding Rayleigh numbers are presented in Table 5.6. According to the boundary conditions given in Table 5.6, the Rayleigh number ranges from  $8.59 \cdot 10^9$  to  $1.41 \cdot 10^{10}$ . Here, the Rayleigh number is defined as

$$Ra_H = \frac{g\beta}{\nu\alpha} (T_H - T_C) H^3 \quad (5.13)$$

where the average temperature values  $T_H$  and  $T_C$  were determined using the measured surface temperatures SFIG1 to 6 (for  $T_H$ ) and PFOG1 to 6 (for  $T_C$ ). The Rayleigh numbers calculated using Equation 5.13 increase with increasing temperature values, as shown in Table 5.6.

Table 5.6. Experimental measurement values and calculated Rayleigh numbers

Experiment#	<i>PFOG</i>			<i>SFIG</i>			$T_C$	$T_H$	Ra
	$T_{1,2avg}$	$T_{3,4avg}$	$T_{5,6avg}$	$T_{1,2avg}$	$T_{3,4avg}$	$T_{5,6avg}$			
1	-0.16	2.74	6.25	6.82	9.25	12.00	2.94	9.36	8.59E+09
2	0.79	3.71	7.35	8.51	11.30	14.22	3.95	11.34	9.74E+09
3	0.89	4.38	8.95	8.96	12.06	16.20	4.74	12.41	1.00E+10
4	1.46	4.80	8.29	10.63	13.67	17.62	4.85	13.97	1.16E+10
5	1.60	5.22	8.90	11.42	14.78	19.32	5.24	15.17	1.25E+10
6	1.97	5.76	9.58	12.48	16.08	21.15	5.77	16.57	1.34E+10
7	2.94	7.03	11.13	14.12	17.91	23.48	7.03	18.50	1.41E+10

#### 5.2.3.4. Results and Discussions

According to the boundary conditions given in Table 5.6, the Rayleigh number ranges from  $8.59 \times 10^9$  to  $1.41 \times 10^{10}$ . In Figure 5.22, the velocity variations along the cavity width are shown at  $y=1.73$  m for the different experimental conditions. Although the temperature difference inside the cavity changes in each experiment, the velocity variation maintained almost constant at the center of the cavity from 0.05 m to 10.20 m. On the other hand, the air close to the cold and hot surfaces was affected by the buoyancy forces that are caused by the density differences induced by the temperature gradients. Figure 5.22 shows that similar velocity variations were obtained at the cold and hot surfaces along the streamwise direction for different Ra numbers and that the highest Ra number (for the last numerical experiment) was more than double that of the first numerical experiment.

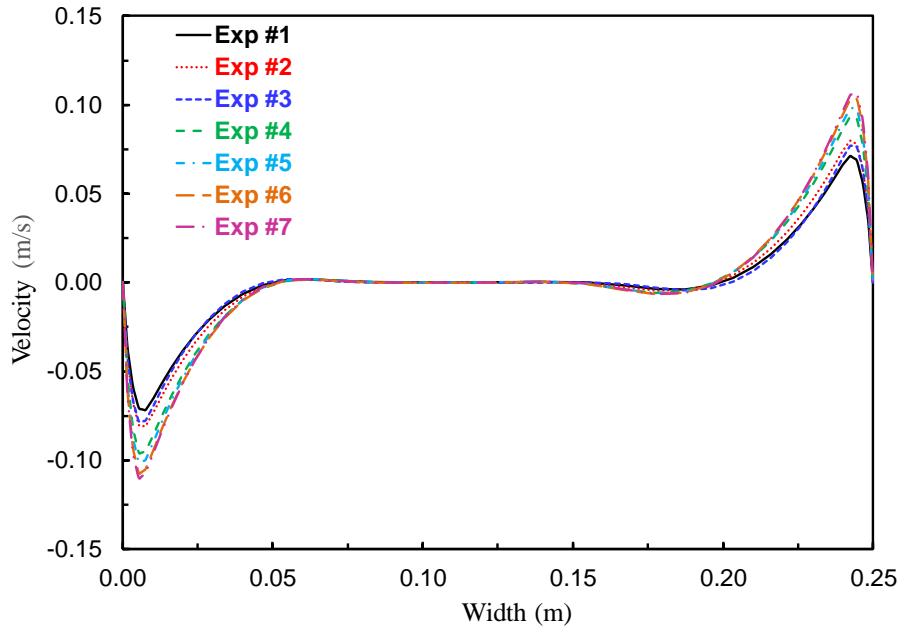


Figure 5.22. Velocity variations inside the cavity for different numerical experiments at  $y=1.73$  m

The isotherms on the  $z=L/2$  plane are shown in Figure 5.23. Because the Rayleigh number varies in a relatively narrow range, there is not a significant difference in the temperature ranges. However, as the surface temperatures increase along the flow direction, the air temperature also increases, and the hot zones in the cavity expand.

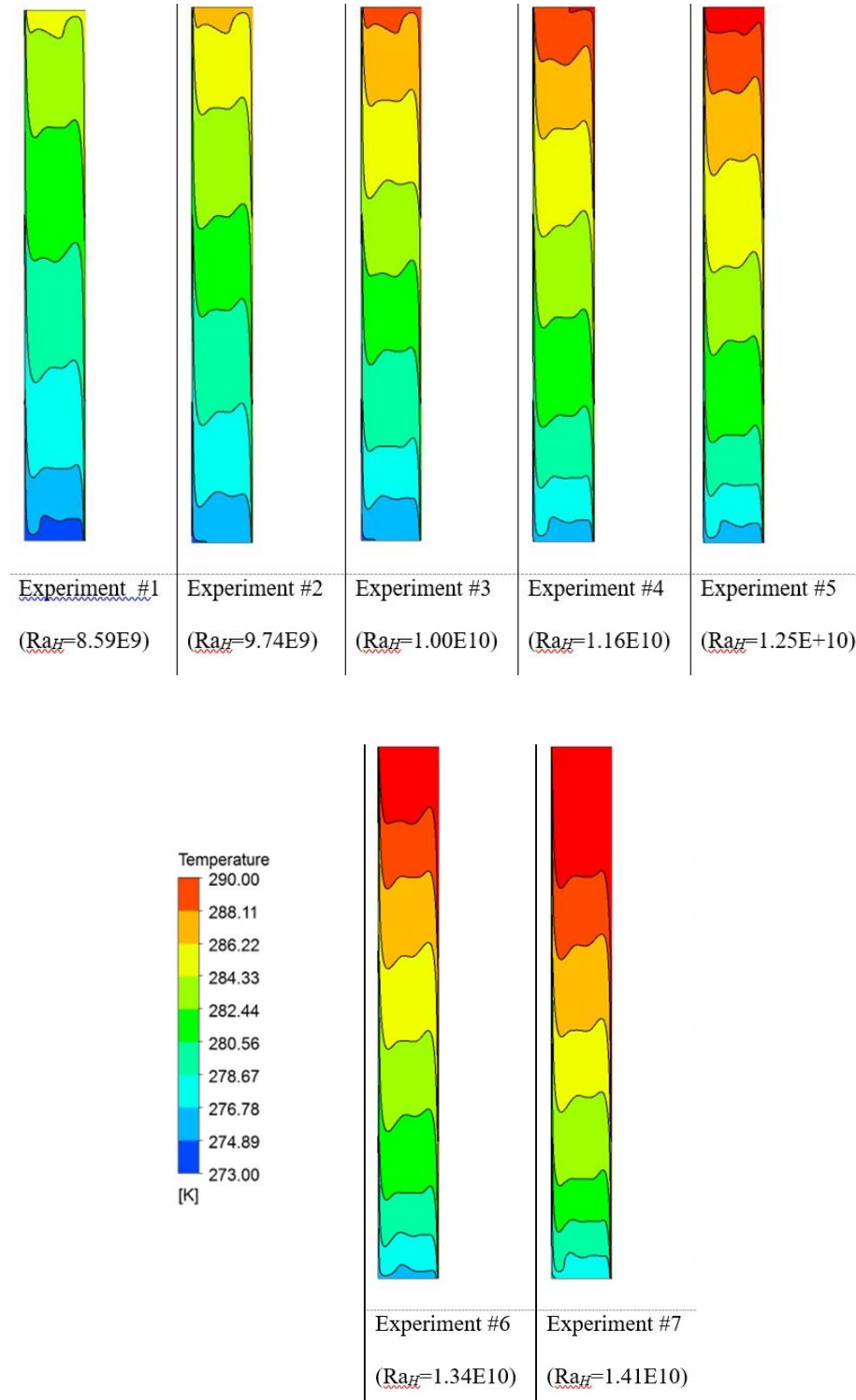


Figure 5.23. Temperature variations on the  $z = L/2$  plane for different Ra numbers

In Figure 5.24, the temperature variations inside the cavity are compared with the experimental measurements at the height of  $y=1.73$  m. Different surface temperatures were tested in the experiments, and different temperature-location slopes were created in the cavity. When the dimensionless temperature values are taken into



account, it is seen that, similar to the velocity ranges, the temperature ranges are identical in form. It is clear that the temperature variations have similar tendencies for each experiment but that they are shifted by varying the Rayleigh number. The temperature measurements from the experiments are also shown in Figure 5.24 by solid markers. The experimental results match the numerical results well. The largest difference was less than  $1^{\circ}\text{C}$  for the comparisons between the numerical and experimental results. These differences could be mainly caused by the measurement point uncertainties for the y-direction as well as for the x- and z-directions, as shown in Figure 5.21.

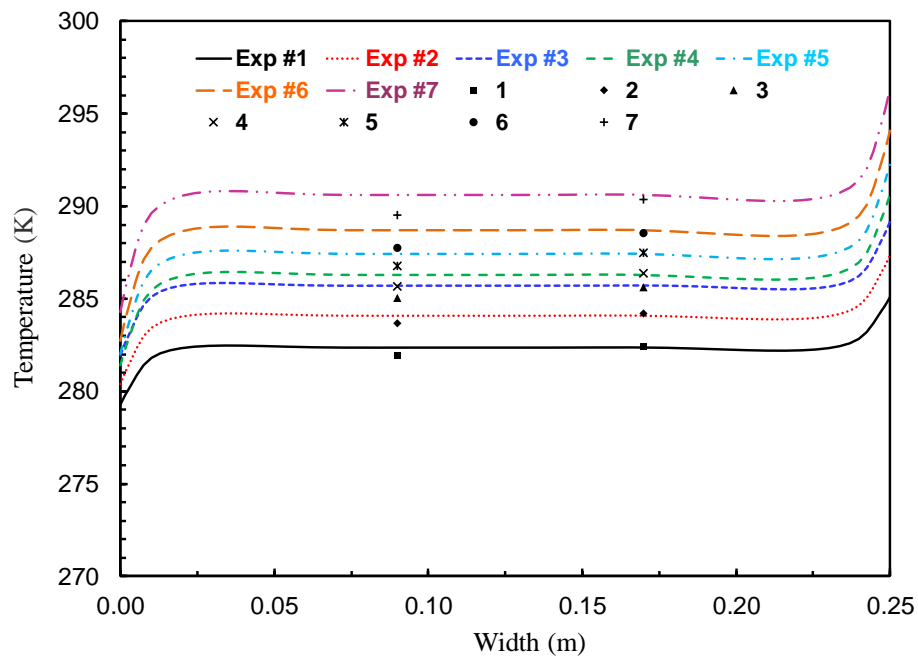


Figure 5.24 The temperature distributions along the cavity width for different numerical experiments at  $y=1.73$  m

Variations of the heat fluxes along the cavity height at two separate surfaces can be seen in Figure 5.25 for different Ra numbers. The heat flux values increase with increasing Rayleigh number and reach the maximum and minimum values at the top and bottom of the cavity, respectively.

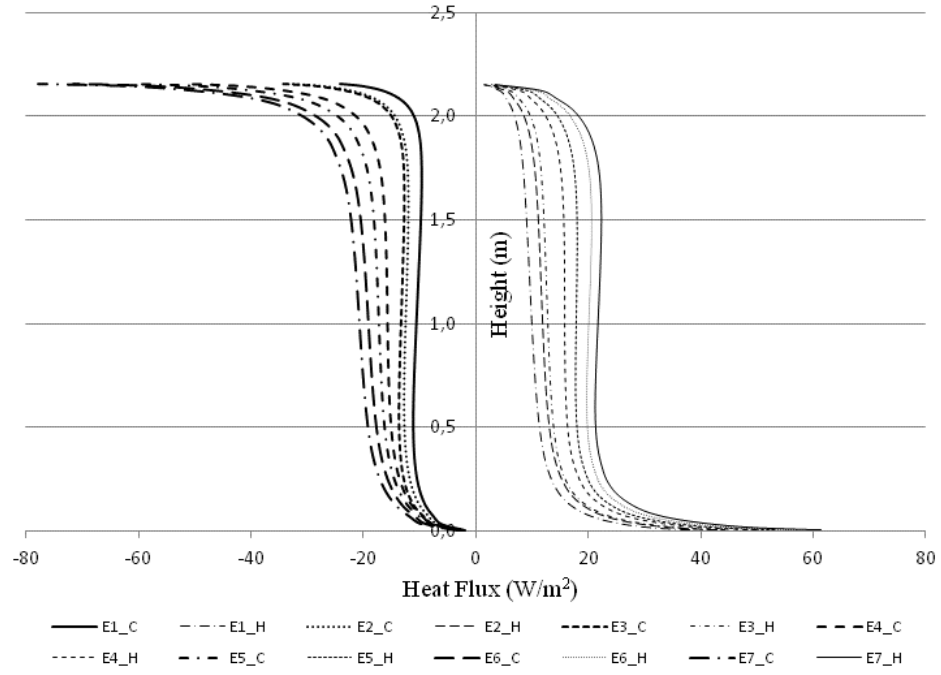


Figure 5.25. Variations of the heat fluxes along the cavity height at the cold and hot surfaces for different numerical experiments

The Nusselt numbers were also evaluated using the mean heat flux values on the hot surface of the cavity through Equation 5.14,

$$Nu_H = \frac{q''}{\Delta T} \frac{W}{k} \quad (5.14)$$

The Nusselt number distributions at the hot surface along the cavity height are shown in Figure 5.26. The average Nusselt number increased with increasing Rayleigh number and reached the maximum value at the top of the cavity. Because of the restricted heat transfer at the bottom of the cavity, the Nusselt numbers start from the minimum values; throughout the cavity, there is no large difference between the Nusselt values as there was for the Rayleigh numbers.

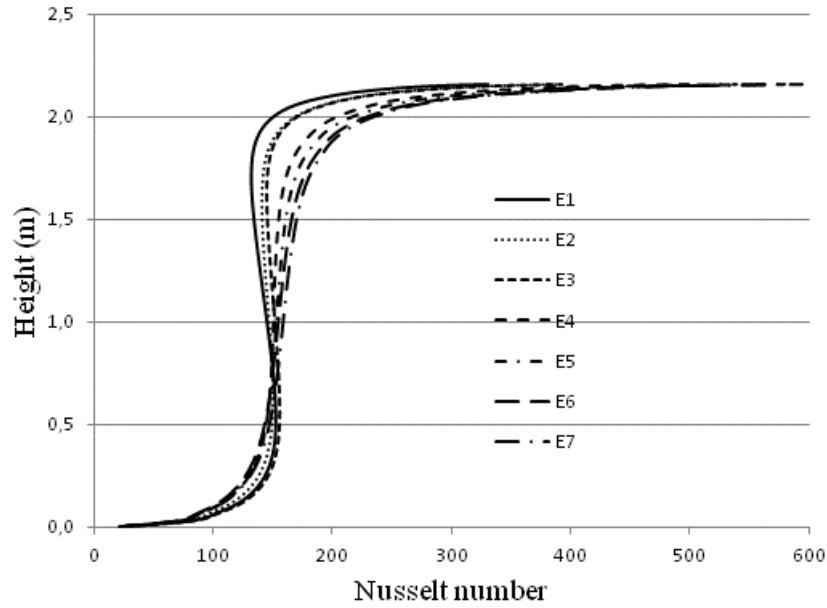


Figure 5.26. Variations of the Nusselt numbers at the hot surface along the cavity height for different numerical experiments

The average Nusselt numbers for each experimental case are given in Table 5.7 for the hot surface of the cavity. The Nusselt number increases with buoyancy forces that are created by the temperature differences of the surface and air, which is induced by the density gradients.

Table 5.7. Average Nusselt numbers at the hot surface of the cavity for each experimental case

Exp. Number	#1	#2	#3	#4	#5	#6	#7
Nusselt numbers	142.6	147.7	152.5	156.5	160.9	165.2	168.8

These non-dimensional variables are introduced in the governing equations, and the velocity and temperature variations in the cavity arise in terms of the Nusselt and Rayleigh numbers. The results can be generalized by a correlation to predict the heat transfer rate using the Nusselt number for the double skin facade operating with the airtight condition and a Rayleigh number of approximately  $10^{10}$ . Thus, the Nusselt number is a power function of the Rayleigh number,

$$Nu = C \cdot Ra^m \quad (5.15)$$

The Rayleigh and Nusselt numbers given in Tables 5.6 and 5.7 were used in a regression analysis to evaluate the indices  $C$  and  $m$  in Equation 5.15; these values were calculated to be 0.082 and 0.325, respectively. Therefore, the correlation for the airproof cavity investigated in this study can be given as,

$$Nu = 0.082 \cdot Ra^{0.325} \quad (5.16)$$

The Nusselt and Rayleigh numbers for each case were drawn with the power function, as shown in Figure 5.27. The coefficient of determination,  $R^2$ , was found to be 0.982, and the data fit well.

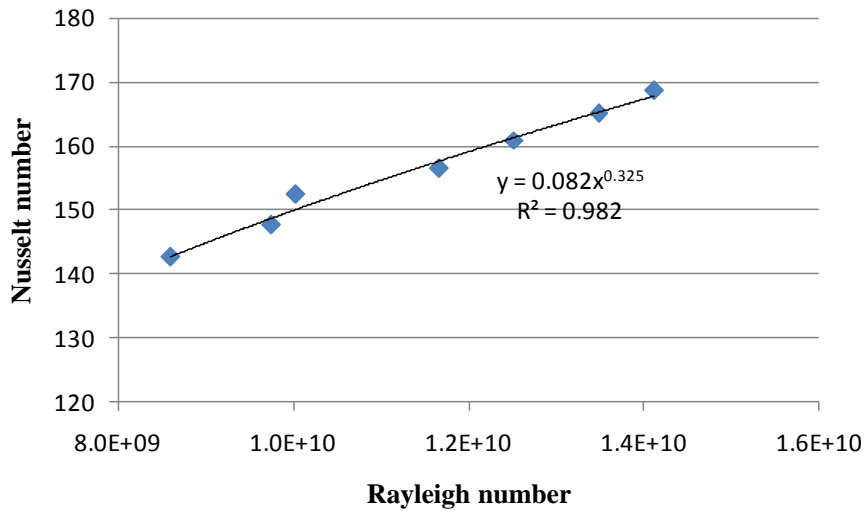


Figure 5.27. Nusselt numbers as a function of Rayleigh numbers for the experimental case

In this study, numerical and experimental studies were conducted to investigate the flow and heat transfer characteristics inside a double skin facade. A numerical model was developed to simulate the steady state natural convection inside a tall cavity. The comparative results show that the current model can successfully predict the velocity field and temperature variations inside the domain. The following conclusions can be obtained from the current study:

- The velocity field variations showed that increasing the temperature difference to approximately 65% did not cause a large difference in the working conditions.
- Even though the velocity field remained constant, the heat transfer increased by approximately 20% by increasing the temperature difference from 7K to 11.8K.

- A correlation was developed to predict the Nusselt numbers with the Rayleigh number ranging from  $8.59 \times 10^9$  to  $1.41 \times 10^{10}$  for an airproof double skin facade.

### **5.3. Case 3: Experimental and numerical investigation of forced convection in a double skin facade by using CFD tool**

Flow and heat transfer behaviors of the air channel which is between the two glass facades in the test room with double skin facade which was designed in the box window type and set up for measurements in the laboratory environment was evaluated by making its numerical modelling in the ANSYS-CFD environment and analysis under different working conditions. In this chapter, by using data from the experimental studies, the verification of the numerical studies was conducted and the air movements in the channel between the two glass facades and thermal interactions were examined numerically in detail.

#### **5.3.1. Experimental Study**

The channel geometry in the test room which has double skin facade whose numerical study was conducted is shown in Figure 5.28. The height and width of the channel geometry are respectively;  $H = 2.90$  m ve  $L = 1.40$  m. The depth of the cavity was  $W = 0.25$ - $0.325$  and  $0.40$  m and studied for three different situations. In order to adjust the depth of the cavity, limitless-gearred mechanisms which were triggered by electric motors from bottom and top were used to adjust the desired span (Figure 5.28.) The depth of the cavity was checked by measuring from the points which are close to the four corners of the cavity and the middle point of the cavity and for each situation, the maximum value of deviation was detected as  $\pm 2$ mm as a result of the measurements which were taken with the lazermeter.



Figure 5.28. The mechanism which is used to adjust the depth of the cavity and the cavity air inlet vent.

In the exterior glass, there are air entrance and exit spans which lie along the width of the cavity at the height of 0.2m and which can be opened and closed when it is necessary (Figure 5.29.) In the numerical study, the glass and aluminium elements which surround the cavity were not modelled, only the air in the cavity was modelled. In this channel which has three different depths of cavity in between two glass surfaces, the effects of the different air flow rates will be analysed in detail in the further sections.

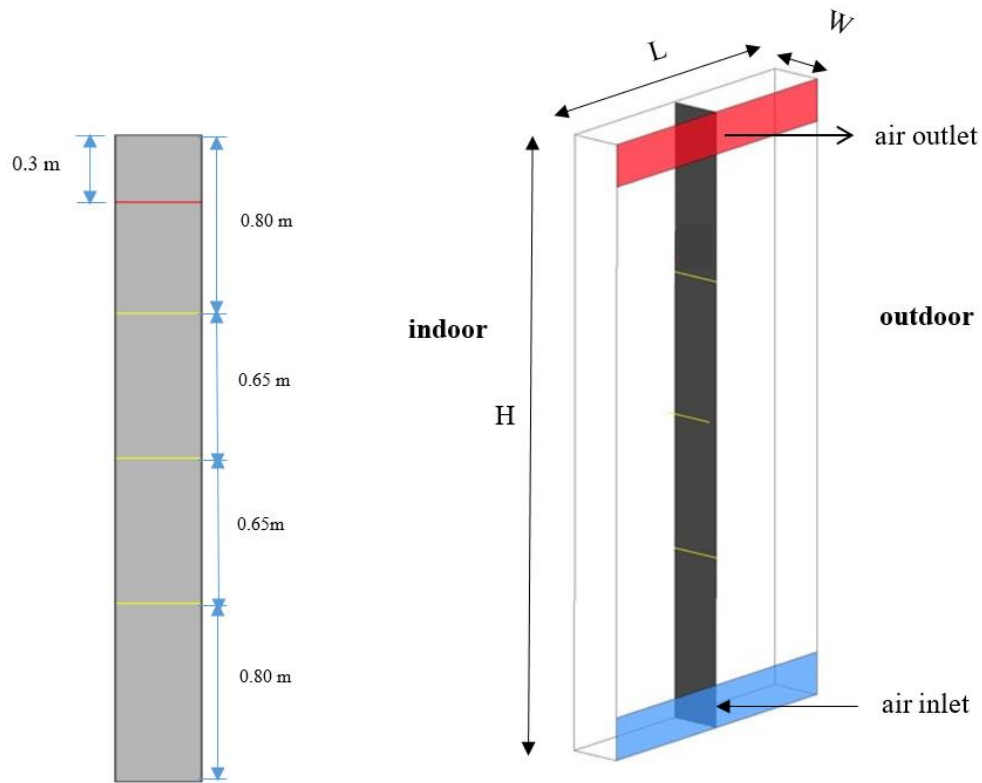


Figure 5.29. Model geometry

In this numerical model, the air flow mode which is named as the exterior air curtain in the literature, in which the air entrance and exit spans in the interior glass are closed and the air interaction in the cavity is only provided by the air entrance and exit spans on the exterior glass facade surface was analysed. Apart from the interior and exterior glass surfaces, all the other surfaces were accepted as adiabatic. For the temperatures of the surfaces of the interior and exterior glass which face the cavity, the results which were acquired from the experimental studies were used. For this, using the averages of the two temperature measurements which were taken from three different height levels, the temperature changes along the whole surface were defined as the limit condition for the surfaces of the interior and exterior facades of the DSF which faces the cavity. Through the vent on the bottom surface of the exterior glass facade, the air flow is taken uniformly into the channel and it is disposed to the atmosphere pressure through the vent in the top of the exterior facade. In the experimental study, perforated plate was placed on air inlet in order to provide uniform velocity distribution. Air inlet velocities can be found in Table 5.8 for various cavity depths and mass flow rates. All experimental measurements reflect the average of long term measurements taken after all system reached to thermal equilibrium. While cavity depth is 25cm in experiment 1,

2 and 3, it is 32.5cm in the experiment 4,5,6 and 40cm in the experiment 7,8 9.  $T_{inlet}$  defines the air inlet temperature to cavity, while  $V_{inlet}$  defines air inlet velocity. Six T-type thermocouples were placed on two different surfaces to measure the inner surface temperatures of the double skin facade. These thermocouples are numbered in Table 5.8 from  $T_{1,2avg}$  (the average of the two thermocouple at the 0.80 m level) to  $T_{5,6avg}$  (the average of the two thermocouples at the 2.10 m level) for primary facade outer glass (PFOG) for the portion of the primary facade facing the cavity and from  $T_{1,2avg}$  to  $T_{5,6avg}$  for the portion of the secondary facade inner glass (SFIG) facing the cavity. Under these different working conditions, the velocity and temperature changes in the channel were examined numerically in detail and using the temperature distribution, the changes of the heat transfer rate which occurs from the unit surface area along the cavity height were acquired. Using these changes in the heat flux, depending on the flow (dimensionless number of  $Re$ ), a correlation which gives the changes in the dimensionless number of  $Nu$  were produced.

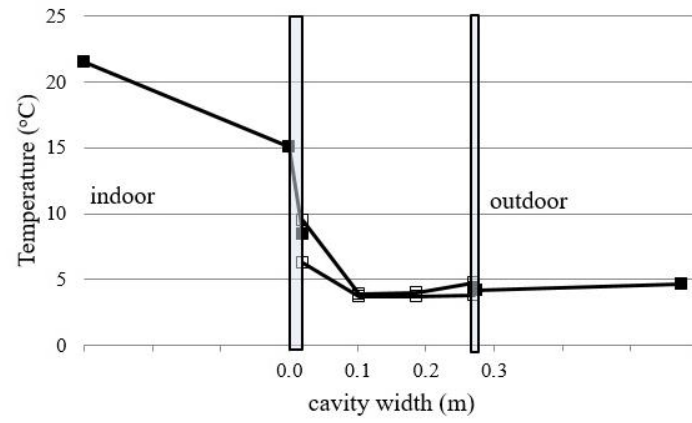
Table 5.8. Experimental results (CFD inputs)

Exp.#	°C	m/s	PFOG (°C)			SFIG (°C)		
	$T_{inlet}$	$V_{inlet}$	$T_{1,2avg}$	$T_{3,4avg}$	$T_{5,6avg}$	$T_{1,2avg}$	$T_{3,4avg}$	$T_{5,6avg}$
1	4.40	1.250	6.28	8.41	9.45	3.79	4.41	4.73
2	4.52	1.810	5.84	7.83	8.6	3.53	4.01	4.31
3	3.34	2.340	4.53	6.45	7.13	2.3	2.56	2.89
4	5.71	1.230	7.45	9.22	10.41	4.95	5.44	5.78
5	5.03	1.670	6.31	7.98	9.06	3.84	4.11	4.49
6	3.78	2.150	5.03	6.76	7.76	2.66	2.78	3.2
7	6.40	1.400	8.3	10.14	11.34	5.53	5.95	6.33
8	6.36	1.920	7.86	9.58	10.58	5.15	5.29	5.63
9	5.89	2.350	7.18	8.84	9.76	4.75	4.6	4.92

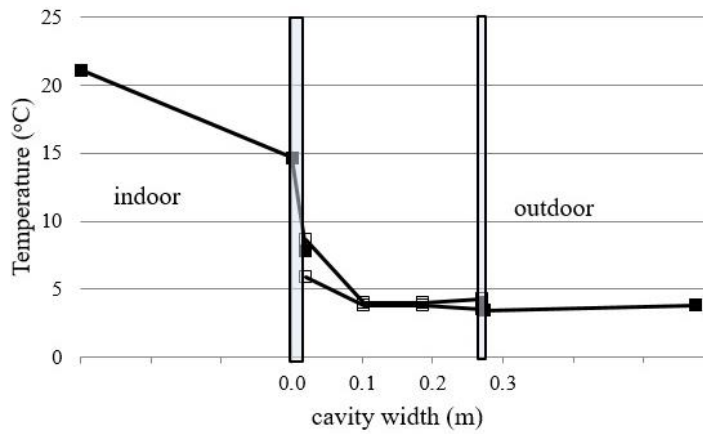
Considering the Experiment 1, which shows low flow rate with the cavity depth of 25 cm, it can be seen that while the average temperature of the indoor environment is 21.45 °C, the average temperature of the outdoor environment is 4.70 °C. While the average temperature of the measurements which were taken from the middle point of the surface of the primary facade which faces the indoor environment (primary facade indoor glass, PFIG) is 15.07 °C, the average of the measurements which were taken from the middle point of the surface of the primary facade which faces the cavity (1.45 m level) is 8.41 °C. While the average temperature of the measurements which were taken from the middle point of the surface of the secondary facade which faces the



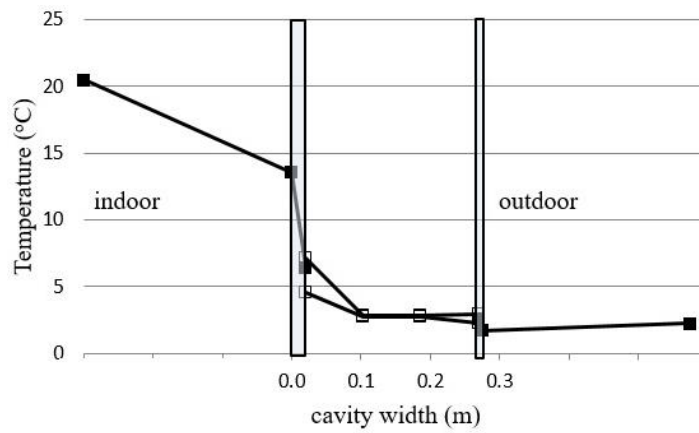
cavity is 4.41 °C, the average temperature of the measurements which were taken from the middle point of the surface of the secondary facade which faces the outdoor environment is 4.17 °C (Figure 5.30a). In the Experiment 3, which shows high flow rate with the cavity depth of 25 cm, while the average temperature of the indoor environment is 20.48 °C, the average temperature of the outdoor environment is 2.23 °C. Also, while the average temperature of the measurements which were taken from the primary facade outdoor glass, Primary facade indoor glass (PFIG) is 13.57 °C, it is seen that the average temperature of the measurements which were taken from the middle point of the surface of the primary facade which faces the cavity (1.45m level) is 6.45 °C. While the average temperature of the measurements which were taken from the middle point of the surface of the secondary face which faces the cavity is 2.56 °C, the average of the temperature of the measurements which were taken from the middle point of the surface of the secondary facade which faces the outdoor environment is 1.74 °C (Figure 5.30c). It has been observed that in the Experiment 1, for the indoor environment temperature, the standard deviation value is in the interval of 0.05-0.1 °C, for the glass surface temperatures it is in the interval of 0.09-0.16 °C, for the cavity air temperature it is in the interval of 0.12-0.18 °C and for the outdoor environment, it is in the interval of 0.16-0.2 °C. Furthermore, in the Experiment 2, for the indoor environment temperature, the standard deviation value is in the interval of 0.27-0.37 °C, for the glass surface temperatures it is in the interval of 0.08-0.12 °C, for the cavity air temperature it is in the interval of 0.10-0.12 °C and for the outdoor environment, it is in the interval of 0.16-0.2 °C. And in the Experiment 3, for the indoor environment temperature, the standard deviation value is in the interval of 0.05-0.12 °C, for the glass surface temperatures it is in the interval of 0.07-0.12 °C, for the cavity air temperature it is in the interval of 0.08-0.11 °C and for the outdoor environment, it is in the interval of 0.13-0.22 °C.



a) Low flow rate



b) Medium flow rate

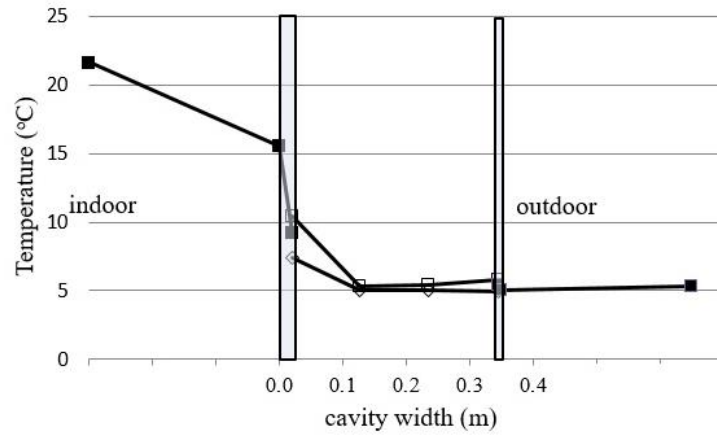


c) High flow rate

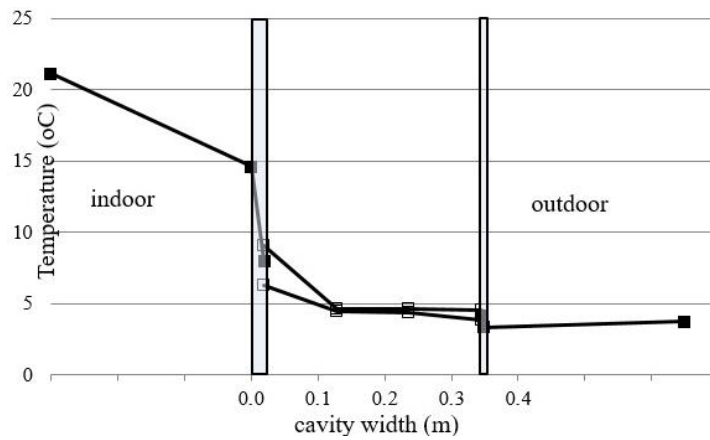
Figure 5.30. Variation of temperature from indoor environment to the outdoor environment for the 25 cm cavity width condition (Exp1, Exp2 and Exp3)

When we look at the Experiment 4, which has low flow rate with the cavity depth of 32.5 cm, we see that while the average temperature of the indoor environment is 21.65 °C, the average temperature of the outdoor environment is 5.37 °C. While the

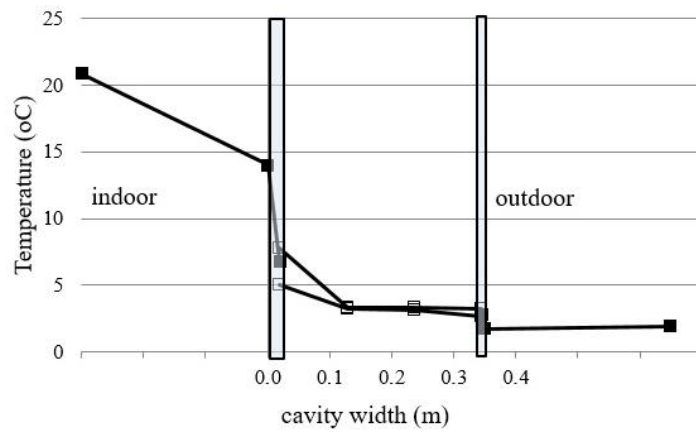
average of the temperature of the measurements which were taken from the middle point of the primary facade outdoor glass, Primary facade indoor glass (PFIG) is 15.55 °C, it is seen that the average temperature of the measurements which were taken from the middle point of the surface of the primary facade which faces the cavity (1.45m level) is 9.22 °C. Also, while the average temperature of the measurements which were taken from the middle point of the surface of the secondary facade which faces the cavity is 5.44 °C, the average temperature of the measurements which were taken from the middle point of the surface of the secondary facade which faces the outdoor environment is 5.03 °C (Figure 5.31a). When we consider the Experiment 4, which has high flow rate with the cavity depth of 32.5 cm, while the average temperature of the indoor environment is 20.85 °C, the average temperature of the outdoor environment is 1.95 °C. While the average of the temperature of the measurements which were taken from the middle point of the primary facade outdoor glass, Primary facade indoor glass (PFIG) is 14.00 °C, it is seen that the average temperature of the measurements which were taken from the middle point of the surface of the primary facade which faces the cavity (1.45m level) is 6.76 °C. And, while the average temperature of the measurements which were taken from the middle point of the surface of the secondary facade which faces the cavity is 2.78 °C, the average temperature of the measurements which were taken from the middle point of the surface of the secondary facade which faces the outdoor environment is 1.74 °C (Figure 5.31c).



a) Low flow rate



b) Medium flow rate

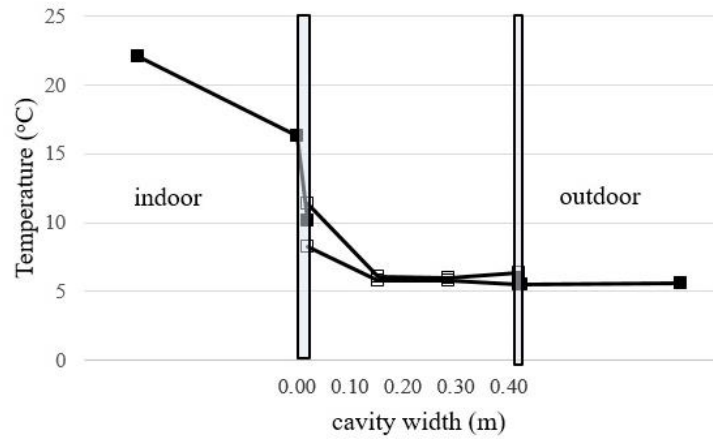


c) High flow rate

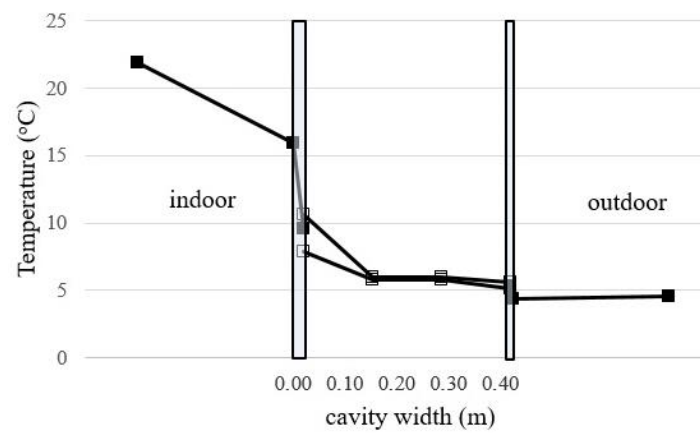
Figure 5.31. Variation of temperature from indoor environment to the outdoor environment for the 32.5 cm cavity width condition (Exp4, Exp5 and Exp6)

When we look at the Experiment 7, which has low flow rate with the cavity depth of 40 cm, we see that while the average temperature of the indoor environment is 22.09 °C, the average temperature of the outdoor environment is 5.59 °C. While the

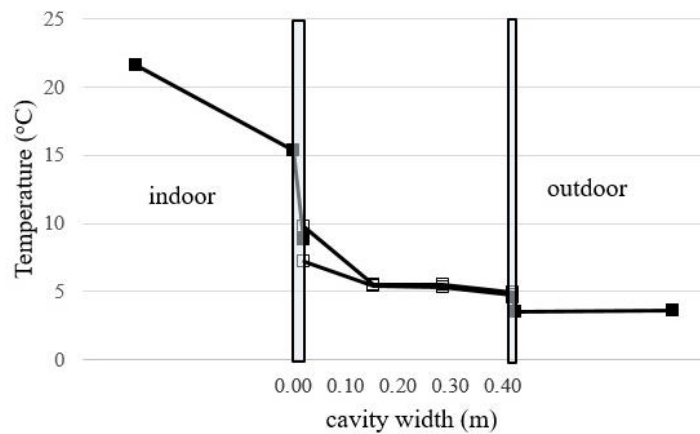
average of the temperature of the measurements which were taken from the middle point of the primary facade outdoor glass, Primary facade indoor glass (PFIG) is 16.29 °C, it is seen that the average temperature of the measurements which were taken from the middle point of the surface of the primary facade which faces the cavity (1.45m level) is 10.14 °C. While the average temperature of the measurements which were taken from the middle point of the surface of the secondary facade which faces the cavity is 5.95 °C, the average temperature of the measurements which were taken from the middle point of the surface of the secondary facade which faces the outdoor environment is 5.49 °C (Figure 5.32a). When we consider the Experiment 9, which has high flow rate with the cavity depth of 40 cm, while the average temperature of the indoor environment is 21.56 °C, the average temperature of the outdoor environment is 3.60 °C. While the average of the temperature of the measurements which were taken from the middle point of the primary facade outdoor glass, Primary facade indoor glass (PFIG) is 15.36 °C, it is seen that the average temperature of the measurements which were taken from the middle point of the surface of the primary facade which faces the cavity (1.45m level) is 8.84 °C. And, while the average temperature of the measurements which were taken from the middle point of the surface of the secondary facade which faces the cavity is 4.60 °C, the average temperature of the measurements which were taken from the middle point of the surface of the secondary facade which faces the outdoor environment is 3.56 °C (Figure 5.32c).



a) Low flow rate



b) Medium flow rate



c) High flow rate

Figure 5.32 Variation of temperature from indoor environment to the outdoor environment for the 32.5 cm cavity width condition (Exp7, Exp7 and Exp9)

With the increase in the velocity of the liquid which enters the cavity, for all of these three experiments in the cavity, it is observed that there are decreases in the

surface temperatures of the primary and secondary facades in all of the experiments. Due to the heat transfer which is from the interior environment to the cavity, temperatures along the cavity and in its air flow increase on both of the surfaces (Table 1). This increase is more visible in the primary facade (Figure 5.30, 5.31, 5.32)

### **5.3.2. Numerical Study**

By taking a longitudinal section along the channel height and depth in the middle of the width of the double skin air cavity, the numerical results in this longitudinal section were examined (Figure 5.29). A line route which lies along the cavity depth and at the height of 1.45 m, the middle point of this longitudinal section, was determined. Determining two horizontal line routes 0.65 m above and below this line route, the temperature changes on these line routes were compared with the experimental results. While determining these horizontal line routes on this longitudinal section, in order to observe the stable condition more clearly, it was given attention that these horizontal line routes are as far as possible from the air entrance and exit directions. Velocity profiles have been acquired numerically for the different heights of the section which has been placed in the middle zone of the cavity and the numerical velocity distribution in the 260 cm above of the floor was compared with the experimental measurement results. Calculations were conducted in the ANSYS-FLUENT environment, which is based on the approach of the control volumes, by forming the three dimensional numerical model of the geometry in the ANSYS environment (ANSYS, 2009.) Accordingly, for the numerical solution, these were accepted:

- The flow is steady, fully turbulent and three dimensional.
- In the numerical solution, the approach of realizable k-epsilon turbulence model was used.
- In the solution of the governing equations, SIMPLE solution algorithm was applied.
- In the separation of the term of pressure, Standard method was used,
- For the other transport equations, Second Order Upwind separation scheme was applied.

The governing equations in the Case 2 were exactly reused, only the y-momentum equation was redefined like below:

$$\frac{\partial}{\partial x}(\rho uv) + \frac{\partial}{\partial y}(\rho vv) + \frac{\partial}{\partial z}(\rho wv) = -\frac{\partial p}{\partial y} + (\mu + \mu_t) \left[ \frac{\partial^2 v}{\partial x^2} + \frac{\partial^2 v}{\partial y^2} + \frac{\partial^2 v}{\partial z^2} \right] \quad (5.17)$$

In the model, there are 2473800 mesh elements in the hexahedra type. It has been observed that while the minimum mesh volume is 1.305582e-08 m<sup>3</sup>, the maximum mesh volume is 1.646515e-06 m<sup>3</sup>. The total volume is 1.015000e+00 m<sup>3</sup>'tür. In order to analyse the changes which occurred where the air entrance and exit vents are located more precisely, the number of meshes in these zones were increased (Figure 5.33.) It has also been observed that the convergence criterion was approximately at 10<sup>-5</sup> levels in all of the conducted analyses.

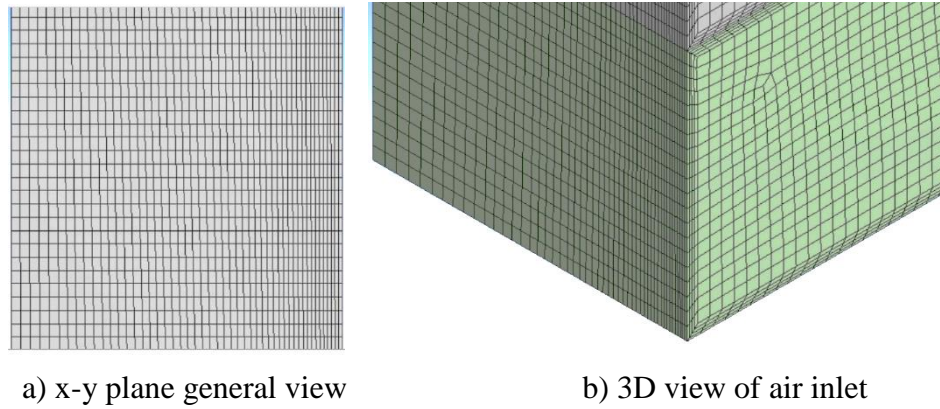


Figure 5.33. Grid configurations

### 5.3.3. Numerical Results

Depending on the parameters which are given in Table 5.7, the numerical studies were conducted. In the further chapters in order, firstly by comparing the velocity and temperature values which were acquired from the experimental measurements with the numerical results, validation was conducted. Then, the distributions of velocity in the cavity were examined and streamlines for different working conditions were obtained. And later, the dimensionless heat transfer correlations which were acquired from these results were discussed in the end.



### **5.3.3.1. Velocity changes on the horizontal lines which are in the middle of the channel: cavity 25 cm**

As a result of the study which was conducted under the condition that the cavity depth was 25 cm, velocity changes at various lengths on the longitudinal section were compared with the velocity values at 2.6 m height of the cavity which was experimentally measured (Figures 5.34-5.36.) It is seen that the measurements which were taken at the 2.60 m height of the cavity in the experimental setup along the cavity depth on the horizontal line are very coherent with the results of the simulations. Depending on the surface temperature, it is observed that there are more effects of the buoyancy in the section which is close to the interior glass surface, whereas there are less effects of the buoyancy in the section which is close to the exterior glass surface. At low velocities, there are more effects of buoyancy and that shows the effect of natural convection. However, here the actual driving force comes from the forced flow. When we look at all of the models which have low, mid and high flow rates, it is seen that the velocity values increase as it gets closer to the interior glass surface. Forced flow, which is oriented through the cavity height right after the cavity entrance provides that the air is lifted mostly by PF with the effect of the 90° turn here and creates reverse flows in the SF side. Also, we see that as we go further from the section (0.125 m) which is close to the middle point of the cavity depth, the velocity values decrease and forced flows appear at the cavity height of 0.8 m. As the flow continues above to its situation of fully developed flow, it gets affected by the section of the cavity exit. In this way, for all of the working conditions, air flow is in the entrance region hydrodynamically and thermally. In the turbulent flow, fully developed flow hydrodynamically and thermally begins after approximately 10 times of the hydrolic diameter. In the conducted experimental studies, only for the first condition (that the cavity depth is 25 cm) the beginning of the fully developed flow appears in the section which is close to the exit zone and due to the exiting effect, its flow form changes. Therefore, in all of the studies which were conducted here, the experimental and numerical analyses of the flow conditions in the entrance region were conducted.

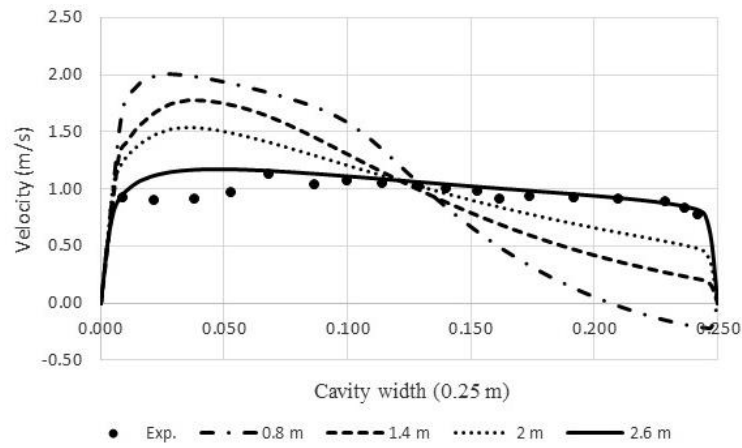


Figure 5.34. Velocity profiles and experimental measurement results at different cavity heights (Cavity: 25 cm, low flow)

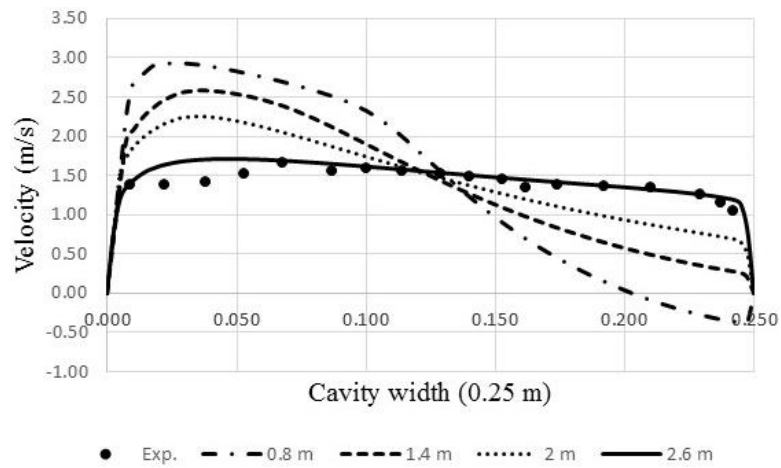


Figure 5.35. Velocity profiles and experimental measurement results at different cavity heights (Cavity: 25 cm, medium flow)

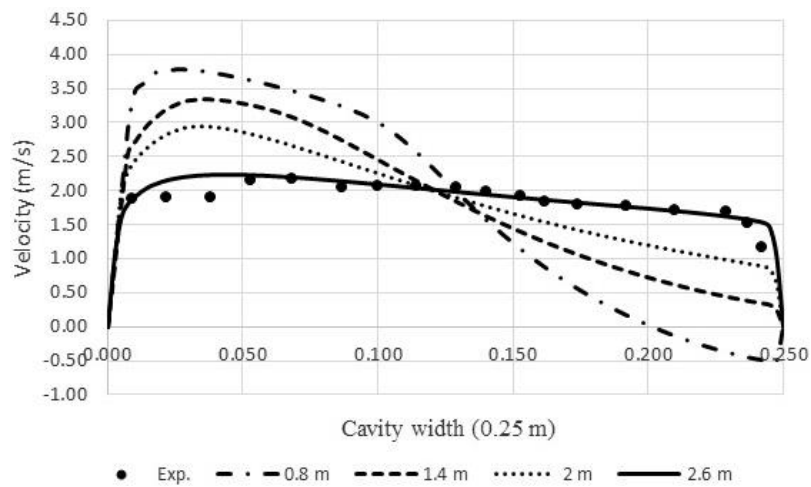


Figure 5.36. Velocity profiles and experimental measurement results at different cavity heights (Cavity: 25 cm, high flow)

### 5.3.3.2. Velocity changes on the horizontal lines which are in the middle of the channel:: Caviy 32.5 cm

As a result of the study which was conducted under the condition that the cavity depth was 32.5 cm, velocity changes at various lengths on the longitudinal section were compared with the velocity values at 2.6 m height of the cavity which was experimentally measured (Figures 5.37-5.39.) When we look at all of the models which have low, mid and high flow rates, it is seen that the velocity values increase as it gets closer to the interior glass surface. As we go further from the section which is close to the middle point of the cavity depth, the velocity values decrease. At 0.8 and 1.4 m heights of the cavity in the simulation results, it is observed that there are reverse flows. Also, it is seen that in the experimental setup at 2.60 m height of the cavity the measurements which were taken along the cavity depth are coherent with the simulation results.

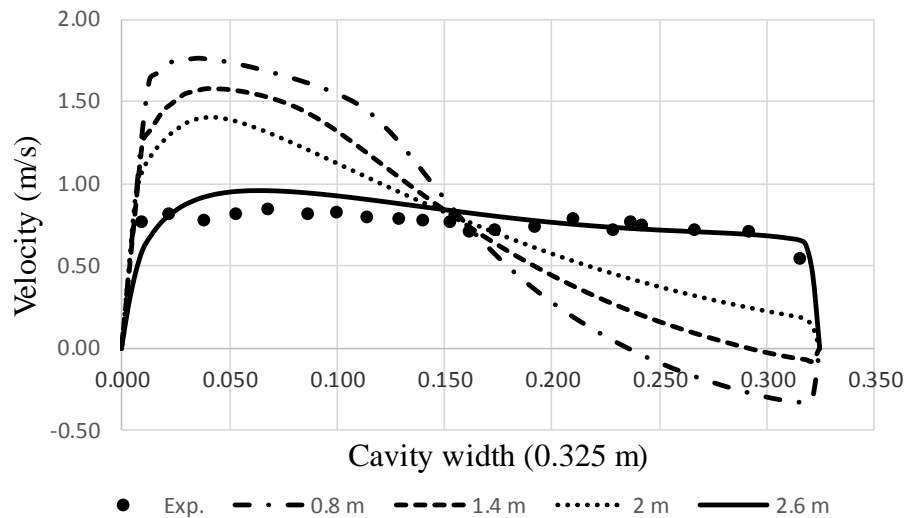


Figure 5.37. Velocity profiles and experimental measurement results at different cavity heights (Cavity: 32.5 cm, low flow)

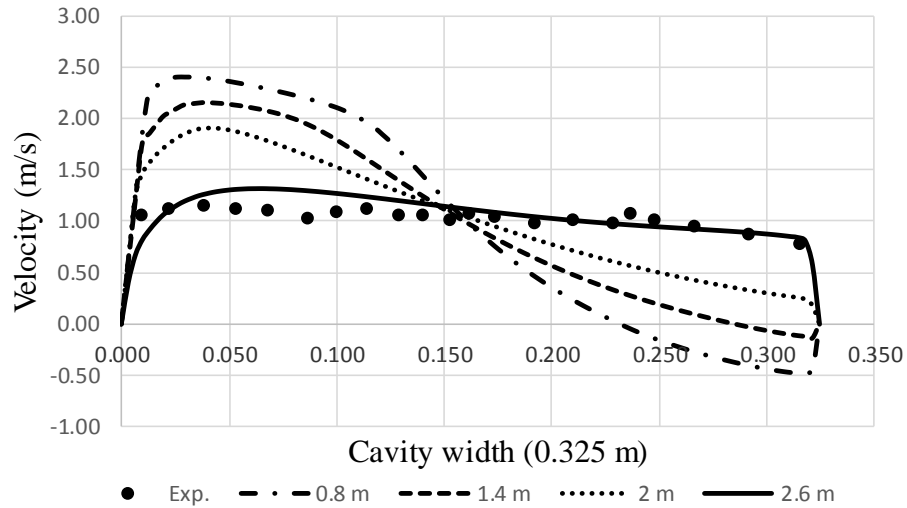


Figure 5.38. Velocity profiles and experimental measurement results at different cavity heights (Cavity: 32.5 cm, medium flow)

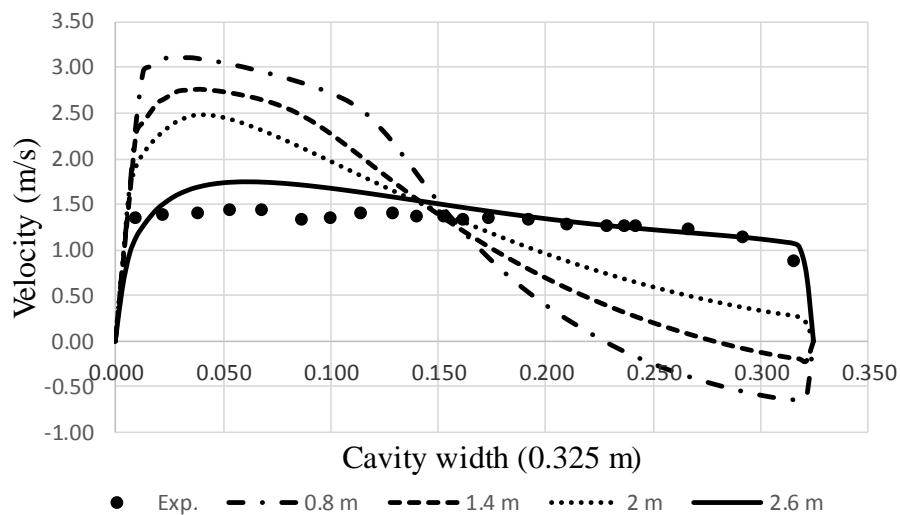


Figure 5.39. Velocity profiles and experimental measurement results at different cavity heights (Cavity: 32.5 cm, high flow)

### 5.3.3.3. Velocity changes on the horizontal lines which are in the middle of the channel: Cavity 40 cm

Velocity changes which are on different heights along the cavity depth were examined for the condition that the cavity depth is 40 cm. Simulation results were used to draw the velocity profiles at different heights of the cavity and the velocity simulation results at 2.6 m of the cavity were compared with the experimental velocity measurements (Figure 5.40-42.) When we look at all of the models which have low,

medium and high flow rates, here it is also seen that the velocity values increase as it gets closer to the interior glass surface. It is observed that as we go further from the section which is close to the middle point of the cavity depth to the exterior glass surface, the velocity values decrease and reverse flows appear in the simulation results at 0.8 and 1.4 m height of the cavity. With the measurements which were taken along the cavity depth on the horizontal line at 2.60 m height of the cavity in the experimental setup, the simulation results are seen in the figure. It has been observed that from the middle point of the cavity depth, measurement results are more coherent with the simulation results. Furthermore, it is observed in the simulation results that flow is separated from the PF surface with the existence of the exit effect.

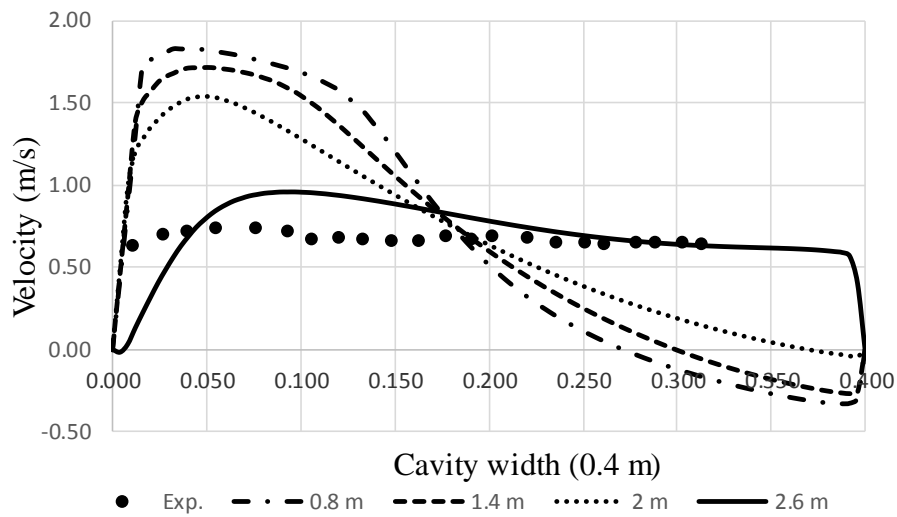


Figure 5.40. Velocity profiles and experimental measurement results at different cavity heights (Cavity: 40 cm, low flow)

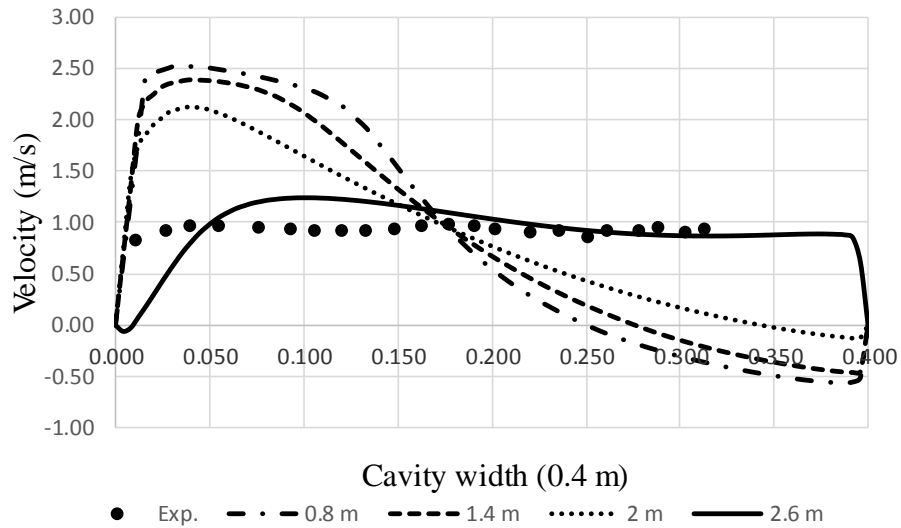


Figure 5.41. Velocity profiles and experimental measurement results at different cavity heights (Cavity: 40 cm, medium flow)

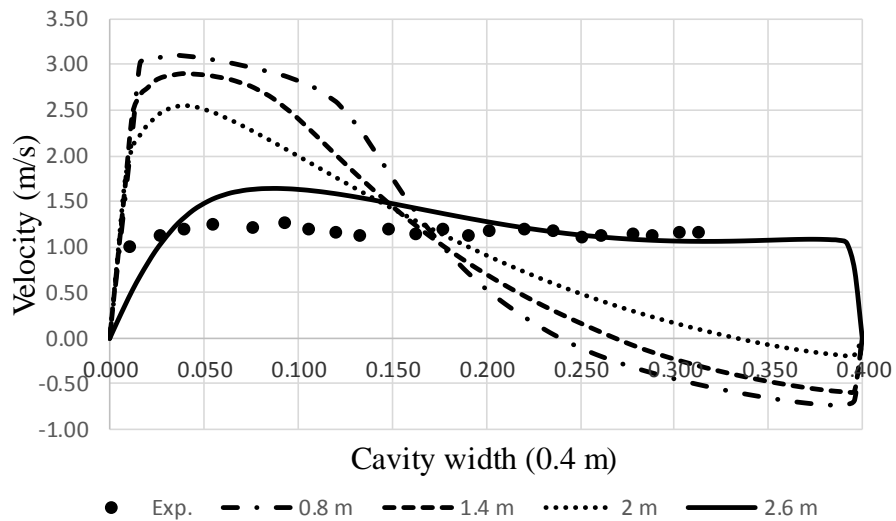


Figure 5.42. Velocity profiles and experimental measurement results at different cavity heights (Cavity: 40 cm, high flow)

#### 5.3.3.4. Temperature changes on the top horizontal line which is located in the middle of the channel

In Figures 5.43-5.45, for different working conditions, temperature changes on the flow and glass surfaces (primary and secondary facade surfaces) are examined. The surface temperature of the primary facade is higher than the air entrance temperature and the surface temperature of the secondary facade in all models. For the air temperature in the cavity, measurements which were taken with thermocouples at two

levels were compared with the simulation results. While on the exterior glass surface where the air entrance vent is placed in the low-flow-rate models numbered 1, 4 and 7 a decrease in the temperature values is observed, in the models numbered 2, 5 and 8 which have mid flow rate and high-flow-rate models numbered 3, 6 and 9 there occurs a slight increase of the temperature value on the exterior glass surface and it is seen that towards the interior glass surface there are temperature increases. When measurement and simulation results are compared, it is observed that model and measurement results generally behave coherently with each other. Also, while there is a difference at levels of 0.3-0.5 °C in the cavity air temperature for the measurements and simulations at 25 cm cavity depth, for the cavity depths of 32.5 and 40 cm temperature differences at levels of 0.2-0.3 °C in the cavity air were observed.

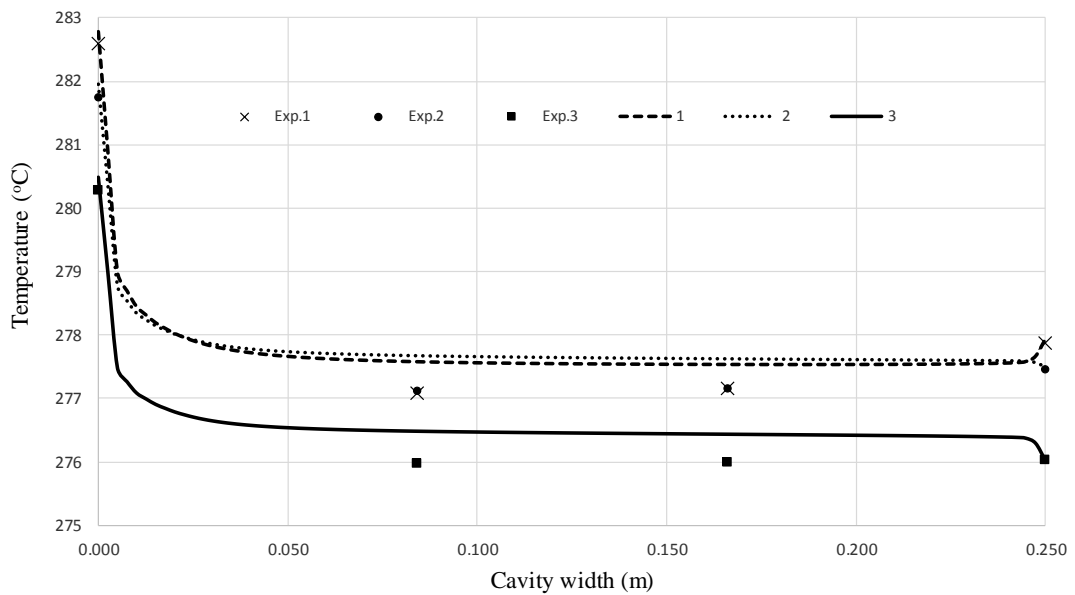


Figure 5.43. Numerical temperature profiles and their comparison with the experimental results (Cavity: 25 cm, three different flow rates)

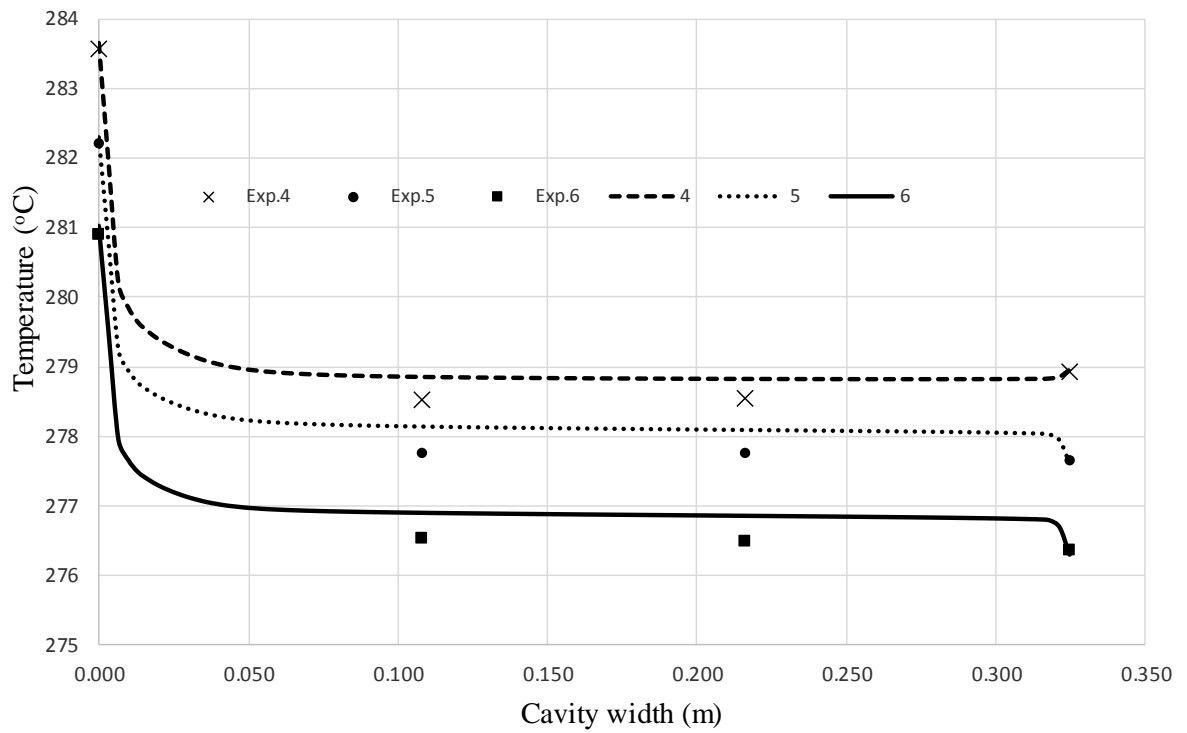


Figure 5.44. Numerical temperature profiles and their comparison with the experimental results (Cavity: 32.5 cm, three different flow rates)

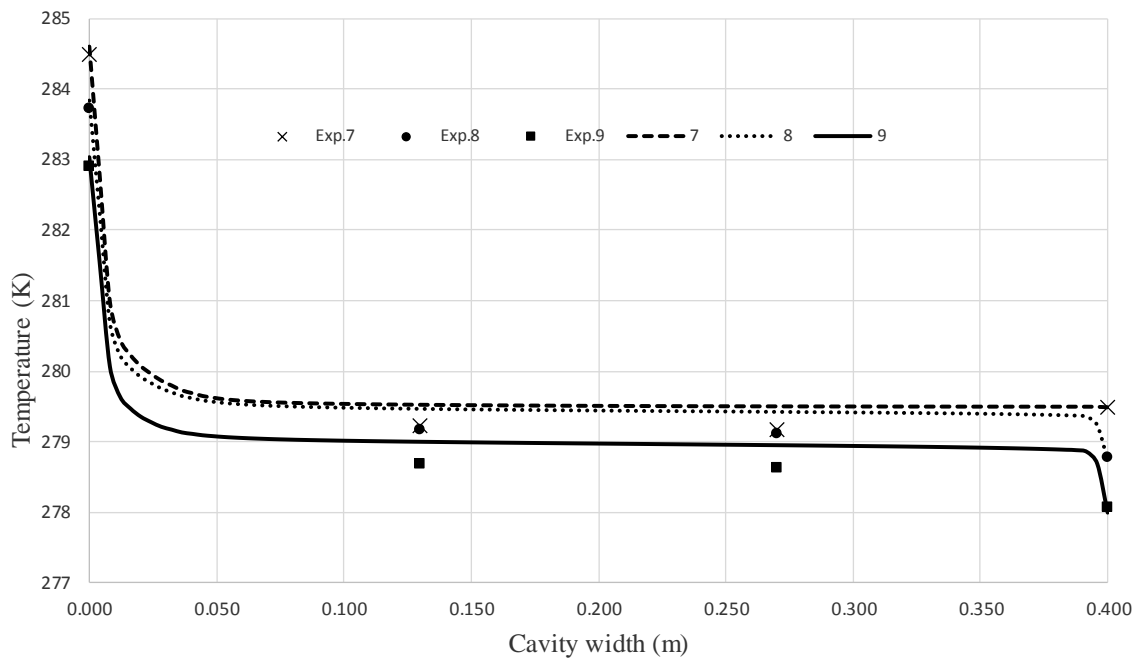


Figure 5.45. Numerical temperature profiles and their comparison with the experimental results (Cavity: 40 cm, three different flow rates)



### 5.3.3.5. Distributions of velocity on the vertical section in the middle of the channel: Cavity 25 cm

For the cavity depth of 25 cm, distribution of different velocity values on the longitudinal section is given in Figure 5.46. Since the interior surface temperature is high, velocities with a low effect of buoyancy are observed in the interior surface. As the velocity increases, the buoyancy loses its effect against the inertia forces. Due to the conditions of entrance and exit to the cavity, the flow mostly rises along the PF surface, maintains at lower values on the SF surface and reverse flows occur. This shows the importance of the design of air vent size in DSF. There are applications in which the flow is directed to the cavity in the entrance and this negative effect is reduced.

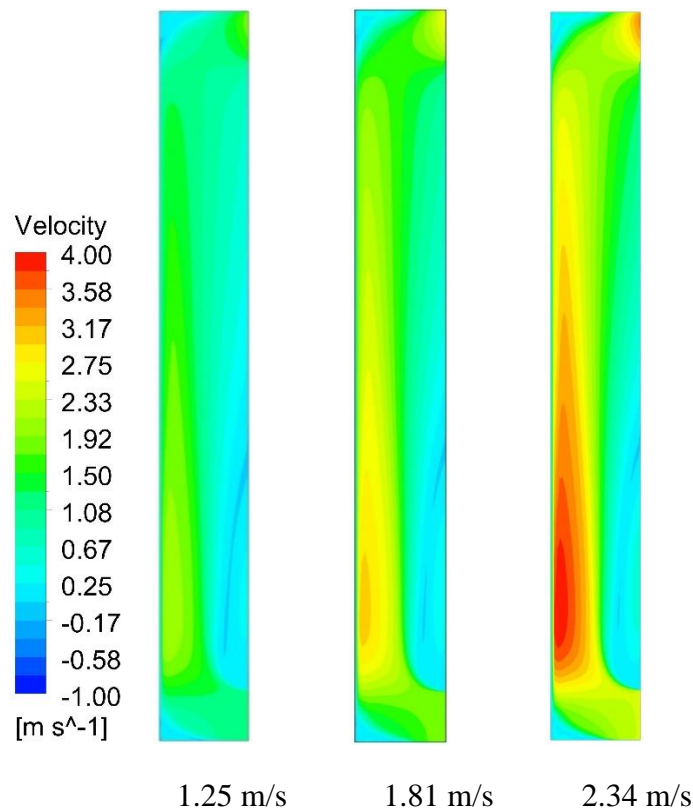


Figure 5.46. Distributions of velocity on the vertical section (Cavity: 25 cm)

### 5.3.3.6. Distributions of velocity on the vertical section in the middle of the channel: Cavity 32.5 cm

For the condition that the cavity depth is 32.5 cm, depending on different mass flow values, the distribution of the velocities in the longitudinal section which is placed in the middle of the channel is seen in Figure 5.47. In low velocity values, the region in the top section of the cavity with low velocity naturally spans a larger area comparing to the other parts which have relatively higher velocity. Here also the flow increases mostly along the PF.

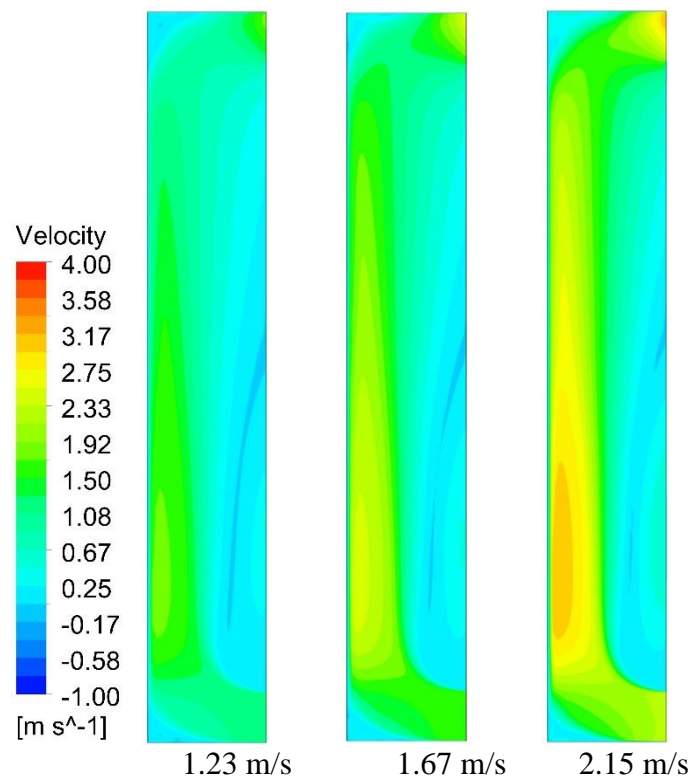


Figure 5.47. Velocity distributions in the vertical section: Cavity: 32.5 cm

### 5.3.3.7. Distributions of velocity on the vertical section in the middle of the channel: Cavity 40 cm

For the condition that the cavity depth is 40 cm, depending on different velocity values, the distribution of the velocities on the longitudinal section which is placed in the middle of the channel is seen in Figure 5.48. Due to mostly the conditions of entrance and exit to the cavity, and the condition of low mass flow rate and the

difference between the temperatures of the entrance of the air and the interior glass surface is relatively high, the flow reaches high velocity values in the zones which are close to the interior glass surface. This effect becomes more visible on the interior glass surface, especially close to its bottom (approximately 1/3 of the cavity height) with the effect of the air entrance vent and this similar effect is also seen on the exterior glass surface where air is swept close to the air exit vent.

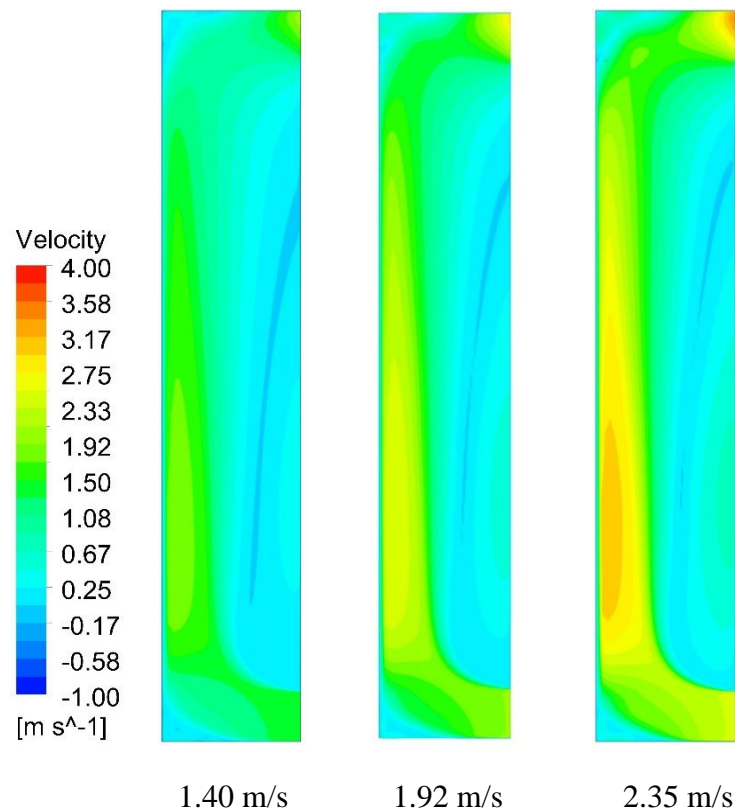


Figure 5.48. Velocity distributions on the vertical section: Cavity 40 cm

### 5.3.3.8. Velocity Streamlines in the vertical section in the middle of the channel: Cavity 25 cm

Streamline graphics which were acquired for the numerical studies in which the entrance to the cavity velocity values when the cavity depth is 25 cm respectively 1.25, 1.81 and 2.34 m/s are seen in Figure 5.49. Where the liquid is taken inside from the bottom vent, there occurs a circulation zone in the top section of the vent which is close to the exterior surface. In this circulation zone, negative velocity values occur. Removing this effect is important in terms of the design of the DSF. Therefore, it is also

important how to choose the appropriate flow rate as much as the design of the air inlet and outlet vent design.

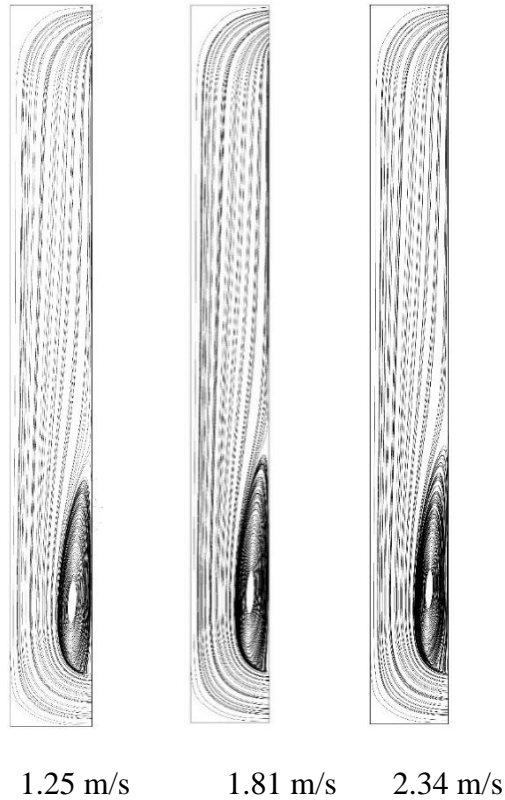


Figure 5.49. Streamlines in the velocity field through the DSF's cavity for different mass flow rates (Cavity: 25 cm)

#### **5.3.3.9. Velocity Streamlines in the vertical section in the middle of the channel: Cavity 32.5 cm**

When the cavity depth is 32.5 cm and accepting that the velocity values uniformly enter the cavity, streamline graphics which were acquired from the numerical studies for three different mass flow rate values are seen in Figure 5.50. Here there are three different entrance to the cavity velocity value were taken as 1.23, 1.67 and 2.15 m/s. Where the liquid is taken into the cavity through the bottom vent, there occurs a circulation zone in the top section of the vent which is close to the exterior surface (to the secondary facade.) This circulation zone takes the form of a larger loop as the width of the cavity increases. Reverse flows occur in this zone and reverse flow velocity values which occur in a larger zone increase in parallel to the cavity width.

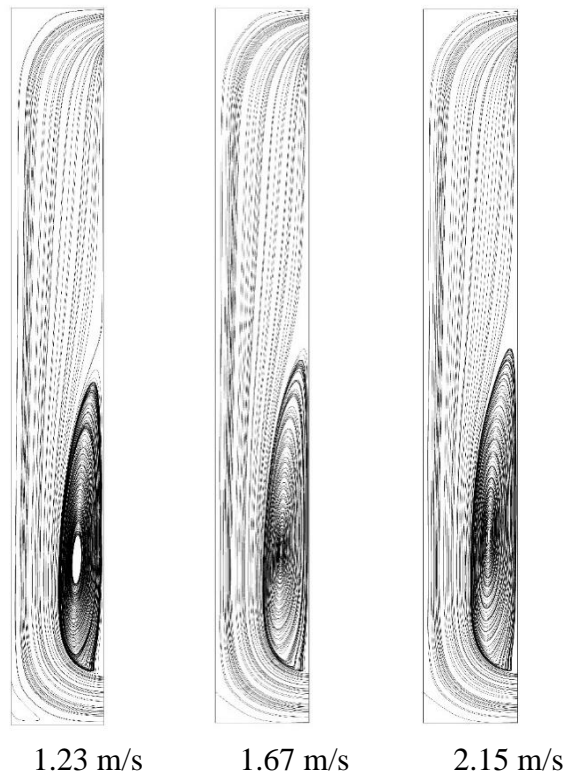


Figure 5.50. Streamlines in the velocity field through the DSF's cavity for different mass flow rates (Cavity: 32.5 cm)

#### **5.3.3.10. Velocity Streamlines in the vertical section in the middle of the channel: Cavity 40 cm**

When the cavity depth is 40 cm and accepting that the velocity values uniformly enter the cavity, streamline graphics which were acquired from the numerical studies for three different mass flow rate values which are respectively 1.40, 1.92 and 2.35 m/s are seen Figure 5.51. The circulation zone which occurs in the top section of the vent which is close to the exterior surface (to the secondary facade) where the liquid is taken into the cavity through the bottom vent here covers a larger area comparing to the other cavity depths. Also, as the width of the cavity increases, loops occur in the corners facing the air entrance and exit vents. As the velocity increases, this effect becomes more visible. Therefore, as it was emphasized before, in the DSF design, it is equally important that there should be a slight transition without sharp turns on the corners where these reverse flows occur with the effect of the cavity entrance and exit vent on the flow.

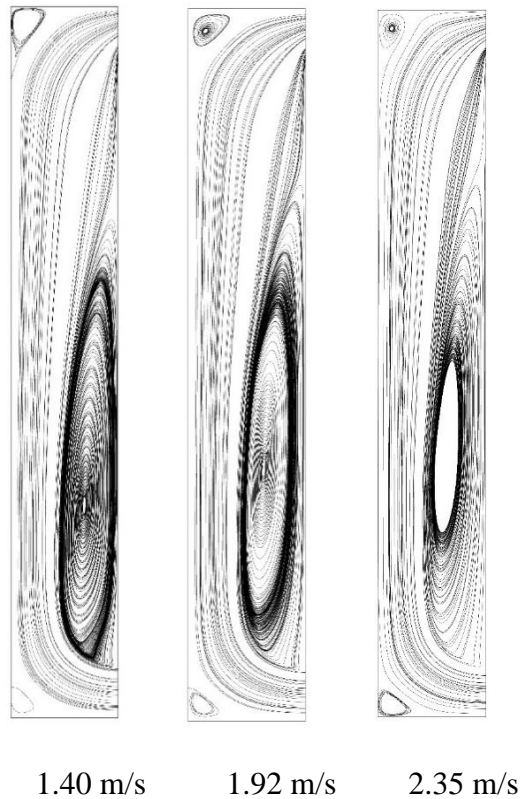


Figure 5.51. Streamlines in the velocity field through the DSF's cavity for different mass flow rates (Cavity:40 cm)

#### **5.3.3.11. The average pressure drop on the vertical section in the middle of the channel: Cavity 25 cm**

As it is seen from the velocity distributions in the cavity and streamlines, air entrance and exit vents have an important effect on the velocity field. However, sharp turns here cause visible pressure drops. This increases the required fan capacity and also the energy consumption. Also, it increases the possibility of appearance of voice and vibration as the material loses its time-dependent features. In the cavity depths of 25, 32.5 and 40 cm, pressure change curves along the cavity which were acquired for nine different numerical experiments are seen in Figures 5.52-5.54. Here as the cavity width increases, pressure drop decreases and depending on the increase of the velocity in the cavity, pressure drops increase.

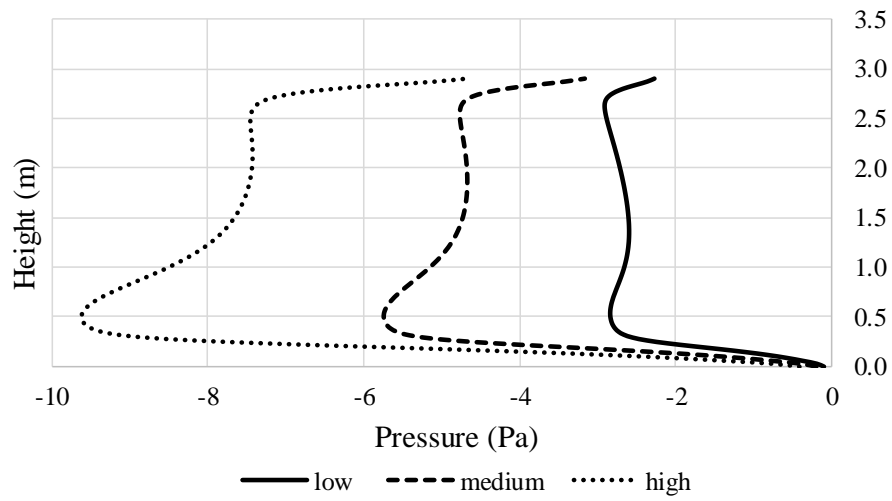


Figure 5.52. Pressure drops: cavity: 25 cm

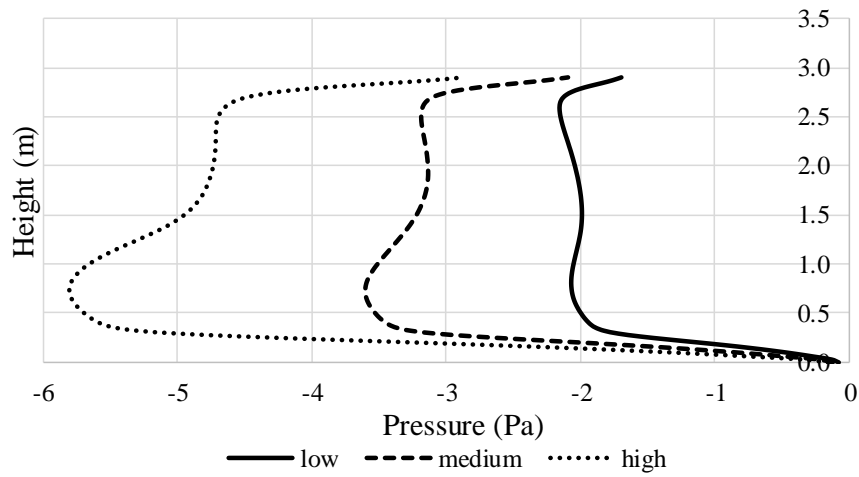


Figure 5.53. Pressure drop: Cavity :32.5

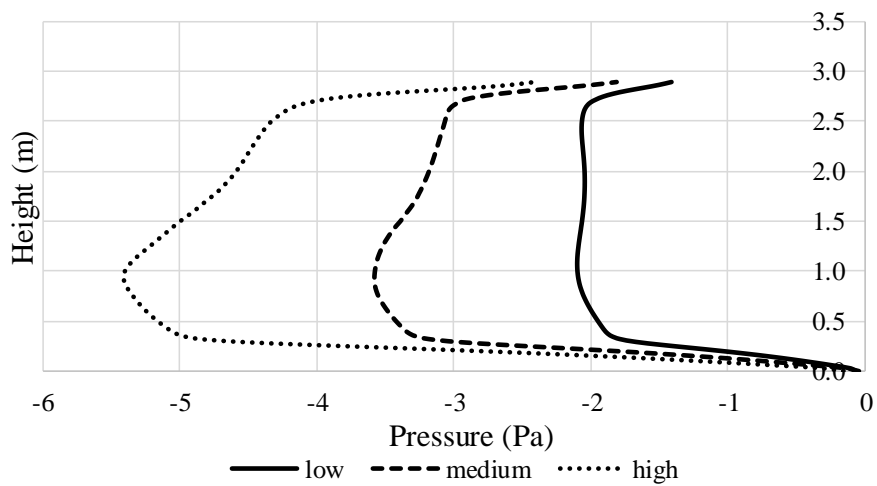


Figure 5.54. Pressure drop: Cavity :40 cm

### **5.3.3.12. Temperature distributions on the vertical section in the middle of the cavity: Cavity 25cm**

As it is seen in Figure 5.55, in the section which is close to the air exit vent there are higher temperature gradients. With the increase in the velocity, while the zone where the temperature gradients are located in the top region gets dense in the corner in the interior glass facade, it significantly decreases in the exterior glass facade where the exit vent is located. Because the liquid which comes with high velocities sweeps a larger area in the air exit vent and disposes. As there is relatively more difference between the surface temperature of the cavity and the liquid, it is observed that temperature gradients get dense as they are close to the surface of the interior glass facade. However, in the section which is close to the SF surface the temperatures of the liquid and surface temperatures are very close to each other and the temperature change is more limited. It is seen that temperature gradients increase with the velocity increase in the top section of the air exit vent which is located in the exterior glass facade. In low velocities, these temperature gradients are dense in the corner which faces the air exit vent and on the ceiling. In high flow rate, as the heat convection coefficient value increases, heat transfer from the PF surface to the cavity liquid and this shows how much important the selection of the flow rate in the applications in which the flow is provided with using fan is. Here in parallel to this relatively high entrance velocity, reaching to higher velocity values as the flow mostly proceeds through the PF surface after entering the entrance vent also has increased the heat transfer. This shows the importance of the cavity entrance design in the DSF. There are applications in which the flow is directed to the cavity in the entrance and this negative effect is reduced. Along the cavity height in the primary facade, in parallel to the occurring heat transfer, while there is more temperature change, it was observed that this temperature change is smaller in the secondary facade. This happens as the temperature difference between the cavity air entrance temperature value and the average surface temperature of the secondary facade is closer. For instance, in the Figure in the model in which there is the liquid which enters the cavity with the velocity of 1.25 m/s, while the average surface temperature of the primary facade is 8.04 °C, the average surface temperature of the secondary facade is 4.31 °C. It was observed that the entrance temperature of the air which enters the cavity was 4.40 °C, which is a close value to the surface temperature of the secondary facade (Table 5.8.)



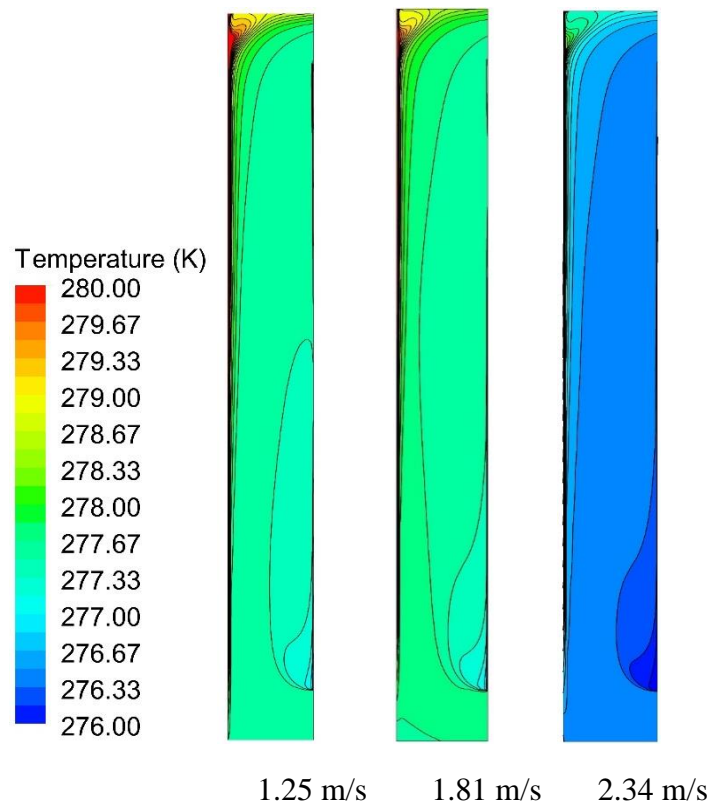


Figure 5.55. Temperature distributions through the DSF's cavity for different mass flow rates (Cavity: 25 cm)

### 5.3.3.13. Temperature distributions on the vertical section in the middle of the cavity: Cavity 32.5 cm

Two of the parameters that affect the heat transfer are surface temperature and convection coefficient. Heat convection coefficient increases with an increase in the velocity of the fluid flowing over a solid surface. Thus, temperature gradients tend to increase in parallel with heat transfer on primary facade (PF) especially at the top part of the cavity. (Figure 5.56). On the other hand, slight temperature gradients can be seen on the secondary facade above the air inlet, then they decrease. The average temperature of secondary facade is slightly lower than the air inlet temperatures while the average surface temperature of primary facade is prominently higher than the air inlet temperatures. Therefore, heat transfer occurs from the primary facade to the cavity air while heat transfer occurs from the cavity air to the secondary facade.

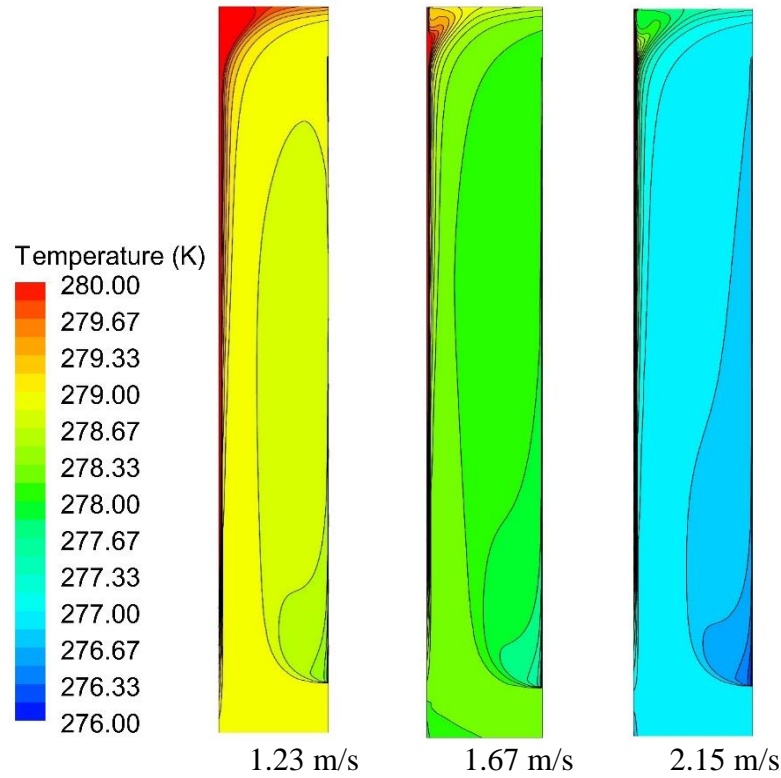


Figure 5.56. Temperature distributions through the DSF's cavity for different mass flow rates (Cavity: 32.5 cm)

#### 5.3.3.14. Temperature distributions on the vertical section in the middle of the cavity: Cavity 40 cm

As observed in Figure 5.57, high temperature gradients occur on inner glass surface and near to the air outlet. The fluid coming with a high velocity sweeps the fluid in a wider area near to the air outlet and evacuate the fluid to the outside from the cavity. Therefore, with velocity increase, the temperature gradients area in the top of the cavity concentrated in the corner side of the primary facade while it decreases in secondary facade near to the air outlet. There is a greater energy exchange in the cavity air at high velocities. Thus, temperature gradients are more explicit in a wide area of the cavity section. A small change occurs over a wide area in air temperature at high velocities.

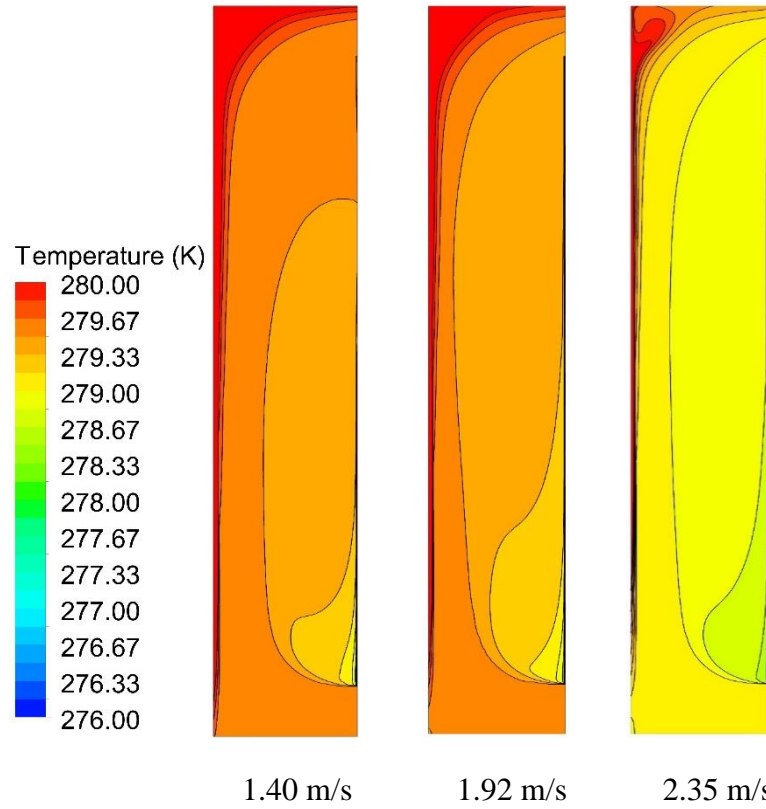


Figure 5.57. Temperature distributions through the DSF's cavity for different mass flow rates (Cavity: 40 cm)

The air inlet temperatures and air inlet velocities from the experimental measurements are given in Table 5.8. Air inlet temperatures and secondary facade surface temperatures are quite close to each other. Considering the Experiment 1, while air inlet temperature is 4.40 °C, the average temperature of the measurements which were taken from the bottom point of the surface of the secondary facade facing to the cavity ( $T_{1,2avg}$ ) is 3.79 °C, the average temperature of the measurements which were taken from the middle point of the surface of the SF ( $T_{3,4avg}$ ) is 4.41 °C, the average temperature of the measurements which were taken from the top point of the surface of the SF ( $T_{5,6avg}$ ) is 4.73. While the average temperature of the measurements which were taken from the bottom of the surface of the primary facade which faces the cavity (PFOG) ( $T_{1,2avg}$ ) is 6.28 °C, the average temperature of the measurements which were taken from the middle point of the surface of the PF ( $T_{3,4avg}$ ) 8.41 °C, the average temperature of the measurements which were taken from the top point of the surface of the PF ( $T_{5,6avg}$ ) is 9.45. The average temperature of secondary facade is lower than the air inlet temperatures while the average surface temperature of primary facade is higher than the air inlet temperatures. Therefore, heat transfer occurs from the primary facade to the cavity air while heat transfer occurs from the cavity air to the secondary facade.

The air taken from the air inlet to the cavity at high velocities is vented quickly from the air outlet on the top surface of the secondary facade. Thus, the temperature values have not increased enough. In contrast, higher temperature differences are observed between the air inlet and air outlet at low velocities. There is more heat transfer at low velocities. For instance, considering the Experiment 1 and 3, which shows low flow rate and high flow rate respectively (1.250 m/s and 2.340 m/s) with the cavity depth of 25 cm, it can be seen that while the temperature difference between the air inlet and outlet is 0.27 K at low flow rates, while the temperature difference between the air inlet and outlet is 0.12 K. Temperature variation and heat transfer in models decrease with velocity increase. Considering the Experiment 9, which has 2.35 m/s air inlet velocity with the cavity depth of 40 cm, the average temperature of primary facade (PF) is 8.59 °C while the average temperature of secondary facade is 4.76 °C. Moreover, considering Experiment 3, which has 2.34 m/s air inlet velocity similar with Experiment 9 except the cavity depth, while the average temperature of primary facade 6.04 °C, the average temperature of secondary facade is 2.58 °C.

In all experiments, mass and energy balance is controlled and it is observed that they are conserved in each experiment. Considering the Experiment 1, while the air mass flow entering to the cavity is 0.4420498 kg in a second, it is 0.44204962 kg in the air outlet (In Table 5.8 and 5.9). The equality of entering and releasing air is acceptable level and mass and energy are conserved. The difference between air outlet and air inlet shows the energy exchange in fluid. While heat transfer from primary facade (PF) is shown as wall\_inside, it is shown as wall\_outside in secondary facade. Therefore, total energy balance is provided (Table 5.9)

Table 5.9. CFD outputs of heat and mass transfer rates for Experiment 1

Mass Flow Rate	(kg/s)
outflow	-0.44204962
velocity_inlet	0.4420498
Net	1.7881393e-07
Total Heat Transfer Rate	(w)
outflow	9045.5723
velocity_inlet	-9164.7666
wall_inside	119.90074
wall_izole	-0
wall_outside	-1.0167923
Net	-0.31038666

Obtained results from the nine numerical experiments were shown in Table 5.10. In Table 5.10, obtained results according to the boundary condition defined in simulations were observed for each condition given in Table 5.8. The experiment numbers were given in the first column and in the second column the average temperature of the air in the air outlet section of the cavity was given in Kelvin (K). Heat transfers between primary and secondary facade and the air energy change of the cavity were given in the next four columns showing the energy balance of cavity. Energy balance was provided for each case. Pressure drop in the cavity are shown in subsequent columns. Pressure values in air inlets are high-order in each of the high flow cavity depth models and the pressure increase with velocity increase. The pressure at the outlet vent is equal to atmospheric pressure. In the last column, entering and releasing mass flow rates to the cavity is given and it is observed that mass is conserved in each condition.

Table 5.10. CFD outputs and energy/mass balance

Exp.	K	Q (W)				Pascal	m-inlet (kg/s)		
	T <sub>outlet</sub>	PF	SF	Δ <sub>air</sub>	ΔE	ΔP	m <sub>i</sub>	m <sub>o</sub>	Δ
1	277.82	119.900	-1.017	118.573	-0.310	1.753	0.44204980	0.44204962	1.788E-07
2	277.83	124.700	19.994	104.285	-0.421	3.152	0.64110140	0.64110191	-5.364E-07
3	276.62	142.023	-30.802	110.551	-0.670	4.608	0.83308649	0.83308619	2.980E-07
4	279.06	94.339	-7.224	86.773	-0.342	1.878	0.43359959	0.43359985	-2.682E-07
5	278.30	98.098	-25.357	72.265	-0.477	2.635	0.59128022	0.59128016	5.960E-08
6	277.05	120.811	-29.322	90.900	-0.589	3.867	0.76466095	0.76466018	7.749E-07
7	279.73	100.283	-10.254	89.612	-0.418	1.937	0.49215615	0.49215606	8.941E-08
8	279.63	108.603	-26.712	81.446	-0.445	2.780	0.67640877	0.67640847	2.980E-07
9	279.14	116.771	-34.663	81.458	-0.650	3.565	0.83000046	0.83000070	-2.384E-07

The Nusselt number distributions at the hot surface along the cavity height are shown in Figures 5.58-5.60. The average Nusselt numbers increased with increasing Reynolds numbers and reached the maximum value at the top of the cavity. Because of the restricted heat transfer at the bottom of the cavity, the Nusselt numbers start from the minimum values; throughout the cavity, there is no large difference between the Nusselt values as there was for the Reynold numbers. As described before, heat transfer increase with high temperature changes slightly above from the air inlet. Therefore, firstly a sudden increase is shown in Nu numbers, then low difference is observed. Similar with air inlet, unsteady condition observed in air outlet and a sudden decrease

was observed in Nusselt numbers. Due to the flow was entry region along the cavity in all working conditions, the slope of temperature gradient on primary facade (PF) decrease along the cavity height. In paralel convection coefficient and Nu numbers decrease. While fluid was thermally fully developed towards to the end of cavity, (the condition of Nu constant) it released from the cavity. While it was observed for 25 cm cavity width that the Nu number stayed constant towards the end of the cavity, it was still fully entry region especially on the 40 cm cavity width and Nu number continue changing.

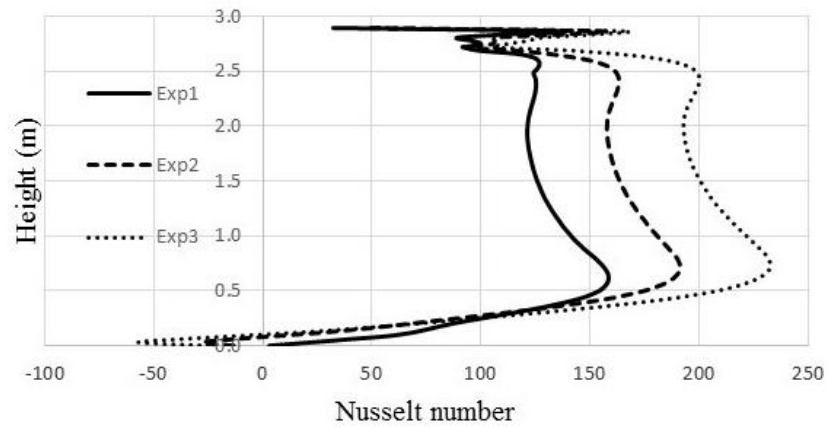


Figure 5.58. Variations of the Nusselt numbers at the hot surface along the cavity height for different flow rates (cavity width: 25 cm)

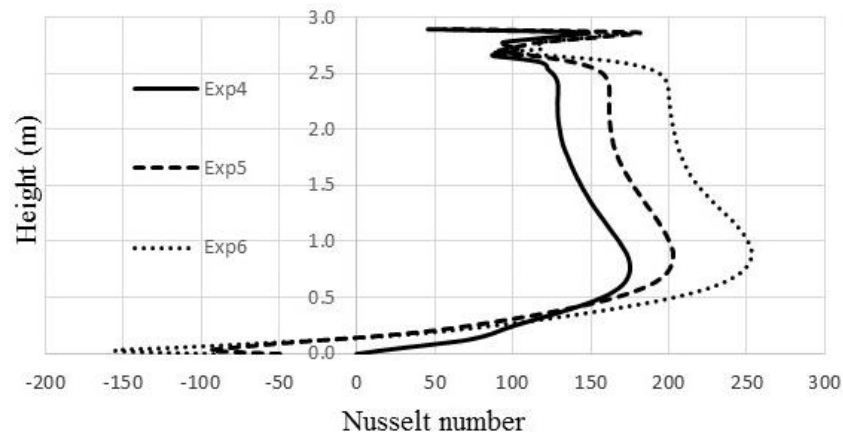


Figure 5.59. Variations of the Nusselt numbers at the hot surface along the cavity height for different flow rates (cavity width 32.5 cm)

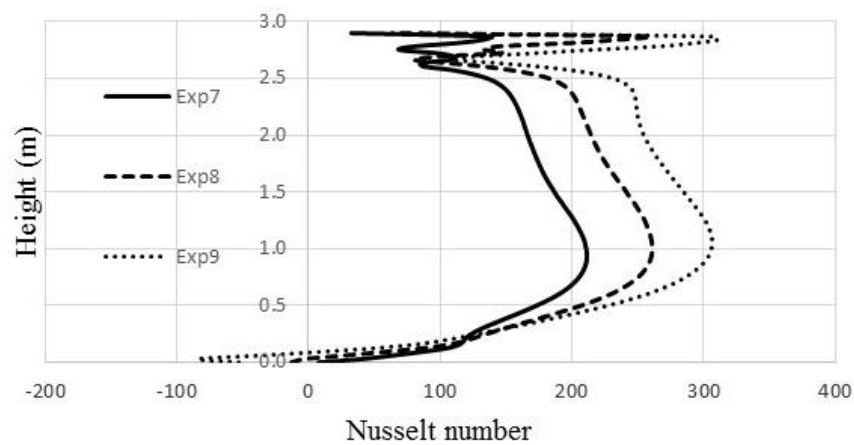


Figure 5.60. Variations of the Nusselt numbers at the hot surface along the cavity height for different flow rates (cavity width 40 cm)

The average Nusselt numbers for each experimental case were given in Table 5.11 for the PF surface of the cavity. There Nusselt numbers were acquired by calculating the average value for the 2 m portion of the cavity, which is from 0.5 m to 2.5 m without considering the values at the entrance and exit. The Nusselt number increases with inertia forces that are induced by the pressure differences created by an air fan system (or can be a wind driven effect). Flow is turbulent in the all numerical experiments as shown in Reynolds' numbers which is defined in Equation 5.1.

Velocity values were calculated for each situation separately (because inlet cross section area is not equal to the cavity's cross section area). The hydraulic diameter is described here:

$$D_h = 4A_c/P \quad (5.18)$$

where  $A_c$  is the cavity's cross section area, and  $P$  is the wetted perimeter of it. Nusselt number is also defined as;

$$Nu = hD_h/k_f \quad (5.19)$$

All thermophysical properties were selected using average air (for Re numbers) and film (for Nu numbers) temperatures in the cavity.

Table 5.11. Average Nusselt and Reynold numbers at the PF surface of the cavity for each experimental case

Exp. Number	#1	#2	#3	#4	#5	#6	#7	#8	#9
Re	30190	43720	56530	28150	38540	49650	31010	42520	52050
Nu	134.290	169.451	206.593	148.167	177.884	220.385	184.099	231.377	272.104

These non-dimensional variables are introduced in the governing equations, and the velocity and temperature variations in the cavity arise in terms of the Nusselt and Reynolds numbers. The results can be generalized by a correlation to predict the heat transfer rate using the Nusselt number for the double skin facade operating with the external air channal condition and a Reynolds number of approximately 25000 to 55000. Thus, the Nusselt number is a power function of the Reynolds number.



$$Nu = C \cdot Re^m \quad (5.20)$$

The Reynolds and Nusselt numbers given in Table 5.11 were used in a regression analysis to evaluate the indices C and m in Equation 1; these values were calculated to be 0.1168 and 0.6826 for cavity width 25 cm, experimental cases 1,2 and 3; 0.1184 and 0.695 for the cavity width 32.5 cm, experimental cases 4,5, and 6; and 0.0772 and 0.7518 for the cavity width 40 cm, experimental cases 7, 8 and 9, respectively.

$$Nu = 0.1168 \cdot Re^{0.6826} \quad (\text{cavity width: 25 cm, dimensionless length: 0.1}) \quad (5.21)$$

$$Nu = 0.1184 \cdot Re^{0.695} \quad (\text{cavity width: 32.5 cm dimensionless length: 0.13}) \quad (5.22)$$

$$Nu = 0.0772 \cdot Re^{0.7518} \quad (\text{cavity width: 40 cm dimensionless length: 0.16}) \quad (5.23)$$

The Nusselt and Reynolds numbers for each case were drawn with the power function, as shown in Figures 5.61-5.63. The coefficient of determination,  $R^2$ , was found to be nearly 1, and the data fit well.

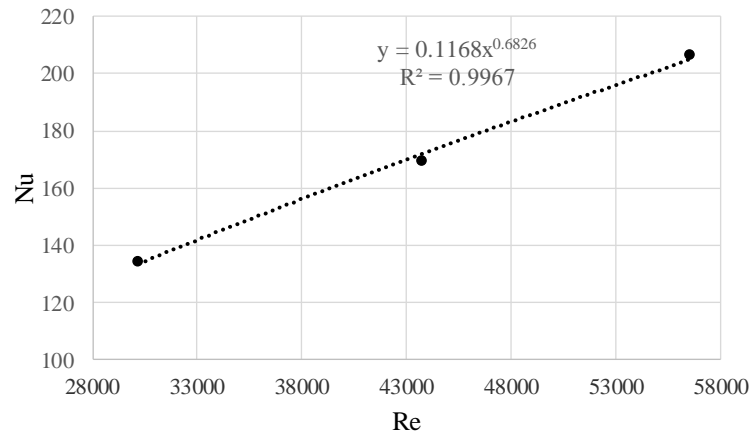


Figure 5.61. Nusselt numbers as a function of Reynolds numbers for the experimental cases 1, 2 and 3

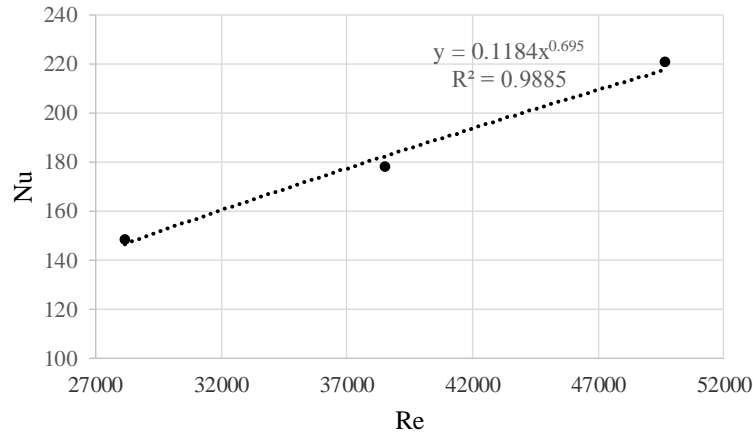


Figure 5.62. Nusselt numbers as a function of Reynolds numbers for the experimental cases 4, 5 and 6

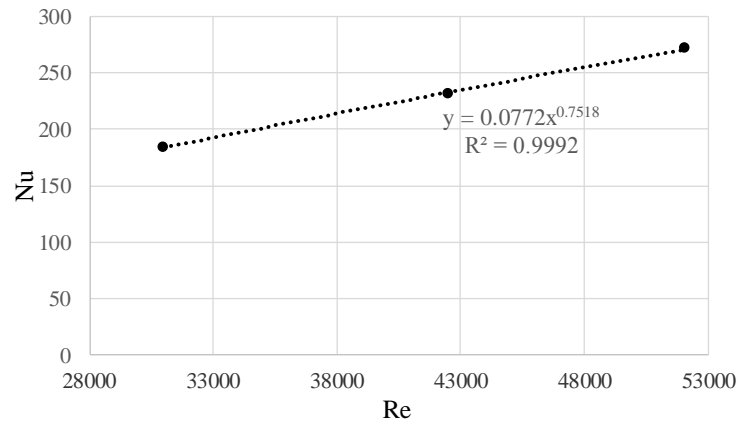


Figure 5.63. Nusselt numbers as a function of Reynolds numbers for the experimental cases 7, 8 and 9

By calculating the averages of the low, mid and high flow rates of the all of the cavity depths, for the Reynolds and Nusselt numbers regression analysis was conducted and a general equation was acquired (Figure). In this way, this equation also includes the value of characteristic length (W/H). Therefore, the correlation for the external air channel condition investigated in this study can be given as,

$$Nu = 0.1101 \cdot Re^{0.7035} \quad (5.24)$$

Here the coefficient of determination,  $R^2$ , was found to nearly 1, and the data fit well as shown in Figure 5.64.

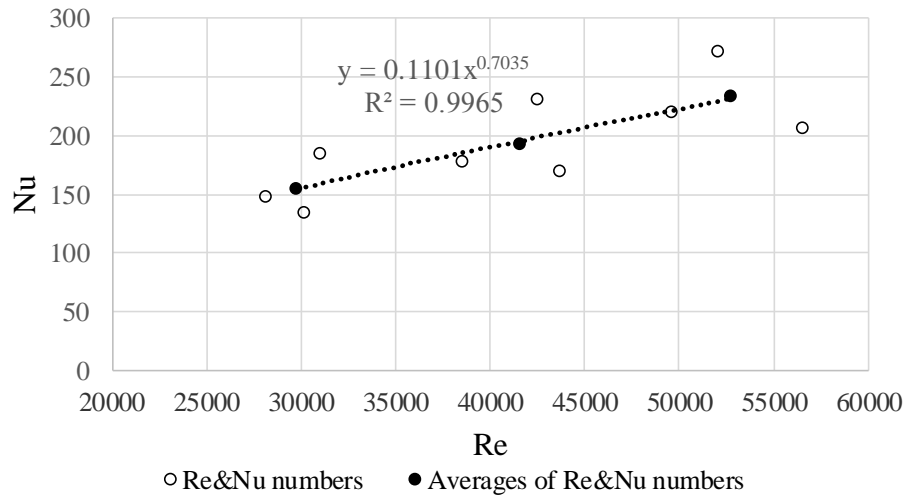


Figure 5.64. Nusselt numbers as a function of Reynold numbers for the averages of Reynolds and Nusselt numbers

Numerical and experimental studies were conducted to investigate the flow and heat transfer characteristics through the double skin facade with an external air flow mode in this study. A numerical model was developed to simulate the steady state forced convection inside a DSF cavity. The comparative results show that the current model can successfully predict the velocity field and temperature variations inside the domain. The following conclusions can be obtained from the current study:

- Flow through the DSF cavity were in the thermal and hydrodynamic entrance region for almost all numerical experiments.
- Design of cross section area of air inlet and outlet is significant. Because, high pressure drop and heat transfer values can be observed at this sections.
- A correlation was developed to predict the Nusselt numbers with the Reynolds number ranging from 28000 to 56000 for a double skin facade with an external airflow mode. Moreover, the correlations could be used for different characteristic length which was between 0.1 to 0.16.

#### **5.4. Case 4: Experimental and numerical investigation of forced convection in a double skin facade by using nodal network approach**

In this study, temperature change of the fluid in the cavity according to different cavity depths, different mass flow rates and different solar radiation values and temperature changes of the primary and secondary facades' surfaces which face the cavity have been examined by calculating along the height of the cavity. Average values of the room temperature, the exterior environment temperature, air entrance temperature, velocity and solar load are given in Table 5.12. These values reflect the average of the measurements which have been taken every 2 seconds depending on time after the whole system reaches the thermal balance. In the cavity, exterior air curtain air flow mode has been used. In other words, the air which is taken through the bottom outlet of the double skin facade system is disposed through the top outlet to the outside.

##### **5.4.1. Experimental inputs**

Figure 5.65 includes the schematic representation of a limited zone of the DSF, in which the experimental and numerical studies have been conducted. Here PF defines the primary double skinned glazed facade (primary facade,) SF the secondary single glazed facade (secondary facade,) and CA (cavity air) the air inside of the cavity.  $T_{air,in}$  shows the temperature of the air which enters the limited zone where the numerical analysis would be conducted, whereas  $T_{air,out}$  shows the temperature of the air which exists from this limited zone. In this way, depending on the heat transfer in the cavity, the air temperature in the cavity changes.  $T_{PF}$  represents the temperature of the surface of the primary facade which faces the cavity and  $T_{SF}$  represents the average temperature of the surface of the secondary facade which faces the cavity. Furthermore,  $T_{in}$  shows the average interior temperature of the experiment room, whereas  $T_{out}$  shows the average value of the exterior environment temperature.  $h_{in}$  defines the indoor heat transfer coefficient,  $h_{out}$  the outdoor heat transfer coefficient,  $h_{i,PF}$  the primary facade heat transfer coefficient and  $h_{i,SF}$  the secondary facade heat transfer coefficient.  $h_r$  shows the radiant heat transfer coefficient which is used to define the thermal radiation

on the facing surfaces of the primary and secondary facades. Also, the solar radiation which comes to the system is defined as  $I_{\text{solar}}$ .

Table 5.12. Experimental inputs

Exp.	$I_{\text{solar}}$ (W/m <sup>2</sup> )	$T_{\text{out}}$ (°C)	$T_{\text{in}}$ (°C)	$T_{\text{inlet}}$ (°C)	V (m/s)	y (m)	CA	PF	SF
10	195.9	15.51	15.03	9.36	0.711	0.80	9.60	12.07	13.55
						1.45		13.98	15.00
						2.10	10.11	14.12	15.61
11	197.26	14.63	14.78	11.08	0.990	0.80	11.11	12.68	13.55
						1.45		14.16	14.51
						2.10	11.43	14.11	15.20
12	188.09	12.24	14.64	10.95	1.255	0.80	10.91	12.25	12.62
						1.45		13.58	13.20
						2.10	11.15	13.48	14.00
13	365.4	27.36	24.97	17.02	0.769	0.80	18.38	22.55	26.43
						1.45		25.56	27.99
						2.10	19.16	25.22	28.40
14	362.82	25.50	25.18	18.38	1.028	0.80	19.23	22.40	25.04
						1.45		25.09	26.42
						2.10	19.77	24.62	26.97
15	364.64	22.32	25.19	18.23	1.316	0.80	18.95	21.69	23.68
						1.45		24.20	24.66
						2.10	19.37	23.65	25.37
16	176.65	16.37	15.27	10.29	1.086	0.80	10.56	12.27	13.74
						1.45		14.03	14.85
						2.10	10.97	14.04	14.91
17	174.08	15.28	15.40	11.69	1.621	0.80	11.67	12.82	13.64
						1.45		14.25	14.43
						2.10	11.90	14.14	14.48
18	180.75	13.82	15.37	11.89	2.108	0.80	11.88	12.82	13.34
						1.45		14.11	13.87
						2.10	12.05	13.91	13.98
19	330.75	26.23	23.61	17.06	1.405	0.80	18.39	20.91	24.53
						1.45		23.66	25.75
						2.10	18.84	23.20	25.29
20	331.54	24.23	23.72	16.88	1.694	0.80	17.84	20.02	22.82
						1.45		22.62	23.83
						2.10	18.20	22.10	23.58
21	334.86	22.14	23.66	17.38	2.124	0.80	18.15	19.90	22.13
						1.45		22.27	22.85
						2.10	18.39	21.65	22.66
22	170.908	14.62	26.67	8.30	1.134	0.80	8.73	12.44	12.31
						1.45		15.33	13.79
						2.10	9.32	15.72	14.03
23	176.484	13.30	26.55	9.32	1.704	0.80	9.47	12.16	11.74
						1.45		14.74	12.85
						2.10	9.83	14.97	13.09
24	178.677	11.88	26.28	9.85	2.156	0.80	9.85	12.07	11.51
						1.45		14.43	12.28
						2.10	10.11	14.51	12.55
25	196.831	16.39	28.28	10.13	0.690	0.80	10.47	15.11	14.88
						1.45		17.99	16.39
						2.10	11.14	18.48	16.92
26	192.406	15.44	28.26	11.41	0.908	0.80	11.54	15.09	14.51
						1.45		17.65	15.65
						2.10	11.98	17.94	16.19
27	196.831	12.90	28.00	11.38	1.170	0.80	11.46	14.44	13.52
						1.45		16.79	14.27
						2.10	11.80	16.98	14.92

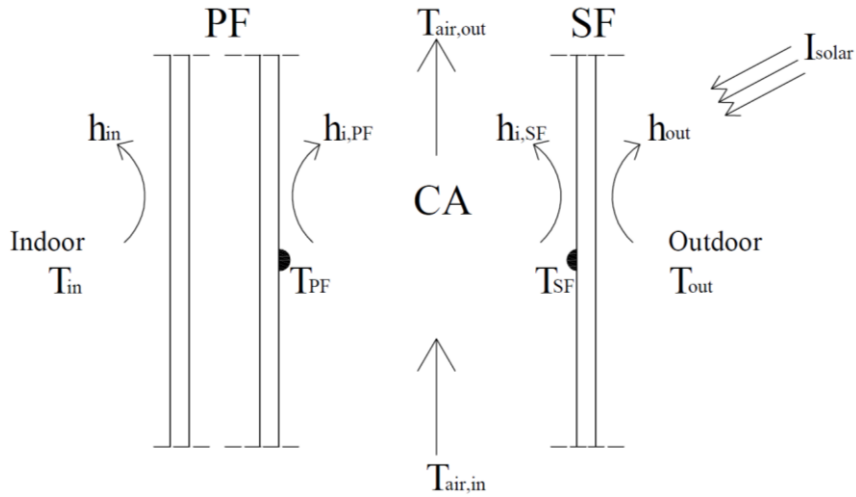


Figure 5.65. Schematic view of DSF

### 5.4.2. Nodal Network Approach

For the DSF in Figure 5.65, nodal energy analysis has been conducted like below. For this purpose, DSF has been examined by dividing it into three main zones. These are Primary Facade (PF), Secondary Facade (SF) and Cavity Air (CA.) In the related graphics, the cavity air temperature is shown as  $T_f$ , whereas the surface temperature of the primary facade is shown as  $T_{PF}$  and the secondary facade temperature is shown as  $T_{SF}$ . Energy balance is set up for these temperature nodes. These are:

#### Energy balance for Secondary Facade (SF)

$$I_{solar} \alpha_{SF} = U_{SF}(T_{SF} - T_{out}) + h_{i,SF}(T_{SF} - T_{air}) + h_r(T_{SF} - T_{PF}) \quad (5.25)$$

#### Energy balance for Cavity air (CA)

$$\dot{m}c_p \frac{dT_{air}}{dy} = h_{i,PF}L(T_{PF} - T_{air}) + h_{i,SF}L(T_{SF} - T_{air}) \quad (5.26)$$

#### Energy balance for Primary Facade (PF)

$$I_{solar} \tau_{SF} \alpha_{PF} = U_{PF}(T_{PF} - T_{in}) + h_{i,PF}(T_{PF} - T_{air}) + h_r(T_{PF} - T_{SF}) \quad (5.27)$$

With the solution of this equation set with three unknowns (Equations. 5.25, 5.26 and 5.27,) together with the change in the air temperature in the cavity, the temperature values of the interior surface of the DSF which faces the cavity can be calculated. For

this solution, firstly, interior surface temperatures of DSF depending on the cavity air temperature is shown in Equations 5.28 and 5.29 below (Eicker, 2003):

$$T_{SF}(y) = \frac{(B\alpha_{SF} + h_r\tau_{SF}\alpha_{PF})I_{solar} + h_rU_{PF}T_{in} + BU_{SF}T_{out}(Bh_{i,SF} + h_rh_{i,PF})T_f(y)}{AB - h_r^2} \quad (5.28)$$

$$T_{PF}(y) = \frac{(A\tau_{SF}\alpha_{PF} + h_r\alpha_{SF})I_{solar} + AU_{PF}T_{in} + h_rU_{SF}T_{out} + (Ah_{i,PF} + h_rh_{i,SF})T_f(y)}{AB - h_r^2} \quad (5.29)$$

Equation 5.28 and 5.29 are used to describe  $T_{PF}$  and  $T_{SF}$  as a function of cavity air temperature,  $T_f$ . In order to calculate  $T_{PF}$  and  $T_{SF}$  values along the height of the cavity, first, cavity air temperature, the change in  $T_f$  along the height of the cavity have been solved depending on the separation of the variables (Eicker, 2003). The result is given in Equation (5.30):

$$T_f(y) = (1 - e^{-Zy}) \frac{C_1T_{in} + C_2T_{out} + C_3I_{solar}}{C_4} + T_{inlet}e^{-Zy} \quad (5.30)$$

Here  $C_1$ ,  $C_2$ ,  $C_3$  and  $C_4$  values and  $Z$  parameter are defined like below (Eicker, 2003):

$$C_1 = \frac{h_{i,SF}h_rU_{PF} + h_{i,PF}AU_{PF}}{AB - h_r^2} \quad (5.31)$$

Here  $A$  and  $B$  are defined in Equation 5.8 and 5.9 like this below:

$$A = U_{SF} + h_{i,SF} + h_r \quad (5.32)$$

$$B = U_{PF} + h_{i,PF} + h_r \quad (5.33)$$

$$C_2 = \frac{h_{i,PF}h_rU_{SF} + h_{i,SF}BU_{SF}}{AB - h_r^2} \quad (5.34)$$

$$C_3 = \frac{h_{i,SF}h_r\tau_{SF}\alpha_{PF} + h_{i,SF}B\alpha_{SF} + h_{i,PF}h_r\alpha_{SF} + h_{i,PF}A\tau_{SF}\alpha_{PF}}{AB - h_r^2} \quad (5.35)$$

$$C_4 = h_{i,SF} + h_{i,PF} - \frac{(2h_{i,SF}h_{i,PF}h_r + h_{i,SF}^2 B + h_{i,PF}^2 A)}{AB - h_r^2} \quad (5.36)$$

$$Z = \frac{C_4}{c_p \dot{m}} \quad (5.37)$$

The coefficients  $C1$  to  $C4$  are related to the convective heat transfer coefficients and thermal radiation in the cavity, and the heat transfer coefficients to the indoor and to the outdoor surfaces. Solar radiation value and radiation features of both of these glasses are also used in calculating these values ( $C1$  to  $C4$ ). As these coefficients are temperature dependent,  $T_{PF}$ ,  $T_{SF}$  and  $T_f$  are determined iteratively.

Figure 5.66 includes the nodal representation of the DSF in Figure 5.65 and it is used in calculations of the equations which are given in Equations 5.25, 5.26 and 5.27.

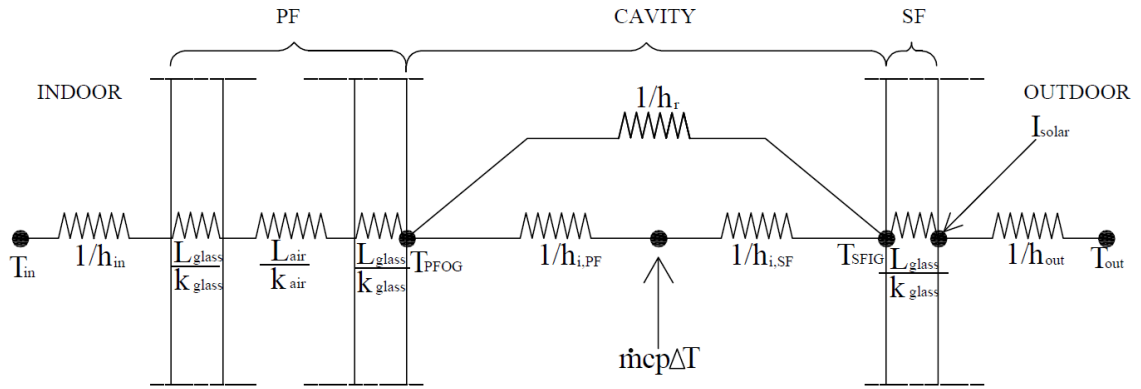


Figure 5.66. Nodal model of DSF

The parameters and thermophysical data which are used here are defined in detail respectively below.

### **SF**

The values which are given in Equation (5.25) are seen in Table 5.12. Here the transmissivity coefficient ( $\tau_{SF}$ ) are accepted as 0.71 and the absorption coefficient ( $\alpha_{SF}$ ) as 0.12 and the heat conductivity coefficient of the glass ( $k_{glass}$ ) is taken as 0.92W/m°C (Çengel, 2011). The value of outdoor convective heat transfer coefficient ( $h_{out}$ ) has been calculated depending on the velocity as it is given in Equation 5.38 (Liu and Harris,



2007) In this way, the value of the overall heat transfer coefficient of the secondary facade ( $U_{SF}$ ) has been calculated like below in Equation (5.37):

$$U_{SF} = \left( \frac{L}{k_{glass}} + \frac{1}{h_{out}} \right)^{-1} \quad (5.37)$$

$$h_{out} = 7.42 * V_{out} + 2.98 \quad (5.38)$$

In calculating the secondary facade convective heat transfer coefficient ( $h_{i,SF}$ ), the Equation 5.24 which we acquired as a result of the CFD analyses in Case 5.3. has been used:

$$Nu = 0.1101 * Re^{0.7035} \quad (5.24)$$

Reynolds number calculation is defined in Equation 5.25. In there the  $v$  value is defined for each condition depending on the temperature. Depending on the geometry, the  $D_h$  value has been calculated like below.

$$D_h = 4A_c/P \quad (5.18)$$

By using the mass flow rate which was experimentally measured, the average  $V$  value has been calculated by using equation. Here the change of the density of the air depending on the temperature has been considered.

$$\dot{m} = \rho AV \quad (5.39)$$

Nusselt number is calculated like:

$$Nu = \frac{h_{i,SF} D_h}{k_f} \quad (5.40)$$

Here the conductivity coefficient of the air has been defined for each condition depending on the  $k_f$  temperature. From here,  $h_{i,SF}$  value is calculated.

To calculate the radiative heat transfer coefficient, the following equation below is used (Saadon et al., 2016). Emissivity coefficient of both primary facade (PF) and secondary facade (SF) are equal to 0.9 (Cengel, 2011). Temperature values are given in K in Equation (5.41).

$$h_r = 4\sigma \left( \frac{T_{PF} + T_{SF}}{2} \right)^3 \left( \frac{1}{\frac{1}{\epsilon_{PF}} + \frac{1}{\epsilon_{PF}}} \right) \quad (5.41)$$

The values which have been acquired by using all these equations are given together with the other values below in Table 5.13.

### **Cavity**

In Equation 5.26, the equation of the cavity energy balance, the  $y$  direction shows the height of the cavity. Accordingly, the value of  $\frac{dT_{air}}{dy}$  gives the change of the air of the cavity along the height of the cavity.  $c_p$  is the specific heat of air and it has been defined depending on the change in the temperature of the air. Here the average convection coefficient for the interior surface of the cavity in the primary facade has been regarded as the equal with the other surface ( $h_{ipf}=h_{isf}=h_{ca}$ ). These values can be seen in Table 5.13.

### **PF**

The transmissivity coefficient ( $\tau_{PF}$ ) which has been expressed in the Equation 3 has been accepted as 0.83 and the value of the absorption coefficient ( $\alpha_{PF}$ ) as 0.22. For PF, the overall heat transfer coefficient is given in Equation 5.42.:

$$U_{PF} = \left[ \frac{1}{h_{in}} + \left( \frac{L}{k_{glass}} * 2 \right) + \frac{L_{air}}{k_{air}} \right]^{-1} \quad (5.42)$$

In the calculation of  $h_{in}$ , experimental data have been used. Accordingly, the energy balance for the double glass:

$$U_{DG}(T_{PFIG} - T_{PFOG}) = h_{in}(T_{PFIG} - T_{in}) \quad (5.43)$$

Here  $U_{DG}$  is the overall heat transfer coefficient of the double glass and it is calculated as in Equation 5.44:

$$U_{DG} = \left( 2 * \frac{L}{k_{glass}} + \frac{L_{air}}{k_{air}} \right) \quad (5.44)$$

Here the change of  $k_{air}$  depending on the temperature has been considered. All the numerical analysis mentioned above were done under steady state conditions. After validation explained below time dependent analysis was studied for two different climates of Turkey, namely İstanbul and İzmir.

### 5.4.3. Discussion and Results of Steady-State Study

In the calculation of the outdoor convective heat transfer coefficient,  $h_{out}$ , experimental data have been also used for the time dependent analysis. Accordingly, the average velocity of the air in the unit which simulates the exterior environment has been calculated approximately from the mass balance in the Equation (5.26). Here the change of the density of the air depending on the temperature has been considered and the value of  $h_{out}$  has been defined depending on the velocity in Equation (5.38) (Liu and Harris, 2007). All the calculated parameters explained above are shown in Table 5.13.

Table 5.13. Convection and radiation coefficients and related Nusselt and Reynolds numbers

Exp. #	$h_{out}$	$h_{in}$	$h_r$	Re	Nu	$h_{i,pr} \& h_{i,sf} \& h_{ca}$
	$W/m^2\text{°C}$			-	-	$W/m^2\text{°C}$
10	4.619	6.10	3.79	28389.9	149.4	6.42
11	5.262	3.83	4.41	39062.6	187.1	8.07
12	5.873	6.17	4.37	49587.8	221.3	9.54
13	4.753	1.34	5.01	28990.8	151.7	6.69
14	5.350	2.19	4.96	38575.5	185.4	8.21
15	6.013	3.97	4.89	49480.9	220.9	9.76
16	4.768	7.91	4.41	32458.6	164.2	9.37
17	5.649	7.03	4.41	48112.8	216.6	12.41
18	6.451	7.51	4.39	62524.1	260.4	14.93
19	5.293	1.98	4.90	40009.3	190.2	11.12
20	5.769	4.21	4.83	48400.0	217.5	12.70
21	6.477	5.07	4.80	60604.8	254.8	14.89
22	4.847	2.79	4.42	34252.0	170.5	9.68
23	5.786	2.83	4.38	51287.7	226.6	12.80
24	6.530	2.81	4.36	64755.6	267.0	15.20
25	4.570	2.77	4.54	27301.4	145.4	6.26
26	5.073	2.82	4.52	35727.6	175.7	7.59
27	5.677	2.86	4.46	46068.7	210.1	9.08

Together with the change in the temperature of the liquid, along the cavity on the surfaces of the primary facade (PF) and secondary facade (SF) which faces the cavity, the comparisons of the values of the temperature which have been calculated by using the nodal network model with the experimental measurement results are shown below for the different working conditions. It is seen that the air temperature ( $T_f$ ) in the cavity at two points which have been acquired from the experimental measurement results are very coherent with the numerical results which are shown with straight lines in the figures (Figures 5.67-5.72). When the surface temperatures are compared depending on the experimental measurement and nodal network results, it is seen that the temperature are very coherent with the measurements in the middle of the glass surfaces. However, it is seen that the model behaves more incompatibly with the measurements at the bottom and top levels where the measurements have been taken. The reason of this is that the liquid temperature measurements in this zone are taken in a zone which is relatively closer to the air inlets and outlets. While this difference is more visible in the measurements which are close to the entrance zone, in the section which is close to the exit zone, it is possible to observe relative coherence. This difference especially in the entrance zone occurs due to the fact that it is not fully developed yet and is affected by the entrance conditions. Therefore, heat transfer calculations have been conducted by

taking half meters of intervals from the bottom and top of this point based on the measurements in the middle zone. Also, using unit length in the horizontal section, the values of the heat transfer which have occurred from the unit surface area have been given as the result.

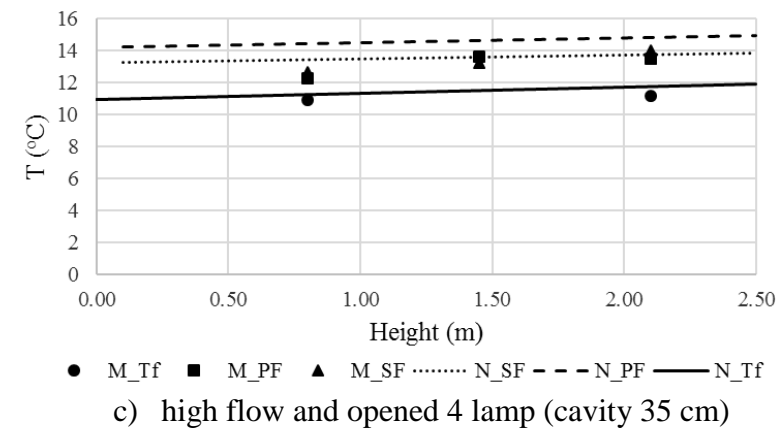
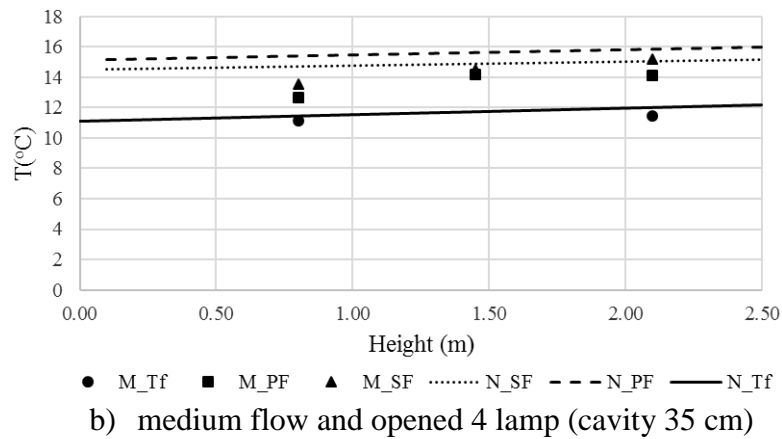
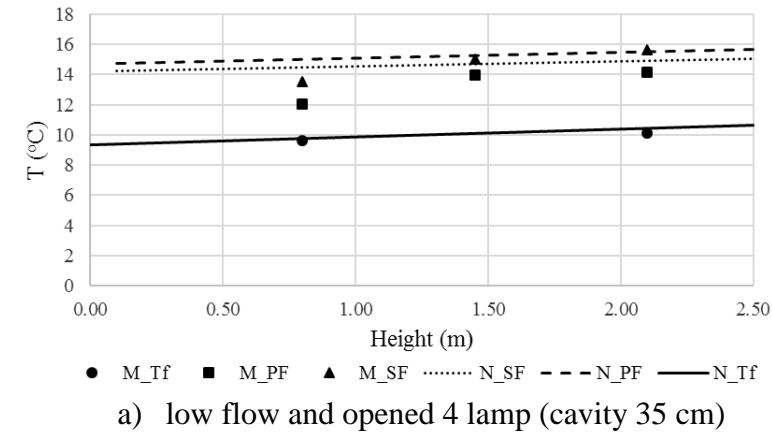


Figure 5.67. Temperatures by measurements and nodal model

In Figure 5.67, when the cavity is 35 cm, numerical and experimental results for three different mass flow rates are given. In these experimental studies, 4 lamps of the solar simulator was left open and the average solar radiation values which have been calibrated have been acquired. These studies in the Figure 5.67 are related to the experimental results numbered 10, 11 and 12, which are given in the Table 5.12.

In Figure 5.68, numerical and experimental results for different mass flow rates when the cavity is 35 cm can be seen. In these experiments, 8 lamps of the solar simulator were left open and in Table 5.12, the calibrated average solar radiation values of these experiments which have been coded as the numbers of 13, 14 and 15 are seen. Also in Figure 5.69, numerical and experimental results for different mass flow rates when the cavity is 35 cm are given. In these experimental studies, 4 lamps of the solar simulator were left open and in Table 5.12, the average solar radiation values of these experiments which have been coded as the numbers of 16, 17 and 18. And, in Figure 5.70, numerical and experimental results for three different mass flow rates when the cavity is 25 cm can be seen. 8 lamps of the solar simulator were left open in these experimental studies and the calibrated average solar radiation values which can be seen in Table 5.12 have been acquired. These studies in Figure 5.70 are related to the experimental results numbered 19, 20 and 21.

In Figure 5.71, the numerical and experimental results for three different mass flow rates when the cavity is 25 cm and the indoor environment of the test room temperature is high are seen. In these experimental studies, 4 lamps of the solar simulator were left open and the calibrated average solar radiation values which are given in Table 5.12 have been acquired. These studies in Figure 5.71 are related to the experimental results which are numbered as 22, 23 and 24. Furthermore, the numerical and experimental results for three different mass flow rates when the cavity is 35 cm and the indoor environment of the test room temperature is high are seen in Figure 5.72. Again, in these experimental studies, 4 lamps of the solar simulator were left open and the calibrated average solar radiation values which are given in Table 5.12 have been acquired. These studies in Figure 5.71 are related to the experimental results which are numbered as 25, 26 and 27.

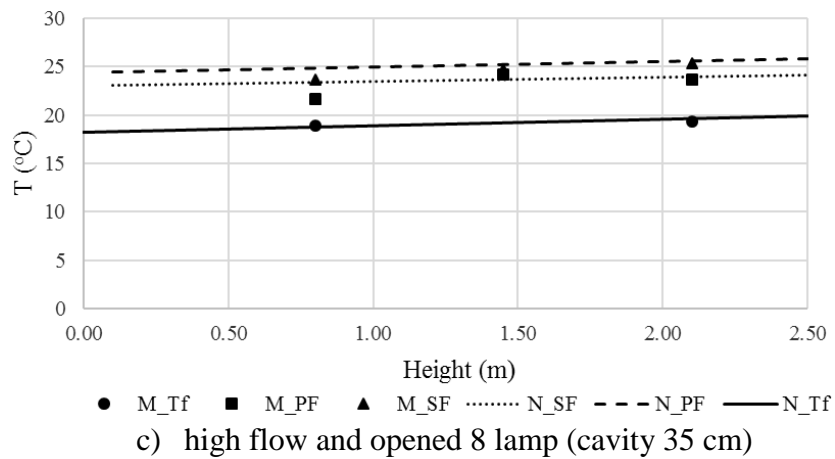
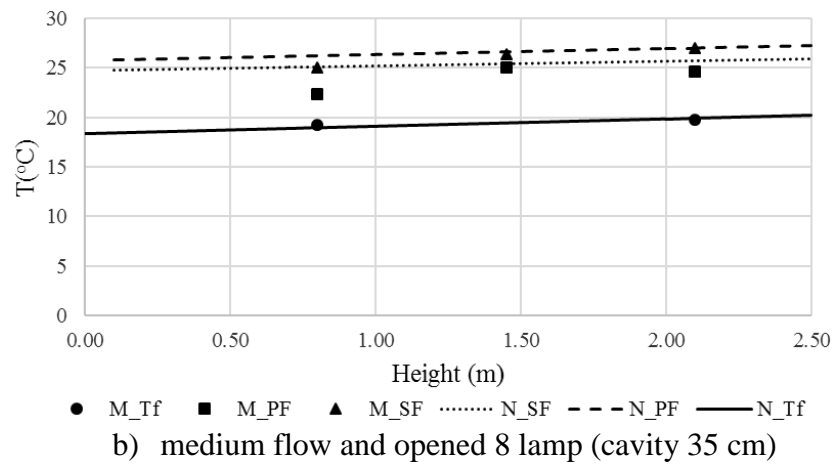
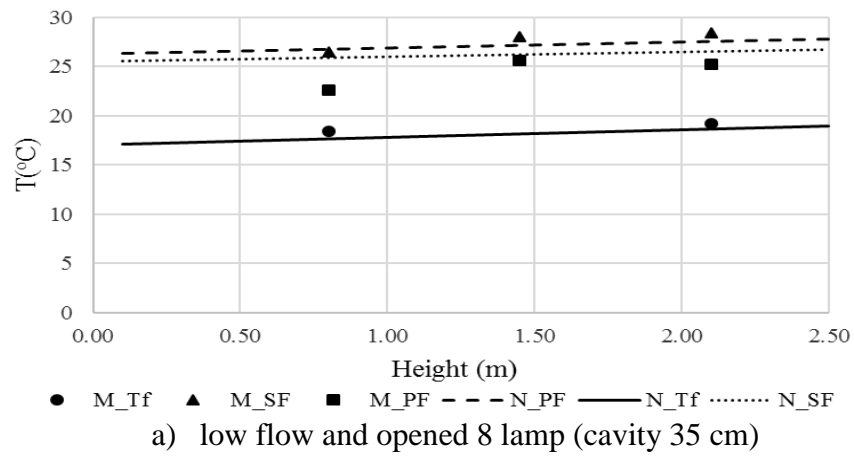


Figure 5.68. Temperatures by measurements and nodal model

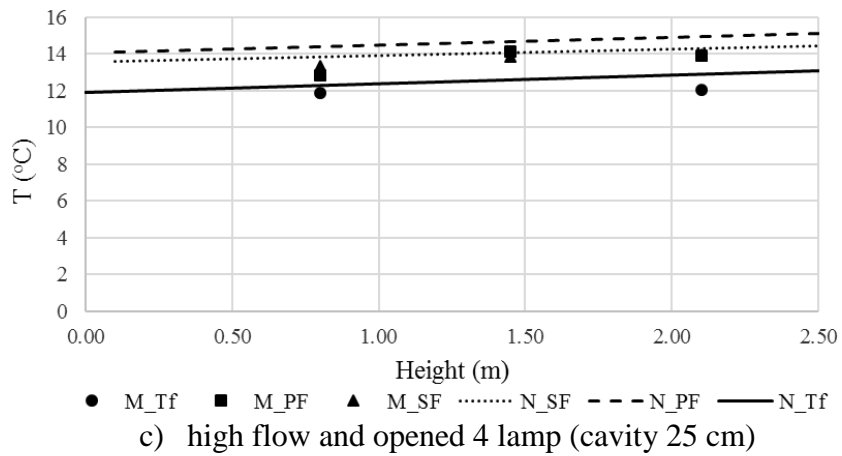
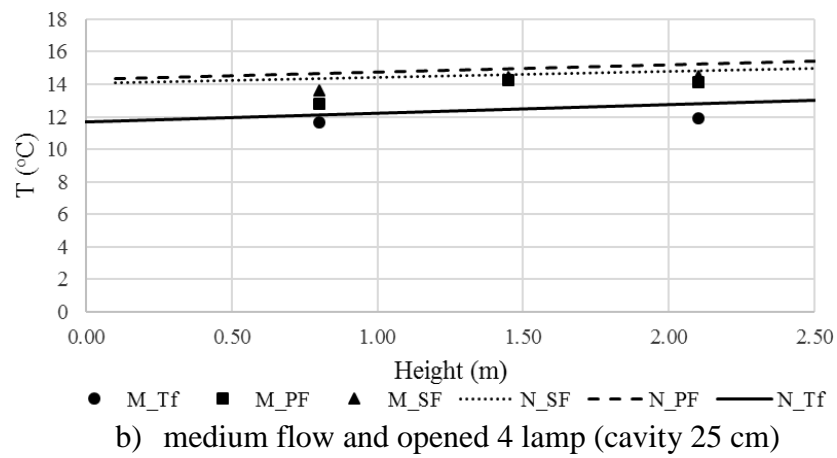
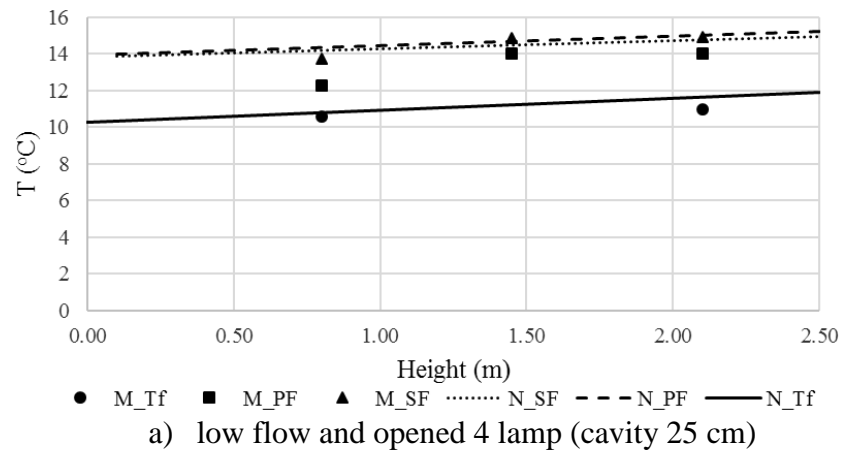


Figure 5.69. Temperatures by measurements and nodal model



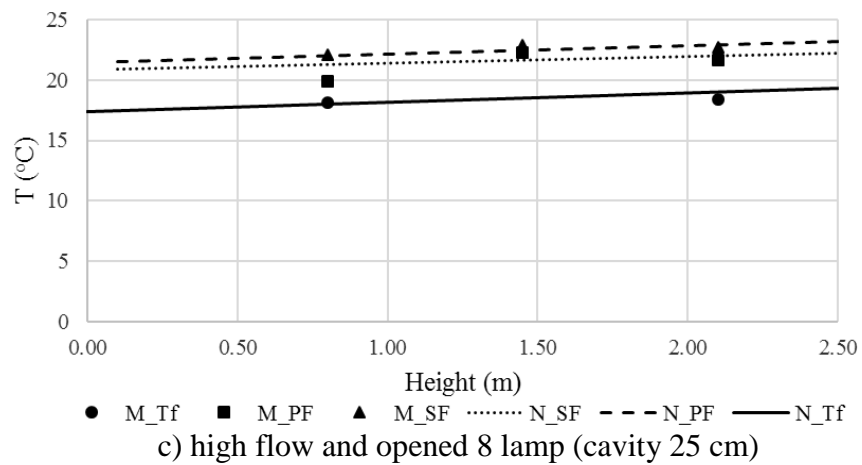
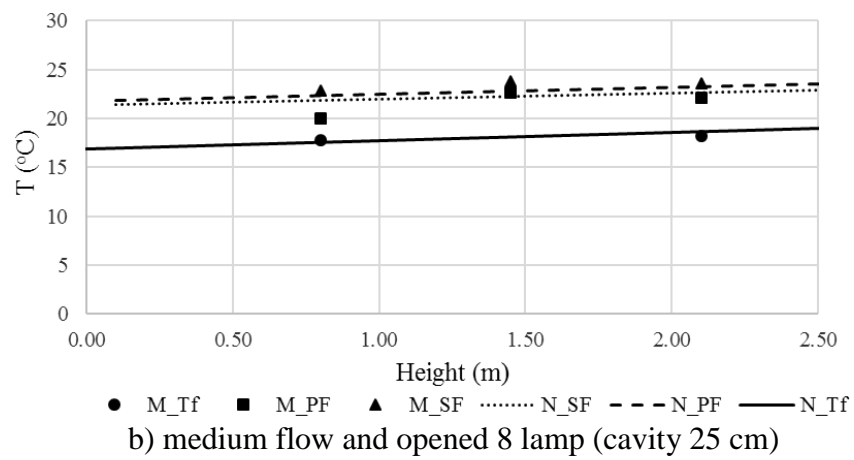
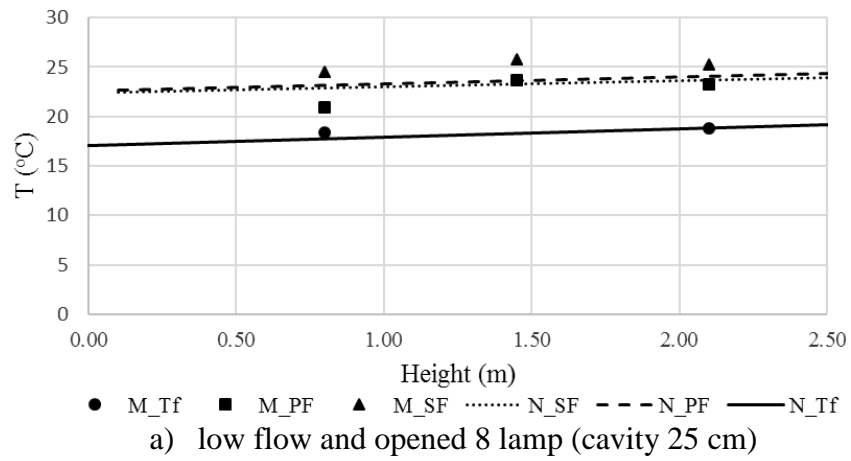


Figure 5.70. Temperatures by measurements and nodal model

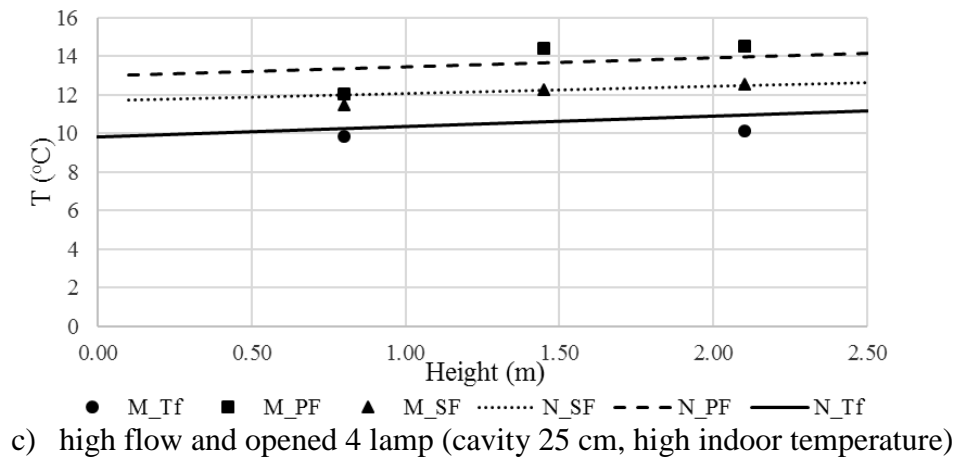
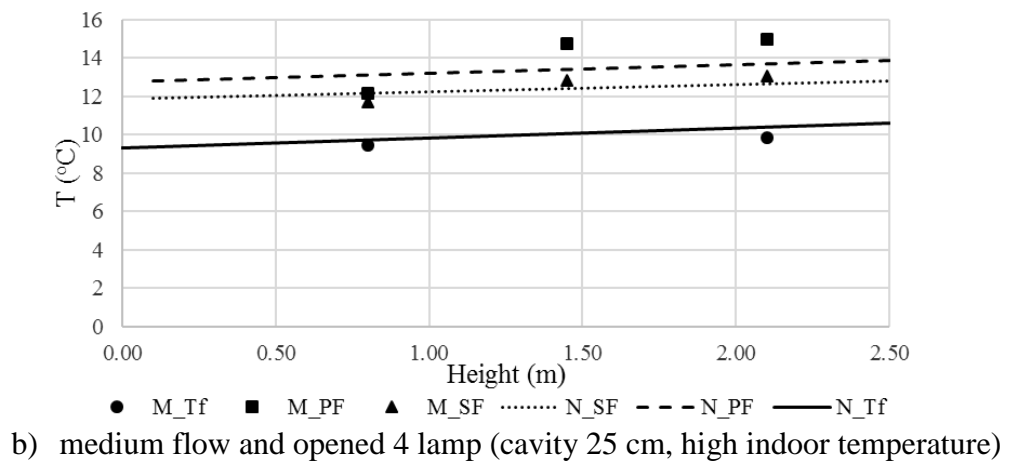
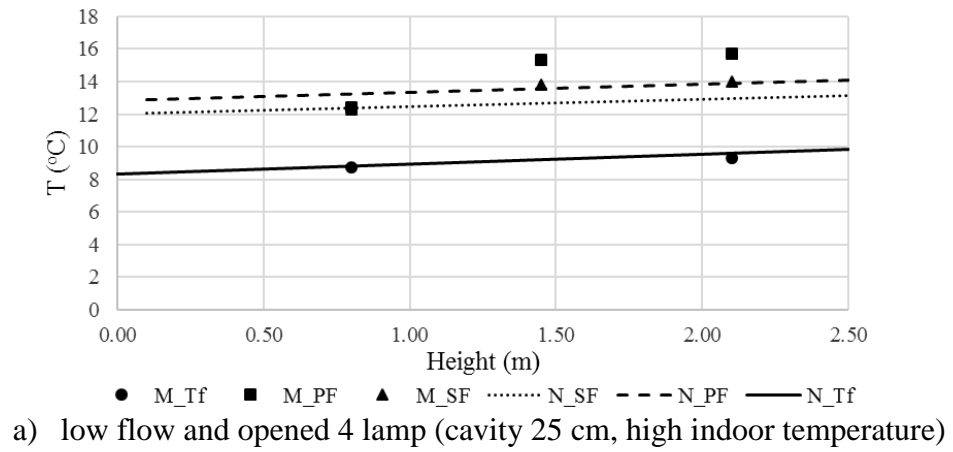
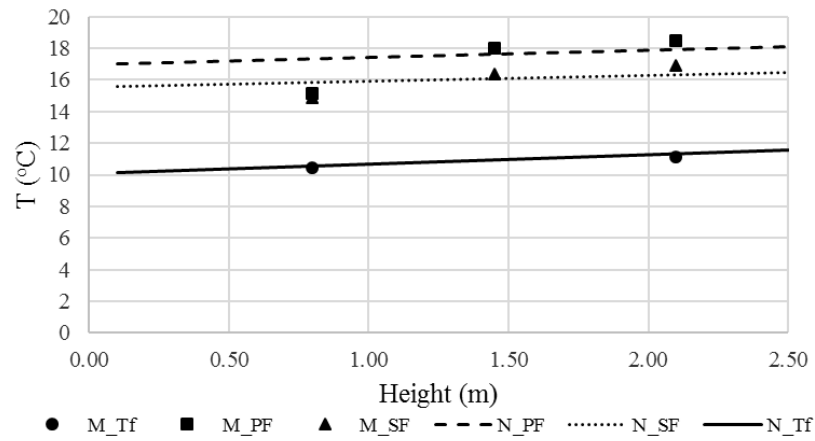
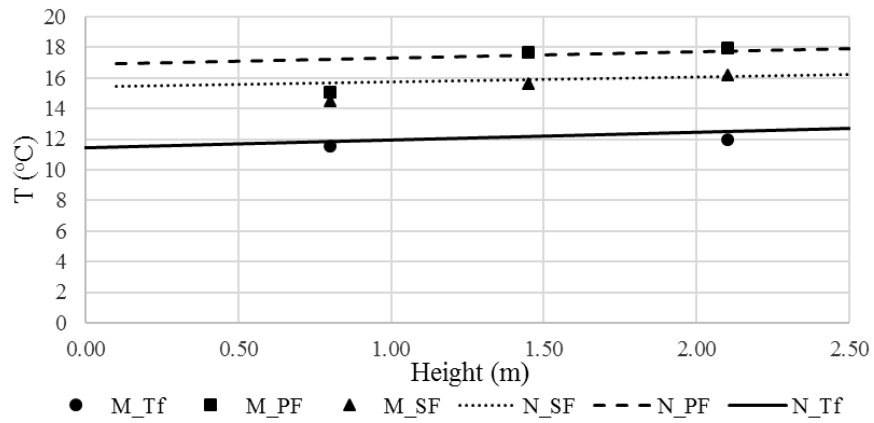


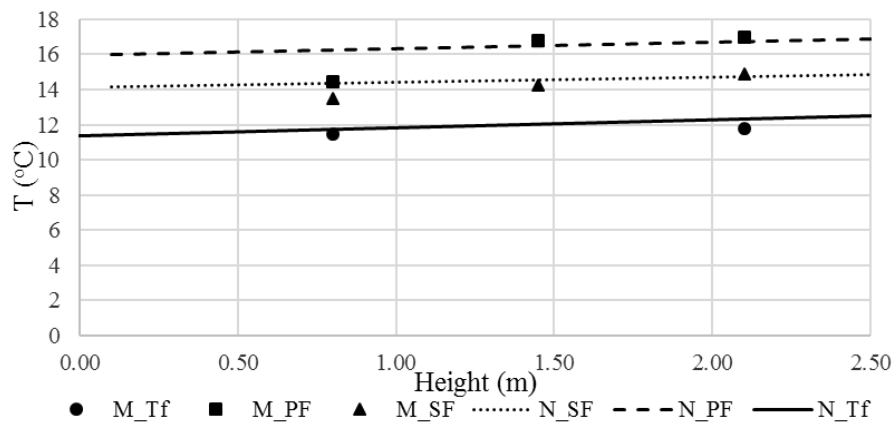
Figure 5.71. Temperatures by measurements and nodal model



a) low flow and opened 4 lamp (cavity 35 cm, high indoor temperature)



b) medium flow and opened 4 lamp (cavity 35 cm, high indoor temperature)



c) medium flow and opened 4 lamp (cavity 35 cm, high indoor temperature)

Figure 5.72. Temperatures by measurements and nodal model

#### 5.4.4. Discussion and Results of Unsteady Study

Using all of the parameters in the nodal network model which was prepared for the steady state condition, the nodal network model for the average climate data for İstanbul province was operated again. By using the monthly average daily meteorological data of İstanbul province in January and July (temperature, wind, solar radiation) depending on the placement of the double skin facade on the all cardinal points and intercardinal points, its energy performance is given by comparing it to the single skin facade. The interior environment temperature for January was accepted as 20°C and for July as 24°C. For the other working conditions, using the same value intervals in the previous model, the value of the mass flow rate was accepted as 0.5 kg/s and the cavity width as 30 cm. Different from the previous model, for İstanbul example, for the all of the nodal network models, the indoor heat transfer coefficient was taken as 1/0.13. (Eicker, 2001). However, the value of the outdoor heat transfer coefficient was calculated as in the Equation 5.45 (Liu and Harris, 2007). Here  $V_{out}$  is the value of the wind velocity which is taken from the meteorological data.

$$h_{out} = 6.31 * V_{out} + 3.32 \quad (5.45)$$

The temperature of entrance to the cavity of the air,  $T_{inlet}$  was considered to be equal to the exterior environment temperature ( $T_{out}$ ) in the nodal network models which were prepared for İstanbul province. As the temperature of the entrance to the cavity was measured in the previous model, it was used instead of the exterior environment temperature. However, in the experimental study, small temperature differences were measured for each condition (Table 5.12.) Similar temperature distribution was obtained for the DSF cavity according to the İstanbul data in the time-dependent numerical analysis. In Figure, temperature distribution was given for north and south facades at 12 am from the time dependent analysis by using monthly average daily data on january for İstanbul. Dashed lines defines the south facade (vertical axes on left side) while straight lines define north facade (vertical axes on right side). Temperature changes in the DSF cavity was displayed with fine lines on both facades. As it was seen in Figure 5.73, south facade has more heat gains due to the solar radiation effects and more temperature differences occur between the surfaces.

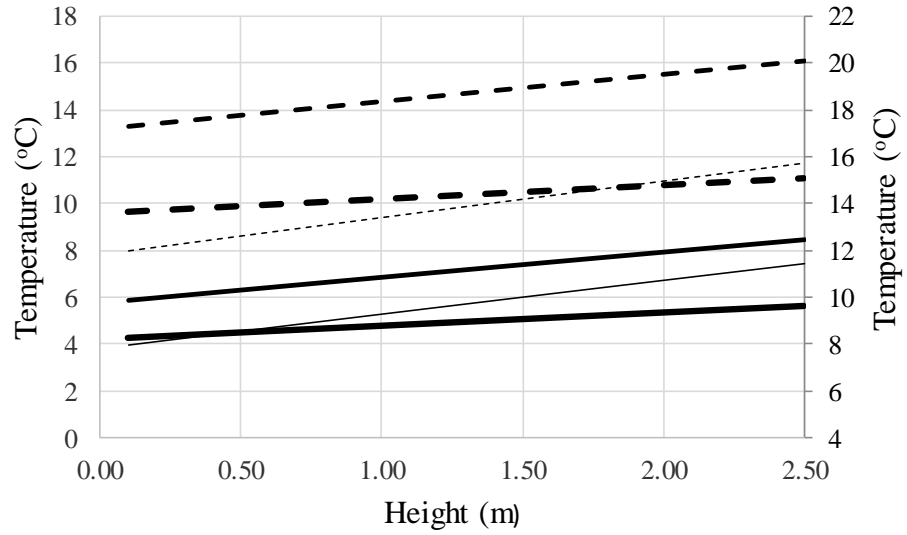


Figure 5.73. Temperature distribution for north and south facade on January at 12 am.

Using these calculations, in order to calculate the heat transfer rate per unit area from DSF due to the temperature difference, Equation 5.46 was used:

$$\dot{q} = U_{PF}(T_{PFOG} - T_{in}) \quad (5.46)$$

By using monthly average daily data for İstanbul, Figure 5.74 and 5.75 were drawn respectively for January and July. As it is seen in Figure 5.74, due to the temperature difference, all day, for each direction, heat loss (heating load) values occurred for the DSF application and since the solar radiation was present during daytime, heat losses from the south facade relatively decreased. In July, although the average exterior temperature was below 24°C at nighttime, thanks to the DSF application, heat loss/gain do not occur and thanks to the thermal inertia of the DSF, positive values were seen around 9 pm-11 pm. A similar effect of thermal inertia and the heat flux values in the east and west directions formed different curves despite the symmetrical solar radiation effect.

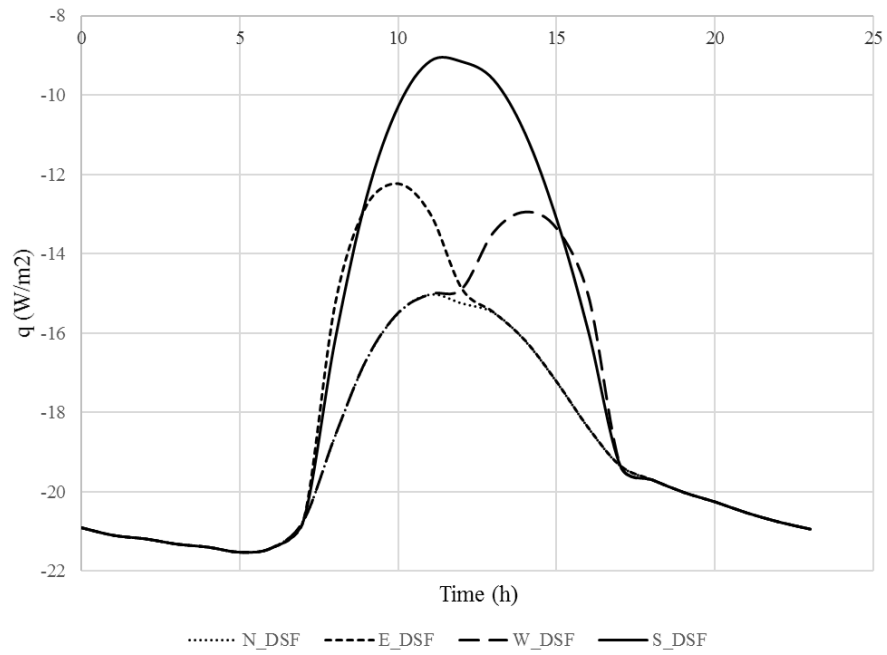


Figure 5.74. Heat transfer rate per unit area due to temperature difference for DSF using monthly average daily climatic data in January for İstanbul.

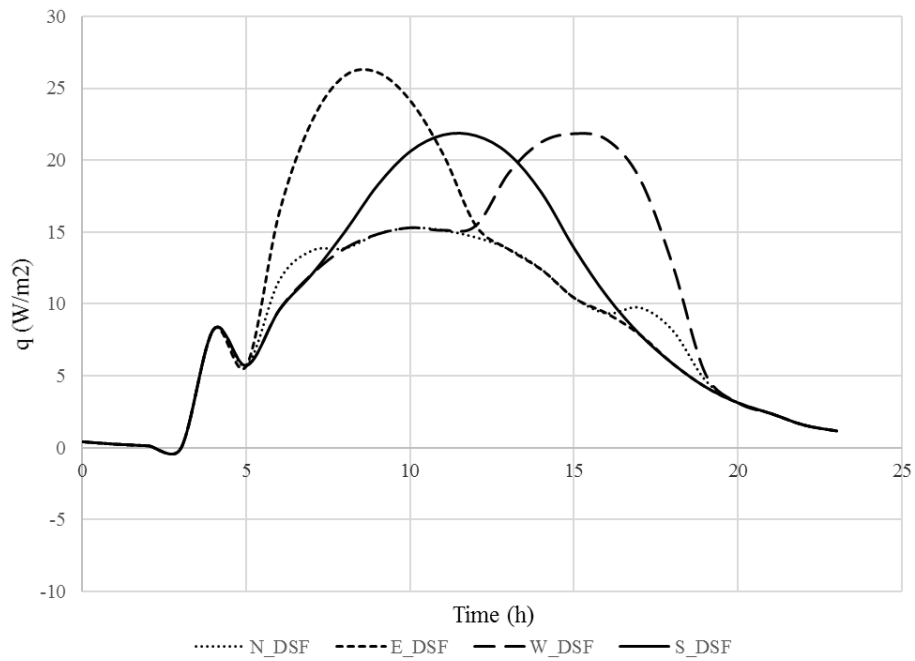


Figure 5.75. Heat transfer rate per unit area due to temperature difference for DSF using monthly average daily climatic data in July for İstanbul.

In order to compare DSF with SSF, a similar nodal network approach was also used for SSF. Similarly, the monthly average daily meteorology data for İstanbul were used for SSF. The schematic model of the single skin facade which will be used for the purpose of comparison and its nodal network illustration are seen in Figure 5.76.

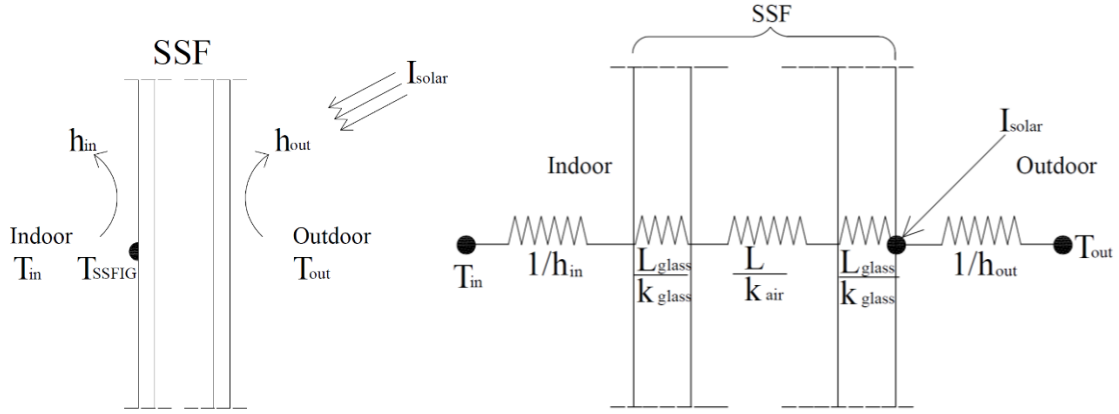


Figure 5.76. Schematic view and nodal model of Single Skin Facade (SSF)

According to the nodal network in Figure 5.76, the energy balance is given in Equation 5.47 below:

$$I_{solar} \propto_{SSF} = U_{SSF}(T_{SSFIG} - T_{out}) + h_{in}(T_{SSFIG} - T_{in}) \quad (5.47)$$

Here the values of  $I_{solar}$  and  $T_{out}$  were taken from the CMSAF (<http://re.jrc.ec.europa.eu/pvgis/apps4/pvest.php>) and general directorate of meteorology (<http://www.mgm.gov.tr/>) references as monthly average daily solar radiation and exterior environment temperature values for January and July. The value of the  $U_{SSF}$  overall heat transfer is calculated as

$$U_{SSF} = \left[ \frac{1}{h_{out}} + \left( \frac{L}{k_{glass}} * 2 \right) + \frac{L_{air}}{k_{air}} \right]^{-1} \quad (5.48)$$

In this way, using the temperature values  $T_{SSFIG}$  which are acquired from the Equation 5.47, the heat flux values due to SSF are calculated by using the Equation 5.49:

$$\dot{q} = h_{in}(T_{SSFIG} - T_{in}) \quad (5.49)$$

Accordingly, the heat transfer rate per unit area due to the temperature difference from SSF were drawn in Figure 5.77 and 5.78 respectively by using the monthly average daily data for İstanbul for January and July. In Figure 5.78, due to the relatively low temperature values, although the heat loss values at nighttime continued below 20°C thanks to the presence of the solar radiation during daytime, there were positive values as heat gain as the temperature of the glass increased. With the effect of the solar beam which came perpendicular to the glass surface, the SSF on the south facade received more thermal energy comparing to the other directions. However, at nighttime, heat losses from each direction is equal as there is no effect of solar radiation. Also, the total thermal energy per unit in July reached very high values with the effect of the solar radiation (Figure 5.78.) Heat losses which occurred as the exterior environment average temperature values at night were below 24°C, with the effect of the solar radiation during daytime were transformed into heat gain. Heat gain (cooling load) from the SSF on the east and west facades are higher than the other facades as the sun rays come more perpendicular to the surface.

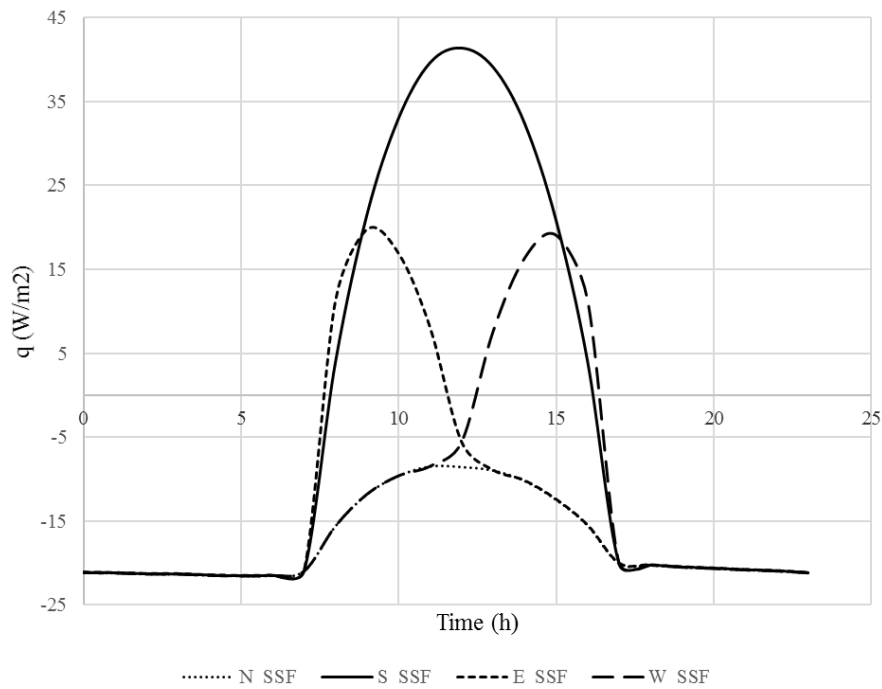


Figure 5.77. Heat transfer rate per unit area due to temperature difference for SSF using monthly average daily climatic data in January for İstanbul



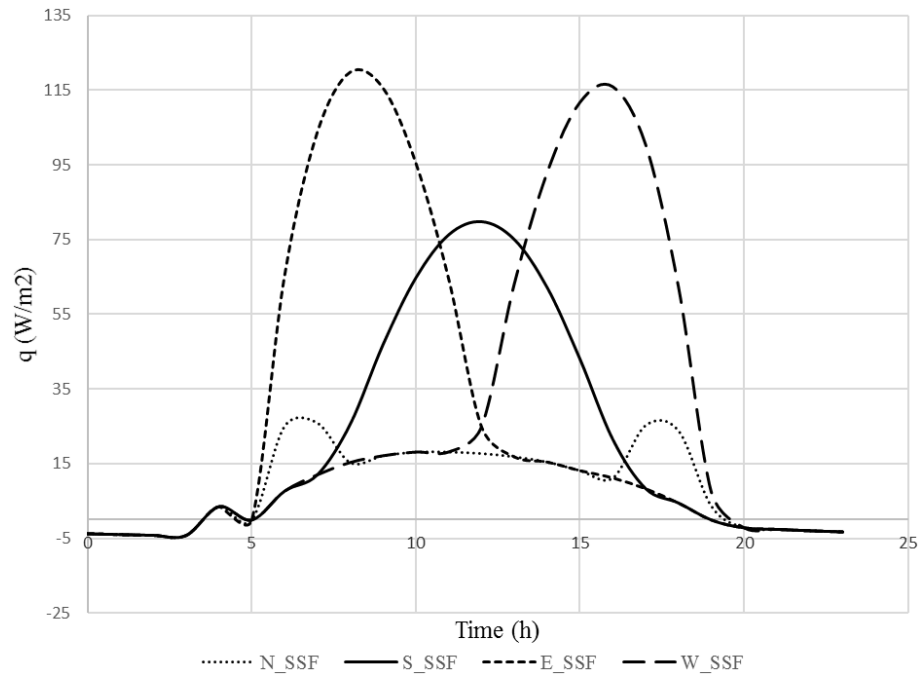


Figure 5.78. Heat transfer rate per unit area due to temperature difference for SSF using monthly average daily climatic data in July for İstanbul

After the heat loss/gain graphics due to the temperature difference, heat gains thanks to the solar radiation effect for the DSF and SSF applications are given in Figures 5.79-5.82 by using the monthly average daily data for January and July. Here the radiation features of glass were considered the same for each condition.

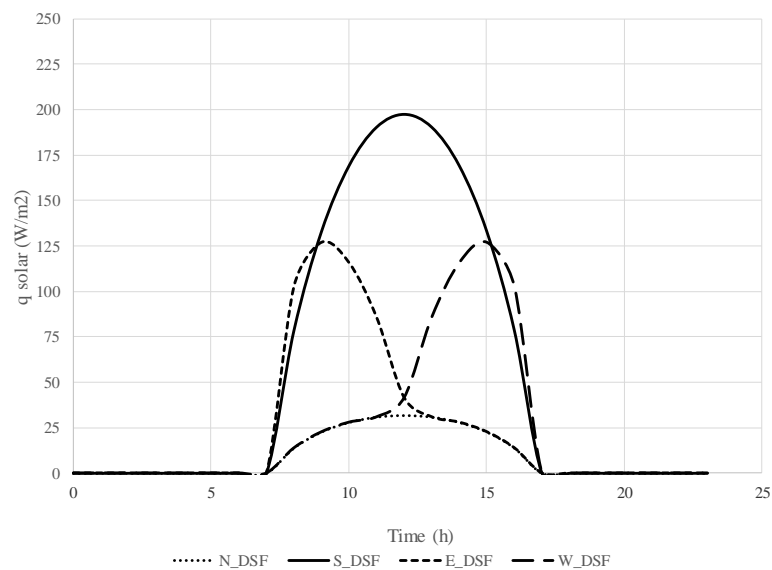


Figure 5.79. Heat gain from the solar radiation transmitted from DSF by using monthly average daily data of January in İstanbul for different directions

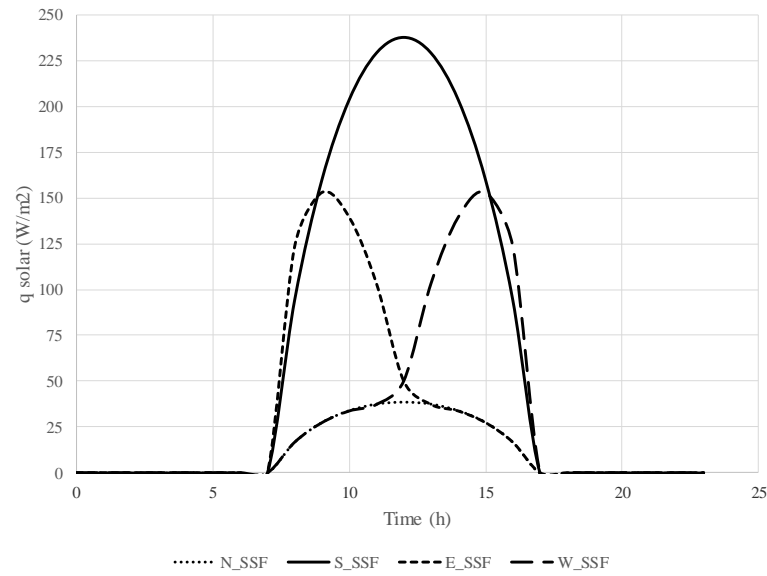


Figure 5.80. Heat gain from the solar radiation transmitted from SSF by using monthly average daily data of January in İstanbul for different directions

While using DSF decreased the heat gain from sun in winter in comparison to SSF and the heating load was affected negatively (Figures 5.79-5.80), it reduced the heat gain of the solar radiation in summer and contributed positively to the cooling load (Figures 5.81-5.82). The decrease in the cooling load is significantly larger than the disadvantage of the heating load.

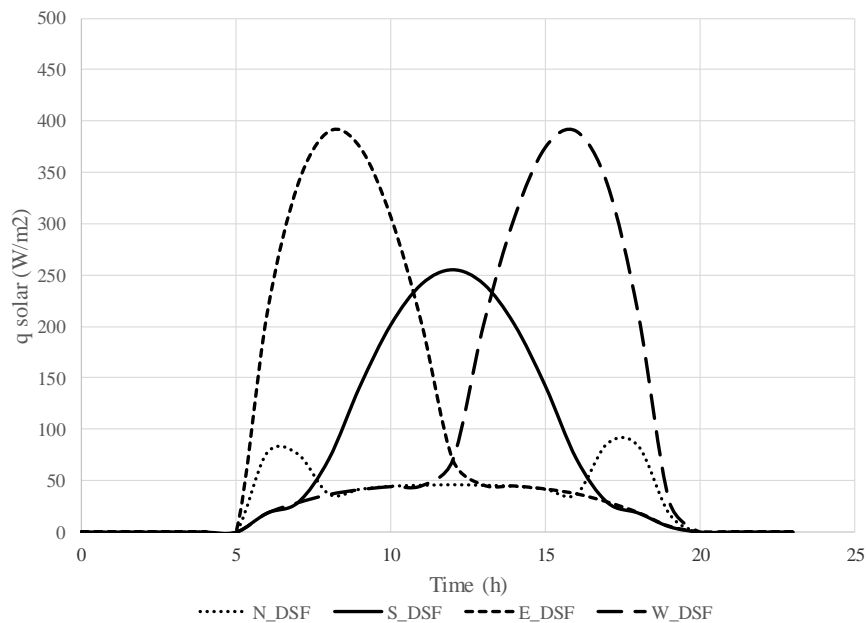


Figure 5.81. Heat gain from the solar radiation transmitted from DSF by using monthly average daily data of July in İstanbul for different directions

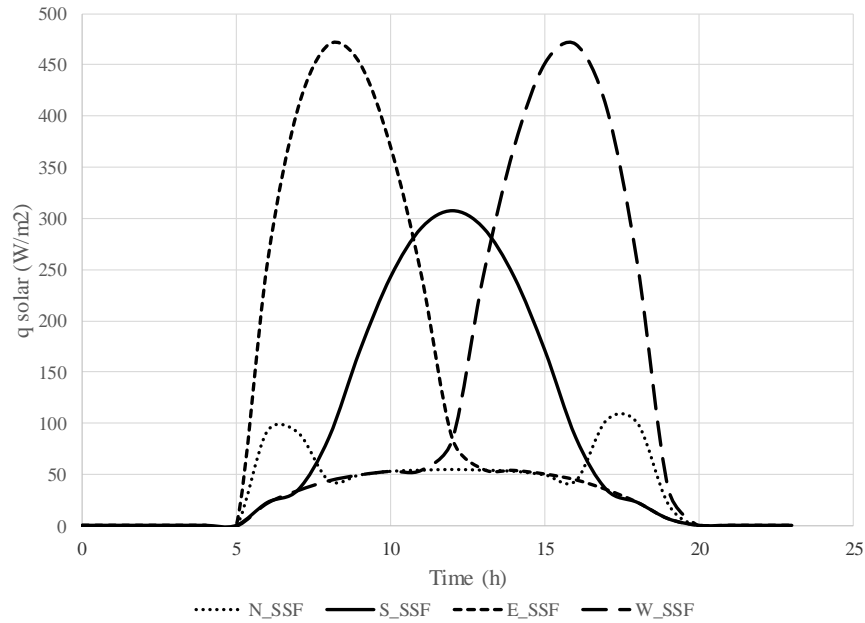


Figure 5.82. Heat gain from the solar radiation transmitted from SSF by using monthly average daily data of July in İstanbul for different directions

Another important result which was acquired in the nodal network energy analysis is that the change of the energy of the air in the DSF cavity. While this energy gain in winter can be used for preheating purposes in HVAC system, if the required temperature levels are reached, it can be directly released inside (Figure 3.6e and 3.6f). In Figure 5.83, at the length of the cavity (and considering the width of the unit cavity) the rate of increasing of the energy level of the air is given depending on different directions by using January data of İstanbul. For these working conditions, these rate of increasing values at the energy rate of the air is at a significant level when the heat loss-gain values in the previous graphics are considered. Therefore, using this energy in terms of reducing the heating load in winter will provide a significant contribution. The rate of increase at the thermal energy of the air in the DSF cavity on the south facade is higher comparing to the other directions, as it is expected.

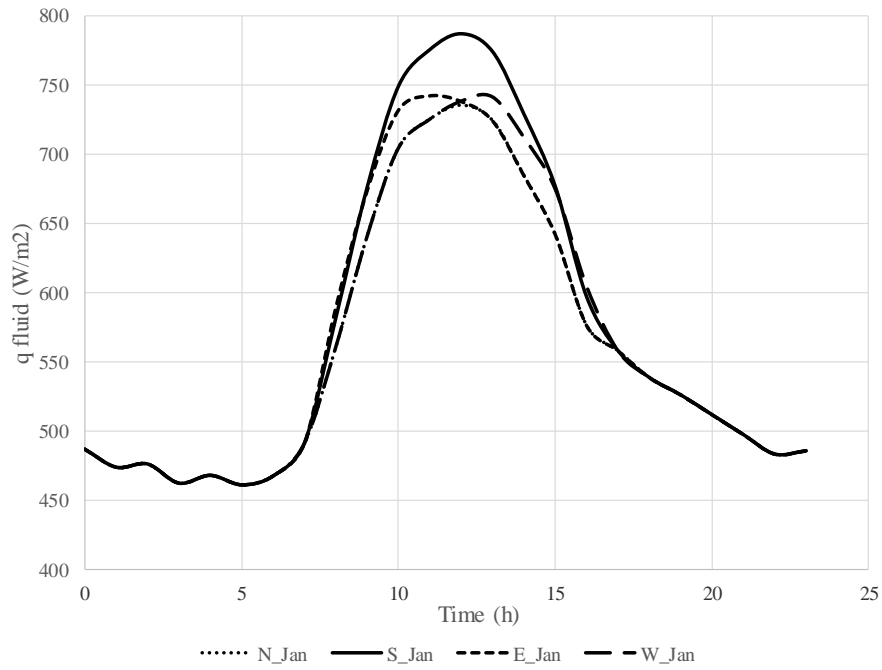


Figure 5.83. Air energy rate gain per unit area of DSF through the cavity by using monthly average daily data of January in İstanbul for different directions

Using the monthly average daily data for İstanbul for July, the change of the thermal energy of the air in the DSF cavity is significantly higher than the January values (Figure 5.84.) It is very important to dispose this energy from the cavity to outside (Figure 3.6b). Or, an application in which this thermal energy can be used (such as an absorption cooling system) can be integrated to the building, a significant gain can be acquired.

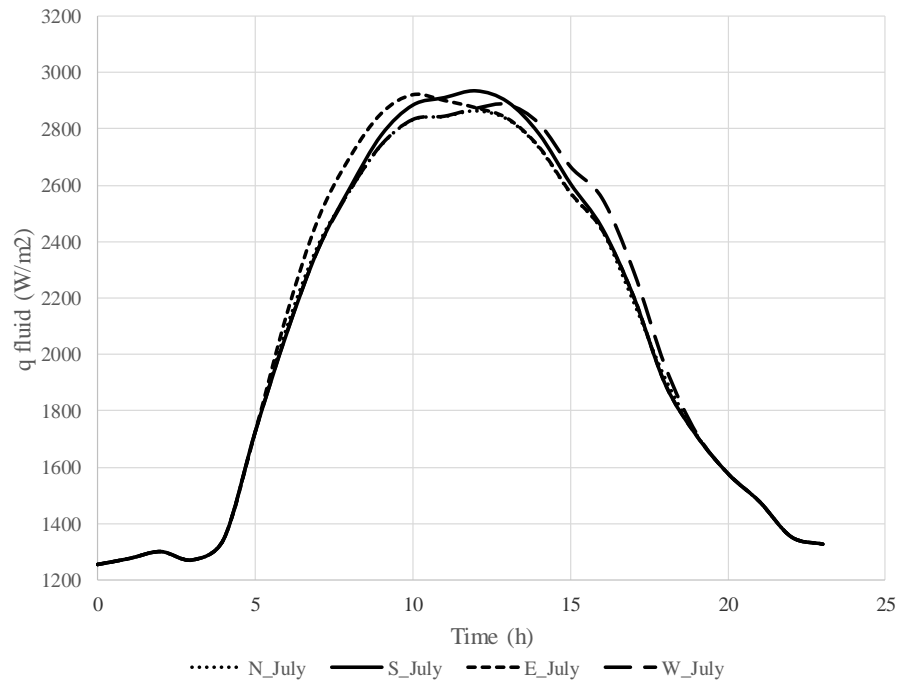


Figure 5.84. Air energy rate gain per unit area of DSF through the cavity by using monthly average daily data of July in İstanbul for different directions

The daily changes in all these heat transfer rate values, as daily total energy transfer for İstanbul, for winter (considering January when the exterior environment temperature is lowest) and for summer (considering July when the exterior environment temperature is highest) are given in Figures 5.85 and 5.86 for different directions in the form of  $\text{Wh}/(\text{m}^2\text{day})$ .

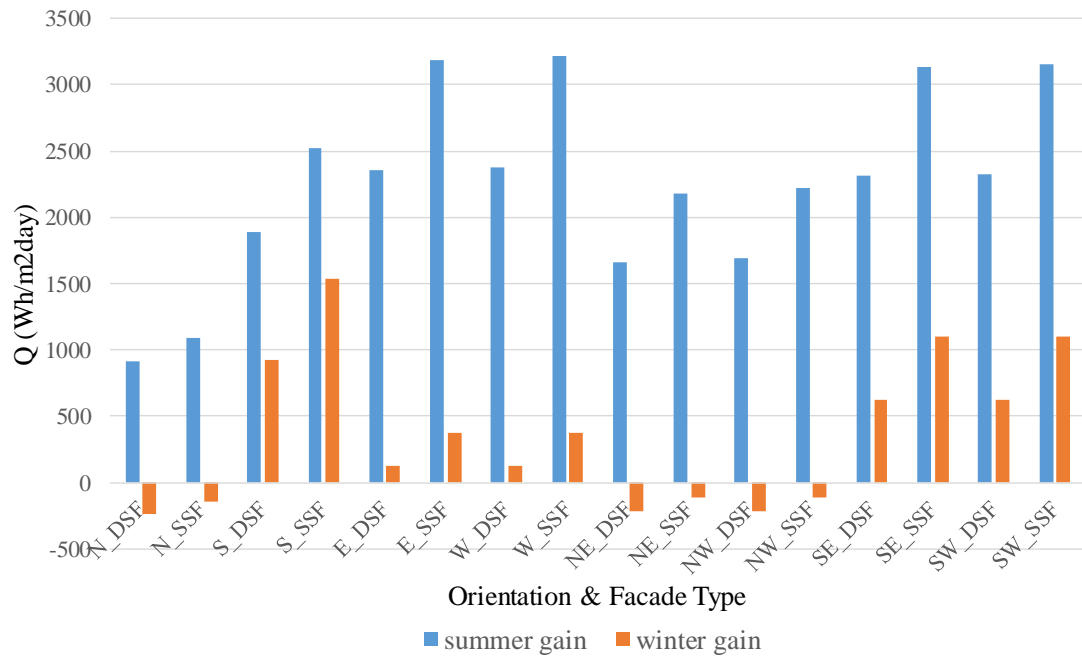


Figure 5.85. Heat transfer comparison of DSF and SSF for different orientation and season in İstanbul

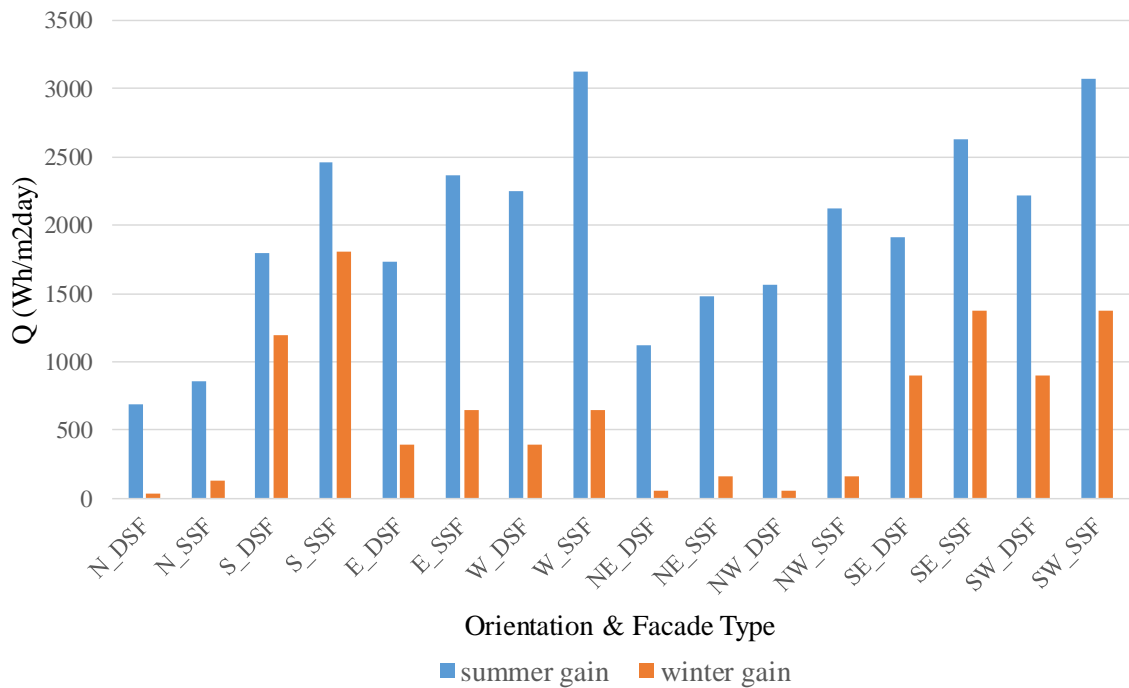


Figure 5.86. Heat transfer comparison of DSF and SSF for different orientation and season in İstanbul (for 8h-18h)

When we examine Figure 5.85, it is seen that for the double skin facade system in which the air flow mode is used, considering all of the directions, the double skin

facade system offers more advantages than the single skin facade in summer. For instance, while in a double skin facade system which is installed on the south facade, there is an average of daily  $1892 \text{ Wh/m}^2$  heat gain, this value is calculated in a traditional single skin facade system as  $2516.86 \text{ Wh/m}^2$  in the nodal model. In this case, it is seen that the double skin facade system is more advantageous than the traditional single skin facade system. Considering all of the double skin facade systems, it is seen that heat gain for the lowest summer month is acquired from the double skin facade which is located on the north direction. However, when the traditional single skin facade (SSF) and double skin facade (DSF) conditions are compared in all directions, it is observed that this advantage is more significant in the south, east and west directions comparing to the single skin facade. Considering the cardinal points, it is seen that using DSF in the north direction, the cooling load decreases 16% comparing to the single skin facade, using DSF in the south direction, the cooling load decreases 24%, and using DSF in both east and west facades, the cooling load decreases 26%. While examining the DSF on the intercardinal points, it is found that comparing to the single skin facade, for the DSF on the NorthEast (NE) and NorthWest (NW), there is a 23% decrease in the cooling load, and for the DSF on the SouthEast (SE) and SouthWest (SW), there is a 26% decrease in the cooling load. These findings have been acquired with the nodal model in which the exterior air curtain of the cavity were ventilated with the air flow mode. As there is significance heat gain at the liquid temperature in the cavity, it is important that the cavity is ventilated and this gain is disposed out of the cavity.

For winter, the double skin facade system in which this exterior air curtain flow mode is used is disadvantageous on all directions comparing to the single skin facade. For instance, while there is a heat gain of  $920 \text{ W/m}^2$  in the double skin facade system which is installed on the south facade, it is calculated that there is a heat gain of  $1534.75 \text{ W/m}^2$  in the traditional single skin facade system in the nodal model. However, the disadvantage which occurs in winter is relatively lower comparing to the advantage in summer conditions. It is required to use the energy which is gained from the heated air and relate it to an AHU system. In summer, the cavity should be ventilated. As it is seen in the model, the exterior air curtain flow mode is an appropriate air flow mode for summer time.

The daily changes in all these heat transfer rates, as daily total energy transfer for İzmir, for winter (considering January when the exterior environment temperature is lowest) and for summer (considering July when the exterior environment temperature is

highest) are also given in Figure 5.87 for different directions in the form of  $\text{Wh}/(\text{m}^2\text{day})$ . These values given total heat transfer are found to be significantly higher than İstanbul's values given in Figure 5.87.

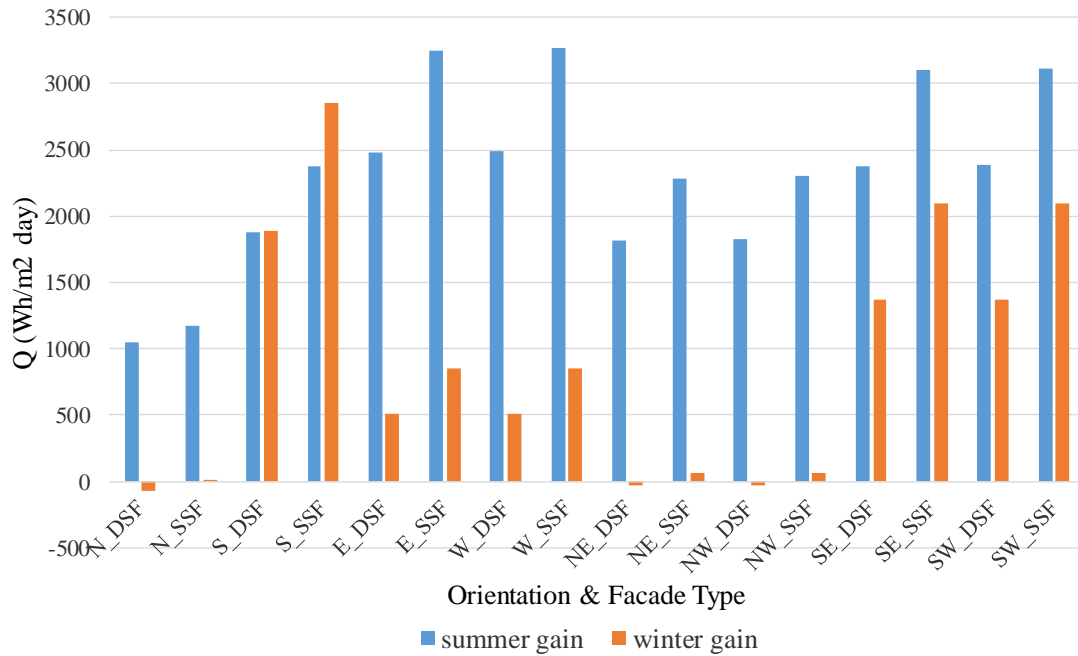


Figure 5.87. Heat transfer comparison of DSF and SSF for different orientation and season in İzmir

In this study, firstly the nodal network approach which was described by using the results obtained from the experiments was compared for that working conditions. This nodal energy balance approach was used for İstanbul and İzmir's climatic condition after reaching acceptable results for the external airflow mode in the cavity. Heating and cooling loads in DSF for İstanbul and İzmir were analyzed and compared with single skin facade (SSF). In the nodal model, thermophysical parameters of the materials from the experiments were used.

Convective heat transfer coefficients inside the both cavity surfaces were determined by using the correlation obtained from the CFD analysis. In general, while the usage of DSF showed unfavorable results rather than SSF both İzmir and İstanbul for the external airflow mode in cavity in winter, it showed good energy performance in summer in both İzmir and İstanbul. On the other hand, a considerable energy gain was observed in the cavity during the airflow. Extracting of this energy to the outside in



summer season and linking the heated air with HVAC and indoor environment in winter season is significant in terms of energy efficiency of DSF.

### **5.5. Case 5: Experimental and numerical investigation of natural convection in a double skin facade by using nodal network approach**

In this study, the cavity is blocked for entry/exit of air flow as an airproof double skin facade. Six experiments from 46 to 51 (Table 4.1) are performed for the natural convection under the steady state condition. The cavity depth is taken as 25 cm for all experiments. In each experiment, the whole system is activated in order to equilibrate thermally at the desired conditions.

#### **5.5.1. Experimental results**

Temperature changes of the fluid in the cavity and temperature changes of the primary and secondary facades' surfaces which face to the cavity have been examined along the height of the cavity according to different lamp configuration, different solar radiation values.

Average values of the indoor temperature, the exterior environment temperature, solar load, primary (PF) and secondary facade (SF) temperatures facing to the cavity and cavity air (CA) temperatures are given in Table 5.14. This values reflect the average of the measurements which have been taken every 2 seconds depending on time after the whole sytem reaches the thermal balance.  $T_{in}$  shows the average temperature of the air in the indoor environment of the expermental test room, whereas  $T_{out}$  shows the temperature of the air in the outdoor environment of the test room.  $T_{PFOG}$  represents the temperature of the surface of the primary facade which faces the cavity and  $T_{SFIG}$  represents the average temperature of the surface of the secondary facade which faces the cavity. Moreover, the solar radiation which comes to the system is defined as  $I_{solar}$ .

Table 5.14. Experimental measurements

	$I_{\text{solar}}$	$T_{\text{out}}$	$T_{\text{in}}$	y	CA	PFOG ( $^{\circ}\text{C}$ )			Avg.	SFIG ( $^{\circ}\text{C}$ )			Avg.
$\neq$	( $\text{W}/\text{m}^2$ )	( $^{\circ}\text{C}$ )	( $^{\circ}\text{C}$ )	(m)	( $^{\circ}\text{C}$ )	$T_{1,2\text{avg}}$	$T_{3,4\text{avg}}$	$T_{5,6\text{avg}}$	$T_{\text{PF}}$	$T_{1,2\text{avg}}$	$T_{3,4\text{avg}}$	$T_{5,6\text{avg}}$	$T_{\text{SF}}$
46	101	41	15.93	0.43	31.34	28.08	30.24	31.57	29.96	34.50	37.62	39.55	37.22
				1.08									
				1.73	37.04								
47	176	12.17	14.16	0.43	14.95	15.34	17.37	19.49	16.36	12.44	15.09	19.65	15.73
				1.08									
				1.73	20.06								
48	259	18.05	16.74	0.43	21.61	21.42	24.13	25.87	22.78	19.41	22.22	27.45	23.03
				1.08									
				1.73	27.53								
49	350	20.93	21.91	0.43	27.25	27.06	30.06	32.13	28.56	24.21	27.65	33.54	28.47
				1.08									
				1.73	34.09								
50	394	24.58	20.79	0.43	37.55	36.55	39.76	40.41	38.16	35.35	37.54	42.20	38.36
				1.08									
				1.73	42.92								
51	495	35.86	30.48	0.43	41.94	40.83	44.98	46.95	42.91	39.68	43.04	50.09	44.27
				1.08									
				1.73	50.15								

For the first experimental result, the changes in the average temperatures on the interior surfaces of the cavity are shown in Figure 5.88. Accordingly, the system that was thermally stable in the beginning, based on the different temperatures on the interior and exterior, became stable after some time. The temperature values on the exterior surface facing the cavity reflect the average value of the six thermocouples (SFIG1-6). Thermocouples PFOG1-6 give the average temperature values of the interior surface facing the cavity space.

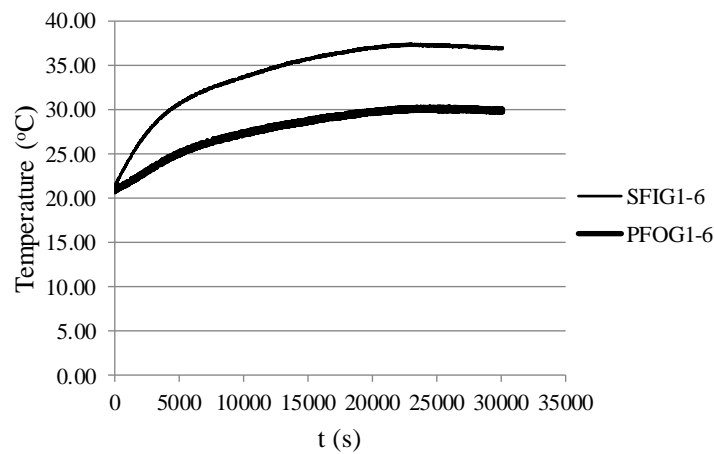


Figure 5.88. Variation of temperature in the cavity surfaces for the first experiment

Along the interior glass surfaces of the cavity, temperature changes occur. These changes are shown in Figure 5.89. Each point refers to the average of two thermocouples placed at the same height of the cavity. As shown in Figure 5.89, the temperature values increase depending on the height. The figure also shows the linear equality that clearly reflects this change. In the numerical study, as a boundary condition, these changes in the temperature were considered, and the average values were used using these linear equations.

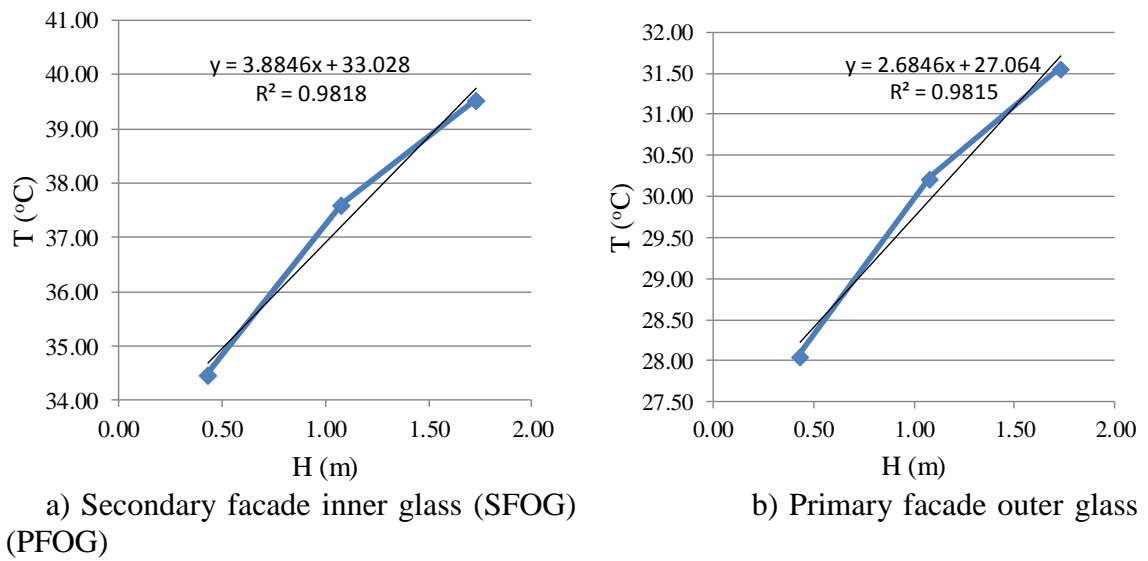


Figure 5.89. Variation of temperature in both interior surfaces along the cavity height for the first experiment

For the first experimental results, to show the oscillation of the temperature values due to the activation of the cooling and heating system after the steady state condition, the average temperature changes on the interior surfaces of the cavity are shown in Figure 5.90. As shown in Figure 5.90, the temperatures were calculated in a very stable way, and the standard deviations are  $0.11^{\circ}\text{C}$  for PFOG while  $0.15^{\circ}\text{C}$  for SFIG.

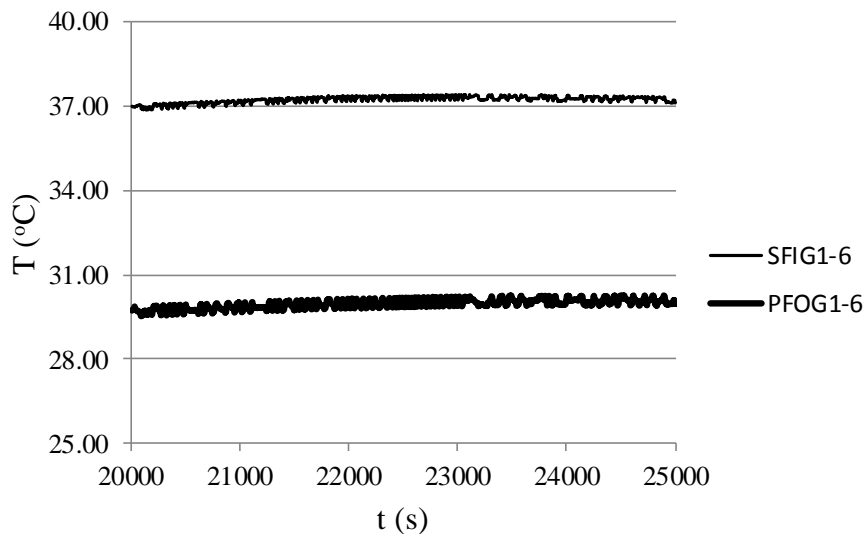


Figure 5.90. Variation of temperatures in both inner surfaces along the cavity height for the first experiment (Exp.1)

For the first experimental study, another time-dependent temperature changes after the steady state condition is shown in Figure 5.91. With the effect of natural convection, the high temperature air is located at the top. “CA1-4” shows the average temperature of the four thermocouples at the bottom, whereas “CA5-8” is the average temperature of the top four thermocouples. The standard deviation is  $0.12^{\circ}\text{C}$  for the cavity air (CA).

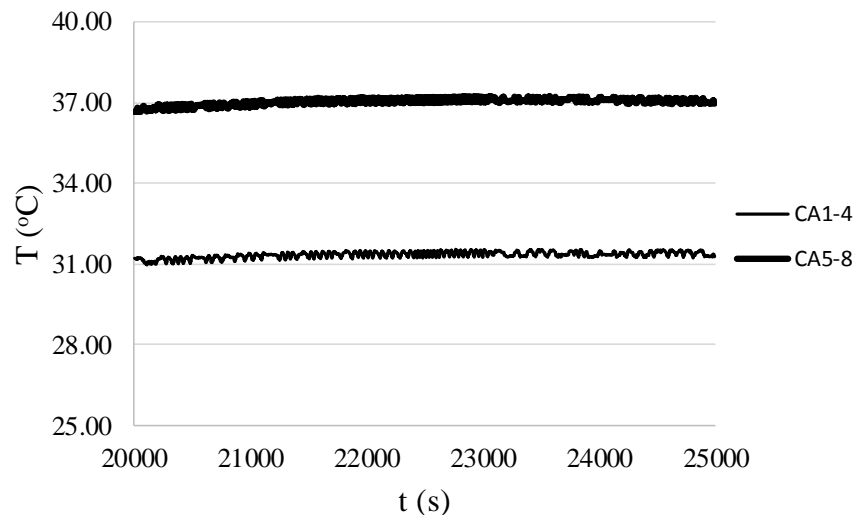


Figure 5.91. Variation of air temperature in the cavity for the first experiment

The average temperature ranges of the two different height sections of the cavity, average temperature of air in the indoor and outdoor environments of the experimental test room after the steady state condition are shown in Figures 5.92 and 5.93. The two points in the middle give the air temperature, and the temperatures on the sides facing to cavity refer to the average surface temperatures measured by two thermocouples on each level (0.80m, 1.45m and 2.10 m height). The point on the primary facade inner surface and secondary facade outer surface give the average surface temperatures measured by two thermocouples each in the middle of the glass surfaces. The point indoor give the average indoor temperature measured by three thermocouples and the point outdoor give the average outdoor temperature measured by two thermocouples. Heat transfer occurs due to these temperature differences between the air and the surface and also artificial solar radiation. Additionally, the change in the air temperature in the cavity depending on the height can be observed.

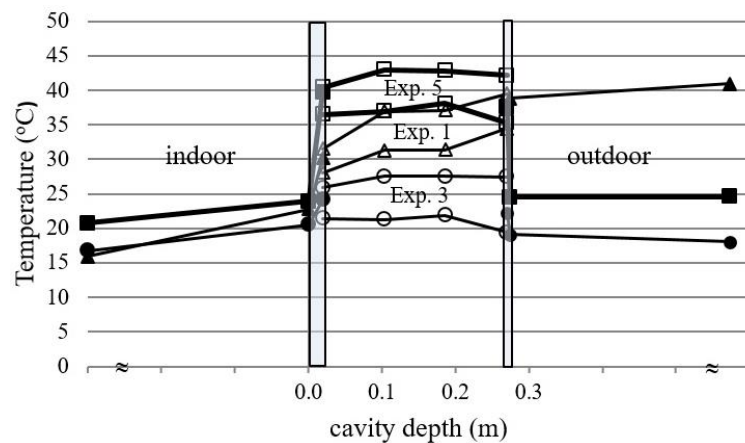


Figure 5.92. Variation of the temperature from the indoor to the outdoor environment for the Experiments numbered 1, 3 and 5

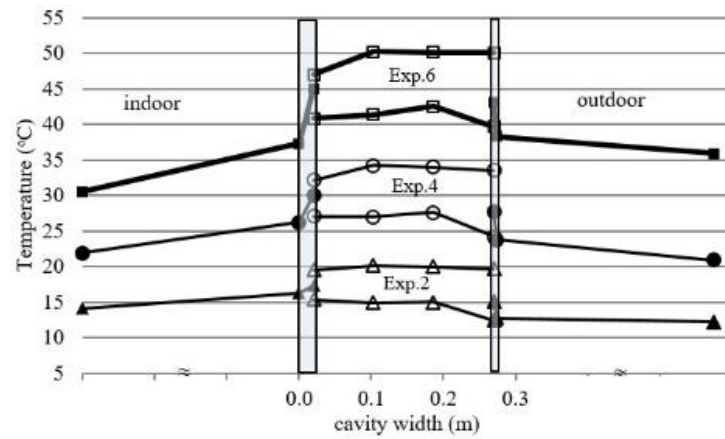


Figure 5.93. Variation of the temperature from the indoor to the outdoor environment for the Experiments numbered 2, 4 and 6

### 5.5.2. Thermal Balance of the Experimental System

Thermal balance control of the experimental system was realized for the DSF having natural convection and variation of the solar simulator lamps. Heat transfer rates which withdrawn from the system with the aid of constant temperature water bath could be observed in Table 5.15 for each of six experiments. According to that, water temperature values entered and got out from the constant temperature water bath and volumetric flow rate values were measured. Thermophysical properties were defined according to the average of the water temperature and heat transfer rates was displayed in the last caloumn in Table 5.15.

Table 5.15. Heat transfer rate values using constant temperature water bath

Exp. #	T <sub>in_wat.</sub>	T <sub>out_wat.</sub>	flow rate	density	mass flowrate	C <sub>p</sub>	Q
C	°C	°C	l/h	kg/m <sup>3</sup>	kg/s	J/kg°C	W
1	7.28	8.36	350	999.80	0.097203	4198.80	<b>440.8</b>
2	6.46	7.38	360	999.82	0.099982	4200.70	<b>386.4</b>
3	7.08	8.18	360	999.79	0.099979	4199.20	<b>461.8</b>
4	11.01	12.27	360	999.50	0.099950	4191.05	<b>527.8</b>
5	13.61	15.15	355	999.17	0.098529	4186.12	<b>635.2</b>
6	16.18	17.84	360	998.70	0.099870	4183.80	<b>693.6</b>

Heat transfer rates withdrawn from the indoor environment given in Table 5.16 must be balanced with the energy rate entered to the system. Heat transfer between indoor environment of experimental setup and laboratory were calculated (with infiltration). The energy transfer rates entered to the system from the DSF were calculated by considering the solar and conduction/convection effects and illustrated in Table 5.16 in detail. The total heat gain entered to the system was given in last column. When obtained results were compared with given values in Table 5.16, it was observed that the results were comparable except the first experiment. Except the first experiment differences in percent 4, 1, 7, 10 and 4 were calculated respectively. In the first experiment the difference reached to the 35 %. Recording error was possible in the measurement of the constant temperature water bath. Moreover, errors from some assumptions influenced the solution. These assumptions:

- convective resistance values were taken as  $0.13 \text{ m}^2\text{C}/\text{W}$  on both inner and outer surfaces of indoor environment.
- Heat resistance of metal profiles on the indoor environment wall were neglected.
- Thermal radiation effects could not be considered.
- Although the DSF cavity was well isolated, an amount of heat transfer could be occurred.
- Thermophysical properties of glass were not measured. They were taken from the references.
- Heat transfer with infiltration from the indoor environment door accepted approximately.
- The calculation of surface area of indoor environment was realized based on outer dimensions. The effect of the corners was not considered.

Table 5.16. Heat loss/gain values from/to the indoor environment.

Exp #	T <sub>in</sub>	TPFOG	U <sub>PF</sub>	A <sub>glass</sub>	Q <sub>glass</sub>	$\tau_{SF}$	$\tau P_F$	I <sub>glass</sub>	T <sub>in</sub>	T <sub>lab</sub>	U	A <sub>wall</sub>	Q <sub>wall</sub>	l	a	RHZ	Q <sub>inf</sub>	Q <sub>tot</sub>
	°C	°C	W/m <sup>2</sup> °C	m <sup>2</sup>	W			W	°C	°C	W/m <sup>2</sup> °C	m <sup>2</sup>	W	m	m <sup>3</sup> /h		W	W
1	15,93	29,96	1,065	2,5488	38,1	0,83	0,71	151,7	15,93	23,84	0,32081	31,5	79,9	5,6	1,20	0,14	7,4	<b>277,2</b>
2	14,16	16,36	0,102	2,5488	0,6	0,83	0,71	264,4	14,16	23,83	0,32081	31,5	97,7	5,6	1,20	0,14	9,1	<b>371,7</b>
3	16,74	22,78	0,760	2,5488	11,7	0,83	0,71	389,0	16,74	22,74	0,32081	31,5	60,6	5,6	1,20	0,14	5,6	<b>467,0</b>
4	21,91	28,56	0,746	2,5488	12,6	0,83	0,71	525,7	21,91	24,26	0,32081	31,5	23,7	5,6	1,20	0,14	2,2	<b>564,3</b>
5	20,79	38,16	1,741	2,5488	77,1	0,83	0,71	591,8	20,79	23,58	0,32081	31,5	28,2	5,6	1,20	0,14	2,6	<b>699,7</b>
6	30,48	42,91	0,987	2,5488	31,3	0,83	0,71	743,5	30,48	25,85	0,32081	31,5	-46,8	5,6	1,20	0,14	-4,4	<b>723,6</b>



### 5.5.3. Nodal Network Approach and the numerical results

Figure 5.94 includes the schematic representation of a limited zone of the DSF, in which the experimental studies have been conducted. Here PF defines the primary double skinned glazed facade (primary facade,) SF the secondary single glazed facade (secondary facade) and CA (cavity air) the air inside of the cavity.

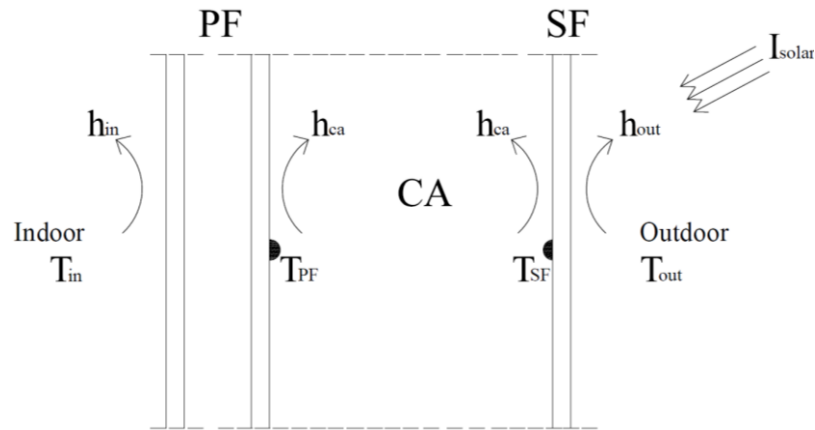


Figure 5.94. Schematic view of DSF

Figure 5.95 includes the nodal network representation of the DSF in Figure 5.94. Energy balance is set up for these temperature nodes.

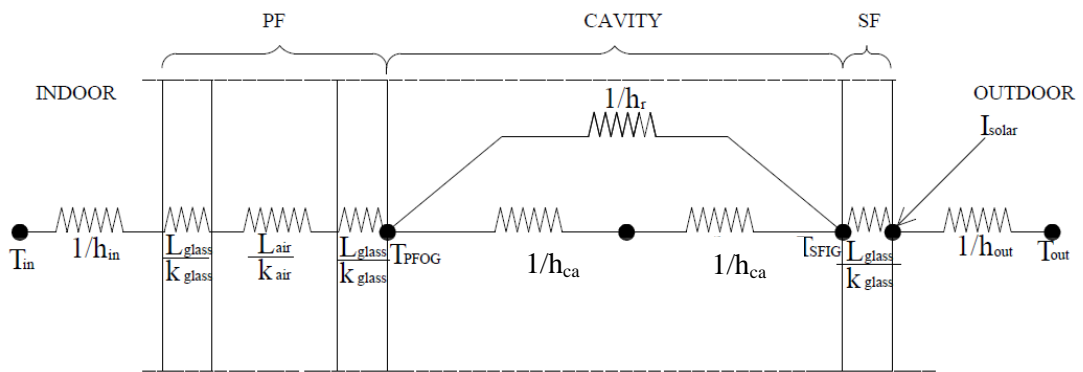


Figure 5.95. Nodal model of DSF

Energy balance can be written separately based on the thermal resistance diagram shown in Figure 5.95:

**Energy balance for Secondary Facade (SF)**

$$I_{solar} \alpha_{SF} = U_{SF}(T_{SF} - T_{out}) + h_{ca}(T_{SF} - T_{ca}) + h_r(T_{SF} - T_{PF}) \quad (5.50)$$

**Energy balance for Cavity air (CA)**

$$\rho W c_v \frac{dT_{ca}}{dt} = h_{ca}(T_{PF} - T_{ca}) + h_{ca}(T_{SF} - T_{ca}) \quad (5.51)$$

**Energy balance for Primary Facade (PF)**

$$I_{solar} \tau_{SF} \alpha_{PF} = U_{PF}(T_{PF} - T_{in}) + h_{ca}(T_{PF} - T_{ca}) + h_r(T_{PF} - T_{SF}) \quad (5.52)$$

With the solution of this equation set with three unknowns (Equations 5.50-52) together with the change by time in the air temperature in the cavity, the temperature values of the interior surface of the DSF which faces the cavity can be calculated. Since the experimental studies are done under steady state condition, time dependent temperature value in the Equation 5.51 is zero. So these equations can be solved by matrix algorithm as;

$$\begin{bmatrix} A & -h_{ca} & -h_r \\ h_{ca} & -2h_{ca} & h_{ca} \\ -h_r & -h_{ca} & B \end{bmatrix} \begin{bmatrix} T_{SF} \\ T_{ca} \\ T_{PF} \end{bmatrix} = \begin{bmatrix} X_1 \\ 0 \\ X_2 \end{bmatrix} \quad (5.53)$$

where A, B, X<sub>1</sub> and X<sub>2</sub> parameter are defined respectively as below:

$$A = U_{SF} + h_{ca} + h_r \quad (5.54)$$

$$B = U_{PF} + h_{ca} + h_r \quad (5.55)$$

$$X_1 = \alpha_{SF} I_{solar} + U_{SF} T_{out} \quad (5.56)$$

$$X_2 = \alpha_{PF}\tau_{SF}I_{solar} - U_{PF}T_{in} \quad .(5.57)$$

The coefficients given above are related to the convective heat transfer coefficients and thermal radiation in the cavity, and the heat transfer coefficients to the indoor and to the outdoor surfaces. Solar radiation value and the radiation features of both of these glasses are also used in calculating these values. As these coefficients are temperature dependent,  $T_{PF}$ ,  $T_{SF}$  and  $T_{ca}$  are determined using thermophysical parameters under temperature consideration. The parameters and thermophysical data which are used here are defined in detail respectively below.

### **SF**

The values which are given in Equation (5.50) are seen in Table 5.16. Here the transmissivity coefficient ( $\tau_{SF}$ ) are accepted as 0.71 and the absorption coefficient ( $\alpha_{SF}$ ) as 0.12 and the heat conductivity coefficient of the glass ( $k_{glass}$ ) is taken as 0.92W/m°C (Çengel, 2011). The value of outdoor convective heat transfer coefficient ( $h_{out}$ ) has been assumed that 1/0.13 W/m<sup>2</sup>°C. In this way, the value of the overall heat transfer coefficient of the secondary facade ( $U_{SF}$ ) has been calculated like below in Equation (5.37):

$$U_{SF} = \left( \frac{L}{k_{glass}} + \frac{1}{h_{out}} \right)^{-1} \quad (5.37)$$

$$h_{out} = 1/0.13 \quad (5.58)$$

In this study, the cavity is closed and analyzed as free convection in a rectangular enclosure. In calculating the cavity facades' convective heat transfer coefficient ( $h_{ca}$ ), the Equation (5.59) has been used based on the reference; MacGregor and Emery (1969):

$$Nu = 0.46 * Ra_L^{1/3} \quad (5.59)$$

where Ra number is calculated like below:

$$Ra_L = \frac{g\beta(T_{SF} - T_{PF})L^3}{\nu\alpha} \quad (5.13)$$

Here  $\beta$ ,  $\nu$  and  $\alpha$  values are defined for each condition depending on the film temperature calculated using average values of  $T_{PF}$  and  $T_{SF}$  plus  $T_{ca}$  and the value is divided by two. So Nusselt number is calculated like:

$$Nu = \frac{h_{ca}L}{k_f} \quad (5.60)$$

Here the conductivity coefficient of the air has been defined for each condition depending on the  $k_f$  temperature. From here,  $h_{ca}$  value is calculated, and the all values are given in Table 5.17:

Table 5.17. Heat transfer convective coefficients,  $h_{ca}$  in the cavity's surfaces namely SF and PF

Exp. #	Film temper.	Thermal diffusivity	kinematic viscosity	Ra	Nu	Thermal conduct.	Convect. Coeff.
	$T_f$ , K	$\alpha$ , m <sup>2</sup> /s <sup>2</sup>	$\nu$ , m <sup>2</sup> /s	-	-	$k_f$ W/m°C	$h_{ca}$ W/m <sup>2</sup> °C
46	307.04	0.00002262	0.00001645	9740297	98.24	0.02654	10.43
47	289.93	0.00002032	0.00001486	1103066	47.53	0.02489	4.73
48	296.89	0.00002124	0.0000155	392059	33.67	0.02542	3.42
49	302.74	0.00002203	0.00001604	128955	23.24	0.02585	2.40
50	312.40	0.00002336	0.00001695	247839	28.89	0.02656	3.07
51	317.97	0.00002413	0.00001748	1554342	53.29	0.02698	5.75

To calculate the radiative heat transfer coefficient, the following equation below is used (Saadon et al., 2016). Emissivity coefficient of both primary facade (PF) and secondary facade (SF) are equal to 0.9 (Cengel, 2011). Temperature values are given in K in Equation (5.41).

$$h_r = 4\sigma \left( \frac{T_{PF} + T_{SF}}{2} \right)^3 \left( \frac{1}{\frac{1}{\varepsilon_{PF}} + \frac{1}{\varepsilon_{PF}}} \right) \quad (5.41)$$

The values which have been acquired by using the Equation 5.41 are given together as; 4.09, 3.81, 3.79, 3.79, 3.79 and 3.84 W/m<sup>2</sup>K, respectively for the experiments numbered 46 to 51.

### **Cavity**

In Equation 5.51, accordingly, the value of  $\frac{dT_{ca}}{dt}$  gives the change of the air of the cavity along the time. So this value is considered using time dependent boundary conditions. If the analysis is steady state, time dependent temperature is zero as the experimental studies here.  $c_p$  is the specific heat of air and it has been defined depending on the change in the temperature of the air. Here the average convection coefficient for the interior surface of the cavity in the primary facade has been regarded as the equal with the other surface. These values can be seen in Table 5.17.

### **PF**

The transmissivity coefficient ( $\tau_{PF}$ ) which has been expressed in the Equation 5.52 has been accepted as 0.83 and the value of the absorption coefficient ( $\alpha_{PF}$ ) as 0.22. For PF, the overall heat transfer coefficient is given in Equation 5.61.

$$U_{PF} = \left[ \frac{1}{h_{in}} + \left( \frac{L}{k_{glass}} * 2 \right) + \frac{L_{air}}{k_{air}} \right]^{-1} \quad (5.61)$$

In the calculation of  $h_{in}$ , experimental data have been used and the results are given in Table 5.18. Accordingly, the energy balance for the double glass:

$$U_{DG}(T_{PFIG} - T_{PFOG}) = h_{in}(T_{PFIG} - T_{in}) \quad (5.43)$$

Here  $U_{DG}$  is the overall hear transfer coefficient of the double glass and it is calculated as in Equation 5.44:

$$U_{DG} = \left( 2 * \frac{L}{k_{glass}} + \frac{L_{air}}{k_{air}} \right) \quad (5.44)$$

Here the change of  $k_{air}$  depending on the temperature has been considered.

Table 5.18. Heat transfer convective coefficients,  $h_{in}$  in the inside's surface

$T_{in}$	$T_{PFOG}$	$T_{PFIG}$	$U_{DG}$	$q$	$U_{PF}$	$h_{in}$
°C	°C	°C	W/m <sup>2</sup> °C	W/m <sup>2</sup>	W/m <sup>2</sup> °C	W/m <sup>2</sup> °C
15.93	29.96	22.83	2.10	14.94	1.06	2.17
14.16	16.36	16.25	2.04	0.22	0.10	0.11
16.74	22.78	20.56	2.07	4.59	0.76	1.20
21.91	28.56	26.20	2.10	4.96	0.75	1.16
20,79	38.16	23.92	2.12	30.24	1.74	9.66
30.48	42.91	37.27	2.18	12.27	0.99	1.81

Together with the change in the temperature of the cavity air and the surface temperatures of the primary facade (PF) and secondary facade (SF) which faces the cavity, the comparisons of the values of the temperature which have been calculated by using the nodal network model with the experimental measurement results are shown below for the different working conditions. It is seen that the air temperature ( $T_{ca}$ ) in the cavity at two points which have been acquired from the half of the experimental measurement results are coherent with the numerical results which are shown with markers in the figures (Figures 5.96-5.101). When the surface temperatures are compared depending on the experimental measurement and nodal network results, it is seen that the temperature are not coherent with the measurements in the middle of the glass surfaces. This difference especially the experiments numbered 49 and 51 can be seen prominently due to the fact that it is not symetric solar radiation effect through the facade surfaces mentioned in the calibration section.

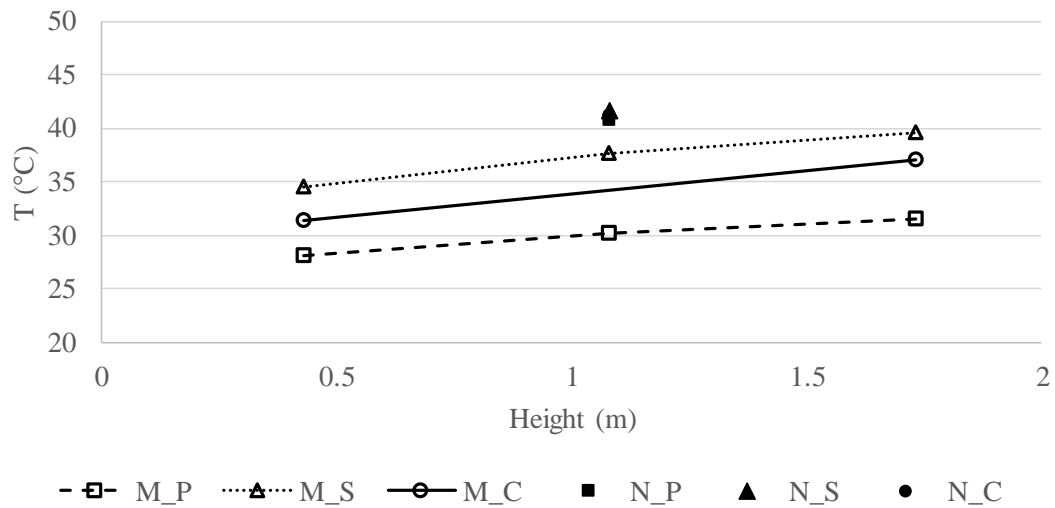


Figure 5.96. Temperatures measurements (denoted by M) versus nodal network model results (denoted by N) for the experiment numbered 46

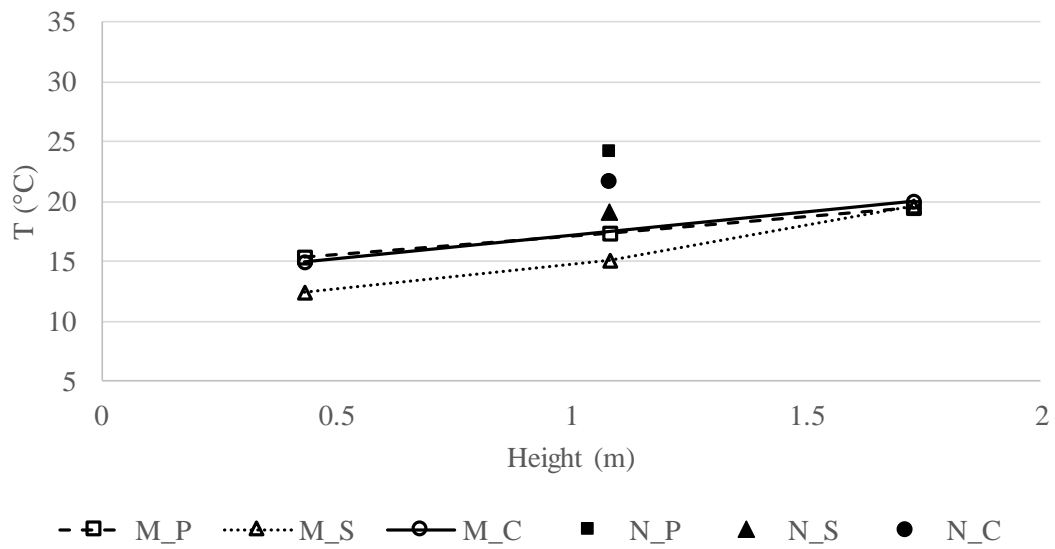


Figure 5.97. Temperatures measurements (denoted by M) versus nodal network model results (denoted by N) for the experiment numbered 47

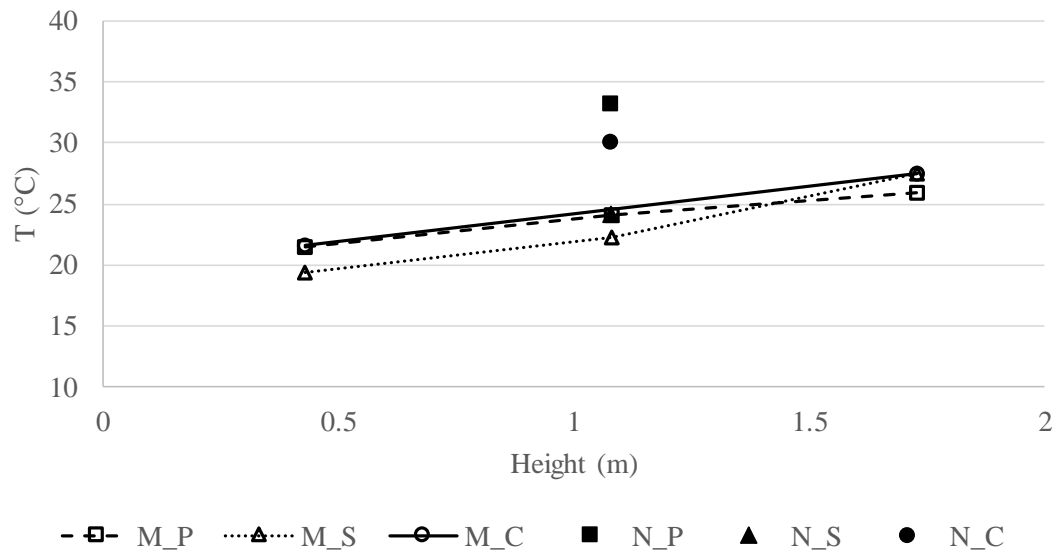


Figure 5.98. Temperatures measurements (denoted by M) versus nodal network model results (denoted by N) for the experiment numbered 48

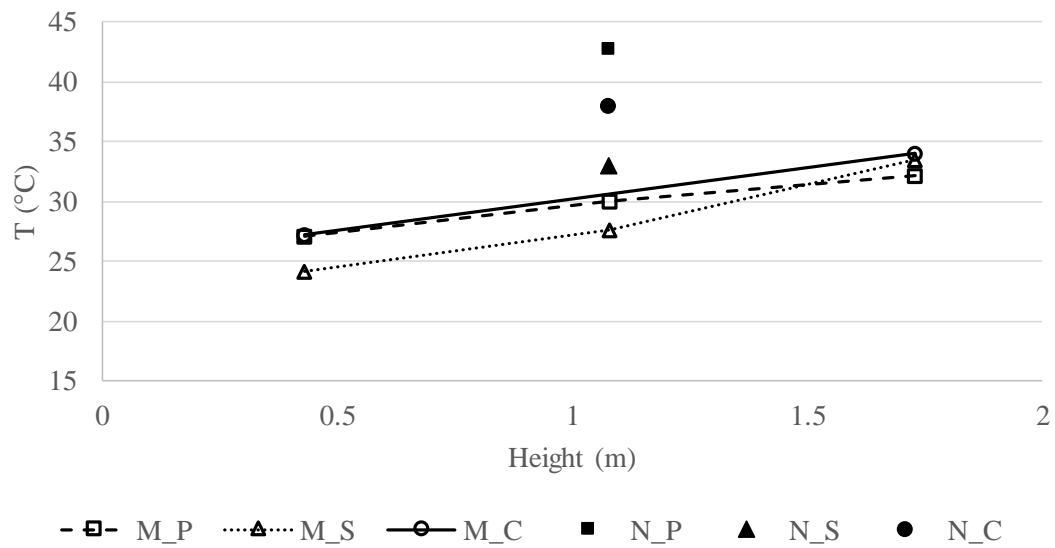


Figure 5.99. Temperatures measurements (denoted by M) versus nodal network model results (denoted by N) for the experiment numbered 49



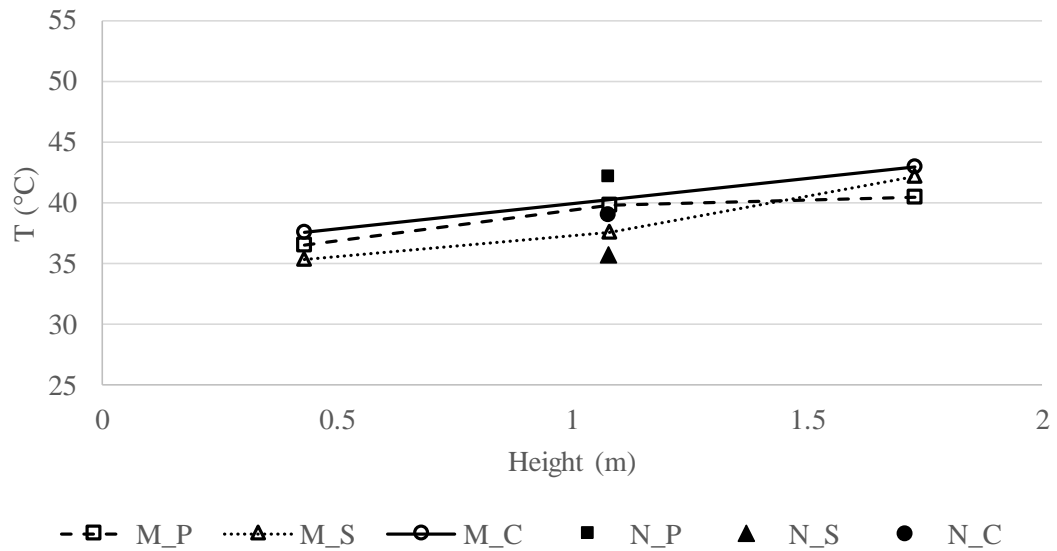


Figure 5.100. Temperatures measurements (denoted by M) versus nodal network model results (denoted by N) for the experiment numbered 50

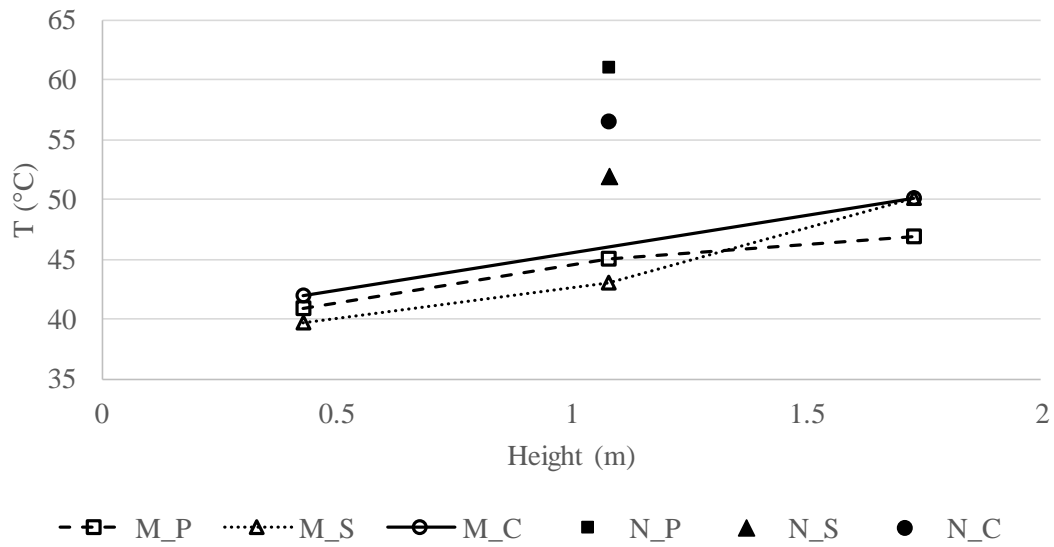


Figure 5.101. Temperatures measurements (denoted by M) versus nodal network model results (denoted by N) for the experiment numbered 51

#### 5.5.4. Discussion and Results of Unsteady Study

In this case, time dependent analyses are realized for buffer zone cavity condition by using monthly average of January and July daily climatic data in Ankara. DSF and SSF are compared. The results were given below. Firstly, Equation 5.53 is

modified and Equation 5.62 is organized. Therefore, the change in the cavity air level is observed.

$$\begin{bmatrix} A & -h_{ca} & -h_r \\ h_{ca} & -2h_{ca} & h_{ca} \\ -h_r & -h_{ca} & B \end{bmatrix} \begin{bmatrix} T_{SF} \\ T_{ca} \\ T_{PF} \end{bmatrix} = \begin{bmatrix} X_1 \\ \rho W c_v \frac{dT_{ca}}{dt} \\ X_2 \end{bmatrix} \quad (5.62)$$

Heat transfer due to the temperature difference from time dependent analyses is given in Figure 5.102 for DSF and SSF in January. Besides, heat transfer due to the solar radiation for DSF and SSF is illustrated in Figure 5.103.

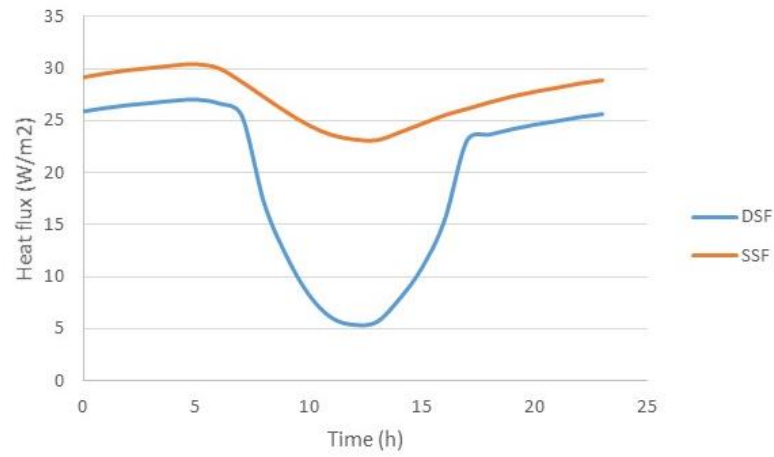


Figure 5.102. Heat transfer rate per unit area due to temperature difference for DSF and SSF using monthly average of January daily climatic data in Ankara for south direction

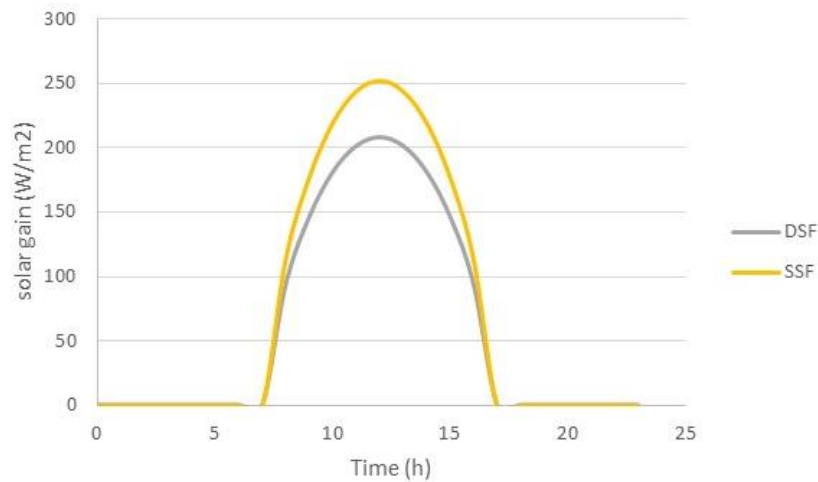


Figure 5.103. Heat gain from the solar radiation transmitted from DSF and SSF by using monthly average daily data of January in Ankara for south direction

Heat transfer due to the temperature difference from time dependent analyses is given in Figure 5.104 for DSF and SSF in July. Besides, heat transfer due to the solar radiation for DSF and SSF is illustrated in Figure 5.105.

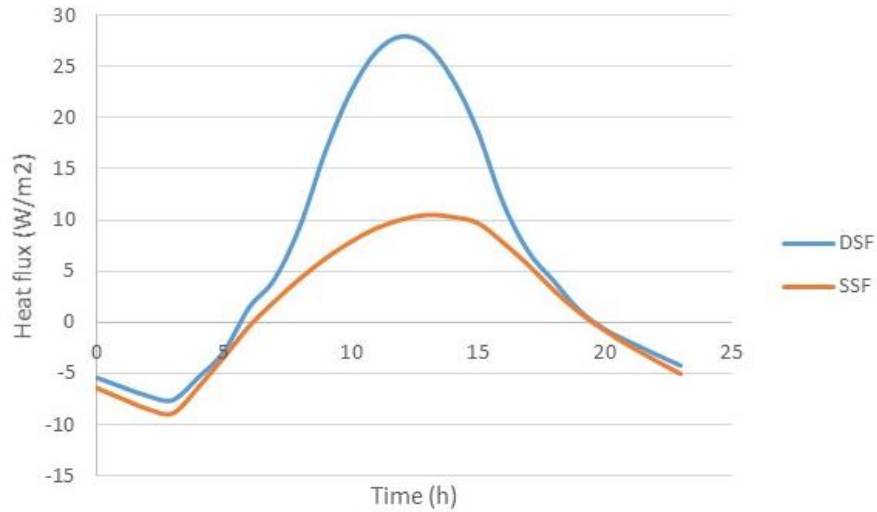


Figure 5.104. Heat transfer rate per unit area due to temperature difference for DSF and SSF using monthly average of July daily climatic data in Ankara for south direction

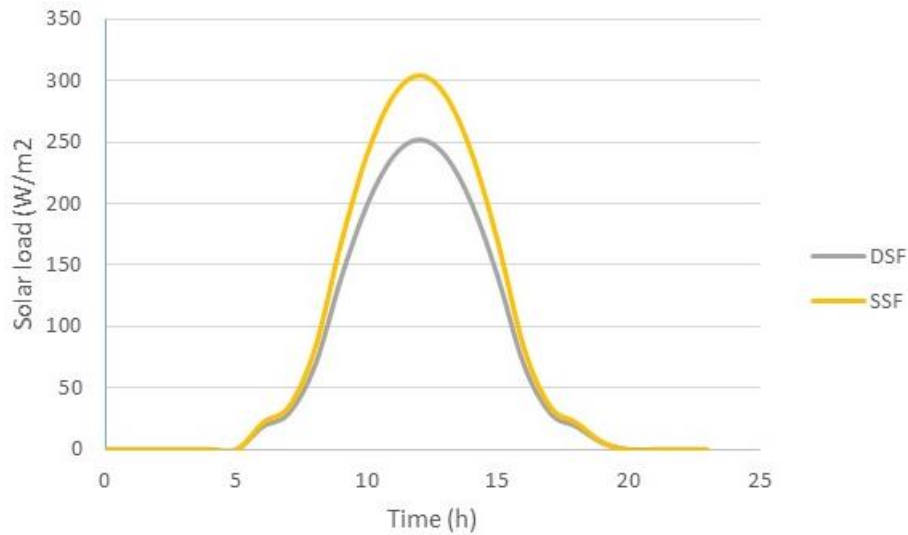


Figure 5.105. Heat gain from the solar radiation transmitted from DSF and SSF by using monthly average daily data of July in Ankara for south different directions

The total heating and cooling load based on orientations for DSF and SSF is given in Figure 5.106 and 5.107 for January and July. While heat gains occur in January from south direction, heat losses occur in January from North direction.

In July, significant heat gains occur from East and West directions due to the solar radiation effects.

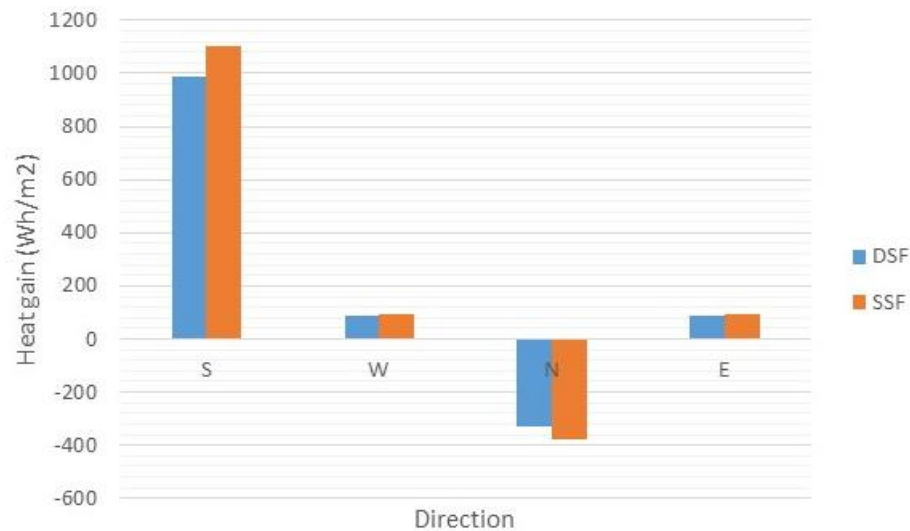


Figure 5.106. Heat transfer comparison of DSF and SSF for different orientation in Ankara for January

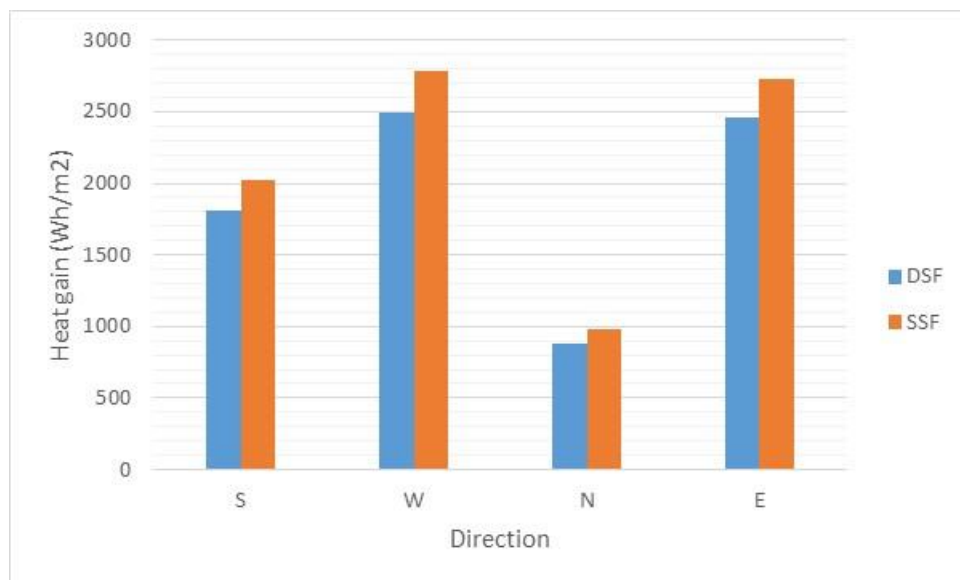


Figure 5.107. Heat transfer comparison of DSF and SSF for different orientation in Ankara for July

Buffer zone air flow mode can be used in Ankara in winter period in the north and south facades. It is meaningless to use DSF in east and west directions, because it causes significant overheating problems in summer period. In order to prevent excessive heating in the cavity, the heated air definitely should be evacuated. Buffer zone mode is not appropriate to use in the east and west facades.

For Ankara, usage of the buffer zone does not make any difference in east and west in terms of heat gain; however, it reduces heat losses in the north facade approximately 15%. Also, it causes an approximately 10% decrease in heat gain in the south facade. In the south facade, for Ankara, both DSF and SSF causes a significant heat gain. In summer period, in east and west directions, for both DSF and SSF heat gains are considerably high. Therefore, application of the buffer zone is not appropriate for east and west direction.

## CHAPTER 6

### CONCLUSIONS

In this study, airflow and heat transfer in a double skin facade (DSF) cavity were examined numerically and experimentally under natural and forced flow conditions. For this purpose, an experimental setup was constructed in the building physics laboratory in the Department of Architecture in IZTECH. Experiments were performed for two different DSF's airflow modes, namely buffer zone (natural flow) and external air channel (forced flow). These experiments were conducted with and without a solar simulator.

The case studies in the thesis were divided into the five groups. In the first case study (Case 1), in order to create a pressure drop in the cavity, two distinct perforated metal sheets were used and the experiments were performed with and without the solar simulator. Air inlets in the upper and lower area of the exterior single glass facade which was also linked to the fan, were opened and two distinguished perforated plates were installed inside of the DSF's cavity for creating pressure drop. Fluid velocity, temperature and solar radiation were measured with pressure loss measurement in the cavity for simulating different kind of elements which cause the pressure drop. This case was evaluated experimentally. In the second case study (Case 2), air inlets in the upper and lower area of the exterior single glass facade were closed. Cavity was designed as airtight. For different interior and exterior temperature levels, temperature distributions occurring with natural convection in the closed cavity were measured. Case 2 was examined both experimentally and numerically. In the third case (Case 3), experiments were carried out at different air flow rates for various cavity depth values by actuating the air channel without using the solar simulator. This case was examined both experimentally and numerically. In the fourth case (Case 4), the case included the one with the solar simulator and the experiments were carried out at various cavity depth values for different air flow rates depending on the lamp configurations obtained different solar radiation loads. In this case, nodal network approach was used with the experimental results. After the validation, the energy performance of DSF applications for different orientations and climatic zones in Turkey (for İstanbul and İzmir climatic conditions) were investigated and compared with the single skin facade (SSF).

Following these four cases, in the last case, the cavity was blocked for entry and exit of the air flow and the experiments were performed for the natural convection under the steady state condition with using the solar simulator. After that, the energy performance of DSF applications for different orientations were also investigated and compared with the SSF applications for Ankara's climatic conditions. In each experimental study, the whole system was activated in order to equilibrate at the desired conditions and following the thermal equilibrium was reached, measurements were performed at the steady state conditions.

In Case 1, pressure drops created by the perforated plates and temperature distributions created by using the conditioned water and the refrigeration based cooling system separately with and without a solar simulator in the cavity of DSF were examined based on experimental measurements. All experimental results with the surfaces and the air temperature distributions in the cavity and pressure drops under three different air flow rates and two distinct perforated plates having different geometric configurations were fully described in the study. The dimensionless pressure drop coefficient,  $Eu$ , versus Reynolds number were determined experimentally for different geometric characteristic of the perforated plates.  $Eu$  numbers were independent of the  $Re$  numbers after 30000 approximately. Results from the 18 experimental studies under steady-state conditions were collected to create an extended data set for the validation of potential numerical studies. A porous media approximation can be useful to predict the air flow characteristics in the cavity for future studies.

Perforated elements, plants and shading devices which are used for different purposes in the cavity create significant pressure drop. Due to the friction effect which is created by these perforated elements, buoyancy forces can be insufficient in the natural convection applications; or as it is in this study, it causes increasing of the necessary fan capacity which is required in forced convection. With this study in which this aspect is firstly focused on, dimensionless pressure drop has been defined under certain conditions. Furthermore, in this study and in other cases a large data set has been formed. These data sets can be used to verify then numerical studies. Correlations which have been acquired for the forced flow conditions can be used for solution of the problems which are faced in different DSF applications.

In the Case 2, numerical and experimental studies were conducted to investigate the flow and heat transfer characteristics inside a double skin facade as an enclosed cavity. A numerical model was developed to simulate the steady state natural

convection inside a tall cavity. The comparative results showed that the current model could successfully predict the velocity field and the temperature variations inside the domain. The velocity field variations showed that increasing the temperature difference to approximately 65% did not cause a large difference in the working conditions. Even though the velocity field remained constant, the heat transfer increased by approximately 20% by increasing the temperature difference from 7K to 11.8K. A correlation was developed to predict the Nusselt numbers with the Rayleigh number ranging from  $8.59 \times 10^9$  to  $1.41 \times 10^{10}$  for an airproof DSF.

In Case 3, numerical and experimental studies were conducted to investigate the flow and heat transfer characteristics through the double skin facade with an external air flow mode. A numerical model was developed to simulate the steady state forced convection inside a DSF cavity. Flow through the DSF cavity were in the thermal and hydrodynamic entrance region for almost all numerical experiments. Design of cross section area of air inlet and outlet was significant. Because, high pressure drop and heat transfer values could be observed at the entrance regions. A correlation was developed to predict the Nusselt numbers with the Reynolds numbers ranging from 28000 to 56000 for a DSF with an external airflow mode. The correlations could be used for different characteristic length which was between 0.1 to 0.16.

The importance of the design of the air inlet and outlet in the cavity has been emphasized for the external air flow mode. Especially as it is in this study, in the air inlet where the air is taken into with a 90 degree turn, there occurs significant pressure losses. This increases the heat transfer due to the high velocities/high convection coefficients at the same time. Therefore, the design of the smooth entrance should be taken into account as an important factor.

For the buffer zone and external air channel air flow mode, İstanbul, Ankara and İzmir provinces, which demonstrate three different climate region of Turkey, have been selected and using their climatic data, DSF applications in different directions have been compared with SSF.

In Case 4, firstly the nodal network approach which was described by using the results obtained from the experiments was compared for that working conditions. This nodal energy balance approach was used for İstanbul and İzmir's climatic condition after reaching acceptable results for the external airflow mode in the cavity. Heating and cooling loads in DSF for İstanbul and İzmir were analyzed and compared with single skin facade (SSF). Convective heat transfer coefficients inside the both cavity surfaces



were determined by using the correlation obtained from the CFD analysis in Case 3. Double skin facade in which the external air flow mode is used is not appropriate to use in east and west facades for the Izmir and Istanbul provinces for solar radiation gain in summer period. In the south facade in the winter period, while the usage of DSF creates an approximately 30% disadvantage, in summer period, it provides approximately an advantage of 20%. In the north facade, heating cooling loads are both low in DSF and SSF (single skin facade) applications. Exhausting of this energy to the outside in summer season is very important. Intake of the heated airflow linking the cavity air connected with a HVAC system in winter season is very significant in terms of energy efficient usage of DSF. Therefore, the energy level of the air in the cavity of DSF significantly increases in the external air flow mode. When this energy is used for preheating purpose in HVAC system, usage of DSF gains more meaning.

In Case 5, Buffer zone mode in Ankara can only be used north and south directions in winter period. In summer period, the heated air in the cavity must be evacuated in the north and south facades. Buffer zone mode is not appropriate to use in the east and west facades because of causing significant overheating problems in summer period. In order to prevent excessive heating in the cavity, the heated air definitely should be evacuated. Buffer zone mode reduces heat losses in the north facade approximately 15% and it causes an approximately 10% decrease in heat gain in the south facade. It has been observed that glass usage in east and west is not appropriate for all of the three climate regions namely Izmir, Istanbul and Ankara.

## REFERENCES

ANSYSInc. (2009). ANSYS-FLUENT 14.0 Theory Guide.

Arici, M. and Karabay, H. (2010). Determination of optimum thickness of double-glazed windows for the climatic regions of Turkey. *Energy and Buildings*, 42, 1773–1778.

Arons, D.M.M., and Glicksman, L.R. (2001). Double skin, airflow facades: Will the popular European model work in the USA? *Proceedings of ICBEST*, International Conference on Building Envelope Systems and Technologies, Ottawa, Canada, 1, 203-207.

Asdrubali, F. and Baldinelli, G. (2007). A new double skin facade with integrated movable shading systems: numerical analysis and evaluation of energy performance. Energy, climate and indoor comfort in mediterranean countries. *Proceedings*, Genova, Italy, 5-7 September 2007.

Azarbayjani, M. and Anderson, J. (2010). Beyond Arrows: CFD modeling of a new, naturally ventilated, double skin facade configuration in a chicago high-rise office building. *Simbuild, Fourth National Conference of IBPSA-USA* New York City, New York, August 11-13.

Baker, P., Saelens, D., Grace, M., and Inoue, T. (2000). Advanced Envelopes—Methodology, Evaluation and Design Tools, Final report IEA Annex 32 (IBEPA), Leuven: Acco.foesterle.

Balocco, C. (2002). A simple model to study ventilated facades energy performance. *Energy and Buildings*, 34, 469-475.

Bayazit, Y., Sparrow, E.M., and Joseph, D.D. (2014). Perforated plates for fluid management: Plate geometry effects and flow regimes, *International Journal of Thermal Sciences*, 85, 104-111.

Betts, P.L., and Bokhari, I.H. (2000). Experiments on turbulent natural convection in an enclosed tall cavity, *International Journal of Heat and Fluid Flow*, 21 (6), 675–683.

- Betts, P.L., and Bokhari, I.H. (2000). Experiments on turbulent natural convection in an enclosed tall cavity, *International Journal of Heat and Fluid Flow*, 21 (6), 675-683.
- Cengel, Y. (2011). Heat and mass transferi, Güven press, 3th edition, İzmir.
- Chan, A.L.S., Chow, T.T., Fong, K.F., and Lin Z. (2009). Investigation on energy performance of double skin facade in Hong Kong. *Energy and Buildings*, 41,1135–42.
- Choi, S.K., Kim, E.K., Wi, M.W., Kim, S.O. (2004). Computation of a turbulent natural convection in a rectangular cavity with the low-reynolds-number differential stress and flux model, *KSME International Journal*, 18 (10), 1782-1798.
- Choi, W., Joe, J., Kwak, Y., and Huh, J.H. (2012). Operation and control strategies for multi-storey double-skin facades during the heating season, *Energy and Buildings*, 49 454-465.
- Chou, S.K., Chua, K.J., and Ho, J.C. (2009). A study on the effects of double skin facades on the energy management in buildings. *Energy Conservation and Management* 50, 2275-2281.
- Chow, C.L. (2012). Full-scale burning tests on double-skin facade fires. Fire and Materials. Published online in Wiley Online Library (wileyonlinelibrary.com). DOI: 10.1002/fam.1127.
- Chow, W.K. and Hung, W.Y. (2006). Effect of cavity depth on smoke spreading of double-skin façade. *Building and Environment*, 41, 970-979.
- Compagno, A. (2002). Intelligente Glasfassaden: Material, Anwendung, Gestaltung = Intelligent glass facades: material, practice, design. Intelligent glass facades, Basel; Boston:183.
- Davis, G.D.V. (1968) Laminar natural convection in an enclosed rectangular cavity, *International Journal of Heat and Mass Transfer*, 11(11), 1675–1693.
- Ding, W., Hasemi, Y., and Yamada, T. (2005). Natural ventilation performance of a double-skin facade with a solar chimney. *Energy and Buildings*, 37, 411-418.

- Eicker, U. (2003). Solar Technologies for buildings, John Wiley & Sons Inc. USA.
- Eicker, U., Fux, V., Bauer, U., Mei, D., and Infield, D. Facade and summer performance of buildings. *Energy and Building*, 40, 600-611.
- Evins, R., Pointer, P., and Vaidyanathan, R. (2011). Multi-objective Optimisation of the Configuration and Control of a Double-Skin Facade. *Proceedings of Building Simulation*, 1343-1350. 12th Conference of International Building Performance Simulation Association, Sydney, 14-16 November.
- Faggebauu, D. (2006). Heat transfer and fluid-dynamics in double and single skin facades. Universitat Politècnica de Catalunya (UPC). Doctoral Thesis.
- Fang, W., Xiaosong, Z., Junjie, T., and Xiuwei, L. (2011). The thermal performance of double skin facade with Tillandsia usneoides plant curtain, *Energy and Buildings*, 43 (9) 2127-2133.
- Fossa, M., Menezo, C., Leonardi, E. (2008). Experimental natural convection on vertical surfaces for building integrated photovoltaic (BIPV) applications, *Experimental Thermal and Fluid Science*, 32 (4), 980–990.
- Gavan, V., Woloszyn, M., and Kuznik, F., J.J. Roux. (2010). Experimental study of a mechanically ventilated double-skin facade with venetian sun-shading device: A full-scale investigation in controlled environment, *Solar Energy*, 84, 183-195.
- Gavan, V., Woloszyn, M., Kuznik, F., and Roux, J.J. (2010). Experimental study of a mechanically ventilated double-skin facade with venetian sun-shading device: A full-scale investigation in controlled environment. *Solar Energy*, 84, 183-195.
- Gavan, V., Woloszyn, M., Roux, J.J., Muresan, C. and Safer, N. (2007). An investigation into the effect of ventilated double-skin facade with venetian blinds: Global simulation and assessment of energy performance. *Proceedings: Building simulation*.
- Gelesz, A., and Reith, A. (2011). Classification and Re-Evaluation of Double Skin Facades 17th Building Services, Mechanical and Building Industry Days. *Urban Energy Conference*, 13-14 October 2011, Debrecen, Hungary 65-72.

- Gosselin, J.R. (2005). IEA-ECBCS Annex 44, Subtask A contribution to the state of the art Report.
- Gratia, E. and De Herde, A. (2007). Guidelines for improving natural daytime ventilation in an office building with a double-skin facade. *Solar Energy*, 81, 435-448.
- Gratia, E., and Herde, A. (2004). Optimal operation of a south double-skin façade. *Energy and Buildings*, 36, 41-60.
- Guardo, A., Coussirat, M., Egusquiza, E., Alavedra, P., and Castilla, R. (2009). A CFD approach to evaluate the influence of construction and operation parameters on the performance of Active Transparent Facades in Mediterranean climates. *Energy and Buildings*, 41, 534–542.
- Høseggen, R., Wachenfeldt, B.J., and Hanssen, S.O. (2008). Building simulation as an assisting tool in decision making Case study: With or without a double-skin facade? *Energy and Buildings*, 40, 821-827.
- Haase, M. and Amato, A. (2009). A study of the effectiveness of different control strategies in double skin facades in warm and humid climates. *Journal of Building Performance Simulation*, 2(3), 179–187.
- Haase, M., and Amato, A. (2005). Development of a double-skin facade system that combines airflow windows with solar chimneys. *The 2005 World Sustainable Building Conference*, 763-770, 27-29 September 2005, Tokyo, Japan.
- Haase, M., and Amato, A. (2005c). Fundamentals for climate responsive envelopes. *Glass in Buildings 2 Conference*, Bath, UK.
- Haase, M., and Wong, F., and Amato, A. (2007). Double–Skin Facades for Hong Kong. *Surveying & Built Environment*, 18 (2), 17-32.
- Haase, M., Marques da Silva, F. and Amato, A. (2009). A. Simulation of ventiated facades in hot and humid climates. *Energy and Buildings*, 41, 361-373.
- Hamdan, M.A. (1994) Thermal gains through windows. *Energy Conservation and Management*, 35, 861-872.

- He, Y., Chen, M., and Wang, X. (2012). A Brief Discussion and Analysis on Methods of High Performance Architecture Facades Design. *Advanced Materials Research*, 368-373, 3757-3760.
- Hendriksen, O.J., Sørense, H., Svensson, A. and Aaqvis, P. (2001). Double Skin Facades – Fashion or a Step Towards Sustainable Buildings.  
[http://ptp.irb.hr/upload/mape/kuca/01\\_Ole\\_Juhl\\_Hendriksen\\_Double\\_Skin\\_Facades\\_Fashion\\_or\\_a\\_step.pdf](http://ptp.irb.hr/upload/mape/kuca/01_Ole_Juhl_Hendriksen_Double_Skin_Facades_Fashion_or_a_step.pdf).
- Hensen, J. Bartak, M. and Drkal, F. (2002). Modeling and simulation of a double-skin facade system/discussion, *ASHRAE Transactions*, 108, 1251-1259.
- Holman, J.P. (2011). *Experimental Methods for Engineers*, Eighth Edition, McGraw-Hill.
- Huang, S., Mac, T., Wang, D., and Lin, Z. (2013). Study on discharge coefficient of perforated orifices as a new kind of flowmeter, *Experimental Thermal and Fluid Science*, 46, 74–83.
- Infield, D. Mei, L. Eicker, U. 2004. Thermal performance estimation for ventilated PV façades, *Solar Energy*, 76, 93-98.
- Iyi, D., Hasan, R., and Penlington, C. (2014) Underwood, Double skin façade: Modelling technique and influence of venetian blinds on the airflow and heat transfer, *Applied Thermal Engineering*, 71 (1), 219-229.
- Jiru, T.E., and Haghighat, F. (2008). Modeling ventilated double skin facade-A zonal approach, *Energy and Buildings*, 40 (8), 1567-1576.
- Jiru, T.E., Tao, Y.X. and Haghighat, F. (2011). Airflow and heat transfer in double skin facades. *Energy and Buildings*, 43, 2760–2766.
- King, K.J. (1989). Turbulent natural convection in rectangular air cavities, Ph.D. dissertation, Queen Mary College, University of London.
- Kleiven, T. (2003). Natural ventilation in buildings. Norwegian University of Science and Technology, Faculty of Architecture and Fine Art, Department of Architectural Design, History and Technology.

- Kuznik, F., Catalina, T., Gauzere, L., Woloszyn, M., and Roux, J.J. (2011). Numerical modelling of combined heat transfers in a double skin façade-Full-scale laboratory experiment validation, *Applied Thermal Engineering*, 31 (14-15), 3043-3054.
- Kuznik, F., Catalina, T., Gauzere, L., Woloszyn, M., and Roux, J.J. (2011). Numerical modelling of combined heat transfers in a double skin façade- Full scale laboratory experiment validation, *Applied Thermal Engineering*, 31, 3043-3054.
- Lancour, X., Deneyer, A., Blasco, M., Flament, G., and Wouters, P. (2005). Ventilated Double Skin Façades. Belgian Building Research Institute (BBRI). Contributed Report 03.
- Larsen, S.F., Filippin, C., and Lesino, G. (2014). Thermal simulation of a double skin façade with plants, *Energy Procedia*, 57, 1763-1772.
- Lau, G.E., Yeoh, G.H., Timchenko, V., and Reizes, J.A. (2012). Application of dynamic global-coefficient subgrid-scale models to turbulent natural convection in an enclosed tall cavity, *Physics of Fluids*, 24, <http://dx.doi.org/10.1063/1.4753944>.
- Leonard, B.P., and Mokhtari, S. (1990). Ultra-Sharp Nonoscillatory Convection Schemes for High-Speed Steady Multidimensional Flow, NASA TM 1-2568 (ICOMP-90-12), NASA Lewis Research Center.
- Li, S.S. (2001). A Protocol to Determine the Performance of South Facing Double Glass Façade System. Faculty of the Virginia Polytechnic Institute and State University, Architecture department, Master Thesis.
- Li, Y. and Delsante, A. (2001). Natural ventilation induced by combined wind and thermal forces. *Building and Environment*, 36, 59-71.
- Liu, Y. and Harris, D.J. (2007). Full scale measurements of convective coefficient on external surface of a low-rise building in sheltered conditions, *Building and Environment*, 42, 2718-2736.
- Lancour X., Deneyer A., Blasco M., Flamant G. and Wouters P. (2004). Ventilated Double Facades - Classification & illustration of facade concepts. Rapport de la 2ème biennale du proj'Doubles Façades Ventilées', CSTC, Décembre, Bruxelles.

- Loncour, X., Deneyer, A., Blasco, M., Flament, G. and P. Wouters (2004). Ventilated Double Skin Façades, Belgian Building Research Institute (BBRI), Contributed Report 03.
- Loncour, X., Blasco, M., Flamant, G., Martin, Y., Parmentier, B., Deneyer, A., Schietecat, J., Dupont, E., and Wouters, P. (2003). Evaluation of the existing standard/requirements applying on buildings equipped with double ventilated facades - overview of the existing documents and potential problems. Research report, BBRI.
- Loua, W., Huang, M., Zhang, M., and Linc, N. (2012). Experimental and zonal modeling for wind pressures on double-skin facades of a tall building, *Energy and Buildings*, 54, 179–191.
- Lstiburek J.W. (2008). Why green can be wash. *ASHRAE Journal*, 50(11), 28–36.
- MacGregor, R.K., and Emery A.P. (1969). Free Convection Through Vertical Plane Layers: Moderate and High Prandtl Number Fluids. *Journal of Heat Transfer*, 91(3), 391-401.
- Malavasi, S., Messa, G., Fratino, U., and Pagano, A. (2012). On the pressure losses through perforated plates, *Flow Measurement and Instrumentation*, 28, 57–66.
- Manz, H. (2004). Total solar energy transmittance of glass double façades with free convection, *Energy and Buildings*, 36 (2), 127–136.
- Marco Perino, Valentina Serra. (2006). Advanced Integrated Façades: An Overview based on “Advanced integrated façades state of the art”, Final Report of Subtask A, IEA- ECBCS-ANNEX 44, ed. by F. Marques da Silva, J. Gosselin, dec. 2005. 4th Annex 44 Forum / TORINO / 29 March 2006.
- Mingotti, N., Chenvidyakarn, T., and Woods, A.W. (2011). The fluid mechanics of the natural ventilation of a narrow-cavity double-skin facade. *Building and Environment*, 46, 807-823.
- Missoum, A., Elmir, M., Belkacema, A., Naboua, M., and Draouia, B. (2013). Numerical simulation of heat transfer through a double-walled facade building in arid zone, *Energy Procedia*, 36, 834 – 843.



- Nansteel M.W., and Grief, R. (1984). Natural convection in enclosures with two- and three dimensional partitions, *International Journal of Heat and Mass Transfer*, 27 561–571.
- Nasrollahi, N., and Salehi, M. (2015). Performance enhancement of double skin facades in hot and dry climates using wind parameters, *Renewable Energy*, 83, 1-12.
- Oesterle, E., Lieb, R., Lutz, M., and Heusler, W. (2001). Double-skin Façades – integrated planning. Munich, Prestel Verlag.
- Oesterle, Lieb, Lutz and Heusler. (2001). Double-Skin Façades – Integrated Planning, Prestel Verlag, Munich, Germany.
- Pappas, A. and Zhai, Z. (2008). Numerical investigation on thermal performance and correlations of double skin façade with buoyancy-driven airflow, *Energy and Buildings*, 40, 466-475.
- Pappas, A., and Zhai, Z. (2008). Numerical investigation on thermal performance and correlations of double skin façade with buoyancy-driven airflow, *Energy and Buildings* 40 (4), 466-475.
- Park, C.S. (2003). Occupant-Responsive optimal control of smart facade systems, Ph.D. thesis, Department of Architecture, Georgia Institute of Technology.
- Park, C.S., Augenbroe, G., Messadi, T., Thitisawat, M., and Sadegh, N. (2004). Calibration of a lumped simulation model for double-skin facade systems. *Energy and Building*, 36, 1117-1130.
- Parkin, S. (2003). Development of a contemporary classification for ventilated double-skin facades, *Proceedings of the PLEA 2003 conference*, CHILE, 9-12 November 2003.
- Parkin, S. (2004). A description of a ventilated double-skin façade classification. International Conference on Building Envelope Systems & Technology, Sydney, Australia.
- Pasquay, T. (2004) Natural ventilation in high-rise buildings with double-facades, saving or waste of energy. *Energy and Buildings*, 36, 381-389.

- Pasquay, T. (2004). Natural ventilation in high-rise buildings with double facades, saving or waste of energy. *Energy and Buildings*, 36, 381–389.
- Pasut W., Carli M. De. (2011). Evaluation of various CFD modelling strategies in predicting airflow and temperature in a naturally ventilated Double Skin Façade, *Applied Thermal Engineering*, doi: 10.1016/j.applthermaleng.2011.11.028.
- Pasut, W., and Carli, W.D. (2012). Evaluation of various CFD modelling strategies in predicting airflow and temperature in a naturally ventilated double skin façade, *Applied Thermal Engineering*, 37, 267-274.
- Patankar, (1980). Numerical Heat Transfer and Fluid Flow, Hemisphere, Washington, D.C.
- Perino, M (2005). IEA-ECBCS Annex 44, Subtask A contribution to the state of the art report.
- Poirazis, H. (2006). Double skin façades. International Energy Agency(IEA) Solar Heating and Cooling (SHC) Task 34/IEA Energy Conservation in Buildings and Community Systems ECBCS Annex 43.
- Poirazis, H. (2006). Double Skin Façades. Report of IEA SHC Task 34 ECBCS Annex 43.
- Saadon, S., Gaillard, L., Giroux-Julien, G., and Menezo, C. (2016). Simulation study of a naturally- ventilated building integrated photovoltaic/thermal (BIPV/T) envelope, *Renewable Energy*, 87, 517-531.
- Saelens, D. (2002). Energy Performance Assessments of Single Storey Multiple-Skin Facades. PhD thesis, Laboratory for Building Physics Department of Civil Engineering, Catholic University of Leuven Belgium Weaddress: [http://envelopes.cdi.harvard.edu/envelopes/contentresources/pdf/case\\_studies/PhD\\_Dirk\\_Saelens.pdf](http://envelopes.cdi.harvard.edu/envelopes/contentresources/pdf/case_studies/PhD_Dirk_Saelens.pdf)
- Saelens, D. Carmeliet, J., and Hens, H. (2003). Energy Performance Assessment of Multiple-Skin Facades. *Hvac & R Research*, 9(2), 167-185.
- Saelens, D., Roels, S., and Hens, H. (2008). Strategies to improve the energy performance of multiple-skin facades. *Building and Environment*, 43(4), 638-650.

- Safer, N., Woloszyn, M. and Roux, J.J. (2005). Tree-dimensional simulation with a CFD tool of the airflow phenomena in single floor double-skin facade equipped with a venetian blind. *Solar Energy*, 79, 193-203.
- Safer, N., Woloszyn, M., and Roux, J.J. (2005). Tree-dimensional simulation with a CFD tool of the airflow phenomena in single floor double skin facade equipped with a venetian blind, *Solar Energy*, 79 (2) 193-203.
- Salat, J., Xin, S., Joubert, P., Sergent, A., Penot, F., and Quéré, P.L. (2004). Experimental and numerical investigation of turbulent natural convection in a large air-filled cavity, *International Journal Heat Fluid Flow*, 25 (5), 824–832.
- Saury, D., Rouger, N., Djanna, F., Penot, F. (2011). Natural convection in an air-filled cavity: Experimental results at large Rayleigh numbers, *International Communications in Heat and Mass Transfer*, 38, 679–687.
- Serra, V., Zanghirella, F., and Perino, M. (2010). Experimental evaluation of a climate facade: Energy efficiency and thermal comfort performance. *Energy and Buildings*, 42, 50–62.
- Shameri, M.A., Alghoul, K., Sopian, M., Fauzi, M., Zaina, O.E: (2011). Perspectives of double skin facade systems in buildings and energy saving. *Renewable and Sustainable Energy Reviews*, 1468–1475.
- Silva, F.M., Gomes, M.G., and Rodrigues, A.M. (2015). Measuring and estimating airflow in naturally ventilated double skin facades, *Building and Environment*, 87, 292-301.
- Singh, M.C., Garg, S.N., and Jha, R. (2008) Different glazing systems and their impact on human thermal comfort-Indian scenario. *Building and Environment*, 43,1596-1602.
- Stec, W.J. (2005). Modelling the double skin facade with plants. *Energy and Buildings*, 37(5), 419-427.
- Stec, W.J. van Paassen, A.H.C., and Maziarz, A. (2005). Modelling the double skin facade with plants, *Energy and Buildings*, 37 (5), 419-427.

- Stec, W.J., and van Paassen, A.H.C. (2005). Symbiosis of the double skin façade with the HVAC system, *Energy and Buildings*, 37 (5), 461-469.
- Tanaka, H., Okumiya, M., Tanaka, H., Yoon, G.Y., and Watanabe, K. (2009). Thermal characteristics of a double-glazed external wall system with roll screen in cooling season. *Building and Environment*, 44, 1509-1516.
- Tascón, M.T.(2008). Experimental and Computational Evaluation of Thermal Performance and Overheating in Double Skin Facades. University of Nottingham, Doctor of Philosophy.
- Tian, Y.S., and Karayiannis, T.G. (2000). Low turbulence natural convection in an air filled square cavity. Part I. Thermal and fluid flow fields, *International Journal of Heat and Mass Transfer*, 43, 849–866.
- Tian, Y.S., and Karayiannis, T.G. (2000). Low turbulence natural convection in an air filled square cavity. Part II. The turbulence quantities, *International Journal of Heat and Mass Transfer*, 43, 867–884.
- Tokuç, A., Başaran, T., and Yesügey, S.C. (2015). An experimental and numerical investigation on the use of phase change materials in building elements: the case of a flat roof in İstanbul, *Energy and Buildings*, 102, 91-104.
- Trias, F.X., Gorobets, A., Soria, M., and Oliva, A. (2010). Direct numerical simulation of a differentially heated cavity of aspect ratio 4 with Rayleigh numbers up to 1011 — Part I: numerical methods and time-averaged flow, *International Journal of Heat and Mass Transfer*, 53 (4), 665–673.
- Trias, F.X., Gorobets, A., Soria, M., Oliva, A. (2010). Direct numerical simulation of a differentially heated cavity of aspect ratio 4 with Rayleigh numbers up to 1011 — Part II: heat transfer and flow dynamics, *International Journal of Heat and Mass Transfer*, 53 (4), 674–683.
- Wachenfeld B.J., and Bell, D. (2003). Building integrated energy systems in smart energy efficient buildings - A state of the art. Sintef Report, Trondheim, Norway.
- Weber, L.J., Cherian, M.P., Allen, M.E., Muste, M. (2000). Headloss characteristics for perforated plates and flat bar screens. Technical report. Iowa City, USA: Iowa Institute of Hydraulic Engineering, College of Engineering, University of Iowa. Mar. Report no. 411.

- Widdington, M., and Harris, J. (2002). *Intelligent Skins*, Reed Educational and Professional Publishing.
- Wong, P.C., Prasad, D., and Behnia, M. (2008). A new type of double-skin façade configuration for the hot and humid climate. *Energy and Buildings*, 40, 1941-1945.
- Xaman, J., Alvarez, G., Lira, L., and Estrada, C. (2005). Numerical study of heat transfers by laminar and turbulent natural convection in tall cavities of facade elements, *Energy and Buildings*, 37 (7), 787–794.
- Xu, X., and Yang, Z. (2008). Natural ventilation in the double skin facade with venetian blind, *Energy and Buildings*, 40 (8), 1498-1504.
- Yılmaz, Z. (2006). Tesisat mühendisliği dergisi, 91, 7-15.
- Yılmaz, Z. and Çetintaş, F. (2005). Double skin facade's effects on heat losses of office buildings in Istanbul. *Energy and Buildings*, 37, 691-697.
- Yuan, Y., Zeng, J., Zhu, Y., and Lin, B. (2007). A lumped model of double skin facade with cavity shading. *Proceedings: Building Simulation*.
- Zeng, Z., Li, X., Li, C., Zhu, Y. (2012). Modeling ventilation in naturally ventilated double-skin façade with a venetian blind, *Building and Environment*, 57, 1-6.
- Zhang, Y. and Altan, H. (2011). A comparison of the occupant comfort in a conventional high-rise office block and a contemporary environmentally-concerned building. *Building and Environment*, 46, 535-545.
- Zhou, C. and Xue, N. (2012). The study of vent form of double-skin facade based on CFD. *Advanced Materials Research*, 374-377, 440-444.
- Zhou, J. and Chen, Y. (2010). A review on applying ventilated double-skin facade to buildings in hot-summer and cold-winter zone in China. *Renewable and Sustainable Energy Reviews*, 14, 1321–1328.
- Zöllner, A., Winter, E.R.F. and Viskanta, R. (2002). Experimental studies of combined heat transfer in turbulent mixed convection fluid flows in double skin facades. *International Journal of Heat and Mass Transfer*, 45, 4401-4408.

<http://www.arkiv.com.tr/p9568>

[http://www.eie.gov.tr/turkce/en\\_tasarufu/konut\\_ulas/bina\\_ulas.html](http://www.eie.gov.tr/turkce/en_tasarufu/konut_ulas/bina_ulas.html) (25.02.2010).

Dusseldorf City Gate. (2014, October 28). Retrieved from  
<http://panoramio.com/photo/9668628>

Dusseldorf City Gate. (2014, October 28) Retrieved from  
<http://inhabitat.com/dusseldorfs-hi-tech-energy-efficient-gate/>

Deichtor Office Building. (2014, October 27)  
<http://www.panoramio.com/photo/22361320>

GSW building. (2014, October 28).  
<http://architecturerevived.blogspot.com/2010/04/gsw-headquarters-berlin-germany.html>

SysOpen Tower. (2014, October 28). <http://taloforum.fi/viewtopic.php?t=457>

Seattle Justice Centre. (2014, October 28).  
[http://www.pambeyette.com/artplans.php?item\\_id=35&page=1](http://www.pambeyette.com/artplans.php?item_id=35&page=1)

İstanbul Sapphire. (2014, October 28). <http://www.arkiv.com.tr/p9568>

Küçükçekmece Municipal Services Building. (2014, October 28).  
<http://www.ilkdogadostukamubinası.com/images/etc/Kucukcekmece-Yeni-Binasi-Tanitim.pdf>

Istanbloom building. (2014, October 28).  
<http://www.arkiv.com.tr/proje/istanbloom/2704>

Ankara Telecom Headquarter. (2014, October 28).  
<http://www.atarim.com.tr/tr/proje/turk-telekom>

## APPENDIX A

### MEASUREMENT DEVICES

Table A1. Characteristics of solar simulator

General Characteristics	Value
System Type	Automatic Air Ventilated - Closed Matrix type
Total Electrical Power	13kW (kilo watt)
Number of Lamp	12
Fan	Automatic and can be forced to start manually
Motorized Motion	40cm up down
Lamp Power	1000W (each)
Lamp Type	Metal Halide
Lamp Base	E40
Average Lamp Life	9000 h
Luminaire Types	Symetric Open Luminaire
Cold Start-up Time	4 minutes (average value under normal condition)
Hot restart waiting time	At Least 15 minutes
Main System Supply Voltage	400V Three Phase 50 hz
Initial Lumens	85000 (each)
Colour temperature	7250K
Colour rendering index	90Ra
Structure	Alluminium
Dimensions	3000mm X 1500mm X 2000mm (HxWxD)
Weight	~450Kg

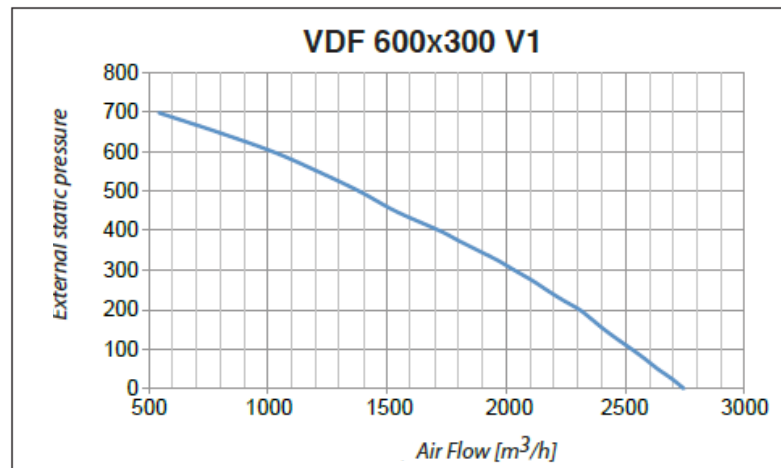


Figure A1. Fan characteristic of the system



Figure A2. Characteristics of HIOKI Data Logger

It consists of 4 units and each unit has 15 channels. The number of input channels can be expanded maximum 60 channels. Channels 1 to 15 provide 10-ms sampling and channels 16 to 30 provide 20-ms sampling. These channels allow you to track waveforms not possible with earlier models. Also comes with high withstand voltage; isolated inputs required when measuring and recording battery cell voltages

Measure and record:

- Temperature & humidity
- A variety of transducer outputs (DC voltage)
- Resistance values



Table A2. MS-410 Characteristics of MS-410 Pyranometer

General Characteristics	Value
System Type	Automatic Air Ventilated - Closed Matrix type
Total Electrical Power	13kW (kilo watt)
Number of Lamp	12
Fan	Automatic and can be forced to start manually
Motorized Motion	40cm up down
Lamp Power	1000W (each)
Lamp Type	Metal Halide
Lamp Base	E40
Average Lamp Life	9000 h
Luminaire Types	Symetric Open Luminaire
Cold Start-up Time	4 minutes (average value under normal condition)
Hot restart waiting time	At Least 15 minutes
Main System Supply Voltage	400V Three Phase 50 hz
Initial Lumens	85000 (each)
Colour temperature	7250K
Colour rendering index	90Ra
Structure	Alluminium
Dimensions	3000mm X 1500mm X 2000mm (HxWxD)
Weight	~450Kg

Table A3. Differential pressure transmitter, DPT 2500-R8

Technical Specifications	
Response time	0.8/4 s selectable by jumper
Measuring unit	selectable by jumper (Pa, kPa,mbar,inchWC, mmWC, psi)
Accuracy	$\pm 1.5\%$ +1Pa
Electrical interface	Supply voltage:24 VAC or VDC $\pm 10\%$
	Power consumption: < 1.0 W (<1.5W with I <sub>out</sub> 20mA
Output signal	0...10 VDC, Load R minumum 1k $\Omega$ or
	4....20 mA, maximum load 500 k $\Omega$
Weight	150 g
Dimensions	90.0x71.5x36.0 mm
Temperature range	Operation -10...+50°C
	Storage -20...+70°C
Ambient humidity	0 to 95 % RH

Table A4. Delta OHM HD 4V3T S1

Technical Specifications	
Standard measuring range	0.2-40.0 m/s
Measurement accuracy	$\pm (0.2\text{m/s}+3\%\text{f.s.})$
Response time (integration)	0.2s
selected by jumper	2s
Operating temperature electronics	0...+60°C
Operating temperature probe	0...+80°C
Compensation temperature	0...+80°C
Storage temperature	-10...+70°C
Electronics protection class	IP67
Sensor working conditions	Clean Air, RH<80%
Case dimensions	58x65x35

## VITA

Tuğba İNAN was born in Akçadağ / MALATYA in August 1, 1985. After graduation from Architecture Department of Suleyman Demirel University, she carried on her M.Sc. and Ph.D. studies as a research assistant in Izmir Institute of Technology.

### **Education**

Doctor of Philosophy in Architecture, (2010-2016)

Master of Science in Architecture, (2007-2010)

Bachelor of Architecture, (2003-2007)

### **Publications**

- Inan, T and Basaran, T. (2012). Evaluation of Effective Design Parameters on Energy Performance of Double Skin Facades. UGHEK 2012, *III. Ulusal Güneş ve Hidrojen Enerjisi Kongresi*, Osmangazi University, Turkey, 14-15 June 2012.
- Inan, T and Basaran, T. (2012). Investigation of Energy Efficient Double Skin Facades. UGHEK 2012, *III. Ulusal Güneş ve Hidrojen Enerjisi Kongresi*, Osmangazi University, Turkey, 14-15 June 2012.
- Inan, T and Basaran, T. (2012). Çift Cidarlı Cephe Sistemlerinin İncelenmesi, *Yapı Dergisi*, September, 122-127.
- Inan, T and Basaran, T. (2013). Çift Cidarlı Cepheler:Avantajları ve Dezavantajları. *II. Ulusal Tesisat Mühendisliği Kongresi*, 17-20 April 2013.
- Inan, T and Basaran, T. (2013). Effective Architectural Design Decisions in Double Skin Facades. *Sakarya University Graduate School of Applied & Natural Sciences Journal* 17(3), 427,436.
- Inan, T and Basaran, T. (2014). A General Evaluation on Double Skin Facades. Yıldız Technical University, Faculty of Architecture *Megaron E-Journal*, 9(2),132-142.
- Inan, T and Basaran, T. (2015). Çift Cidarlı Cepheler:Avantajları ve Dezavantajları. *Tesisat Mühendisliği Dergisi*, 146, 80-86, Mart/Nisan 2015.
- Inan, T., Ezan, M.A., Başaran, T., and Ereğ, A. (2015). Çift Cidarlı Cephelerdeki Akış ve Isı Transferinin Sayısal Analizi, *12. Ulusal Tesisat Mühendisliği Kongresi*, 8-11 April 2015.
- Kutluay, P., İnan, T., Ersoy, U., and Başaran, T. (2015). Türkiye'den ve Dünyadan Örnekler Işığında Çift Cidarlı Cephelerin Gelişimi, *12. Ulusal Tesisat Mühendisliği Kongresi*, 8-11 April 2015.
- İnan, T, Başaran, T and Ezan, M.E. (2016). Experimental and numerical investigation of natural convection in a double skin facade, *Applied Thermal Engineering* (106), 1225-1235.